Reactive/Adsorptive Transport in (Partially-) Saturated Porous Media

from pore scale to core scale

Amir Raoof

Environmental Hydrogeology Group

Utrecht University

Reactive/Adsorptive Transport in (Partially-) Saturated Porous Media

from pore scale to core scale

Reactief/Adsorbtie Transport in (on)verzadigde poreuze Media

van Porieschaal tot Macroschaal

(met een samenvatting in het Nederlands)

PROEFSCHRIFT
ter verkrijging van de graad van doctor aan de Universiteit Utrecht op gezag van de rector magnificus, prof.dr. G.J. van der Zwaan, ingevolge het besluit van het college voor promoties in het openbaar te verdedigen op woensdag 7 september 2011 des middags te 2.30 uur
door

Amir Raoof
geboren op 11 September 1979, te Tehran

Promoter: Prof.dr.ir. S.M. Hassanizadeh

The Reading Committee

Dr. Bradford, S. A., US Salinity Laboratory, USDA

Prof. Celia, M. A., Princeton University

Prof. Lindquist, B. W., Stony Brook University

Prof. Rossen, W. R., TU Delft

Prof. van der Zee, S. E. A. T. M., Wageningen University

ISBN/EAN:	978-90-393-56272
Title:	Reactive/Adsorptive Transport in (Partially-) Saturated Porous Media; from pore scale to core scale
Keywords:	pore scale; reactive/adsorptive transport; Partially Saturated; dispersion; relative permeability, fully implicit numerical scheme
Author:	Raoof, A.
Publisher:	Utrecht University, Geosciences Faculty, Earth sciences department
Printing:	Proefschriftmaken.nl Printyourthesis.com
NUR-code:	934
NUR-description:	Hydrologie
Series:	Geologica Ultraiectina
Series Number:	300
Number of pages:	256

- Cover photo: Pore-scale flow simulation using CFD methods; visualization by John Serkowski (PNNL).
- Cover design: Amir Raoof
- This research was supported financially by the Utrecht Center of Geosciences and NUBUS international research training group.

Acknowledgements

> *The acknowledgement is definitely an important part of the case. The case was never about money primarily. The case is about accountability.*
>
> *Sam Dubbin*

It is a pleasure to thank several individuals who contributed to the completion of this study, and assisted me during its preparation.

First and foremost, my utmost gratitude to my supervisor Majid Hassanizadeh. It has been an honor to be his Ph.D. student. Majid, you have always supported me throughout my research with your insightful knowledge while at the same time allowing me to work independently. I always enjoyed our discussions and learned so much from it.

Furthermore, I would like to thank Ruud Schotting for all his support. I am grateful to Toon Leijnse and Sjoerd van der Zee from Wageningen University for their valuable advice on numerical simulations and pore scale modeling. A sincere gratitude to Scott Bradford from USDA, for reading this dissertation. Scott, you invited me to UC Riverside, where we had extensive discussions about pore scale modeling of adsorption. Your wonderful hospitality made my visit from Riverside unforgettable. I would also like to thank Brent Lindquist from Stony Brook University for his careful review and constructive comments on this thesis. His input greatly improved production of this book. I would like to show gratitude towards Mike Celia from Princeton University for very fruitful discussions we had during meetings and conferences. I would like to thank Helge Dahle, who invited me to visit University of Bergen. We had constructive discussions on pore scale modeling. I enjoyed being involved in NUPUS international research training group. I had very useful discussions with Rainer Helmig, and other colleagues from University of Stuttgart, during several meetings and throughout my visit to Stuttgart. I would like to acknowledge Hamid M. Nick for having useful discussions on numerical programming.

My colleagues and other staff in the Hydrogeology group at UU have contributed immensely to my personal and professional development. The group has been a source of friendships, as well as good advice and collaboration. I would like to thank my friends: Saskia, Vahid, Nikos, Niels, Jack, Reza, Marian, Simona, Mariene, Brijesh, Imran, Qiu, Mojtaba, Wouter, and Shuai, as well as Leonid who visited our group from University of Bergen. Special thank to Margreet, who was of great help whenever trying to figure out all those administrative issues. Margreet, I always enjoyed our short talks during the "koffiepauze"!

From November 2010 I have started my postdoc research, on pore scale modeling of reactive solutes, at the experimental rock deformation group / HPT-lab, Utrecht University. I would like to thank Chris Spiers for his support. I am enjoying my postdoc research a lot. A big thank goes to my other friends and colleagues in HPT-lab: Colin, Hans, Magda, André, Jon, Eimert, Gert, Peter, Anne, Tim, Nawaz, Elisenda, Sabine, Sander, Bart, Reinier, Loes, Sabrina, and Ken.

From the time I came to Holland I was so lucky to meet many great people, that later became my friends. They have contributed indirectly to this study. I would like to mention a few in particular: Babak, Pasha, Marzieh, Vyron, Angelique, David, Bamshad, Baukje, Eefje, Eric, Farnoush, Rory, Lotte, Sander, Guillaume, Maartje, Mohammad, Moniek, Renée, Rick, Roeland, Veerle, Hajar, Roza, Sanaz, and Sourish.

Lastly, and most importantly, I wish to thank my family; in particular my parents, Parvin and Abbass, who raised me, supported me, taught me, and loved me. To them I dedicate this thesis.

این پایان نامه را با احترام به خانواده ام بویژه مادر و پدرم تقدیم می کنم.

بیا تا گل برافشانیم و می در ساغر اندازیم   فلک را سقف بشکافیم و طرحی نو دراندازیم
اگر غم لشکر انگیزد که خون عاشقان ریزد   من و ساقی به هم تازیم و بنیادش براندازیم

Amir Raoof
Utrecht
August 2011

CONTENTS

LIST OF FIGURES

LIST OF TABLES

CHAPTER 1

INTRODUCTION

If we knew what it was we were doing, it would not be called research, would it?

Albert Einstein

FLUID flow and mass transport in porous media is an important process in natural composite materials (soils, rocks, woods, hard and soft tissues, etc.) and many engineered composites (concrete, bioengineered tissues, etc.), at various spatial and temporal scales. Each of these scales contains specific information about the underlying physical process. Pore-scale modeling together with upscaling techniques allow the transfer of information, i.e., laws which are given on a micro-scale to laws valid on a larger scales. To do so, it is necessary to identify and understand (multiphase) flow and (reactive) transport processes at microscopic scale and to describe their manifestation at the macroscopic level (core or field scale). In the case of virus and colloid transport in porous media, understanding the transport mechanisms has recently attracted significant attention, especially in the case of groundwater polluted by contaminants that could adsorb to colloids. Colloids can enhance pollutant mobility [McCarthy and Zachara, 1989], and field-based results suggest the importance of colloids in the transport of low-solubility contaminants [Vilks et al., 1997, Kersting et al., 1999]. Enhanced mobility together with very limited acceptable concentrations of hazardous solutes (in the range of few parts per billion) have raised more attention to the modeling and accurate prediction of the migration and distribution of contaminants.

The design of successful subsurface remediation technologies is based upon the understanding of the (reactive) transport processes at the smaller scales. This information can be obtained by extensive experimental characterization, which is usually very expensive and time-consuming. As such, mathematically based numerical modeling has provided an indispensable tool to reduce experimental investigations and to make them more cost-effective.

At the pore scale, a porous medium system consists of a series of void spaces distributed heterogeneously, and one or more fluid phases present simultaneously (e.g. as air and water under partially saturated conditions). As a solute transports within these phases, it may undergo absorption, reaction, and transformation. These transport processes are further complicated by the heterogeneity within the subsurface system's physical and chemical characteristics. The inherent pore scale heterogeneity, as well as the complexity involved in the physics of (partially-) saturated systems, result in a significant challenge to the development of fundamental theories of flow and transport, which are crucial to the design and investigation of new remediation technologies. To date, many difficult problems still remain to be resolved, and standard theories which have been in existence for several decades have proven to be inadequate to solve these problems. The purpose of this research is to improve the understanding of (partially-) saturated flow and (reactive) transport in porous media by using an alternative modeling approach: Pore Network Modeling (PNM). For a better understanding of the macroscopic modeling, the scale issues in subsurface systems should be understood first.

1.1 Issues of scale

Since modeling in porous media involves transfer of data over several length scales, scaling effects are of great importance. If the solute undergoes reaction and adsorption, reactive parameters must also be included in upscaling processes. The state of the system (e.g., whether saturated, wether occupied by different phases) is also a critical factor which can affect the macro-scale behavior of the system. Indeed, many studies of flow and transport in porous media were motivated by one central question, namely, how do pore scale processes in a medium influence the effective upscaled transport parameters? Without good insight into such influence, accurate forecasting models and sound remediation techniques cannot be developed. Pore scale modeling and the upscaling process contain three components: (i) defining or conceptualizing pore scale geometry and structure, (ii) composing and solving the equations of physics at the pore scale and (iii) defining macroscopic parameters, or upscaling. Through upscaling, appropriate parameter values are assigned to larger scale models. Discrepancies between measured values under static conditions and the results obtain though dynamic experiments and modeling show the need for a comprehensive study of upscaling from pore-to-core scales in which parameters are much easier to measure. While modeling at a larger scale, it is usually not feasible to take all pore scale properties, such as interfaces, into account. However, without inclusion of these effects in macro-scale descriptions, neither the techniques nor can their predictions gain credibility.

The length scale of interest in porous medium systems may vary from a molecular level (on the order of 10^{-11} to $10^{-9}m$) to a mega level (on the order of $10^{+2}km$ for some regional applications). The scale hierarchy associated with flow and transport problems in porous media, is often divided into: molecular scale, micro or pore scale, macro or lab scale, meso or field scale, and mega or regional scale. Because natural porous media are neither homogeneous nor uniformly random, measurements of constitutive parameters may have meaning with respect to one scale. Instrumentation used in measuring parameters at one scale may appear to have little relevance to other scales [Celia et al., 1993]. As a result, developing models that reflect the broad range of scales in a systematic and consistent way is an open problem with enormous complexity [Miller and Gray, 2002].

1.2 Continuum modeling approach

It is sometimes difficult to verify solutions at the pore scale because most instruments are available for characterizing systems at a larger scale, often in terms of parameters that are not defined at the pore scale. The standard way to overcome this difficulty is to define macroscopic variables by averaging microscopic values over a representative elementary volume (REV) [Bear, 1972], in which laboratory experiments can be carried out. This will be the continuum scale where the standard porous medium continuum modeling approach applies. The standard approach starts from various balance equations governing the fluid flow in porous media by averaging variables over an REV. Through averaging, the intricate variations due to the microscopic heterogeneity are smoothed out, and the governing equations can be considered as equations that describe an equivalent homogeneous system. In applying the continuum approach, macroscopic medium parameters, such as permeability, saturation, upscaled adsorption rates, and dispersion coefficients need to be introduced. As the microscopic governing equations contain no information regarding these macroscopic parameters, they form an undetermined system, insufficient to be closed unless further equations are supplied. The additional equations, which are an important part of the continuum theory, are known as constitutive relations. These relations, such as the relation between permeability and pore properties of porous media, depend upon the internal constitution of the particular porous material considered. By upscaling from the pore scale, constitutive relations can be determined for a specific case. Because the constitutive relations are ultimately used to model macro-scale problems, understanding of the pore-scale processes and proper incorporation of their effects in larger-scale relations must be accomplished.

Although applying the continuum modeling approach is a common practice, there are some difficulties and drawbacks involved when applying the continuum approach. Performing experiments to reveal the constitutive relationship is usually difficult and costly. For example, serious experimental difficulties are encountered in measuring relative permeabilities or solute dispersivity in a porous medium. The lack of available constitutive data is frequently cited by both petroleum and groundwater engineers as a primary barrier to acceptable predictions (e.g. Abriola and Pinder [1985], Aziz and Settari [1979]). In addition, although constitutive relations have a crucial bearing on the accuracy of subsurface flow models, they are approximate solutions and often uncertain [Miller et al., 1998, Genabeek and Rothman, 1996]. Over the past two decades, much effort has been expended to develop alternate theories to the standard approach. For example, Gray and Hassanizadeh have suggested a more complete approach of modeling multiphase flow based on integration over a REV to produce mass, momentum, and energy conservation equations that are formulated based on volume, interfacial area and contact lines [Gray and Hassanizadeh, 1991b, Hassanizadeh and Gray, 1993, 1979, 1980, Gray and Hassanizadeh, 1991a].

1.3 Pore-scale modeling approach

Pore-scale modeling provides opportunities to study transport phenomena in fundamental ways because detailed information is available at the microscopic pore scale. This offers the best hope for bridging the traditional gap that exists between pore scale and macro (lab) scale descriptions of the process. As a result, consistent upscaling relations can be performed, based on physical processes defined at the appropriate scale. Pore-scale modeling offers an important tool to develop constitutive relations that are difficult and even impossible to obtain by lab experiments. The basic strategy is to perform numerical experiments analogous to those performed in the laboratory. However, the pore-scale simulation provides more versatility in choice of parameters, a greater variety of quantitative data and frequency of observation, and more importantly, easier design of numerical experiments. Recent advances in micro-model experiments and high-resolution tomographic imaging (e.g. Spanne et al. [1994], Soll et al. [1994], Buckles et al. [1994], Ferreol and Rothman [1995]), which allows for accurate representation of pore morphology, have spurred an explosion of interest in pore-scale modeling. The effect and significance of these pore-scale processes are then able to be incorporated into constitutive theories to achieve an accurate description of larger-scale phenomena of interest. Moreover, pore-scale modeling provides a significant means to investigate closure relations involving new variables, such as interfacial area and common line length, and new theories that seek to describe the behavior of these new variables.

Despite the large number of numerical studies of single-phase and multiphase systems that have been done, pore-scale study in porous media is still in its scientific infancy, since it is only over the last decade that relatively inexpensive high-performance computers have become available. Current pore-scale applications are limited to relatively small domains and simple problems [Pereira, 1999, Blunt, 2001]. However, the dramatic evolution of computational capabilities offers us new opportunities for simulating larger domains and modeling a wider range of processes. This makes pore-scale approaches potentially attractive for industrial or field applications as measurement tools to compute transport properties, such as relative permeability and unsaturated dispersivity of a particular subsurface system. One can imagine that computer simulations may be employed to complement processes such as dispersivity measurements under different degrees of saturations that normally can take up as long as months to perform in the laboratory. In particular, if the current rate of increase in computing power continues, one can foresee, perhaps on the order of a decade, the capability of simulating microscopic flows that include large-scale heterogeneities.

One well-known method for pore-scale modeling in porous medium is Pore Network Modeling (PNM) [Fatt, 1956b]. In PNM, fluid flow and (reactive) solute transport processes are simulated directly at the microscopic scale without assuming a priori the traditional macroscopic equations (such as the famous Darcy law). This is done by creating a simulated porous medium made by pore bodies and pore throats of different sizes (the "geometry" of the porous medium) variably connected to each other (the "topology" of the porous medium) and then simulating through this network the fluid flow and (reactive) solute transport process of interest at the microscale, with the relevant physics implemented on a pore to pore basis. Compared to other pore scale modeling methods, such as the lattice-Boltzmann method, pore-network models are computationally effective. Recent advances have allowed modeling a degree of irregularity in pore cross-sectional shape that was not available in earlier PNMs. In addition, pore-network models are capable of incorporating some important statistical characteristics of porous media such as pore sizes [Øren et al., 1998b, Lindquist et al., 2000], coordination number distributions [Raoof and Hassanizadeh, 2009] and topological parameters such as Euler number [Vogel and Roth, 2001].

Pore network modeling can provide flow, relative permeabilities, capillary pressures and solute concentration data in an efficient way, which could be difficult to measure through experimental methods. In addition, using PNM, one can explore the sensitivity of these data to a variety of different conditions. Indeed the scope for utilization of PNM is in fact much wider and extends to the study and optimization of a variety of transport processes and to most of those cases where laboratory investigation would be long, costly or technically very difficult. As examples, pore-network models have been widely used to study: multiphase flow in porous media [Celia et al., 1995, Blunt, 2001, Joekar-Niasar et al., 2008b, 2010]; chemical and biological processes, such as the dissolution of organic liquids [Zhou et al., 2000b, Held and Celia, 2001, Knutson et al., 2001b]; biomass growth [Suchomel et al., 1998c, Kim and Fogler, 2000, Dupin et al., 2001]; and adsorption [Sugita et al., 1995b, Acharya et al., 2005b, Li et al., 2006b]. In recent pore-scale modeling, various types of adsorption reactions have been used: linear equilibrium (e.g., Raoof and Hassanizadeh [2009]) and nonlinear equilibrium [Acharya et al., 2005b]; kinetic adsorption (e.g., Zhang et al. [2008]); and heterogeneous adsorption in which adsorption parameters were spatially varying (e.g., Zhang et al. [2008]).

Pore geometry and topology have a major influence on solute transport and/or multiphase flow in porous systems. Sok et al. [2002] concluded that it is extremely important to ensure that a pore-network model captures the main features of the pore geometry of porous medium. The primary topological feature of a pore system is the coordination number distribution. Physical flow and solute transport properties on the other hand require, in addition, exact or approximate equations of motion. Often this involves steady or unsteady state transport of physical quantities such as mass, energy, charge or momentum. Pore-network models are commonly based on an idealized description of pore spaces [Scheidegger, 1957, De Jong, 1958]. However, in order to mimic realistic porous media processes, network models should reproduce the main morphological and topological features of real porous media. This should include pore-size distribution, and coordination number and connectivity [Helba et al., 1992, Hilfer et al., 1997, Øren et al., 1998b, Ioannidis and Chatzis, 1993a, Sok et al., 2002, Arns et al., 2004]. In the present study, we have used a Multi-Directional Pore Network (MDPN) for representing a porous medium. One of the main features of our network is that pore throats can be oriented not only in the three principal directions, but in 13 different directions, allowing a maximum coordination number of 26, as shown in Figure 1.1.

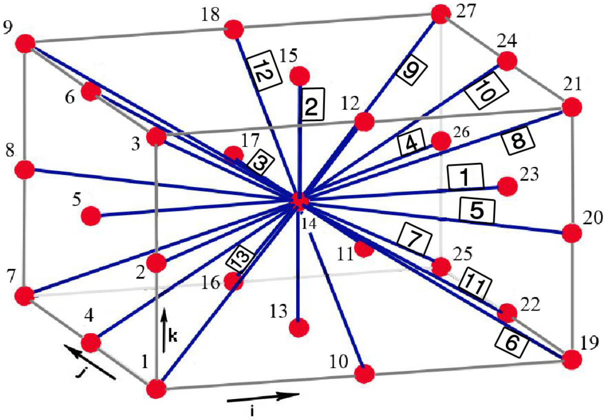

Figure 1.1: Schematic of a 26-connected network. Numbers inside the squares show tube directions and others are pore body numbers [Raoof and Hassanizadeh, 2009].

Flow and transport processes are simulated at the pore scale in detail by explicitly modeling the interfaces and mass exchange at surfaces. The solution of the pore network model provides local concentrations and enables computation of the relationship between concentrations and reaction rates at the macro scale to concentrations and reaction rates at the scale of individual pores, a scale at which reaction processes are well defined [Li et al., 2007a,b]. Comparing the result of pore-scale simulations with and appropriate model representing the macro-scale behavior, one can study the relation between these two scales.

1.4 Research objectives

This research aims to identify and describe the physical/chemical processes that govern the transport of both passive and reactive/adsorptive solutes in porous media by using PNM. We consider mass transfer of reactive/adsorptive solutes though interfaces, under both saturated and partiality saturated conditions. While under saturated conditions the interfaces are only those of solid-water interfaces, under partially saturated conditions, there will be also mass transfer though air-water interfaces.

This study is aimed at describing steady state Newtonian fluid flow in a rigid porous medium. During miscible displacement, reactive solutes in a (partially-) saturated medium are transported in a single fluid phase (water being the carrier). The most common transport case that one encounters is adsorption, which, in large, is controlled by the reactivity of the solutes in the fluid phase and the chemical affinity and physical heterogeneity of the solid phase. In this study, we have utilized a Multi-Directional Pore-Network (MDPN) model [Raoof and Hassanizadeh, 2009]. Fundamental laws of physics are applied at the pore scale, whereas the macroscopic quantities (such as permeability, dispersivity and average concentrations) are obtained through averaging over the pore network domain. To meet our objectives we focus on both physical and topological heterogeneities (different sized pores, variable coordination numbers) and chemical processes. Hence, we focus on a more realistic microscopic structure, applying equations of microscopic physics and chemistry and perform rigorous upscaling. There are many other novel and unique aspects to this thesis, though which we develop more accurate and realistic schemes to study flow and transport under partially saturated conditions. For this purpose we have developed an extensive FORTRAN 90 modular package which covers: generation of random structure networks; simulation of drainage process; discretization of pore spaces on the basis of saturation state of each pore; and solution of flow and reactive transport under both saturated and unsaturated conditions using several algorithms. The governing equations are solved applying a fully implicit numerical scheme; however, efficient substitution methods have been applied which make the algorithm more computationally effective and appropriate for parallel computations.

By averaging over a representative MDPN, we calculate upscaled relevant parameters for saturated conditions, including permeability, dispersion coefficient, coefficient of variation of pore water velocities, measures of plume spreading, and upscaled adsorption parameters. For the case of partially saturated conditions the results consist of the (upscaled) capillary pressured-saturation relation, relative permeability, total interfacial area, specific surface area of reactive interfaces, unsaturated dispersivity-saturation relation, fraction of percolating saturated pores, coefficient of variation of pore water velocities, and adsorption parameters.

The averaging helps to gain a better understanding of the flow and reactive transport at the core scale; whenever possible, we have compared our results with the results of experimental observations and analytical equations. In this way, we evaluate the limitations and sufficiency of available analytical equations and macro scale models for prediction of transport behavior of (reactive) solutes.

1.5 Outline of the thesis

This thesis contains six major themes and hence, each chapter is an independently readable manuscript. However, the formulations, algorithms, and capabilities made in each chapter are included in subsequent chapters which collect all chapters into one piece. On the basis of the physics of the process to be studied, the thesis is divided into three parts:

- **Part I**: Generation of Multi-Directional Pore Network (MDPN)
- **Part II**: Upscaling and pore scale modeling under saturated conditions
- **Part III**: Upscaling and pore scale modeling under partially-saturated conditions

Part I:

Since pore-space structure is one of the major features controlling both flow and transport processes, we have started this research by generating a more realistic pore network compared to the traditional networks used in many earlier studies.

Chapter 2 is devoted to the development of a new approach for construction of MDPN models. According to this technique, the continuum pore space domain is discretized into a network of pore elements, namely pore bodied and pore throats. The Multi-Directional capability of the pore network allows a distribution of coordination numbers ranging between zero and 26, with pore throats orientated in 13 different directions, rather than the 3 directions commonly applied in pore network studies. This property helps to capture a more realistic distribution of the flow field which is essential in determining upscaled parameters such as (relative) permeability or (unsaturated) dispersions coefficients. The generation of the MDPN is optimized using a Genetic Algorithm (GA) method and the morphological characteristics of such networks are compared with those of physical sandstone and granular samples by comparing coordination number distributions. Good agreement was found between simulation results and observation data on coordination number distribution and other network properties, such as numbers of pore bodies, pore throats, and average coordination number. This method can be especially useful in studying the effect of structure and coordination number distribution of pore networks on reactive transport and multiphase flow in porous media systems.

Part II:
The second part, Chapters 3 and 4, covers the upscaling pore scale modeling under saturated conditions.

Chapter 3 deals with the upscaling transport of adsorbing solutes from micro scale to the effective pore scale. We assumed micro scale equilibrium adsorption, which means that concentration of adsorbed solute at a point on the grain surface is algebraically related to the concentration in the fluid next to the grain. We have shown that due to concentration gradients developed within the pore space, the equilibrium adsorption may not hold in the upscaled limit where we deal with average concentrations. The main objective of Chapter 3 is to develop relationships between the pore-scale adsorption coefficient and the corresponding upscaled adsorption parameters. Two approaches are used: theoretical averaging and numerical upscaling. In the averaging approach, equilibrium adsorption is assumed at the pore-scale and solute transport equations are averaged over an REV. This leads to explicit expressions for macro-scale adsorption rate constants as a function of micro-scale parameters such as pore scale Peclet number and the pore scale distribution coefficient. The upscaled adsorption parameters are found to be only weak functions of velocity; they strongly depend on geometry of the pore and the diffusion coefficient as well as the pore-scale distribution coefficient. Results of the two approaches agree very well. The upscaling relations from this chapter are appropriate to be used within core scale models, represented by PNM.

Chapter 4 presents the continuation of upscaling from effective pore scale to the core scale where Darcy-scale flow and transport parameters are applied. This is done by utilizing the upscaling relations developed in Chapter 3 and applying them into the MDPN model developed in chapter 2. This enabled us to scale up from a simplified, but reasonable, representation of microscopic physics to a scale of interest in practical applications. This procedure has resulted in relationships for core scale adsorption parameters in terms of micro-scale parameters. We find relations between core-scale adsorption parameters and local-scale transport coefficients, including molecular diffusion coefficient, specific surface area, and average pore-throat size.
We have shown that even if there is equilibrium adsorption at the pore wall (i.e., grain surface), one may need to employ a kinetic description at larger scales. In contrast to some studies that reported dependency of reaction parameters on flow rate, we found that that these upscaled kinetic parameters are only a weak function of velocity.

Part III:
Part III of the thesis deals with flow and transport of both reactive/adsorptive and passive solutes under partially saturated conditions.

Chapter 5 deals with construction of a new formulation for pore-network modeling of two-phase flow. Pore-network models of two-phase flow in porous media are widely used to investigate constitutive relationships between saturation and relative permeability as well as capillary pressure. Results of many studies show a discrepancy between calculated relative permeability and corresponding measured values. An important feature of almost all pore-network models is that the resistance to flow is assumed to come from pore throats only; i.e., the resistance of pore bodies to the flow is considered to be negligible compare to the resistance of pore throats. We have shown that the resistance to the flow within filaments of fluids in drained pore bodies is comparable to the resistance to the flow within (drained) pore throats. In this study, we present a new formulation for pore-network modeling of two-phase flow, which explicitly accounts for the resistant to the flow within the drained pore bodies and calculates fluxes within drained pore bodies. Steady-state conditions are imposed on the network and the Kirchoff problem is solved numerically by using preconditioned conjugate gradients [Hestenes and Hestenes, 1980]. The solution provides fluxes and the resulting relative permeability-saturation relation under different saturations. In a quantitative investigation, we have shown the significance of this effect under primary drainage conditions, by applying our formulation in a MDPN model. Resulting saturation-relative permeability relationships show very good agreement with measured curves.

Chapter 6 is devoted to the study of the dispersion coefficients under partially saturated conditions using a new formulation. It is known that in unsaturated porous media, the dispersion coefficient depends on the Darcy velocity as well as saturation. The dependency of dispersion on velocity is fairly studied, however, there is not much known about its dependence on saturation and the underlying process. The purpose of this chapter is to investigate how the longitudinal dispersivity varies with saturation. We have represented the porous medium with our MDPN. Both pore bodies and pore throats have volumes and we assign separate concentrations to each of them. Further, since pore geometry and corner flows greatly influence transport properties, efforts are made to include different angular cross sectional shapes for the pore throats. This includes circular, rectangular, and irregular triangular cross sections, which are important especially under unsaturated/two-phase flow and reactive transport. After the construction of the pore network, dispersivity was calculated by solving the mass balance equations for solute concentration in all network elements and averaging the concentrations over a large number of pores. We have introduced a new formulation of solute transport within a pore network which helps to capture the effect of limited mixing under partially-saturated conditions. In this formulation we refine the discretization on the basis of the saturation state of pores. We assign separate concentrations to different corners of a given drained pore body and also assign different concentrations to different corners of a drained angular pore throat. This formulation allows a very detailed description of pore-scale solute transport processes by accounting for limitations in mixing as a result of reduced water content. The numerically computed dispersivities successfully explain the results obtained through experimental studies, and show the underlaying pore scale processes contributing to dispersion under unsaturated conditions.

Chapter 7 deals with transport of adsorptive solute under partially saturated conditions. All of the modeling capabilities developed in previous chapters are included in this chapter. Compared to column scale experimental studies on adsorptive transport, there is lack of pore scale modeling studies, especially under unsaturated porous media. Under unsaturated conditions, the system contains three phases: air, water, and solid. The principal interactions usually occur at the solid-water interfaces (sw) and air-water interfaces (aw) and are thus greatly influenced by water content. In this chapter, we have formulated various types of adsorption: i) two site (sw and aw interfaces) kinetic; ii) two site equilibrium; and iii) one site (sw or aw interfaces) kinetic and one site equilibrium.

To numerically solve the mass balance equations, we have applied a fully implicit numerical scheme for transport of adsorptive solute under unsaturated conditions. Through applying an efficient numerical algorithm, we have reduced the size of system of linear equations by a factor of at least three, which significantly decreases computational time.

1.6 Programming issue

CPNS: Complex Pore Network Simulator

Through this study to generate pore networks and accurately simulate fluid flow and transport of reactive/adsorptive solute, we have developed an advanced FORTRAN 90 modular package. All the above mentioned formulations and capabilities are included in CPNS, which enables one to simulate fluid flow and transport of adsorptive/reactive solutes under both saturated and partially saturated conditions to upscale from pore scale to the core scale. For this study, three programming languages are used: Visual Basic Application (VBA) in Excel, MATLAB programming, and FORTRAN 90 programming. The inputs for the model are inserted into Excel sheets which are then recorded as input files using Excel VBA to be used by the FORTRAN simulator. Throughout the execution of the model, data and results are transferred to MATLAB using MATLAB Engine for possible analysis and post processing. Since various physical (saturated and unsaturated) and chemical (tracer, equilibrium adsorption, kinetic adsorption, system of reactions) conditions should be simulated, to keep numerical commutations efficient, we designed CPNS as a modular package composed of separate interchangeable components, each of which accomplishes one mode of simulation. Figure (1.2) shows the flowchart of CPNS.

The last version of CPNS (not included in this thesis) is capable of simulating transport of multi-competent chemical species undergoing equilibrium and/or kinetic reactions [Raoof et al., 2011]. Both advective and diffusive transport processes are included within the pore spaces. To simulate chemical reactions, MDPN is coupled with the Biogeochemical Reaction Simulator (BRNS) [Regnier et al., 2002, 2003], which performs the reaction part. This gives major advantages for simulation of complicated system of reactions. The coupling between transport and reaction parts is done though a non-iterative sequential splitting operator. After each transport time step, the concentrations of components within pore bodies and pore throats are transferred to BRNS for calculation of chemical reactions. In the case of reactions with the solid surfaces, pore geometries will change which, in turn, causes changes in porosity. In such a cases, the pressure field will be recalculated after each reaction time step to calculate new permeabilities. Through this process we can simulate porosity/permeability evolutions due to chemical reactions, and calculate the relation between permeability and porosity for a specific network [Raoof et al., 2011].

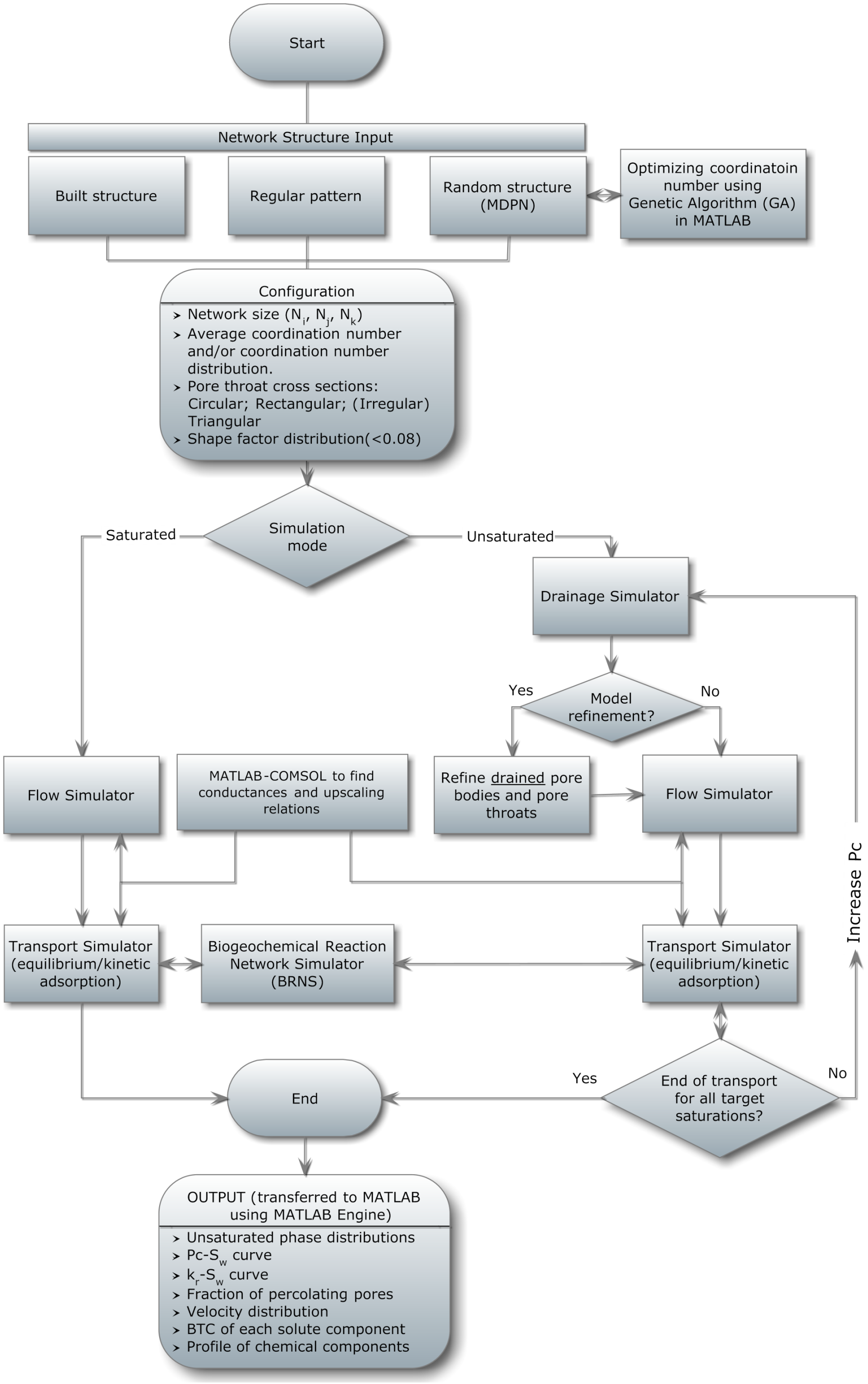

Figure 1.2: Flowchart of CPNS showing the relation between different parts of the model.

Part I

Generation of Multi-Directional Pore Network

Published as: Raoof, A. and Hassanizadeh S. M., *"A New Method for Generating Pore-Network Models of Porous Media"*, Transport in Porous Media, vol. 81, pp. 391–407, 2010.

CHAPTER 2

A NEW METHOD FOR GENERATING MULTI-DIRECTIONAL PORE-NETWORK MODEL

> *Creativity is not the finding of a thing, but the making something out of it after it is found.*
>
> *James Russell Lowell*

Abstract

In this study, we have developed a new method to generate a Multi-Directional Pore Network (MDPN) for representing a porous medium. The method is based on a regular cubic lattice network, which has two elements: pore bodies located at the regular lattice points and pore throats connecting the pore bodies. One of the main features of our network is that pore throats can be oriented in 13 different directions, allowing the maximum coordination number of 26 that is possible in a regular lattice in 3D space. The coordination number of pore bodies ranges from 0 to 26, with a pre-specified average value for the whole network. We have applied this method to reconstruct real sandstone and granular sand samples through utilizing information on their coordination number distributions. Good agreement was found between simulation results and observation data on coordination number distribution and other network properties, such as number of pore bodies and pore throats and average coordination number. Our method can be especially useful in studying the effect of structure and coordination number distribution of pore networks on transport and multiphase flow in porous media systems.

2.1 Introduction

Pore-scale processes govern the fundamental behavior of multi-phase multi-component porous media systems. The complexity of these systems, the difficulty to obtain direct pore-scale observations, and difficulties in upscaling the processes have made it difficult to study these systems and to accurately model them with the traditional averaging approaches. Determination of most multiphase properties (e.g., residual saturation) and constitutive relations (e.g., capillary pressure, relative permeability) has been based primarily on empirical approaches which are limited in their detail and applicability. Pore-scale modeling (e.g., pore-network and Lattice-Boltzmann model) has been used to improve our descriptions of multiphase systems and to increase our insight into micro-scale flow and transport processes. its power and versatility lies in its ability to explain macroscopic behavior by explicitly accounting for the relevant physics at the pore level. However, in order to produce realistic predictions, network models require accurate descriptions of the morphology of real porous medium. Previous works have clearly demonstrated the importance of the geometric properties of the porous media, in particular, the distributions of sizes and shapes of pores and throats and the characterization of porethroat correlations [Larson et al., 1981, Øren and Pinczewski, 1994, Blunt et al., 1994, 1992, Helba et al., 1992, Øren et al., 1992, Ioannidis and Chatzis, 1993b, Paterson et al., 1996b, Pereira et al., 1996, Knackstedt et al., 1998]. Equally important to the geometric properties are network topology parameters such as connectivity or coordination number and coordination number distribution. Coordination number, z, is defined as the number of bonds (or pore throats) associated to a site (or pore body) in the network.

Pore geometry and topology have a major influence on solute transport and/or multiphase flow in porous systems. For example, in multiphase flow, the nonwetting phase may be trapped if it is completely surrounded by the wetting fluid and in this case, no further displacement is possible in a capillarity-controlled displacement. These isolated nonwetting blobs are at residual saturation and their size distribution and shape can have significant effects on fate and transport of dissolved pollutants [Mayer and Miller, 1992, Reeves and Celia, 1996, Dillard and Blunt, 2000]. The nonwetting blobs assume shapes that are influenced by the pore geometry and topology (e.g., aspect ratio, connectivity, and pore-size variability) and their size can range over several orders of magnitude. Sok et al. [2002] have concluded that a more complete description of network topology is needed to accurately predict residual phase saturations. Therefore, it is extremely important to ensure that a pore-network model captures the main features of the pore geometry of porous medium.

The primary topological feature of a network is the coordination number. As has been noted by many authors [Chatzis and Dullien, 1977, Wilkinson and Willemsen, 1983], the coordination number will influence the flow behavior significantly. It also has a significant impact on the trapping of the residual nonwetting phase in multiphase flow; e.g., through bypassing and piston-like pore filling [Fenwick and Blunt, 1998].

A pore network model must represent not only the mean coordination number but also the distribution of the coordination number of the medium. Despite the overwhelming evidence for the presence of a wide range of coordination numbers in real porous media, in most recent network modeling studies, a regular network with a fixed coordination number of six has been used. This means that a given site is connected to six neighboring sites via bonds, which are only located along the lattice axes in three principal directions. This kind of model neglects the topological randomness of porous media. It also shows direction dependence. For example, if the pressure gradient if applied in a diagonal direction, the resulting flow could not happen in this direction as there are no direct network connections in any diagonal direction. We refer to this type of network as a ”three-directional lattice” pore-network.

With respect to coordination number, Ioannidis et al. [1997a] measured the average coordination number, z, for serial sections of a sandstone core and for stochastic porous media [Ioannidis and Chatzis, 2000] and found $z = 3.5$ and $z = 4.1$, respectively. Bakke and coworkers [Bakke and Øren, 1997, Øren et al., 1998b, Øren and Bakke, 2002a, 2003b] developed a process-based reconstruction procedure which incorporates grain size distribution and other petrographical data obtained from $2D$ thin sections to build network analogs of real sandstones. They report mean coordination numbers of $z = 3.5 - 4.5$ [Øren and Bakke, 2002a, 2003b].

Direct measurements of $3D$ pore structure using synchrotron X-ray computed microtomography (micro-CT) [Flannery et al., 1987, Dunsmuir et al., 1991, Spanne et al., 1994] coupled with skeletonization algorithms [Thovert et al., 1993, Lindquist et al., 1996, Bakke and Øren, 1997, Øren et al., 1998b, Øren and Bakke, 2002a, 2003b] indicate that $z = 4$ for most sandstones.

Arns et al. [2004] did a comprehensive study of the effect of network topology on drainage relative permeability. They considered the topological properties of a disordered lattice (rock network) derived from a suite of topological images of Fontainbleau sandstone (z = 3.3-3.8) which displayed a broad distribution of coordination number [Venkatarangan et al., 2000]. They have constructed some different network types and compared them to the rock network. The first network type was a regular cubic lattice network with fixed coordination number of 6 and identical geometric characteristics (pore and throat size distribution). Comparison between the relative permeability curve for the rock network and that computed on the regular cubic lattice showed poor agreement. The second network type was a regular lattice network with average coordination number similar to the rock network. This network also showed poor agreement in comparison with the rock network. Their result showed that matching the average coordination number of a network is not sufficient to match relative permeabilities. Topological characteristics other than mean coordination number are important in determining relative permeability. The third network was a random structure network with coordination number distribution which closely matched that of the equivalent rock network. They observed a more reasonable approximation to the relative permeability curves. Their results clearly show the importance of matching the full coordination number distribution when generating equivalent network models for real porous media. They have increased the size of network and found network sizes up to the core scale still exhibit a significant dependence on network topology.

Direct mapping from a real sample will yield a disordered lattice, whereas statistical mapping, for the sake of convenience, is done on regular lattices. There are some studies showing the equivalence of regular and disordered systems (e.g., Arns et al. [2004], Jerauld et al. [1984]) having the same coordination number distribution. This formally justifies application of work on regular lattices to real porous media.

Studies done by Venkatarangan et al. [2000] involving the use of high-resolution X-ray computer tomography for imaging the porous media have shown that there is a wide-ranging coordination number in real porous media. They used images from four different Fontainbleau sandstone samples, with porosities of 7.5%, 13%, 15%, and 22% to find geometric and topological quantities required as input parameters for equivalent network models. They found coordination numbers larger than 20, depending on medium porosity. For example, they found coordination numbers up to 23 at 15% porosity and 14 at 13% porosity. The maximum coordination number decreased considerably with decreasing porosity.

In fact, most studies [Ioannidis et al., 1997a, Venkatarangan et al., 2000, Øren

and Bakke, 2003b] show that rock samples exhibit a broad distribution of coordination numbers. Whilst the majority of pores were 3-connected, some pores displayed $z > 15$ [Ioannidis and Chatzis, 2000, Venkatarangan et al., 2000, Øren and Bakke, 2003b].
[Øren and Bakke, 2003b] have used information obtained from 2D thin sections to reconstruct 3D porous medium of Berea sandstone. They found the coordination number ranging from 1 to 16 with an average value of 4.45.
In particular, the distribution of z on disordered networks was shown to have a strong effect on the resultant residual phase saturation. Al-Raoush and Willson [2005] have produced high-resolution, three-dimensional images of the interior of a multiphase porous system using synchrotron X-ray tomography. The porous medium was imaged at a resolution of $12.46\mu m$ following entrapment of the nonwetting phase at residual saturation. Then they extracted the physically representative network structure of the porous medium. They found that the mean coordination number of pore bodies that contained entrapped nonwetting phase was 10.2. This was much higher than the mean coordination number of the system, which was 3.78. In this study, we present a new method to generate a Multi-Directional Pore Network (MDPN) for representing a porous medium. The method is based on a regular cubic lattice network, which has two elements: pore bodies located at the regular lattice points and pore throats connecting the pore bodies. One of the main features of MDPN is that pore throats can be oriented in 13 different directions, allowing a maximum coordination number of 26 that is possible in a regular lattice in $3D$ space. The coordination number of pore bodies ranges from 0 to 26, with a pre-specified average value for the whole network.

2.2 Methodology and Formulation

2.2.1 General Network Elements in MDPN

Consider a lattice composed of an array of cubes. Let us call the line intersections, “sites”, and the segments connecting them, “bonds”. A bond is assumed to exist between each pair of nearest neighbor sites in the lattice. In this multidirectional 3D network, the bonds are aligned in 13 different directions. Figure (2.1) shows all possible connections for site no. 14 in the center of a $3 \times 3 \times 3$ network, consisting of 8 cubes. Therefore, in a cubic lattice, one bond can be connected to a maximum 50 neighboring bonds. A site can be connected to a maximum of 26 nearest neighbor sites, which is equal to the maximum coordination number, $z = 26$.

For simplicity of description of the network, let us assume that the flow is from left to the right, as determined by macroscopic pressure gradient. Denote the number of lattice sites in the flow direction by N_i, and let N_j and N_k denote the number of sites in the other two directions. Thus, the size of a 3D network is N_{ijk} $(= Ni \times Nj \times Nk)$.

Let $N_{jk}(= N_j \times N_k)$ be the size of a two-dimensional rectangular grid perpendicular to overall flow direction. Choice of the numbering of lattice bonds directions is not critical; in Figure (2.1), directions $1, 2,$ and 3 are chosen to be parallel to three principal directions of the underlying 3D grid (i.e., directions i, j, and k). Note that, to keep the figure less crowded, we have shown lattice bonds passing through site 14 only. All other lattice bonds in network receive the same direction number as their parallel bond in the Figure (2.1).

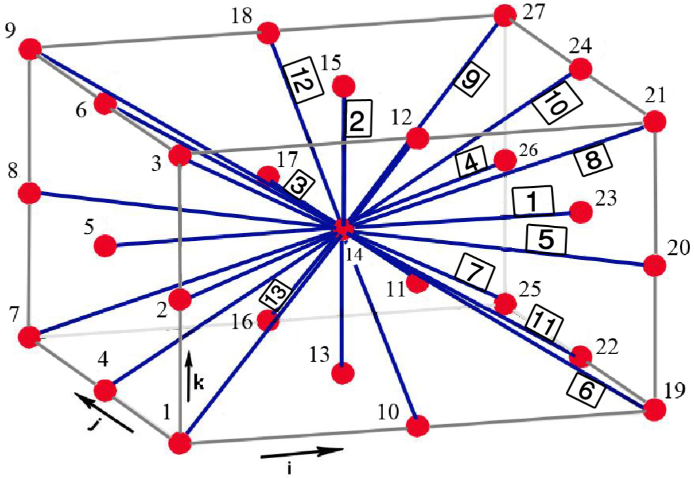

Figure 2.1: Schematic of the Multi-directional pore network consisting of 8 cubes, size: $N_i = 3, N_j = 3, N_k = 3$. Numbers inside the squares show bond directions and others are site numbers. To keep the figure less crowded, only bonds which are connecting site 14 to its neighboring sites are shown.

The lattice numbering system of lattice is shown in (2.1): starting from the first vertical plane at left, within each N_{jk} plane, sites are numbered from bottom right to top left and then continued with the next N_{jk} plane in the overall flow direction.

A given site can be connected to two other sites along any given direction number: one in the forward direction (increasing site number) and one in the backward direction (decreasing site number). For example, in the direction no. 1, site 14 is connected (in forward direction) to site no. 23 and (in backward direction) to site no. 5.

Obviously, sites which are located on the boundaries have smaller coordination numbers. For example, in Figure (2.1), the only site with all connections in all the 13 directions is site number 14, since the rest of the sites are situated on the boundaries of the network.

2.2.2 Network Connections

Based on the numbering system described above and shown in Figure (2.1), we can provide expressions for determining the connections between various sites inside a general network. Table (2.1) gives expressions for finding sites connected to site number N in forward directions. As an illustration, the site numbers connected to site $N = 14$ in Figure (2.1) are also given.

Assuming horizontal overall flow direction, we also assume that sites in the left and right boundaries cannot connect to other sites in the same plane, but can only connect to sites inside the network. As a result of this restriction, assigning different pressure values to different sites on the left or right boundaries would not cause any in-boundary-plane flow.

Table 2.1: Expressions for finding all sites connected to site number N in the forward directions. In example of Figure (2.1), $N_k = 3$ and $N_{jk} = 9$.

Direction number	**General expression for site N**	**Example of Figure (2.1), site N=14**
1	$N + N_{jk}$	23
2	$N + 1$	15
3	$N + N_k$	17
4	$N + N_{jk} + N_k$	26
5	$N + N_{jk} - N_k$	20
6	$N + N_{jk} - N_k - 1$	19
7	$N + N_{jk} + N_k - 1$	25
8	$N + N_{jk} - N_k + 1$	21
9	$N + N_{jk} + N_k + 1$	27
10	$N + N_{jk} + 1$	24
11	$N + N_{jk} - 1$	22
12	$N + N_k + 1$	18
13	$N + N_k - 1$	16

2.2.3 Connection Matrix

Perhaps the best way to get a desired pattern in the network, to generate the bonds, and understand the effect of the network boundaries on the bonds is to examine the matrix of connections. Figure (2.2) shows a fully connected network of size $N_i = N_j = N_k = 3$ and the corresponding connection matrix. The connection matrix is a centrosymmetric matrix (symmetric with respect to both the main diagonal and the anti-diagonal) of size $N_{ijk} \times N_{ijk}$ (27×27 in the example of Figure 2.2). In Figure (2.2b), each row or column number is a site number. The matrix entries are direction numbers. An entry has a nonzero value only if the corresponding sites are connected to each other in the network.

Blank entries in the connection matrix correspond to sites which are not connected to each other or are the effect of network boundaries. The total number of nonzero entries in each row is the coordination number for the site number corresponding to that row. Clearly, coordination number is maximum ($z = 26$) for sites inside a network and has a smaller value for sites on the boundaries. Since, in this example, site 14 is the only site with all 26 connections, only row 14 has 26 nonzero entries.

In the connection matrix, the upper triangle (above the diagonal line in Figure (2.2b)) contains forward connections of the network and the lower triangle contains backward connections. For example, site number 10 is connected to sites $1, 2, 4$, and 5 in the backward direction and to sites $11, 13, 14, 19, 20, 22$, and 23 in the forward direction. Note that all entries in a minor diagonal have the same value, which is a lattice direction number. Because the connection matrix is always symmetric, we only need to keep the upper triangle, which has 13 minor diagonals. Furthermore, the connection matrix is sparse and we can convert the full matrix to compact form by eliminating zero elements.

2.2.4 Elimination Process

Since real porous media are topologically random with a wide distribution of coordination numbers, we generate random networks with topological properties which can be specified arbitrarily. These networks can provide a better match to real porous media topology than regular networks with a fixed coordination number. This results in a random network, which can match both the mean and the distribution of coordination numbers of a porous medium.

The coordination number of 26 is much larger than the commonly observed

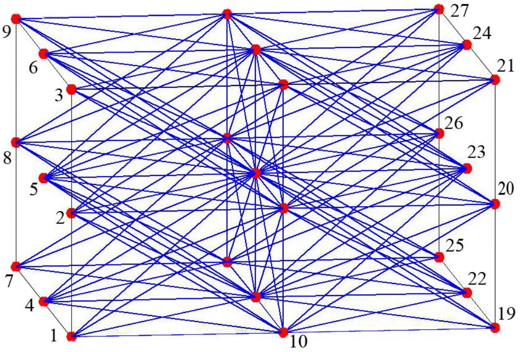

(a)

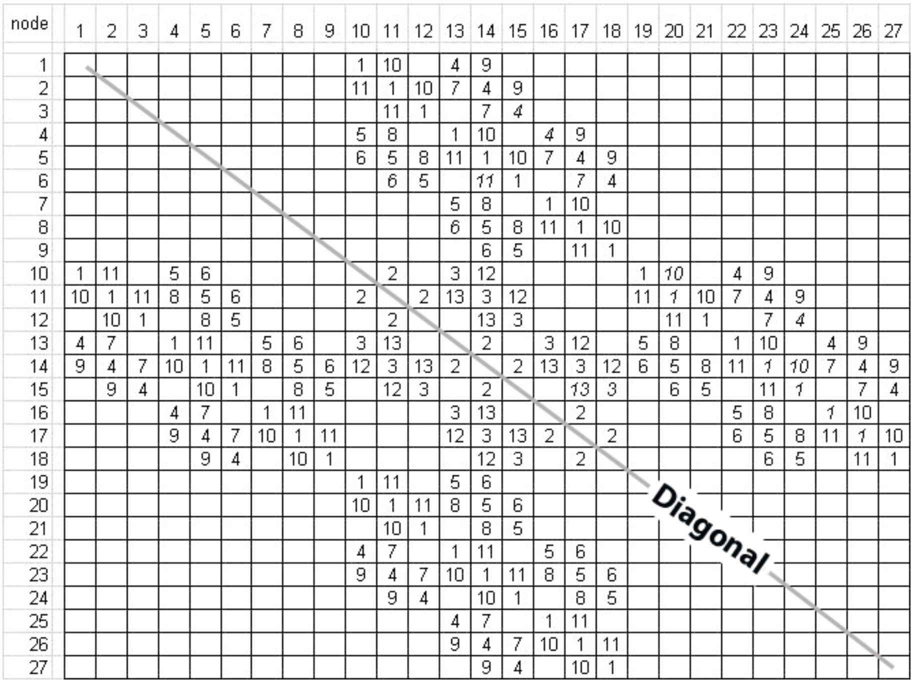

node	1	2	3	4	5	6	7	8	9	10	11	12	13	14	15	16	17	18	19	20	21	22	23	24	25	26	27
1										1	10		4	9													
2										11	1	10	7	4	9												
3											11	1		7	4												
4										5	8		1	10		4	9										
5										6	5	8	11	1	10	7	4	9									
6											6	5		11	1		7	4									
7													5	8		1	10										
8													6	5	8	11	1	10									
9														6	5		11	1									
10	1	11		5	6						2		3	12					1	10		4	9				
11	10	1	11	8	5	6				2		2	13	3	12				11	1	10	7	4	9			
12		10	1		8	5					2			13	3					11	1		7	4			
13	4	7		1	11		5	6		3	13			2		3	12		5	8		1	10		4	9	
14	9	4	7	10	1	11	8	5	6	12	3	13	2		2	13	3	12	6	5	8	11	1	10	7	4	9
15		9	4		10	1		8	5		12	3		2			13	3		6	5		11	1		7	4
16				4	7		1	11					3	13			2					5	8		1	10	
17				9	4	7	10	1	11				12	3	13	2		2				6	5	8	11	1	10
18					9	4		10	1					12	3		2						6	5		11	1
19										1	11		5	6													
20										10	1	11	8	5	6												
21											10	1		8	5												
22										4	7		1	11		5	6										
23										9	4	7	10	1	11	8	5	6									
24											9	4		10	1		8	5									
25													4	7		1	11										
26													9	4	7	10	1	11									
27														9	4		10	1									

(b)

Figure 2.2: Network with full connections with the size: $N_i = 3, N_j = 3, N_k = 3$. (a) Configuration of the network (site numbers are shown for some nodes and system of numbering is the same as in Figure 2.1). (b) The corresponding connection matrix. Empty boxes indicate that no connection between corresponding sites exists.

mean value of coordination numbers. To have a smaller mean coordination number and a desired coordination number distribution, we should eliminate some bonds in the network. It is worth mentioning that, after the elimination process, the connection matrix is no longer centrosymmetric and is only a symmetric sparse matrix. There are many ways to eliminate some of the bonds (see e.g., Arns et al. [2004]). One approach is to eliminate all the connections along some specific direction numbers and keep the rest of connections. In this way, we will construct regular-pattern networks. Figure (2.3) shows the structure of some regular-pattern networks.

In general, one may follow a random or a regular elimination procedure. We have chosen the former approach and have formulated a consistent and flexible procedure. Suppose each bond may exist in only two possible states: "open" or "blocked". We further assume that each bond's state is random and independent of its neighbors. We then determine a set of 13 threshold numbers, $p_i, i = 1, 2, \ldots, 13$, one for each direction. Each p_i value is between zero and one and denotes the probability of having a bond in direction i. Next, during network construction (e.g., putting the connection matrix together), for each and every possible bond, we generate a random number with uniform distribution, also between zero and one, which we call its elimination number. If this elimination number is greater than the threshold number of the corresponding direction, the bond's state is assigned to be blocked; otherwise it is open. So, the larger the threshold number, p_i, the more the chance to have an open (connecting) bond in direction number i. There are two limiting cases: (a) If the threshold number p_i is equal to 1.0, then all the bonds along lattice direction i will be open; (b) If the threshold number p_i is equal to zero it means all bonds along that lattice direction i will be blocked, indicating no connectivity along that direction. By putting $p_1 = p_2 = p_3 = 1.0$ (direction numbers: $1, 2, 3$ in Figure 2.2)) and zero for the other 10 directions, we will end up with the commonly used regular network with $z = 6.0$ with connections only in three principal directions.

If we choose the same value, Π, for all the threshold numbers, say $p_1 = p_2 = \cdots = \Pi$, then as Π increases from zero, more and more sites become connected into one giant cluster. At some point, the connected cluster spans the entire lattice both vertically and horizontally. The threshold number at which this happens (approximately 0.08 for a cubic lattice network of size $30 \times 30 \times 30$) is called the critical probability, p_c, also known as the cubic lattice bond percolation threshold. This elimination procedure varies directly with the proportion

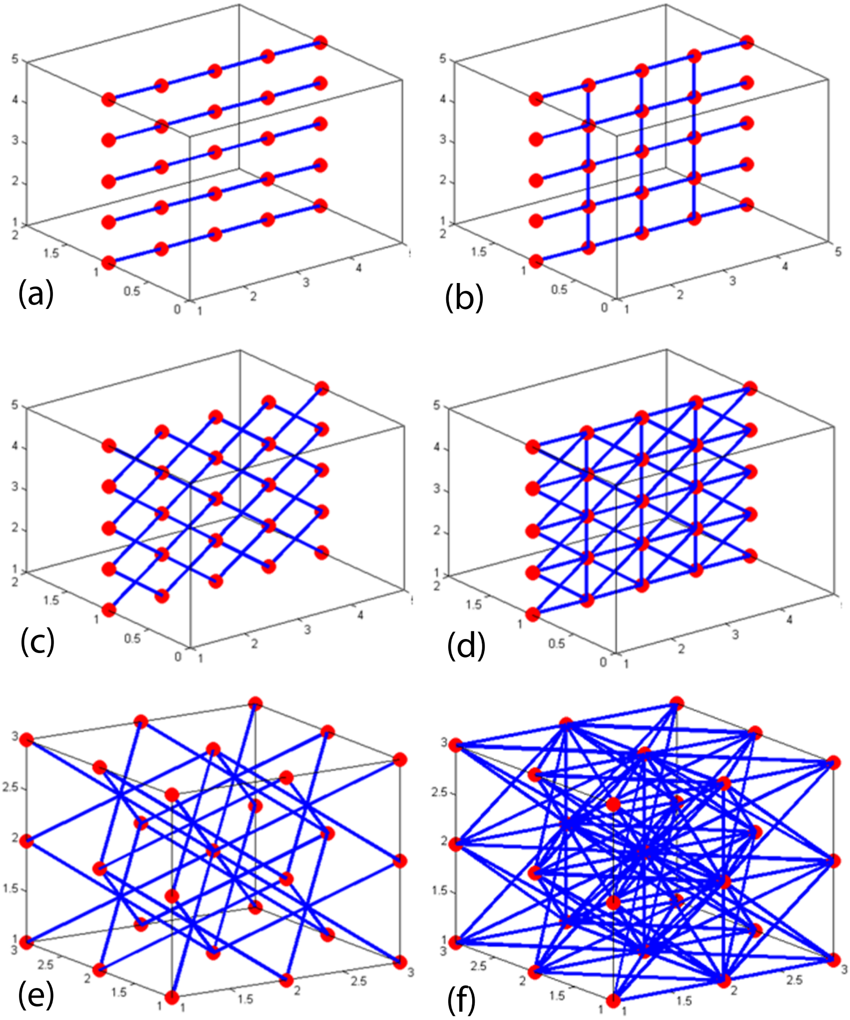

Figure 2.3: Regular-pattern networks constructed by eliminating all the connections along some specific direction numbers. Network (a) is equivalent to the bundle-of-tubes model, and network (b) is the commonly used regular structure network with connections only in principal directions. (c)-(f) show networks with connections in diagonal directions, in 2D and 3D domains.

of open bonds (not the sites), so it is called bond percolation [Berkowitz and Ewing, 1998].

As fluid can flow only through bonds which are “open”, below the (critical) p_c value the lattice will have zero conductivity, while above p_c, the conductivity will rise as p_i increases. Hence, there is a strong relation between connectivity of the elements (the so-called microscopic properties) and the physical properties of the entire system (or the so-called macroscopic properties).

There are some observations which have also been made in earlier studies (e.g., Berkowitz and Ewing [1998]). First, as the proportion of open sites increases, the proportion of blocked sites that have open neighbors also increases. Second, once $\Pi > p_c$, we will find that some bonds can have fluid flowing through them (the ensemble of these bonds is called the backbone of the network), while others are simply isolated clusters or dead-end bonds; the proportion of these branches varies as a function of Π. Third, the clusters grow larger (and merge) with an increase in Π. The reverse happens to the blocked bonds; they reduce in number and become more and more isolated as the probability of open sites increases.

We can generate a network with a pre-specified mean coordination number, z, by choosing a common threshold number $\Pi = z/26$ for all directions. For example, we can generate a network with the mean coordination number of 6 by choosing $\Pi = 6/24 = 0.231$ for all directions. Obviously, the coordination number distribution still ranges from 0 to 26 for any given z.

When threshold numbers are chosen to be all different, we can create different connectivities in different directions. This can result in anisotropic lattices. For example, Friedman and Seaton [1996] considered anisotropic lattices. They found that permeability and diffusive properties depend strongly on anisotropy induced by directionally different coordination numbers, and by anisotropic pore size distributions.

It is also possible to assign correlated elimination numbers in various directions. The correlation length, the range over which status of one bond is correlated with (or influenced by) status of other bonds, can be chosen based on desired lattice spacings or prescribed size of pore bodies. This allows us to create an anisotropic network with more connections, and as a result a larger permeability in certain directions. In an elaborate simulation study, Jerauld and Salter [1990] found that, as the degree of correlation between nearby bonds increased, saturated permeability increased. An explanation for this increase in saturated permeability with increased correlation can be found in the Ambegaokar et al.

[1971] model of hopping conductivity, which holds that flow through a random medium is dominated by a few pathways of high conductivity. Correlation appears to increase the probability and/or the conductance of some individual pathways [Jerauld and Salter, 1990]. Also, Renault [1991] found that as the correlation length was increased from 0 to 5 times that of the site spacing, the percolation threshold decreased. In our study, in the test cases of Sect. 2.3, we have used different threshold numbers for different directions. However, the generated elimination numbers have been uncorrelated.

Another approach to reduce the coordination number from 26 to a pre-specified value is to choose a regular elimination pattern. For example, we may assign blocked states for two successive bonds and an open state for the third bond, and repeat this pattern for all directions. We can also apply a combination of random and regular patterns to obtain specific connectivities and coordination number distributions for the network.

2.2.5 Isolated Clusters and Dead-End Bonds

We now proceed to the issue of conduction through the bonds. Obviously, flow problems are of interest only for $\Pi > p_c$. Note that, after the elimination process, many of the connected bonds will not conduct flow, since they neither belong to the percolating cluster nor do they form dead-end pores. Examples of possible situations are shown in Figure (2.4), where dead-end bonds are shown as hollow circles crossed by a line, and isolated sites and isolated clusters are marked by hollow circles and squares, respectively. The network backbone does not include isolated sites and clusters. Isolated sites and clusters also may cause numerical problems since they lead to a singular or ill-conditioned coefficient matrix for simulating flow within the network. Therefore, we should find all the isolated sites and clusters and eliminate them from our network. Regarding dead-end pores, we may choose to omit them if they are not important for a given process (such as flow), or keep them for processes where they pay a role (such as solute transport with diffusion).

It is worth mentioning that one can avoid this situation (isolated clusters and dead-end pores) through the choice of threshold number. For example, we can put $p_1 = 1.0$ so that all the bonds in the overall flow direction are open. And then we can apply elimination to the other directions.

Dead-end sites (sites with only one bond connected to them) have only one nonzero value in their corresponding row index in the connection matrix. So, we can find them fairly easily and eliminate them from the connection matrix

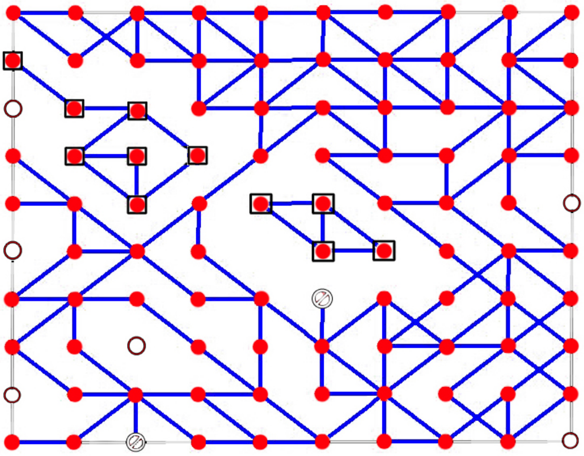

Figure 2.4: Example of eliminated sites, isolated clusters, and dead-end bonds.

or we can keep them as the dead-end pores of porous media.

Finding and eliminating isolated clusters is not as easy as in the case of dead-end sites. To do so, we employ a search algorithm to find the "backbone". We start from one of the boundaries across which flow is allowed. For each and every site on that boundary, we apply a search algorithm to find all the sites connected to it directly or through other sites. At the end, if we reach the other flow boundary, it means that this group of sites forms a backbone. After finding the backbone, we eliminate all other bonds as they belong to isolated clusters. To do tracking, it is crucial to have an efficient search algorithm. We have employed a algorithm based on the frequency of bonds. The details of our algorithm are given in Appendix A. Looking at the topology of the resulting network, our network is of semi-regular type since, after the elimination process, we do not always have a site at each lattice point. In fact, lattice points do not even need to be exactly in regular cubic pattern, and we have freedom to shift them away from the lattice point and/or move them into the position of eliminated pores or clusters, given that they would not have any contact with any other neighboring site (Figure 2.5). This feature along with different pore body sizes (thus, different bond lengths) makes this network a semi-irregular type. However, since such a network is a subset of a regular network (e.g., the cubic lattice network), sites are only connected to their nearest neighbors and the network contains no long bonds. Arns et al. [2004] considered the effect of disordered topology on relative permeability. They generated diluted networks with a disordered topology and $z = 4$, where the positions of the pore centers of the sample were preserved during the network construction. They compared relative permeabilities for these networks with those for a regular network. The effect of topological disorder on relative permeability was minor. Their result is in agreement with the findings of Jerauld et al. [1984] who showed that disordered topology had little effect on the percolation and conduction properties of networks. The observed equivalence of regular and disordered systems formally justifies application of work on regular-based lattices to real porous media.

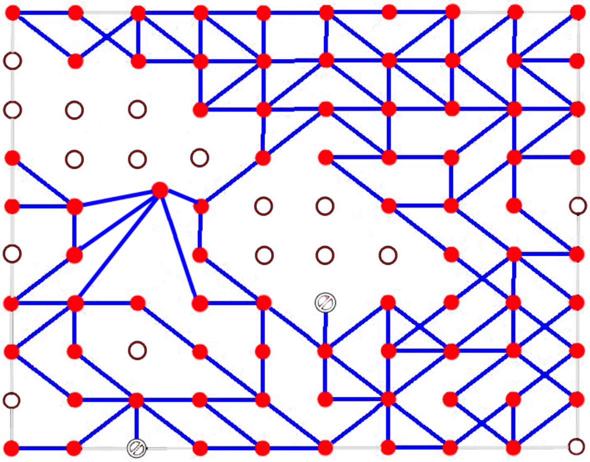

Figure 2.5: A network of size: $N_i = 10, N_j = 1, N_k = 10$. Isolated clusters are eliminated and locations of some sites are modified to get an irregular lattice.

2.3 Test Cases (Optimization Using Genetic Algorithm)

To illustrate the applicability and versatility of our method, we have employed it to generate two different networks, representing a consolidated porous medium and a granular soil sample. In principle, through an optimization process, one can match various characteristics such as coordination number distri-

bution, average coordination number, number of pores, and number of bounds. In the test cases presented here, we have chosen to match the coordination number distribution of the porous media under study. Thus, threshold numbers, Π, are the variables to be optimized. The generated elimination numbers have been chosen to be uncorrelated.
Other porous media characteristics (listed in Table 2.2) have been used to verify the resulting networks after optimization. The optimization is based on minimizing an objective or fitness function. The sum of the absolute values of differences between the coordination number distribution of the real porous medium and the generated network was used as the fitness function. We have employed a genetic algorithm (GA) for the purpose of optimization. GAs have been used to solve difficult problems with objective functions that are not well behaved, i.e., they do not possess properties such as continuity, or differentiability. [Davis, 1991, Goldberg, 1989, Holland, Michalewicz, 1994, Houck et al.]. The genetic algorithm provides a method for solving both constrained and unconstrained optimization problems. In our case, the valid range for threshold numbers is between zero and one. However, to prevent generation of networks with huge variations in connectivities in different directions, we have changed the upper bound constraint to 0.30. By enforcing this condition, we make sure that the generated networks have acceptable connectivities (without meaningless topologies). The genetic algorithm differs from more traditional search algorithms in that it works with a number of candidate solutions (a population) rather than just one solution. The algorithm begins by creating a random initial population. Then at each step, it selects individuals at random from the current population and uses them to produce the next generation. Over successive generations, the population "evolves" toward an optimal solution (for details of the method, readers are referred to [Houck et al.]). We have chosen the initial population size of 70. In order to minimize the objective function, the genetic algorithm produced 200 successive generations. The results of optimization are shown in the following sections.

2.3.1 Generating a Consolidated Porous Medium (Sandstone Sample)

For this test case, we have chosen data reported by Al-Kharusi [2006] on a Fontainebleau sandstone sample. They have utilized the concept of maximal balls [Silin et al., 2003] to compute the locations and sizes of pores and throats

and to create a topologically equivalent representation of 3D images.
As mentioned above, a representative network was created through optimizing threshold numbers, π, such that the coordination number distribution of the resulting network matches the measured coordination number distribution of the sample. These are both shown and compared in Figure (2.6). The optimization was performed through 200 generations using the genetic algorithm.

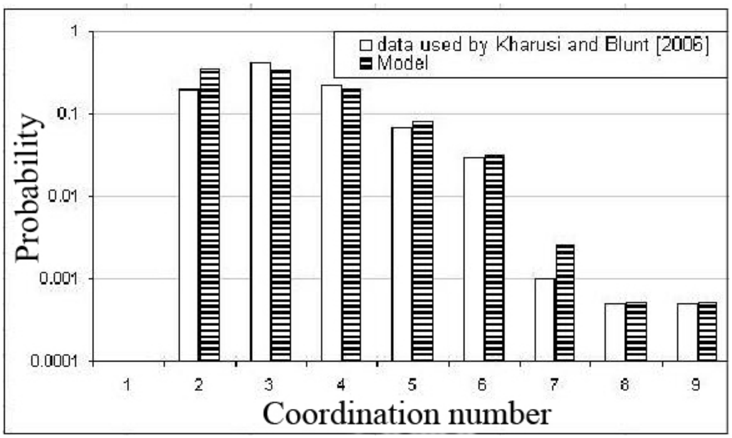

Figure 2.6: Comparison between coordination number distributions from real porous media and generated network.

After optimization, to verify the accuracy of the resulting network, various geometrical characteristics of the generated network were compared with those of the sandstone sample, reported in Table (2.2). It is evident that there is a good agreement between various characteristics of two networks, with relative errors ranging from 0.7% (for porosity and number of pores) to 7.1% (for number of bounds).
After generating the network, we used it as the skeleton and assigned site and bond size distributions to match the measured porosity. The radii of sites were given by an uncorrelated truncated lognormal probability distribution and the radii of bonds were determined by size of the sites which are located at the two ends of each bond. This scheme was adopted from Acharya et al. [2004] and used by Joekar-Niasar et al. [2008b]. The resulting porosity is shown in Table (2.2).

Table 2.2: Properties of the generated network and those reported by Al-Kharusi [2006].

Characteristic	Data reported by Al-Kharusi [2006]	Generated model	Relative error
Number of pores	4997	5030	0.7%
Number of bonds	8192	7605	7.1%
Mean coordination number	3.2	3.03	5.3%
Number of bonds to inlet	227	238	4.8%
Number of bonds to outlet	206	219	6.3%
porosity(%)	13.6	13.5	0.7%

2.3.2 Generating a Granular Porous Medium

For this test case, we have chosen data on coordination distribution of a granular soil. The method to extract the topological information can be found in Thompson et al. [2006]. They presented a new algorithm for extracting topological information of powders and granular materials from high-resolution binary volume data to get a vast amount of morphologic information such as size distribution, porosity, particle aspect ratio, and coordination number.
According to the procedure explained in Sect. 2.3, we have generated a pore network representing of the sample through optimizing threshold numbers, π. The coordination number distribution of the granular sample and the resulting network are shown and compared in Figure (2.7). An independent measure of accuracy of our resulting network is provided by comparing various characteristics of the generated network with soil sample (Table 2.3). There is agreement between the different characteristics of two networks. However, considering the relative errors (between 8.4 and 21.4%), the generated network is not as good as the one for the Fontainebleau sandstone sample.

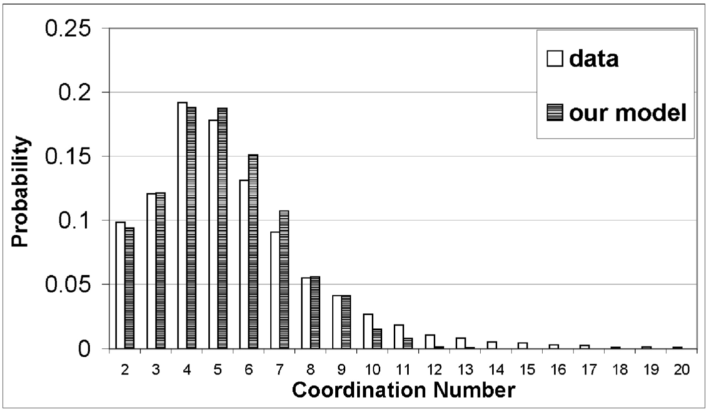

Figure 2.7: Comparison between coordination number distributions from real porous media and generated network.

Table 2.3: Properties of the generated network and those extracted by Thompson et al. [2006].

Characteristic	Physical representative network	Generated model	Relative error
Number of pores	4564	4056	11.1%
Number of bonds	12534	10674	14.8%
Mean coordination number	5.4	4.7	12.9%
Number of bonds to inlet	214	232	8.4%
Number of bonds to outlet	196	238	21.4%

2.4 Conclusions

We have presented a new method to generate a Multi-Directional Pore Network (MDPN) for representing porous media with coordination number up to 26. We used distribution of coordination number and applied the same into multi-directional cubic lattice network rather than using direct mapping into a physically representative disordered network (e.g., based on the X-ray tomographic images).

This new method is straightforward to program and is fast, resulting in reduced running time. For example, for a network with size $N_i = 300, N_j = 100$, and

$N_k = 100$, and average coordination number 6, a CPU time of $20s$ on an Intel $2.40GHz$ processor with $2.00GB$ of RAM is needed to generate the network and detect dead-end bonds and isolated clusters.

It is possible to construct networks with regular or random connection structures with a wide range of coordination number distributions as well as different directional connectivities. A quantitative comparison between properties of our generated network and those of consolidated and granular porous media samples shows that intrinsic properties, such as mean connectivity, coordination distribution, and porosity, are adequately captured in the reconstruction by this semi-regular multi-directional network. An effective optimization process using a genetic algorithm was employed to reproduce the coordination number distributions. The coordination number distributions of the generated networks and the real porous media are in good agreement, showing the genetic algorithm may be a promising and effective approach for optimization purposes in pore networks.

Part II

Upscaling and Pore Scale Modeling; Saturated Conditions

Published as: Raoof, A. and Hassanizadeh S. M., *"Upscaling Transport of Adsorbing Solutes in Porous Media", Journal of Porous Media"*, vol. 13, no. 5, pp. 395–408, 2010.

CHAPTER 3

UPSCALING TRANSPORT OF ADSORBING SOLUTES IN POROUS MEDIA

> *Money won't buy happiness, but it will pay the salaries of a large research staff to study the problem.*
>
> *Bill Vaughan*

Abstract

ADSORPTION of solutes in porous media is commonly modeled as an equilibrium process. Indeed, one may safely assume that within the pore space, the concentration of adsorbed solute at a point on the grain surface is algebraically related to the concentration in the pore close to the grain. The same, however, cannot be said about average concentrations. In fact, during solute transport, concentration gradients develop within the pore space, and these could potentially give rise to a scale-dependent adsorption process. The main objective of this research is to understand better the relations between the adsorption coefficient at the pore scale and the corresponding upscaled adsorption parameters. Two approaches are used for the purpose of upscaling: a)theoretical averaging of solute transport equation, and b) numerical upscaling.

In the averaging approach, pore-scale equations of solute transport are presented. Equilibrium adsorption is assumed to hold at this scale. Next, the equations are averaged and macro-scale equations are obtained. As a result, explicit expressions are derived for macro-scale adsorption rate constants as a function of micro-scale parameters. By examining these expressions, necessary conditions for the equilibrium assumption to hold at the macro-scale are determined. In the second approach (numerical upscaling), two models are employed for the purpose of upscaling: 1) a

Single-Tube Model, in which we simulate solute transport within a single tube, undergoing equilibrium adsorption at the pore wall, and 2) an upscaled 1D model coupled with kinetic adsorption. The flux-averaged concentration breakthrough curves from the Single-Tube Model are used to determine the upscaled adsorption rate constants as functions of pore-scale hydraulic and adsorption parameters. Results theoretical averaging and numerical upscaling agree very well.

3.1 Introduction

The first continuum scale for the description of flow and transport processes is the pore scale. Commonly, physicochemical processes are reasonably well understood and described by simple relationships at the pore scale. For example, mixing due to diffusion is described by Fick's law, equilibrium dissolution is explained by Raoult's law, and adsorption at the grain surface is assumed to follow an equilibrium relationship. In practice, however, we make measurements and model transport phenomena on scales much larger than the pore scale. Much effort is being made to understand and quantify links between these scales; in particular, the dependence of mass transfer on hydrodynamic properties of the system (e.g., Quintard and Whitaker [1995], Wood et al. [2000, 2004, 2007], Edward and David [1995], Edwards et al. [1993], Kechagia et al. [2002], Mauri [1991], Mojaradi and Sahimi [1988], Pagitsas et al. [1986], Ryan et al. [1980], Sahimi [1988], Shapiro and Brenner [1986, 1987, 1988]). Often, discrepancies between observation and theory arise because the large-scale description of transport does not account for some important aspects of small-scale behavior [Bryant and Thompson, 2001, Raje and Kapoor, 2000, Gramling et al., 2002]. Commonly, small-scale effects are lumped into empirical terms or coefficients that depend on porous media properties and structure [Guo and Thompson, 2001]. Hence, inclusion of subscale mass transfer effects in the description of porous systems is essential to develop theoretically sound equations for describing modeling mass transfer at the larger scales.

Because of limitations in measurements at small scale and in observation frequency, experiments alone cannot provide sufficient qualitative and quantitative understanding of transport; theoretical work is also needed. In porous media, upscaling may start either at the molecular level (e.g., Murdoch and Hassanizadeh [2002]) or at the pore scale (e.g., Whitaker [1969, 1986], Hassanizadeh and Gray [1979]). The most common approach is upscaling from the pore scale, where the principal idea is to average the pore-scale transport and reaction processes over a representative support volume to produce a macroscopic model of the reactive transport.

Reaction processes such as adsorption, mineral dissolution, or homogeneous reactions could greatly influence transport of dissolved matter in the soil and groundwater [Serrano, 2003, Bolt, 1979, Weber et al., 1991, van der Zee, 1990, Acharya et al., 2005b]. These processes typically occur at solid-fluid boundaries or fluid-fluid interfaces. Commonly, adsorption is modeled as a (linear) equilibrium process [Weber et al., 1991]. The equilibrium assumption means that the chemical potential of the solute in the fluid next to the solid grain is equal to the chemical potential of the solute adsorbed to the grain. This assumption is probably acceptable in most interactions at the pore scale, that is, at the pore boundaries. The same, however, cannot be said at larger scales, where we work with average solute concentrations. Owing to the variation of concentration within the pore and mass transfer at the grain surface, the solute concentration close to the wall will be different from the average concentration in the bulk fluid [Binning and Celia, 2008, Meile and Tuncay, 2006, Li et al., 2008, Kechagia et al., 2002]. Thus, the adsorbed solute concentration, which could be in equilibrium with the solution concentration close to the adsorbed site, may not be in equilibrium with the average concentration of solution. Instead, one often has to use a so-called kinetic relationship between average concentration of dissolved and adsorbed solutes. This is particularly the case if the porous medium has a microscopically heterogeneous structure, such as found in aggregated porous media or fractured media.

Studies of reactive solute transport commonly involve a series of batch experiments, through which reaction parameters are obtained. Given the fact that in batch experiments, there are no spatial variations in the concentration field (as it is a well-mixed system), the reaction models and reaction parameters actually pertain to the pore scale. In an open system, where diffusion and/or hydrodynamic dispersion occur, gradients in concentration exist, as observed both in experiments (e.g., Rashidi et al. [1996], Kapoor et al. [1998], Taylor [1953], Aris [1999] and through numerical simulations (e.g., Li et al. [2006b], Cao and Kitanidis [1998], Shapiro and Adler [1997]). As such, the reaction rates are an outcome of coupling between the reaction and hydrodynamic processes [Li et al., 2008]; this coupling can be the reason for much faster laboratory measured reaction rates of many minerals than those observed in the field [White and Brantley, 2003, Maher et al., 2004]. Then the question arises as to what extent pore scale reaction models and parameters are applicable at the macroscale.

Recently, Meile and Tuncay [2006] addressed this question for the case of mineral dissolution and homogenous reaction with the aid of a pore-scale numerical model. They found that macro-scale descriptions of these processes are different from pore-scale descriptions because of the effect of small-scale gradients in concentration fields. To investigate these effects, they numerically generated virtual porous media using random placement of identical spherical particles and solved diffusion and reaction in the resulting pore spaces. They showed that upscaled values of reaction and dissolution rates depend on the type of reaction, pore geometry, and macroscopic concentration gradient. They found that differences between these two scales become more significant for surface reactions as compared to homogeneous reactions. A limitation in the work of Meile and Tuncay [2006] is that they considered only diffusion transport and neglected advection. Other modeling studies have shown that the role of advection on the distribution of chemicals at the pore level is very important (e.g., Bryant and Thompson [2001], Knutson et al. [2001a], Robinson and Viswanathan [2003], Szecsody et al. [1998]).

Li et al. [2006b] studied the effect of pore-scale concentration gradients on a mineral dissolution rate influenced by advection. They introduced two kinds of models for minerals that could dissolve at different rates. First, they developed a Poiseuille flow model that coupled the reaction rate to both advection and diffusion within a pore space. Next they developed a “well-mixed reaction” model that assumed complete mixing within the pore. They have shown that concentration gradients could cause scale dependence of reaction rates. Significant concentration gradients would develop when diffusion is slower than the advection process, provided that rates of advection and reaction are comparable. This shows the effect of pore-scale gradients and residence times on the transport of reactive solutes. The effect of residence times on reactive transport was also addressed by Robinson and Viswanathan [2003], who showed the importance of pore-scale gradients, especially for nonlinear reactions; solute pulses of short duration; and systems with broad residence time distribution curves. Characteristic timescales of reaction processes pose constraints for transport models [Mo and Friedly, 2000, Cao and Kitanidis, 1998].

Experimental studies (e.g., Guo and Thompson [2001]) as well as pore-scale numerical models [Knutson et al., 2001a] have shown the dependence of mass transfer coefficients (e.g., in dissolution process) on the hydrodynamics of porous media. For example, Knutson et al. [2001a] found that the dimensionless mass transfer coefficient of dissolution increased with Peclet number, Pe.

Another method for the upscale adsorption process in porous media is the homogenization technique. Auriault and Lewandowska [1996] have used a homogenization technique (double asymptotic developments) to derive a macroscopic equation for the average concentration field of a solute that, at micro scale, is undergoing adsorption. They found effective parameters (e.g., dispersion adsorption tensor) that characterize the medium at the macro scale. Through various characteristic dimensionless parameters, they have shown the practical importance of processes in different flow/transport regimes. The macroscopic parameters were found to be dependent only on the microscopic transport parameters and microscopic geometrical properties. However, they found conditions under which the macroscopic model does not exist, for example, $Pe \ll O\left(\varepsilon^{-1}\right)$ where ε, the homogenization parameter, is the ratio of the micro-scale heterogeneities size to the macro-scale domain size. As, under some conditions, the problem could not be homogenized, they described nonhomogenizable and homogenizable domains in terms of characteristic dimensionless parameters. The existence of nonhomogenizable domains demands caution in applying their method to real situations.

Van Duijn et al. [2008] applied the homogenization technique to study adsorptive solute transport in a capillary slit. They found upscaled equations using the asymptotic expansion technique in terms of the ratio of characteristic transversal and longitudinal lengths under dominant Peclet and Domkohler numbers. They have distinguished different characteristic timescales for longitudinal, transversal, desorption, and adsorption processes. They have derived effective models for various conditions including linear adsorption-desorption, nonlinear reactions, and equilibrium adsorption. They have verified their method through comparison of solutions with numerical solutions of original problems with and without adsorption. They did simulations with high Peclet numbers (larger than 10^4). They found excellent agreement between results of their models and original problems.

This research is aimed at developing upscaled relationships for adsorption in terms of pore-scale properties through both theoretical and numerical averaging. We wish to find relations for upscaled transport coefficients for a solute that, at the pore scale, undergoes diffusion and advection as well as first-order equilibrium reaction at the solid surface. First, the problem of solute transport is formulated at the pore scale utilizing equilibrium adsorption. Then the equations are averaged, and upscaled equations are obtained. As a result, explicit expressions are derived for the mass exchange between fluid and solid phases in terms of average concentrations. Next, steady state flow and transient adsorption in a single tube are simulated numerically. The resulting breakthrough curves from this single-tube model are compared to the solution of the 1-D, continuum scale, transport equation to estimate upscaled adsorption parameters.

3.2 Theoretical upscaling of adsorption in porous media

3.2.1 Formulation of the pore-scale transport problem

Consider the transport of a solute in the pore space of a granular soil. Processes affecting transport are considered to be advection, diffusion, and chemical reaction within the water phase, plus adsorption to the solid phase at the pore boundaries. The general form of the equation of mass balance for the solute is:

$$\frac{\partial c^i}{\partial t} + \nabla \cdot \left(c^i \mathbf{v}\right) + \nabla \cdot \mathbf{j}^i = \widehat{r}^i \tag{3.1}$$

where: $c_i(ML^{-3})$ is the mass concentration of solute i in a pore; $\mathbf{v}$ (LT^{-1}) is the interstitial water velocity; $\widehat{r}^i$ $(ML^{-3}T^{-1})$ is the rate of chemical reaction with other solutes, and $\mathbf{j}^i$ $(ML^{-2}T^{-1})$ is the diffusive flux of the solute. The diffusive flux, $\mathbf{j}^i$, is given by Fick's first law:

$$\mathbf{j}^i = -D_0^i \nabla c^i \tag{3.2}$$

where D_0^i $[L^2T^{-1}]$ is the molecular diffusion coefficient of solute i in water.
In principle, one should solve this equation within the pore space of the soil subject to boundary conditions. At a point on the pore boundary, adsorption causes a flux of solute from the fluid to the solid phase; this gives rise to an increase in the mass density of adsorbed solutes. The rate of adsorption is equal to the solute mass flux normal to the pore boundary, $\left(c^i \mathbf{v} + \mathbf{j}^i\right) \cdot \mathbf{n}$. Thus, the following condition at the pore boundary holds

$$\frac{\partial s^i}{\partial t} = (c^i \mathbf{v} + \mathbf{j}^i).\, \mathbf{n}|_s \tag{3.3}$$

where: s^i $[ML^{-2}]$ is the mass of adsorbed solute per unit area of the solid grains, $\mathbf{n}$ is the unit vector normal to the pore wall; and $|_s$ denotes evaluation of the preceding quantity within the pore but at the solid surface. Because s^i is unknown, an additional equation is needed in order to have a determinate system. That extra equation comes from the continuity of chemical potential at the grain surface. This condition leads to an equilibrium relationship, a linear approximation of which yields

$$s^i = k_D^i \, c^i \big|_s \tag{3.4}$$

where $c^i\big|_s$ is the solute concentration of fluid at the pore wall and k_D^i [L] is an equilibrium, pore-scale distribution coefficient.

The set of Equations 3.1 through 3.4, together with conditions at the outside boundaries of the porous medium and an appropriate set of initial conditions, completely specify the solute transport problem at the pore scale.

3.2.2 Averaging of pore-scale equations

We would like to upscale Equations (3.1)-(3.4) to the macro scale. To do so, we need to define an averaging volume, commonly denoted as the representative elementary volume (REV) [Bachmat and Bear, 1987]. This is a well known concept and has been extensively discussed in the porous medium literature (see, e.g., Bear [1988], Bachmat and Bear [1986], Hassanizadeh and Gray [1979]). Denote the volume occupied an REV by V. Volume V is, in turn, composed of two subvolumes: V^f occupied by the fluid phase and V^s occupied by the solid grains. The boundary of solid grains is denoted A^{fs}; the superscripts, f and s, are used to denote the fluid and solid phases, respectively. Note that the averaging volume V is taken to be invariant in time and space, whereas the subvolumes V^f and V^s may vary both in time and space.

We shall integrate the fluid Equation (3.1) over V^f, and the interface condition (Equation 3.3) will be integrated over A^{fs}. First, we need to define the following average properties:

average mass concentration

$$\overline{c}^i \equiv \frac{1}{V^f} \int\limits_{V^f} c^i dV; \tag{3.5}$$

average flow velocity:

$$\overline{\mathbf{v}}^f \equiv \frac{1}{V^f} \int\limits_{V^f} \mathbf{v} dV; \tag{3.6}$$

Note that this volume-averaged definition of the flow velocity is admissible only if the fluid mass density variations are small (see Hassanizadeh and Gray, 1979, for discussion);

average diffusion flux

$$\overline{\mathbf{j}}^i \equiv \frac{1}{V^f} \int\limits_{V^f} \mathbf{j}^i dV; \tag{3.7}$$

average chemical reaction rate

$$\overline{r}^i \equiv \frac{1}{V^f} \int\limits_{V^f} r^i dV; \tag{3.8}$$

and average adsorbed mass fraction

$$\overline{s}^i \equiv \frac{1}{\rho^s V^s} \int\limits_{A^{fs}} s^i dA, \tag{3.9}$$

where ρ^s $[ML^{-3}]$ denotes the solid mass density.

Note that the average mass density of the sorbed solute is now defined in the form of mass fraction (mass of solute per unit mass of grains), $\overline{s}^i$ $[MM^{-1}]$, as is common in solute transport.

To upscale Equation (3.1), we need to integrate it over V^f. To do so, we need averaging theorems which relate the average of a derivative to the derivative of the average [Whitaker, 1969, 1986, Hassanizadeh et al., 1986, Gray and Hassanizadeh, 1998]. Averaging of Equation (3.1) over V^f results in the (macro-scale) Equation (3.10). Details of averaging are given in Appendix C.

$$\frac{\partial n\overline{c}^i}{\partial t} + \nabla \cdot \left(n\overline{c}^i\overline{\mathbf{v}}\right) + \nabla \cdot \left(n\mathbf{J}^i\right) = n\overline{r}^i - \widehat{U}^i, \tag{3.10}$$

where $\overline{\mathbf{v}}$ is the average flow velocity, and $\overline{r}^i$ is the reaction rate; the macro-scale adsorption term, $\widehat{U}^i$ $[ML^{-3}T^{-1}]$, is defined by

$$\widehat{U}^i = \frac{1}{V} \int\limits_{A^{fs}} \left(c^i \left(\mathbf{v} - \mathbf{w}\right) + \mathbf{j}^i\right) \cdot \mathbf{n} dA \tag{3.11}$$

where $\mathbf{w}$ is the velocity of the solid-fluid interface. In (3.10) $\mathbf{J}^i$ denotes the macro-scale hydrodynamic dispersion vector and accounts for diffusion as well as the mixing of solutes as a result of pore-scale velocity variations

$$\mathbf{J}^i = n\overline{c^i \widetilde{\mathbf{v}}} + n\overline{\mathbf{j}}^i, \tag{3.12}$$

where $\widetilde{\mathbf{v}}$ denotes the pore-scale velocity deviations, defined as

$$\widetilde{\mathbf{v}} = \mathbf{v} - \overline{\mathbf{v}}^f \tag{3.13}$$

Next, the microscopic boundary condition (3.3) is averaged over A^{fs}. The time average theorem and definition (3.9) are needed. The result is the following macroscale differential equation for the averaged adsorbed solute concentration

$$\frac{\partial \left(1 - n\right) \rho^s \overline{s}^i}{\partial t} = \widehat{U}^i \tag{3.14}$$

Equations (3.10) and (3.14) provide two equations to be solved for $\overline{c}^i$ and $\overline{s}^i$, provided that an appropriate relationship is found for the adsorption rate $\widehat{U}^i$. This term represents the exchange of mass between solid grain and the fluid phase. Such a mass exchange could be due to thawing, freezing, dissolution, precipitation, or adsorption. Here we consider the case of adsorption only and assume that adsorbed mass has no effect on the fluid or solid mass density. Phase change, dissolution, and precipitation are neglected.

Because there is no phase change, the normal water flux at the grain boundary, $(\mathbf{v} - \mathbf{w}) \cdot \mathrm{n}$ in Equation (3.11) will be identically zero. Substitution of Fick's law (Equation 3.2) in Equation (3.11) yields

$$\widehat{U}^i = -\frac{1}{V} \int\limits_{A^{fs}} D_0^i \frac{\partial c^i}{\partial n} dA \tag{3.15}$$

where $\frac{\partial(\cdot)}{\partial n}$ denotes the derivative in the direction normal to the grain surface. We now assume that $\frac{\partial c^i}{\partial n}$ can be approximated as follows

$$\left.\frac{\partial c^i}{\partial n}\right|_{A^{fs}} = \left(\left.c^i\right|_s - \left.c^i\right|_{pore}\right) / d \tag{3.16}$$

where $c^i\big|_s$ denotes solute concentration in the fluid at the pore wall, and $c^i\big|_{pore}$ denotes the solute concentration within the pore at some distance d. We now employ Equation (3.4) to eliminate $c^i\big|_s$ from (3.16) and substitute the result back into (3.15)

$$\widehat{U}^i = -\frac{D_0^i}{V k_D^i d} \int\limits_{A^{fs}} s^i dA + \frac{D_0^i}{V\, d} \int\limits_{A^{fs}} c^i\big|_{pore} dA \tag{3.17}$$

There is of course no information on the value of $c^i\big|_{pore}$. However, it is plausible to assume that $c^i\big|_{pore}$ is a function of average fluid concentration, $\overline{c}^i$. This means that we may replace $c^i\big|_{pore}$ by $f(\overline{c}^i)$ in Equation (3.17) and set

$$c^i\big|_{pore} = f(\,\overline{c^i}\,) \tag{3.18}$$

Use of this approximation (Equation 3.18), recognizing the fact that $\overline{c}^i$ is a constant within the averaging volume, and use of Equation (3.4) and (3.9), leads to the following macro-scale relationship

$$\widehat{U}^i = -\frac{D_0^i}{k_D^i d}\,(1-n)\,\rho^s \overline{s}^i + \frac{S D_0^i}{d} f(\,\overline{c}^i) \tag{3.19}$$

where S $[L^{-1}]$ denotes the solid grain specific surface area, $S = A^{fs}/V$. Substitution of this result into the adsorbed mass balance (3.14) yields the standard linear kinetic adsorption equation:

$$\frac{\partial\,(1-n)\,\rho^s \overline{s}^i}{\partial t} = \widehat{U}^i = n k_{att} f(\,\overline{c}^i) - (1-n)\,\rho^s k_{det} \overline{s}^i \tag{3.20}$$

where the kinetic rate coefficients, $k_{att}\, and\, k_{det}$ $[T^{-1}]$, are defined by

$$k_{att} = \frac{S D_0^i}{n d} \tag{3.21a}$$

and

$$k_{\mathrm{det}} = \frac{D_0^i}{k_D^i d} \tag{3.21b}$$

The mass balance equation for the solutes now becomes

$$\frac{\partial n \overline{c}^i}{\partial t} + \nabla \cdot \left(n \overline{c}^i \overline{v}^i\right) + \nabla \cdot \left(n J^i\right) = n \overline{r}^i - n k_{att} f(\,\overline{c}^i) + (1-n)\,\rho^s k_{det} \overline{s}^i \tag{3.22}$$

which, together with Equation (3.20), forms a set of two equations to be solved for $\overline{c}^i$ and $\overline{s}^i$.

3.2.3 Kinetic versus Equilibrium Effects

It is shown here that, even if the adsorption process can be described by a linear isotherm at the pore scale, in general, it has a kinetic nature at the macro scale. The question is "when we can assume an equilibrium isotherm at the macro scale?". That would be the case, of course, if the kinetic process is very fast. This can be studied best if we write the kinetic Equation (3.20) in an alternate form that is commonly employed

$$\widehat{U}^i = \kappa \left(1-n\right) \rho^s \left(K_D^i f(\overline{c}^i) - \overline{s}^i\right) \tag{3.23}$$

where κ and $\mathrm{K}_\mathrm{D}^\mathrm{i}$ are the macro-scale kinetic rate coefficient and distribution coefficient, respectively, and are defined as

$$\kappa = \frac{D_0^i}{k_D^i d} \tag{3.24a}$$

$$K_D^i = \frac{S k_D^i}{\left(1-n\right) \rho^s} \tag{3.24b}$$

From (3.24a), the kinetic rate coefficient can be viewed as the ratio of the micro-scale diffusion mass flux, $D_0^i \Delta c^i / d$, to the amount of mass which is to be adsorbed, i.e. $k_D^i \Delta c^i$. Obviously, the faster the diffusion process, the larger the kinetic coefficient (thus, the smaller the kinetic effect). On the other hand, the larger the amount of mass to be adsorbed, the more important the kinetic effect will be.

It is interesting to note that Equations (3.24) allow us to write the macro-scale kinetic rate coefficient as a function of the macro-scale distribution coefficient; this can be achieved by eliminating k_D^i between the two equations in (3.24a). We obtain

$$\kappa = \frac{S D_0^i}{\rho^s (1-n) d\, K_D^i} \tag{3.25}$$

The inverse of the kinetic coefficient, κ^{-1}, is the characteristic time scale of the kinetic process. If this characteristic time is of the same order of magnitude as, or bigger than, the residence time of solutes in pores, d/v, (i.e., for $\kappa^{-1} \geq d/v$)

then the kinetic process will be important. This condition can be represented by the dimensionless number σ_D

$$\sigma_D = \frac{\rho^s(1-n)vK_D^i}{SD_0^i} \tag{3.26}$$

Thus, if $\sigma_D \geq 1$, then kinetic effects are important. Note that if the flow velocity is very small, then the kinetic effects become negligible. In the limiting case of no flow, as is the case in batch experiments, the equilibrium relationship (3.24) applies with no approximation. Thus, batch experiments can be used to obtain the macro-scale distribution coefficient.

In the following section, we will perform numerical experiments to explore the assumptions leading to Equations (3.24) and also find an approximate value for d in Equation (3.16).

3.3 Numerical upscaling of adsorbing solute transport

Perhaps the simplest step in upscaling is to replace the three-dimensional flow and concentration fields within the pore (or a tube) by 1D fields, whereby velocity and concentration are averaged over the pore cross section. As mentioned in the Introduction, this upscaling has been considered for homogeneous reactions as well as dissolution. Here we treat the upscaling of adsorptive solute transport.

To analyze the scale dependence of adsorption process, we have developed two models: a) a Single-Tube Model in order to simulate details of transport within a pore, and b) an equivalent upscaled 1D model for the cross-sectionally-averaged concentration. These models allow us to investigate some of the assumptions made in our upscaling approach and also to verify results of that approach.

3.3.1 Flow and transport at pore scale (Single-Tube Model)

Consider a long single tube with a constant circular cross section with radius R_0. We assume fully developed, steady-state, laminar flow in the tube (Poiseuille flow) so that the velocity distribution is given by [Daugherty and

Franzini, 1965]

$$v(r) = 2\overline{v}\left[1 - \left(\frac{r}{R_0}\right)^2\right] \tag{3.27}$$

where r is the radial coordinate, $v(r)$ is the local fluid velocity, $\overline{v}$ is the average flow velocity, and R_0 is the radius of the cylinder. In the Single-Tube Model, adsorption occurs only at the wall of tube, Figure (3.1). In this study, changes in the radius of the tube due to the adsorption process are neglected.
The mass transport in the tube is given by

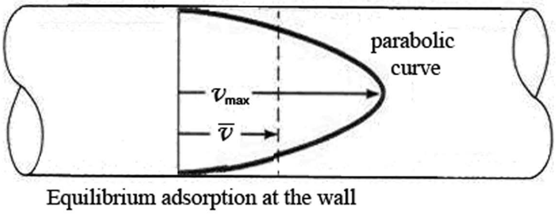

Figure 3.1: Conceptual representation for the Single-Tube Model. The velocity profile is assumed to be parabolic.

$$\frac{\partial c}{\partial t} + 2\overline{v}(1 - \left(\frac{r}{R}\right)^2)\frac{\partial c}{\partial z} = D_0\left[\frac{\partial^2 c}{\partial z^2} + \frac{1}{r}\frac{\partial}{\partial r}\left(r\frac{\partial c}{\partial r}\right)\right] \tag{3.28}$$

where D_0 $[L^2T^{-1}]$ is molecular diffusion coefficient and z is the axial direction along the tube.
In the tube, the wall acts as an adsorbent and therefore, the adsorption relation must appear in the boundary condition to the differential Equation (3.28). Adsorption to the wall may be described by the following equation which prescribes that the diffusive mass flux to the wall is the only source of accumulation at the wall

$$\frac{\partial s}{\partial t} = -D_0\left.\frac{\partial c}{\partial r}\right|_s \tag{3.29}$$

where s $[ML^{-2}]$ is adsorbed mass per unit area. This is just Fick's law, Equation (3.3). As in section 3.2, we assume that linear equilibrium adsorption (Equation 3.4)holds at the wall, characterized by the distribution coefficient value, k_D $[L]$:

$$s = k_D\left.c\right|_s \tag{3.30}$$

We introduce the following dimensionless variables and parameters:

$$c^* = \frac{c}{c_0};\ r^* = \frac{r}{R_0};\ z^* = \frac{z}{R_0};\ t^* = \frac{\bar{v}t}{R_0};\ Pe_p = \frac{\bar{v}R_0}{D_0};\ s^* = \frac{s}{c_0 R_0};\ \kappa = \frac{k_D}{R_0} \tag{3.31}$$

where c_0 is concentration at the inlet boundary. Here Pe_p is the pore-scale Peclet number, which expresses the ratio between the magnitude of the advective and diffusive transport terms.

Substituting in Equation (3.28) gives the pore-scale dimensionless mass transport equation

$$\frac{\partial c^*}{\partial t^*} + 2(1 - r^{*2})\frac{\partial c^*}{\partial z^*} = \frac{1}{Pe_p}\left[\frac{\partial^2 c^*}{\partial z^{*2}} + \frac{1}{r^*}\frac{\partial}{\partial r^*}\left(r^*\frac{\partial c^*}{\partial r^*}\right)\right] \tag{3.32}$$

The dimensionless boundary conditions for our model are

$$at\ \ z^* = \ 0,\ \ c^* = \ 1.0 \tag{3.33a}$$

$$at\ \ z^* = \infty,\ \ \frac{\partial c^*}{\partial z^*} = 0 \tag{3.33b}$$

$$at\ \ r^* = 0,\ \ \frac{\partial c^*}{\partial r^*} = 0 \tag{3.33c}$$

$$at\ \ r^* = 1,\ \ \frac{\partial c^*}{\partial r^*} = -Pe_p\frac{\partial s^*}{\partial t^*} \tag{3.33d}$$

Substitution of Equation (3.30) in the boundary condition (3.33d) results in:

$$\frac{\partial c^*}{\partial r^*} = -Pe_p\,\kappa\frac{\partial c^*}{\partial t^*}\ \ at\ \ r^* \ = \ 1 \tag{3.34}$$

It is evident that Pe_p and κ are the two parameters in this set of Equations (3.32)-(3.34) which control the transport and reaction processes within the tube.

The package, Flex-PDE (Flex, 2005) has been used to numerically solve this set of equations. We have simulated solute transport for a range of values of parameters Pe_p and κ. The solution of Equations (3.32)-(3.34) results in a concentration field $c^*\left(z^*, r^*, t^*\right)$ for different values of Peclet number (Pe_p) and dimensionless distribution coefficient (κ). This concentration field and its cross-sectional average, $\bar{c}^*\left(z^*, t^*\right)$, may be considered to be equivalent to "observation data". We then use these observed data to obtain a relationship for upscaled adsorption parameters.

3.3.2 Flow and Transport at 1-D Tube Scale

One can obtain the first level of upscaling by averaging the pore-scale concentration over the cross section of the tube. This results in the 1D average concentration field, $\bar{c}^* (z^*, t^*)$, to which we refer as the 1D tube scale. Now, the question arises what the governing equation should be for this average concentration. To answer this question, we examine a typical breakthrough curve of average concentration for an adsorbing solute at a position far from the tube inlet (e.g., at $z^* = 100$), as shown in Figure (3.2).

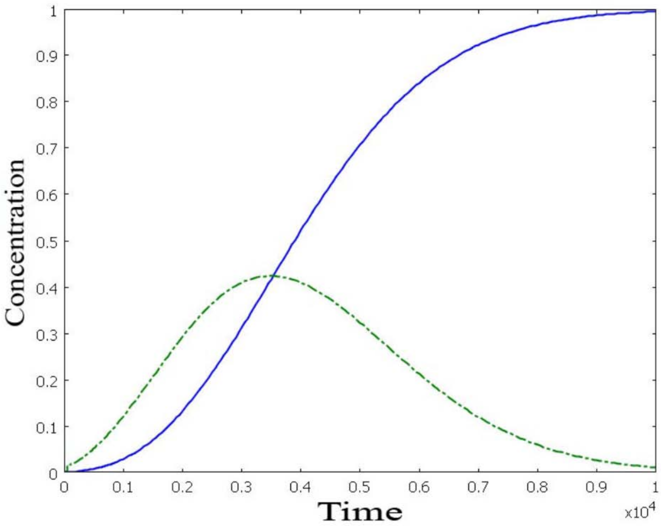

Figure 3.2: Breakthrough curve of average concentration (solid line) and its non-Gaussian derivative (dashed line); based on simulations from Single-Tube Model with continuous input.

It is evident that the breakthrough curve shows a nonideal behavior with a nonsymmetric derivative. The tailing observed here suggests that, at this scale, adsorption would be better to be described as a kinetic process. The governing equations for the $1D$ transport of a kinetically adsorbing solute are

$$\frac{\partial \overline{c^*}}{\partial t^*} + \frac{\partial \overline{c^*}}{\partial z^*} = \frac{1}{Pe} \frac{\partial^2 \overline{c^*}}{\partial z^{*2}} - \frac{\partial \overline{s^*}}{\partial t^*} \tag{3.35}$$

$$\frac{\partial \overline{s^*}}{\partial t^*} = k^*_{att}\overline{c^*} - k^*_{\mathrm{det}}\overline{s^*} \tag{3.36}$$

where, $Pe = \frac{\overline{v}R_0}{D_L}$, which involves the average flow velocity $\overline{v}$ and the longitudinal dispersion coefficient, D_L. Note that Pe is the tube-scale Peclet number; it is different from the pore-scale Pe_p, which is based on a diffusion coefficient (see Equation (3.31)).

Further, k^*_{att} and k^*_{det} are dimensionless adsorption and desorption rate coefficients, respectively. These are related to the dimensional coefficients, k_{att} and k_{det}, through the following relationships:

$$k^*_{att} = \frac{k_{att}R_0}{\overline{v}}, \;\; k^*_{\mathrm{det}} = \frac{k_{\mathrm{det}}R_0}{\overline{v}} \tag{3.37}$$

These equations contain three parameters: Pe, k^*_{att} and k^*_{det}. We have evaluated these parameters by fitting the solution of this set of equations to the average breakthrough concentration, $\overline{c}^*(z^*, t^*)$, obtained from the Single-Tube Model for various values of pore-scale Peclet number (Pe_p) and κ. This procedure results in relationships between the three upscaled parameters (Pe, k^*_{att} and k^*_{det}) and their corresponding pore-scale parameters (Pe_p and κ). We have used the cross-sectional averaged concentrations from the Single-Tube Model to find corresponding upscaled adsorption parameters. A similar approach was used by Li et al. [2008] for upscaling of dissolution processes under steady-state flow conditions. They studied upscaling of mineral dissolution within a single pore. Reactive flow experiments were performed in a cylindrical pore, 500 μm in diameter and 4000 μm long, drilled in a single crystal of calcite. They employed the Single-Tube Model to simulate the concentration of Ca^{2+} resulting from dissolution of calcite. A kinetic calcite dissolution formula (from Chou et al. [1989]) was assumed to hold at the wall of tube. Then, the flux-average concentration of Ca^{2+}, calculated from the Single-Tube Model, was compared to the measured Ca^{2+} concentration from the experiment for different pH and flow conditions. They found excellent agreement between modeling results and results of experiment. This, we believe, is an indication of the applicability of our procedure in upscaling from pore to tube scale.

3.3.3 Upscaled Peclet number (Pe)

Here we assume that the dispersion is not affected by the adsorption process. Therefore, we evaluate the upscaled Peclet number (Pe) for the case of a non-adsorbing solute (i.e., $\kappa = 0$). This is done by fitting the breakthrough curve from the Single-Tube Model to the solution of the 1D transport equation (Equation (3.32)) with no adsorption (i.e., $k_{att} = k^*_{det} = 0$). Figure (3.3) shows the resulting graph, where Pe is plotted as a function of pore-scale Peclet number (Pe_p). In the same figure, the Taylor dispersion formula (Equation 3.38) [Taylor, 1953, Aris, 1999] for the upscaled Peclet number in a tube is also plotted.

$$\frac{1}{Pe} = \frac{1}{Pe_p} + \frac{Pe_p}{48} \tag{3.38}$$

The excellent agreement indicates the accuracy of our numerical code in capturing the transport within the tube and also shows that the Taylor assumption is valid for this problem. We use Equation (3.38) to obtain the upscaled Peclet number (Pe) in the simulations of adsorbing solute in the next section.

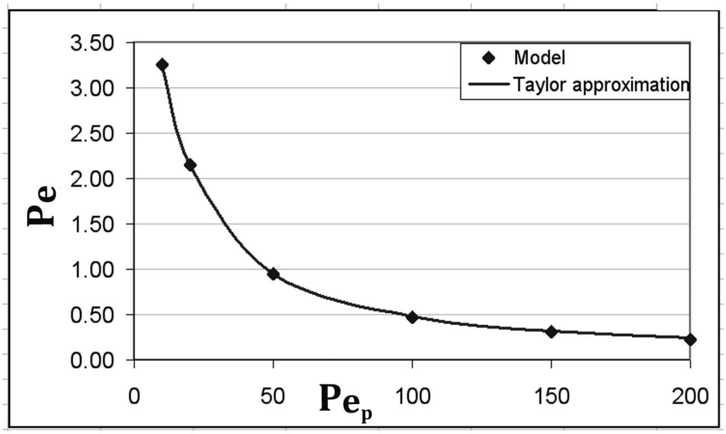

Figure 3.3: Graph of Pe versus Pe_p. The points are the result of fitting of the breakthrough curve of average concentration (with $\kappa = 0$) to Equation (3.32) to find Pe. The solid line shows the Taylor formula, Equation (3.38).

3.3.4 Upscaled adsorption parameters (k^*_{att} and k^*_{det})

As we employ the Taylor formula to estimate the upscaled Peclet number, there are only two upscaled parameters, k^*_{att} and k^*_{det}, left to be determined as a function of pore-scale parameters

$$k^*_{att} = f(Pe_p, \kappa) \tag{3.39a}$$

$$k^*_{det} = f(Pe_p, \kappa) \tag{3.39b}$$

The CXTFIT curve-fitting program [Toride et al., 1995] was used for the purpose of solving Equations (3.35) and (3.36) and fitting to the breakthrough curves. Figure (3.4) shows an example fit to a breakthrough curves and the corresponding parameters. Through the fitting process, we have been checking the covariance matrix to make sure that parameters are not correlated.
This procedure was repeated for a range of pore-scale parameters ($1 < Pe_p < 300$, and $0.1 < \kappa < 20$), and finding the corresponding upscaled k^*_{att} and k^*_{det} we could determine relations between these set of parameters. Figures (3.5) and (3.6) show the resulting plot of k^*_{att} and k^*_{det} as functions of Pe_p and κ.

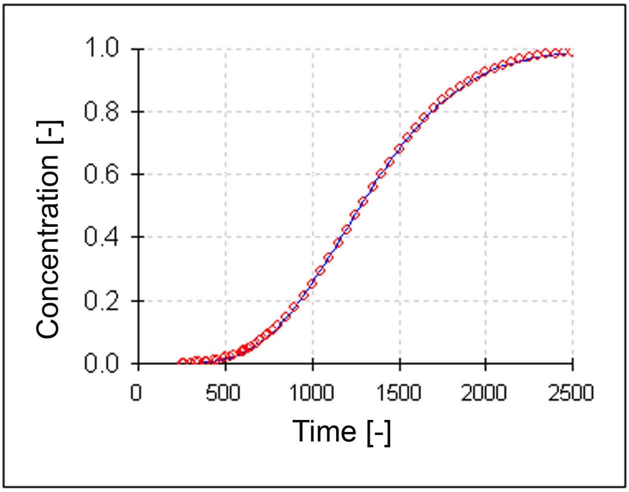

Figure 3.4: The resulting breakthrough curves for pore-scale (circles) and 1D upscale (solid line) models. In this illustration, at the pore-scale parameters are: $Pe_p = 35$ and $\kappa = 5.0$. And the corresponding upscaled parameters by fitting found to be: $k^*_{att} = 0.14$ and $k^*_{det} = 0.05$. Using Equation (3.38), Pe will be 1.3.

From the relations shown in Figures (3.5) and (3.6), we found the best fit formulas (through minimizing the least squares) for k^*_{att} and k^*_{det}

$$k^*_{att} = \frac{4.0(1 - e^{-3\kappa})}{{Pe_p}^{0.95}} \tag{3.40a}$$

$$k^*_{det} = \frac{9.0}{(0.5 + 4.5\kappa){Pe_p}^{0.95}} \tag{3.40b}$$

We define the upscaled distribution coefficient (K_D) by:

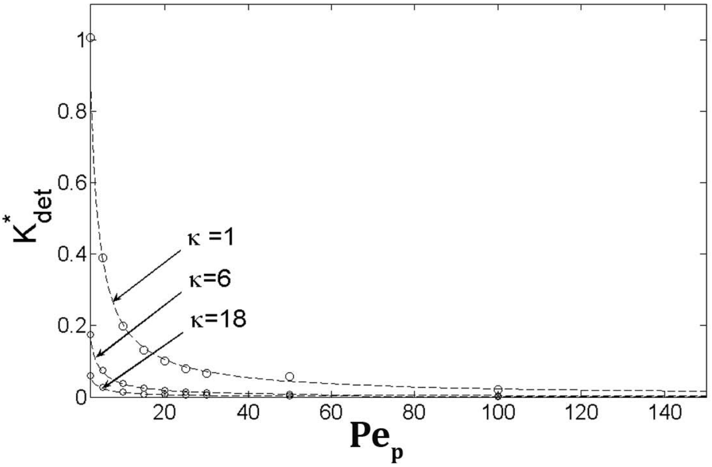

(a)

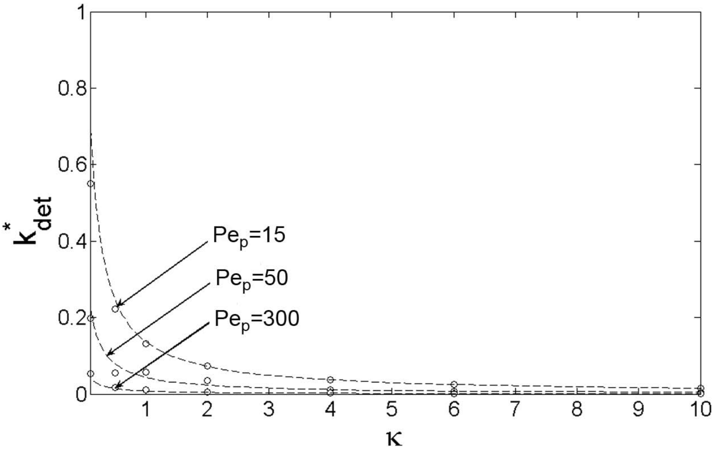

(b)

Figure 3.5: The relation between macro-scale k^*_{det} as a function of pore-scale (a) Pe_p and (b) κ.

$$K_D = \frac{k^*_{att}}{k^*_{\mathrm{det}}} = 0.4\left(1 - e^{-3\kappa}\right)(0.5 + 4.5\kappa) \tag{3.41}$$

According to Equation (3.41), the upscaled distribution coefficient, K_D, is inde-

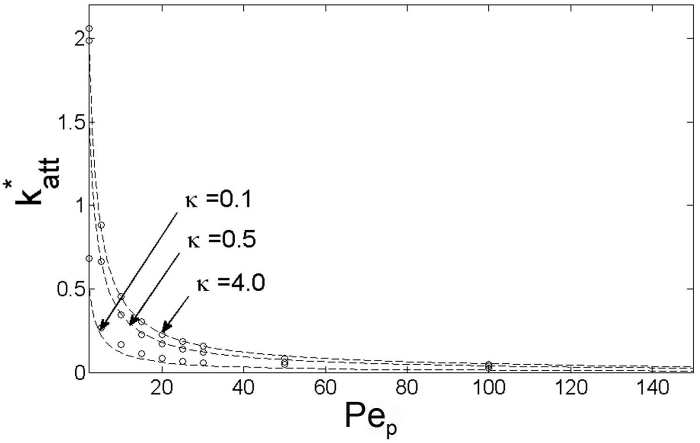

(a)

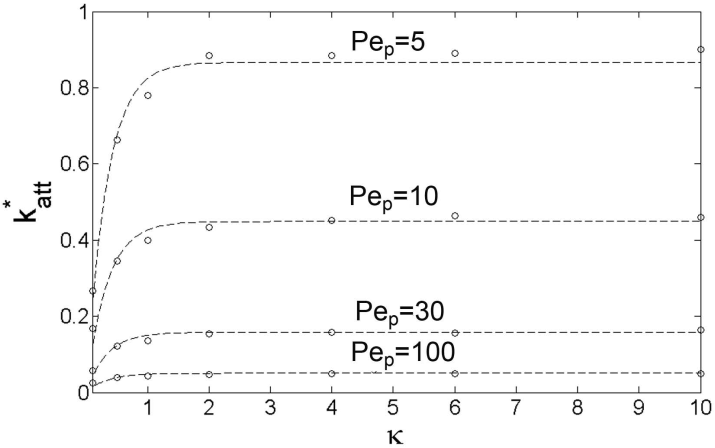

(b)

Figure 3.6: The relation between macro-scale k_{att}^{*} as a function of pore-scale (a)κ and (b) Pe_p.

pendent of Peclet number. It is, practically, a linear function of the pore-scale distribution coefficient, κ, as shown in Figure (3.7).

The linearity of the upscaled distribution coefficient, K_D, as a function of the

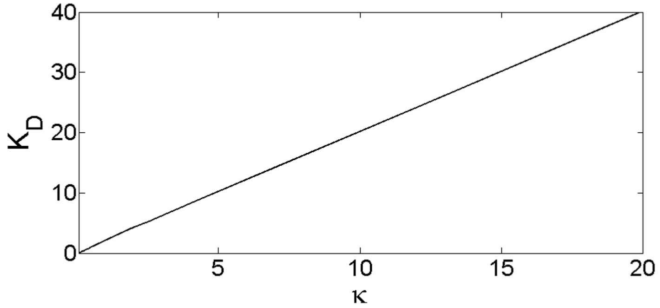

Figure 3.7: The relation between upscaled distribution coefficient ($K_D = k^*_{att}/k^*_{det}$) as a function of the pore-scale dimensionless distribution coefficient, κ for the Single-Tube Model.

pore-scale distribution coefficient, κ, also shows the validity of our upscaling process. Both K_D and κ are a measure of the capacity of the porous medium to absorb mass and thus they should be linearly related.

3.4 Discussion of results

Equations (3.40a) and (3.40b) can be converted to dimensional forms using Equations (3.31) and (3.37). This gives

$$k_{att} = \frac{4.0(1 - e^{-3\frac{k_D}{R_0}})\ \overline{v}^{0.05} D_0^{0.95}}{R_0^{1.95}} \tag{3.42a}$$

and

$$k_{\text{det}} = \frac{9.0\ \overline{v}^{0.05} D_0^{0.95}}{(0.5 + 4.5\frac{k_D}{R_0})R_0^{1.95}} \tag{3.42b}$$

We observe that k_{att} and k_{det} are only weak functions of velocity but they depend strongly on the geometry of the pore space and the diffusion coefficient as well as the pore-scale distribution coefficient. We could compare Equations (3.42) with corresponding equations derived using the averaging method in Section 3.2.2. For the case of the Single Tube, it is plausible to assume that $c^i\big|_{pore}$, at a position somewhere between the pore center and pore wall (denoted by w_{R0}, where $1.0 > w > 0$) will be equal to the average fluid concentration, $\overline{c}^i$. This means that in Equation (3.19) we may set

$$f(\overline{c}) = \overline{c} \;\; \texttt{and} \;\; d = \;\; wR_0 \tag{3.43}$$

As a result Equation (3.19) leads to the following macro-scale kinetic adsorption relationship:

$$\widehat{U}^i = nk_{att}\overline{c}^i - (1-n)\,\rho^s k_{det}\overline{s}^i \tag{3.44}$$

where the kinetic rate coefficients, k_{att} and k_{det} $[T^{-1}]$, are defined by

$$k_{att} = \frac{SD_0^i}{nwR_0} \tag{3.45a}$$

$$k_{\mathrm{det}} = \frac{D_0^i}{k_D^i wR_0} \tag{3.45b}$$

Indeed, if we acknowledge the fact that, for a tube, porosity is unity and the specific surface area is $S = \frac{2}{R_0}$, Equations (3.45) reduce to

$$k_{att}^{avg} = \frac{2D_0}{wR_0^2} \tag{3.46a}$$

$$k_{\mathrm{det}}^{avg} = \frac{D_0}{k_D^i wR_0} \tag{3.46b}$$

where superscript *avg* stands for the averaging method. Recall that w_{R0} denotes the radial position of a point in the pore where point concentration $c^i\big|_{pore}$ is equal to average concentration $\overline{c^i}$ (see Equation 3.43). These equations agree quite well with Equations (3.42) which were obtained through numerical averaging.

In Equations (3.42), if we neglect the dependence on the velocity and the exponential term and approximate $(0.5 + 4.5\frac{k_D}{R_0}) \approx 4.5\frac{k_D}{R_0}$, we obtain the approximation:

$$k_{att} = \frac{4D_0^i}{R_0^2} \tag{3.47a}$$

$$k_{\mathrm{det}} = \frac{2D_0^i}{k_D R_0} \tag{3.47b}$$

We notice that the two equation sets, (3.46) and (3.47), are the same if $w =$

0.5, which means that we should expect concentration $c^i\big|_{pore}$ appearing in Equation (3.16) to be equal to the average concentration, $\overline{c^i}$, at $r = 0.5R_0$. This possibility has been verified by plotting concentration breakthrough curves at $r = 0$, $r = 0.5R_0$ and $r = R_0$, as well as the average concentration, $\overline{c^i}$, in Figure (3.8). The agreement between $\overline{c^i}$ and $c^i\big|_{r=0.5R}$ is excellent. This result suggests that Equations (3.46) provide a very good approximation for the upscaled kinetic adsorption coefficients. The parameters w must be seen as an empirical factor which will be different for different pore structures.

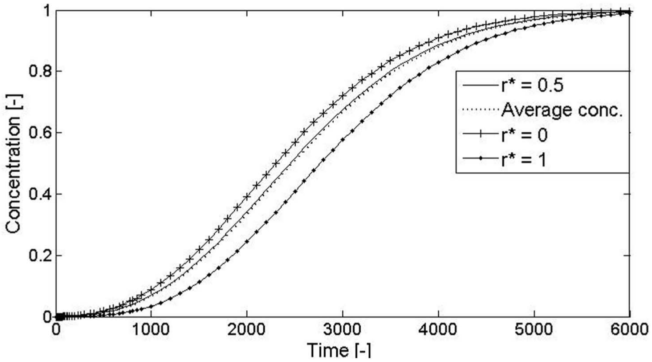

Figure 3.8: Comparison between average concentration breakthrough curve and breakthroughs of concentrations at three different positions in the tube.

3.5 Conclusion

In this work, we have shown that even if there is equilibrium adsorption at the pore wall (or at the grain surface), one may need to employ a kinetic description at the larger scale. This result was obtained through theoretical averaging, from pore to REV scale, as well as numerical averaging, from pore to tube scale. Both approaches result in formulas for macro-scale kinetic adsorption parameters as a function of pore-scale parameters such as Peclet number and distribution coefficient. Formulas from the two approaches agree very well. The upscaled adsorption parameters are found to be only weak functions of velocity; they strongly depend on the geometry of the pore and the diffusion coefficient in the solution as well as the pore-scale distribution coefficient.

The relations for upscaled transport coefficients are appropriate for use in pore-network models where tube-scale relationships are needed to model adsorbing solute transport in individual pore throats. Using the pore-network model we could scale up from the pore scale to the scale of an REV or even to core scale.

Published as: Raoof, A. and Hassanizadeh S. M., *"Upscaling Transport of Adsorbing Solutes in Porous Media: Pore-Network Modeling"*, Vadose Zone Journal, vol. 9, pp. 624-636, 2010.

CHAPTER 4

UPSCALING TRANSPORT OF ADSORBING SOLUTES IN POROUS MEDIA: PORE-NETWORK MODELING

> *Experience is a good school. But the fees are high.*
>
> *Heinrich Heine*

Abstract

THE main objective of this research is to enhance our understanding of, and obtain quantitative relationships between, Darcy-scale adsorption parameters and pore-scale flow and adsorption parameters, using a 3D MDPN model. This involves scale up from a simplified but reasonable representation of microscopic physics to the scale of interest in practical applications. This upscaling will be carried out in two stages: i) from a local scale to the effective pore scale, and ii) from effective the pore scale to the scale of a core. The first stage of this upscaling, from local scale to effective pore scale, has been discussed in Chapter 3. There, we found relationships between local-scale parameters (such as the equilibrium adsorption coefficient, k_d, and the Peclet number, Pe) and effective parameters (such as the attachment coefficient, k_{att}, and the detachment coefficient, k_{det}). Here, we perform upscaling by means of a $3D$ MDPN model, which is composed of a large number of interconnected pore bodies (represented by spheres) and pore throats (represented by tubes). Upscaled transport parameters are obtained by fitting the solution of the classic advection-dispersion equation with adsorption to the average concentration breakthrough curves at the outlet of the pore network. This procedure has resulted in relationships for upscaled adsorption parameters in terms of micro-scale adsorption coefficient and flow velocity.

4.1 Introduction

Transport of reactive/adsorptive solutes in soils and aquifers plays an important role in a variety of fields, including leaching of agrochemicals from the soil surface to groundwater, uptake of soil nutrients by plant roots, and remediation of contaminated soils and aquifers. Geochemical modeling has been widely employed to improve our understanding of the complex processes involved in fluid-solid interactions [Steefel and Lasaga, 1994, Gallo et al., 1998, Bolton et al., 1999] and to study environmental problems related to groundwater and subsurface contamination [Saunders and Toran, 1995, Xu et al., 2000, Mayer et al., 2002]. In reactive solute transport, we should, in general, model various reaction processes including: adsorption-desorption; precipitation-dissolution; and/or oxidation-reduction. Studies of many contaminated field sites have demonstrated that adsorption-desorption is one of the most significant geochemical process affecting the transport of inorganic contaminants [Kent et al., 2008, Davis et al., 2004a, Kohler et al., 2004].

4.1.1 Discrepancy between observations

In practical applications, we are interested in describing solute transport phenomena at scales larger than the scale at which the generic underlying processes take place (e.g., the pore scale). Commonly, in field or in lab experiments, reactive transport coefficients are employed which are obtained from experimental data. Measurement of the reaction coefficients usually employs well-mixed batch or flow-through reactors [Lasaga, 1998]. In batch systems, the assumption is that the aqueous phase is stirred rapidly enough so that concentration gradients are eliminated; this removes the effect of subscale transport by diffusion and/or advection within the pore spaces. In such cases, reaction is surface-controlled and depends only on the uniform chemistry of the aqueous solution. In natural systems, however, reactions are inevitably subject to the influence of transport via advection, molecular diffusion, and/or dispersion. As such, adsorption rates are an outcome of the coupling between reaction and hydrodynamic processes [Li et al., 2007b]. These potential discrepancies between batch experiments and the field can be the reason for much larger, laboratory-measured reaction rates for many minerals than those observed in the field [White and Brantley, 2003, Maher et al., 2004].

For upscaling batch experimental results to the field, we need to know the dependency of the macro scale sorption coefficients on flow velocity and pore-scale properties. Existence of such relations is a question of great interest. However, often, there is no agreement on such dependencies. For example, there is no consensus on the dependency of adsorption coefficients on average flow velocity. Experimental results are conflicting. Some researchers have reported a decrease of retardation coefficient with an increase in pore-water velocity [Kim et al., 2006, Maraqa et al., 1999, Huttenloch et al., 2001, Shimojima and Sharma, 1995, Jaynes, 1991, Pang et al., 2002, Nkedi-Kizza et al., 1983, Schulin et al., 1987, Ptacek and Gillham, 1992]. The reason for this inverse relationship between velocity and retardation factor is pointed to be the interaction time, which decreases as velocity increases. Dependencies of kinetic adsorption/desorption coefficients on velocity have been observed [Akratanakul et al., 1983, Lee et al., 1988, Bouchard et al., 1988, Brusseau et al., 1991a,b, Brusseau, 1992a, Ptacek and Gillham, 1992, Maraqa et al., 1999, Pang et al., 2002]. Kinetic adsorption coefficient has been often found to be inversely related to velocity. The inverse relationship indicates that the degree of nonequilibrium transport increases with pore-water velocity, which is also observed by Bouchard et al. [1988]. Similar results have been also found for physical nonequilibrium [Pang and Close, 1999a].

In contrast to the above-mentioned studies, using pore-scale modeling, Zhang et al. [2008], Zhang and Lv [2009] have found upscaled sorption parameters to be independent of pore-water velocity. Raoof and Hassanizadeh [2010a] have also found a negligible dependency of effective adsorption rate coefficients on pore-water velocity.

4.1.2 Pore scale modeling

A full understanding of the dependence of column and field-scale reactive transport parameters on pore-scale processes would require measurements of concentrations at various scales. Such measurements are, however, very difficult and quite expensive if possible at all. Therefore, alternative ways to understand and transfer pore-scale information to larger scales, and to establish relationships among them, must be found.

Using pore-scale modeling, one can simulate flow and transport at the pore scale in detail by explicitly modeling interfaces and mass exchange at interfaces. By comparing the result of pore-scale simulations with models representing the macro-scale behavior, one can study the relation between these two scales.

The two best-known methods for pore-scale modeling are pore-network models [Fatt, 1956b] and lattice-Boltzmann method [Sukop and Thorne, 2006]. A pore-network model is based on representing the void space of a porous medium as an interconnected network of pores. Commonly, an average pressure and/or concentration is assigned to a given pore body or pore throat. For each pore, change in solute mass is described by mass balance equations [Lichtner, 1985]. Using information on local surface area, and applying an area-normalized reaction rate, a kinetic reaction is calculated for each pore.

Pore-network models have been widely used to study multiphase flow in porous media [Celia et al., 1995, Blunt, 2001, Joekar-Niasar et al., 2008b, 2010] and chemical and biological processes such as: dissolution of organic liquids [Zhou et al., 2000b, Held and Celia, 2001, Knutson et al., 2001b]; biomass growth [Suchomel et al., 1998c, Kim and Fogler, 2000, Dupin et al., 2001]; and adsorption [Sugita et al., 1995b, Acharya et al., 2005b, Li et al., 2006b]. One shortcoming of a pore-network model is its idealization of the pore space using simple geometries; often, pores are assumed to have uniform circular or square cross-sectional shapes. This makes it difficult to simulate some processes, such as biogeochemical reactions, that could lead to a significant change in the pore geometry as a result of dissolution, precipitation, and/or biological clogging. However, pore-network models are computationally cheap, and recent advances have allowed modeling a degree of irregularity in channel cross-sectional shape that was not available in earlier models. In addition, pore-network models are capable of capturing important statistical characteristics of porous media such as pore size distributions [Øren et al., 1998b, Lindquist et al., 2000], together with coordination number distributions [Raoof and Hassanizadeh, 2009] and topological parameters such as Euler number [Vogel and Roth, 2001].

The Lattice Boltzmann (LB) approach [Chen and Doolen, 1998, Tartakovsky et al., 2007] provides a reliable representation of pore geometries, but at the cost of substantial computational effort [Pan et al., 2004, Vogel et al., 2005]. In the area of porous-medium flow, LB methods have been applied to a variety of problems: to simulate the flow field (e.g., Acharya et al. [2007a]) and measure permeability (e.g., Pan et al. [2001, 2006], Zhang et al. [2000]); to simulate two-phase flow (e.g., Shan and Chen [1994], Miller et al. [1998]); to model species transport (e.g., Zhao and Sykes [1996], Gunstensen and Rothman [1993]); and to model interphase mass transfer (e.g., Martys and Chen [1996]). Contrary to pore-network modeling, in which one normally does not discretize within the pores, LB models can directly simulate fluid flow and biogeochemical processes within individual pores, without the need to simplify the pore geometry. In a combination with imaging technologies such as X-ray computed tomography [Wildenschild et al., 2002, O'Donnell et al., 2007], LB models can provide a powerful tool to study flow and transport processes at the pore scale. However, LB models are expensive in terms of both computational storage and run-time requirements, and little work has been done to use LB modeling on real porous media.

4.1.3 Applications of pore-scale modeling to solute transport

Since pore-scale modeling addresses the gap between pore scale and macro scale representation of processes, it has received increased attention as a useful upscaling tool. It can be used to relate concentrations and reaction rates at the macro scale to concentrations and reaction rates at the scale of individual pores, a scale at which reaction processes are well defined [Li et al., 2007a,b]. In recent pore-scale modeling, various types of adsorption reactions have been used, including linear equilibrium (e.g., Raoof and Hassanizadeh [2009]) and nonlinear equilibrium [Acharya et al., 2005b], kinetic adsorption (e.g., Zhang et al. [2008]), and heterogeneous adsorption in which the adsorption parameters were spatially varying (e.g., Zhang et al. [2008]).

Zhang et al. [2008]) used pore-scale modeling to find upscaled adsorption rate coefficients. They simulated spatio-temporal distributions of solutes and obtained upscaled concentrations by averaging the simulated results. Averaged values were used to calculate the upscaled reactive and transport parameters. At the pore scale, they specified linear kinetic adsorption and found that the upscaled adsorption remains first-order kinetic and could therefore be described by a constant rate coefficient. In addition, they found that upscaled adsorptive parameters were independent of flow rate. For the case of heterogeneous adsorption at the pore scale, the upscaled adsorption kinetics continued to be independent of velocity, but could not be described by a constant reaction rate constant.

For practical and/or computational reasons (lack of data and/or insufficient computer power) it is not always possible to simulate problems across widely varying length scales. To overcome this problem, Raoof and Hassanizadeh [2010a] have performed upscaling of adsorptive solute transport for an individual pore. The aim was to find effective pore-scale adsorption parameters for a solute which undergoes local equilibrium adsorption at the solid-water interface. They performed pore-scale simulations for a wide range of local-scale distribution coefficients and Peclet numbers. Through these simulations, they found relationships for the upscaled parameters as a function of underlying pore-scale parameters. Such relations are useful to perform upscaling by means of pore-network model. They have shown that even if there is equilibrium adsorption at the pore wall (i.e., at the grain surface), one may need to employ a kinetic description at larger scales. They have also shown this kinetic behavior through employed volume averaging method, yielding very similar results for upscaled kinetic parameters. These kinetic expressions are sometimes referred to as "pseudokinetics", because they are a result of averaging to larger scales, and are not inherent to the underlying surface reaction [Binning and Celia, 2008]. Scale-dependent pseudokinetics has been observed for relatively simple sorption systems, with local equilibrium [Burr et al., 1994, Espinoza and Valocchi, 1997, Rajaram, 1997].

Li et al. [2006b] used pore-network modeling to investigate scaling effects in geochemical reaction rates accounting for heterogeneities of both physical and mineral properties. In particular, they upscaled anorthite and kaolinite reaction rates under simulation conditions relevant to geological CO_2 sequestration. They found that pore-scale concentrations of reactants and reaction rates could vary spatially by orders of magnitude. Under such conditions, scaling effects are significant and one should apply an appropriate scaling factor; i.e., using lab-measured rates directly in the reactive transport models may introduce errors. To find macro-scale reaction rates analogous to CO_2 injection conditions, Algive et al. [2007b] have used pore-network modeling together with experimental work (on a glass micromodel) to evaluate effects of deposition regimes on permeability and porosity. Diffusion was taken into account in the calculation of the effective reaction coefficient at the macro scale, so that mass-transfer-limited reaction could be studied. They found that both pore-scale and macro-scale transport processes are needed for explaining deposition patterns; while macroscopic parameters controlled the concentration field and its variation, microscopic parameters determined the deposition rate for a given macroscopic concentration field.

Although there are some studies on upscaling of reaction rate coefficients, many of them do not provide an explicit relationship between pore scale and upscaled parameters. In this work, we present a methodology for using a pore-network model to investigate scaling effects in adsorption rates. The aim of this research is to find a relation between macroscopic (Darcy scale) and local scale transport coefficients for an adsorbing solute. We assume that at the solid grain surfaces adsorption occurs as a linear equilibrium process; the corresponding local-scale adsorption coefficient, k_d, is assumed to be constant throughout the porous medium. Upscaling will be carried out in two stages: i) from a local scale to the effective pore scale, and ii) from the effective pore scale to the scale of a core represented by the pore-network model. The first stage of this upscaling, from local scale to the effective pore scale, has been discussed in Chapter 3. There we found relationships between local-scale parameters (such as the local equilibrium adsorption coefficient, k_d, and the Peclet number, Pe) and effective pore-scale parameters such as attachment and detachment coefficient, k_{att} and k_{det}. Here, we perform upscaling by means of a $3D$ MDPN. This procedure results in relationships for upscaled adsorption parameters in terms of local-scale adsorption coefficient and flow velocity.

4.2 Description of the Pore-Network Model

In this study, we have utilized a MDPN model [Raoof and Hassanizadeh, 2009] to simulate porous media. One of the main features of our network is that pore throats can be oriented not only in the three principal directions, but in 13 different directions, allowing a maximum coordination number of 26, as shown in Figure (2.1). To get a desired coordination number distribution, we follow an elimination procedure to block some of the connections. The elimination procedure is such that a pre-specified mean coordination number can be obtained. A coordination number of zero means that the pore body is eliminated from the network, so there is no pore body located at that lattice point. A pore body with a coordination number of one is also eliminated except if it is located at the inlet or outlet boundaries (and it is a part of the flowing fluid backbone). This means that no dead-end pores are included in the network. Details of network generation can be found in Chapter (2).

A $5 \times 5 \times 5$ subset of the network domain and the coordination number distribution used in this study are given in Figure (4.1). The coordination number ranges from 1 to 12, with an average value of $\overline{z} = 4.4$.

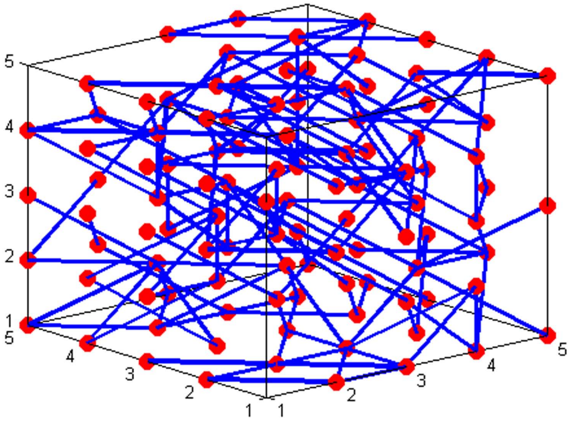

(a)

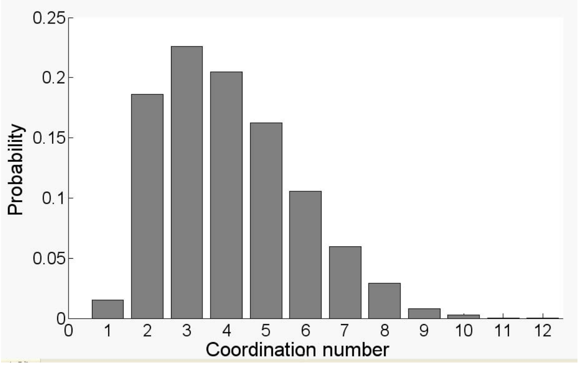

(b)

Figure 4.1: A representative domain of the multi-directional network structure and the coordination number distribution. The average coordination number is equal to 4.4.

4.2.1 Pore size distributions

In this study, we have used three different networks with different pore-throat size distributions. All three networks have the same coordination number distribution and the same pore body size distribution. The radius of pore bodies is given by an uncorrelated, truncated, lognormal probability distribution with an average of $\overline{R} = 0.33\ mm$. The radius of a pore throat is determined from the sizes of the two terminating pore-bodies. Figure (4.2) shows the distribution of pore-body radii together with three distributions for pore throat radii. The pore throat radius distributions were chosen to from different degrees of overlap with the pore-body radius distributions. The network contains 22,491 pores ($N_i = 51, N_j = N_k = 21$).

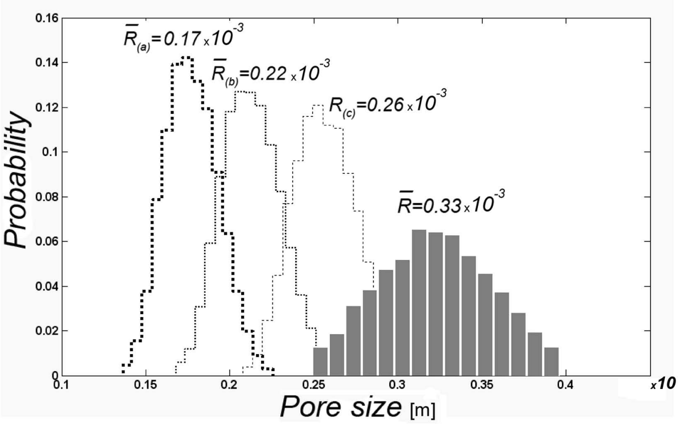

Figure 4.2: The distribution of pore-body radius (solid line) together with distributions of pore-throat radius ($R(a), R(b)$, and $\mathbf{R}(c)$) shown with dotted lines. The average radius of each distribution is shown above it.

4.3 Simulating flow and transport within the network

4.3.1 Flow simulation

In this work, we consider saturated flow through the network. A flow field is established in the network by imposing two different pressures on two opposing boundaries of the network. All other boundaries of the network parallel to the overall flow direction are no-flow boundaries. We assume that the volumetric discharge, q_{ij}, through a given pore throat,ij, can be prescribed by the Hagen-Poiseuille equation [Acharya et al., 2004]

$$q_{ij} = \frac{\pi R_{ij}^4}{8\mu l} \left(P_j - P_i\right) \tag{4.1}$$

where R_{ij} is the radius of the pore throat, μ is the fluid dynamic viscosity, and P_i and P_j are pressures at pore bodies i and j, respectively. Equation (4.1) is valid for laminar flow over a wide range of Reynolds number and is assumed to be appropriate for describing flow in a cylindrical pore [Bear, 1988]. For incompressible, steady-state flow, the sum of discharges of pore throats connected to a pore body must be zero

$$\sum_{j=1}^{z_i} q_{ij} = 0 \qquad j = 1, 2, \ldots, z_i \tag{4.2}$$

where z_i is the coordination number of pore body i. Equation (4.2) is applied to all pore bodies except those on the two flow boundaries where pressures are specified.

The system of Equations (4.1) and (4.2) for all pores results in a linear system having a sparse, symmetric, positive-definite coefficient matrix to be solved for pore body pressures [Suchomel et al., 1998c]. The flow velocity in all pore throats can be calculated using Equation (4.1).

Considering the network as an REV, the average pore water velocity, $\overline{v}$, can be determined as

$$\overline{v} = \frac{QL}{V^f} = \frac{Q}{\theta A} \tag{4.3}$$

where Q is the total discharge through the network (the sum of fluxes through all pore throats at the inlet or outlet boundary of the network), L is the network length in the flow direction, V^f is the total fluid volume present in the network, θ is porosity, and A is the cross-sectional area of the network perpendicular to the overall flow direction. Since we are modeling saturated porous media, the fluid volume is the sum of volumes of all pore bodies and pore throats.

4.3.2 Simulating adsorbing solute transport through the network

Transport through the medium is modeled by writing mass balance equations for each element of the network (i.e., pore bodies and throats). Figure (4.3) shows a schematic example of pore bodies interconnected by means of pore throats within the network.

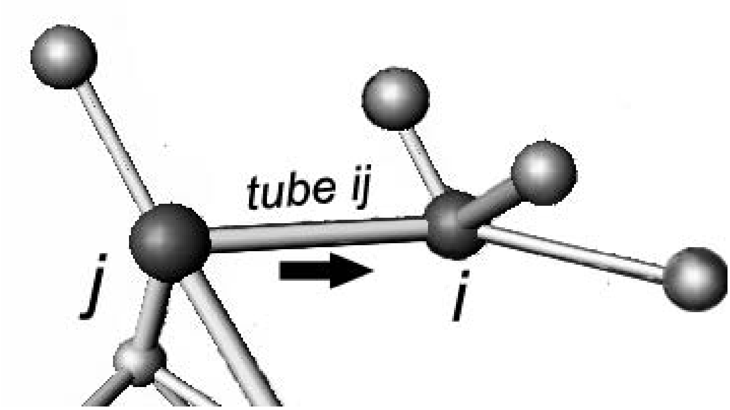

Figure 4.3: An example of interconnected pore bodies and pore throats. Flow direction is from pore body j into pore body i in tube ij. Node j is the upstream node.

We assume that each pore body and pore throat is a fully mixed domain. Therefore, a single concentration is assigned to each pore body or pore throat [De Jong, 1958, Li et al., 2007b]. For a given pore body, i, (e.g., in Figure 4.3) we can write the mass balance equation

$$V_i \frac{dc_i}{dt} = \sum_{j=1}^{N_{in}} q_{ij} c_{ij} - Q_i c_i \tag{4.4}$$

where c_i is the pore-body average mass concentration, c_{ij} is the pore-throat average mass concentration, Q_i is the total water flux leaving the pore body, V_i is the volume of pore body i, and N_{in} is the number of pore throats flowing into pore body i. As the total water flux entering a pore body is equal to the flux leaving it, we have

$$Q_i = \sum_{j=1}^{N_{in}} q_{ij} \tag{4.5}$$

Note that, in Equation (4.4), we have neglected adsorption of solutes to the pore body walls. Adsorption of the solutes to the walls of the pore throats is taken into account as explained below. At the local-scale, i.e., at the wall of the pore throats, the solute adsorption is assumed to occur as an equilibrium process. Assuming linear equilibrium, we may write $s = k_d c|_{wall}$, where s is the adsorbed concentration at the grain surface $[ML^{-2}]$, $c|_{wall}$ $[ML^{-3}]$ is the solute concentration in the fluid phase next to the wall, and k_d $[L]$ denotes the local-scale adsorption coefficient, assumed to be constant for all pores throughout the network.

However, as shown by Raoof and Hassanizadeh [2010a], the adsorption processes averaged over the whole pore throat should, in principle, be modeled as a kinetic process. Thus, the mass transport equation for a given pore throat may be written as:

$$V_{ij}\frac{dc_{ij}}{dt} = |q_{ij}|\,c_j - |q_{ij}|\,c_{ij} - V_{ij}k_{att,ij}c_{ij} + V_{ij}k_{det,ij}s_{ij} \tag{4.6}$$

where V_{ij} is the volume of the pore throat, q_{ij} denotes the volumetric flow within the tube, s_{ij} is the average adsorbed concentration, and $k_{att,ij}$ and $k_{det,ij}$ are attachment and detachment rate coefficients of tube ij, respectively. The first term on the right hand side of Equation (4.6) account for the mass entering from the upstream node j and the second term is the mass leaving the pore throat into the downstream pore body.

We also need an equation for the adsorbed mass concentration:

$$\frac{ds_{ij}}{dt} = k_{att,ij}c_{ij} - k_{det,ij}s_{ij} \tag{4.7}$$

The effective pore-scale kinetic adsorption coefficients, $k_{att,ij}$ and $k_{det,ij}$, depend on the local Peclet number and local-scale equilibrium adsorption coefficient, k_d, at the pore wall. Empirical relationships for a single pore were developed by Raoof and Hassanizadeh [2010a], through simulation of flow and transport within a single tube and then averaging results to get the effective pore-scale adsorption parameters.

The resulting relationships for a pore throat ij are [Raoof and Hassanizadeh, 2010a]:

$$k_{att,ij} = \frac{4.0(1-e^{-3\frac{k_{d,ij}}{R_{ij}}})\ \overline{v_{ij}}^{\,0.05}\,D_0^{0.95}}{R_{ij}^{1.95}} \tag{4.8}$$

$$k_{det,ij} = \frac{9.0\ \overline{v_{ij}}^{\,0.05}\,D_0^{0.95}}{(0.5+4.5\frac{k_{d,ij}}{R_{ij}})R_{ij}^{1.95}} \tag{4.9}$$

where $\overline{v_{ij}}$ is the average velocity, R_{ij} is the radius of the tube ij, and D_0 is the molecular diffusion coefficient.

Combination of Equations: (4.4), (4.6), and (4.7) results in a linear set of equations to be solved for c_i, c_{ij}, and s_{ij}. The number of unknowns is equal to $2 * N_{tube} + N_{node}$ (N_{tube} is number of pore throats and N_{node} is number of pore bodies). To get a more efficient numerical scheme, we have discretized Equations (4.6) and (4.7) for pore throats and then we have substituted them into the mass balance equation for the pore bodies (Equation (4.4)). This reduced the number of unknowns to N_{node} which is much smaller than $2 * N_{tube} + N_{node}$. The detail of discretization of the system of equations is given in Chapter 8, Section 8.2.1. For the accuracy of the scheme, the minimum time step was chosen on the basis of pore throat residence times [Suchomel et al., 1998c, Sun, 1996]

$$\Delta t < min\left\{T_{ij}\right\} = min\left\{V_{ij}q_{ij}^{-1}\right\} \tag{4.10}$$

where T_{ij} denotes fluid residence time pertaining to the pore throat ij. At designated times ($t >> \Delta t$), the concentrations of pore bodies that belong to a particular tier of the pore network are averaged to get breakthrough curves. A tier is defined as the group of pore bodies which possess the same longitudinal coordinate. The concentrations of pore bodies are weighted by their discharges; this results in a flux-averaged concentration. That is, the resulting normalized average concentration, $\overline{c}(x,t)$, is given by

$$\overline{c}(x,t) = \left[\frac{\sum_i^{N_t} c_i(x,t)Q_i}{\sum_i^{N_t} Q_i}\right]\frac{1}{c_0} \qquad i = 1, 2, 3, \ldots, N_t \tag{4.11}$$

where c_0 is the inlet solute concentration and the symbol Nt denotes the total number of pore bodies that are centered at the longitudinal coordinate x. The longitudinal coordinate could be chosen as an interval of ℓ, i.e. $x = 1\ell, 2\ell, \ldots, L$ where ℓ is the distance between centers of two adjacent pore bodies and L is the network length. The breakthrough curves have been obtained by plotting $\overline{c}(x = L, t)$ vs. time. Figure (4.4) shows an example of the breakthrough curve at the outlet of the network.

4.4 Macro-scale adsorption coefficients

The pore-network model described above simulates a 1D column experiment and results in a macro-scale concentration field. Governing equations for solute transport through such a column may be modeled by the Advection Dispersion Equation (ADE)

$$\theta\frac{\partial\overline{c}}{\partial t} + \rho^b\frac{\partial\overline{s}}{\partial t} + \theta\overline{v}\frac{\partial\overline{c}}{\partial x} = \theta D_L\frac{\partial^2\overline{c}}{\partial x^2} \tag{4.12}$$

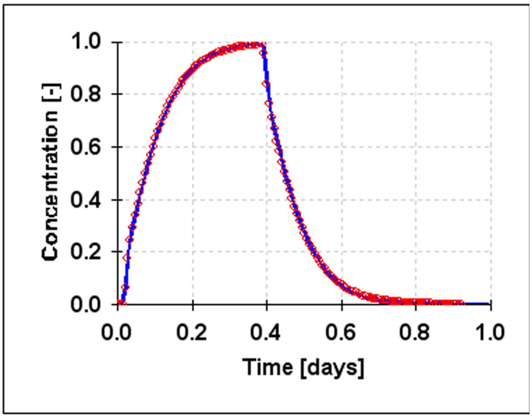

Figure 4.4: Example of resulting breakthrough curve from the network as a result of a pulse input with concentration of $c_0 = 1.0$. The symbols indicate average concentrations computed from the network model and the solid line is the solution of the continuum scale, 1D equation with kinetic adsorption (Equations 4.12 and 4.13)

where $\overline{s}$ $[MM^{-1}]$ is the average adsorbed mass per unit mass of the solid phase, θ is the porosity, ρ^b is the bulk density, $\overline{v}$ is average pore-water velocity, and D_L is the longitudinal dispersion coefficient. Assuming that adsorption follows first-order kinetic behavior at this scale, we also have

$$\frac{\partial \overline{s}}{\partial t} = \frac{\theta}{\rho^b} k^c_{att} \overline{c} - k^c_{det} \overline{s} \tag{4.13}$$

where k^c_{att} `and` k^c_{det} are core-scale attachment and detachment rate coefficients, respectively.

Equations (4.12) and (4.13) contain a number of parameters. The porosity, θ, and bulk density, ρ^b, are known for the pore network. The average pore-water velocity is determined as explained in Section 4.3.1. Dispersion and core-scale adsorption coefficients remain to be determined. One method to determine these coefficients is by fitting the solution of Equations (4.12) and (4.13) to the flux-averaged concentration breakthrough curve at the outlet of the network. These are discussed in the next two sections.

4.4.1 Dispersion coefficient

We assume that dispersion is not affected by the adsorption process. Therefore, we evaluate the longitudinal dispersion coefficient, D_L, by simulating the transport of a non-reactive tracer through the pore network (i.e., $k_d = 0$) and assume that it will be the same for adsorbing solutes. Fitting the analytical solution of Equation (4.12) [Van Genuchten and Alves, 1982] to the breakthrough curve of effluent concentration, dispersion coefficient is computed using the method of least squares. We have checked that the size of the pore network is large enough to obtain asymptotic values of dispersivity. Figure (4.5) shows the dispersion coefficient as a function of average velocity in the network. This is clearly a linear relationship from which we calculate the dispersivity value for our specific network to be $1.4 \times 10^{-3} m$.

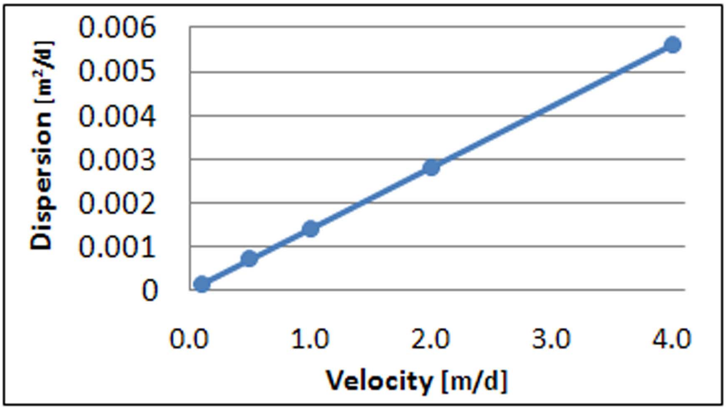

Figure 4.5: Dispersion coefficient as a function of mean pore-water velocity. The slope of the line is equal to dispersivity which is $1.4 \times 10^{-3} m$.

4.4.2 Core-scale kinetic rate coefficients (k^c_{att} and $\mathtt{k}^c_{det}$)

Once the dispersion coefficient is estimated, there are only the two core-scale parameters, k^c_{att} and $\mathtt{k}^c_{det}$, to be determined as a function of average pore-water velocity and local-scale distribution coefficient

$$k^c_{att} = f(k_d, \overline{v}) \tag{4.14a}$$

$$k^c_{det} = f(k_d, \overline{v}) \tag{4.14b}$$

The CXTFIT program [Toride et al., 1995] was used to simulate reactive transport at the macro-scale and to fit the resulting breakthrough curves to the flux-averaged concentration breakthrough curves calculated using the pore-network model. By repeating the procedure for a range of pore-scale parameters ($10^{-4}\,m < k_d < 10^{-2}\,m$, and $0.05\,m/d < \overline{v} < 4.0\,m/d$) and finding the corresponding core-scale parameters, we find relations between these set of parameters. Figures (4.6) and (4.7) show the adsorption parameters (k^c_{att} and k^c_{det}) as a function of the local-scale distribution coefficient, k_d.

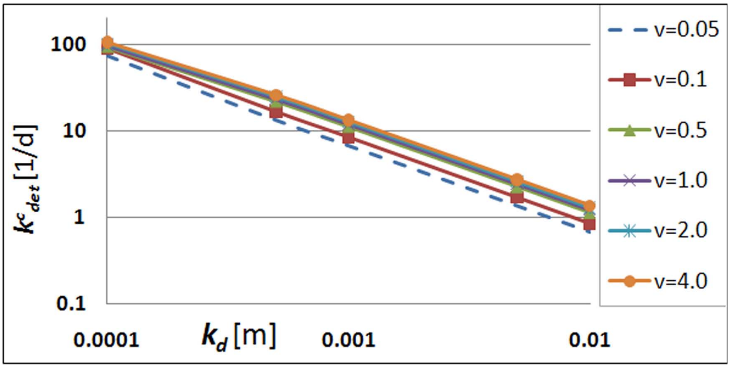

Figure 4.6: Detachment rate coefficient as a function of local-scale distribution coefficient, k_d. The relation is shown in log-log scale.

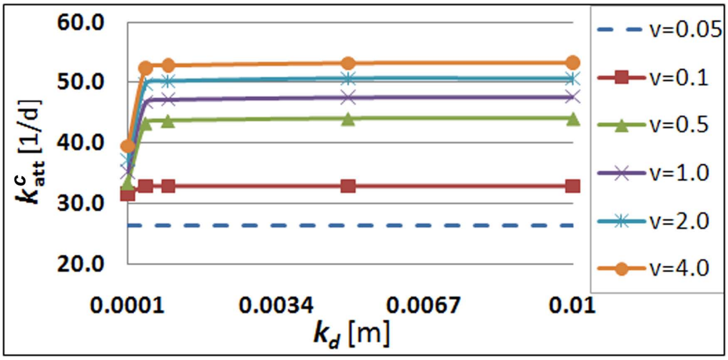

Figure 4.7: Attachment rate coefficient as a function of local-scale distribution coefficient, k_d

Equations (4.8) and (4.9) show that the effective pore-scale attachment and detachment rate constants are very weak functions of velocity. This dependency can cause the core-scale attachment and detachment coefficients to be also a function of average pore-water velocity. Indeed, as shown in Figure 4.10, the core-scale detachment coefficient increases with increase in velocity. However, the dependency decrease at higher velocities. This behavior is to be expected considering the power, 0.05, of the velocity term in Equation (4.9). This means that dependence on velocity is significant only for small velocities.

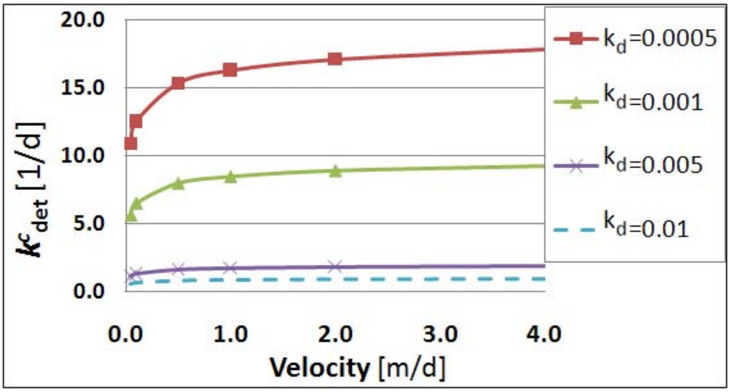

Figure 4.8: Detachment rate coefficient as a function of average pore water velocity.

4.4.3 Core-scale distribution coefficient ($K^c_{_D}$)

We define the core-scale distribution coefficient, $K^c_{_D}$, as

$$K^c_{_D} = \frac{k^c_{att}}{k^c_{det}} \tag{4.15}$$

Since we obtained core-scale coefficients, k^c_{att} and k^c_{det}, we can calculate upscaled distribution coefficient. The result is shown in Figure (4.9). It is evident that $K^c_{_D}$ is a linear function of the pore-scale distribution coefficient, k_d. This linear relationship is a verification of our upscaling process. Since both $K^c_{_D}$ and k_d are a measure of the capacity of the porous medium to adsorb mass, and given the fact that k_d is kept constant for all pores, they should be linearly related. We have found that the proportionality constant in this linear relation is equal to the solid specific surface area, S (the solid surface area divided by the total sample volume) i.e. $K^c_{_D} = Sk_d$. Since in our pore-network model, adsorption is taking place only in the pore throats (pore bodies are considered to be non adsorptive), we use only the surface of pore throats to calculate specific surface. Figure (4.9) is based on results from a network with the value of S equal to $5.28 \times 10^3 m^{-1}$, which is exactly the slope of the line fitting the data points.

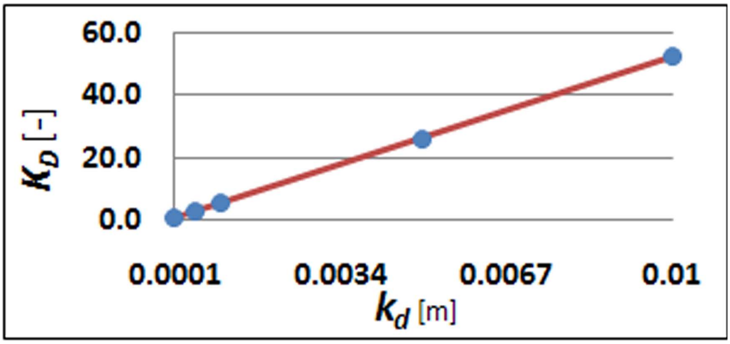

Figure 4.9: Upscaled distribution coefficient, K^c_D, as a function of local-scale distribution coefficient, k_d. The circles are the results of network simulations. A linear equation fits the data: $K^c_D = Sk_d$. S is equal to $5.28 \times 10^3 m^{-1}$.

4.5 Discussion

Figures (4.6) and (4.7) show that the core-scale attachment and detachment rate constants are functions of the local-scale adsorption coefficient and the average pore-water velocity. Combining these graphs results in a surface plot of $k^c_{det}(k_d, \overline{v})$, as shown in Figure (4.10) for the network ($\overline{R}_{throat} = 0.17 \times 10^{-3}\, m$). We have fitted an equation to this surface

$$k^c_{det} = \frac{D_0^{0.95}\ \overline{v}^{0.05}}{(0.02 + 0.5\, k_d)\overline{R}^{0.95}} \tag{4.16}$$

Using a volume averaging method, Raoof and Hassanizadeh [2010a] derived the following relationship for macro-scale kinetic adsorption coefficient for a general porous medium

$$k^c_{det} = \frac{2D_0}{k_d\, \overline{R}} \tag{4.17}$$

If, in Equation (4.16), we neglect the dependency on velocity and approximate $(0.02 + 0.5\, k_d) \approx 0.5\, k_d$, we can confirm that the two equations are in full agreement.

Clearly, knowing the upscaled detachment rate coefficient and the upscaled distribution coefficient, we can obtain a relationship for upscaled attachment coefficient

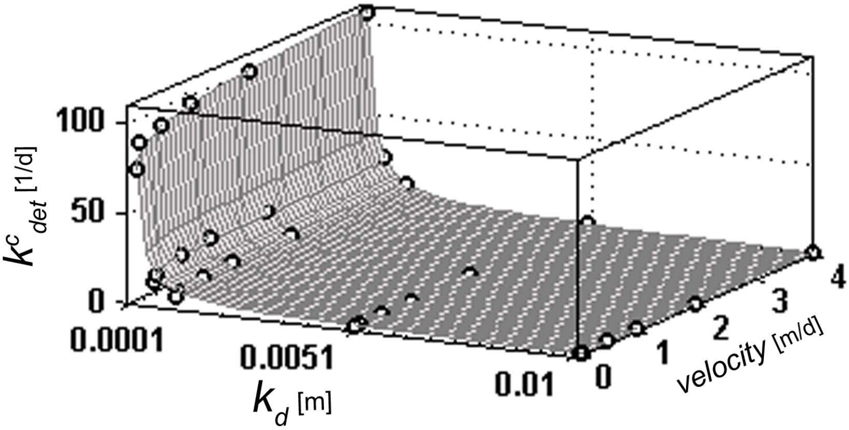

Figure 4.10: Calculated values of the core-scale detachment coefficient, k^c_{det}, as a function of the local-scale distribution coefficient, k_d, and mean pore-water velocity. The circles are data points and the surface represents results of Equation (4.16) fitted to $k^c_{det} - k_d - \overline{v}$ data points.

$$k^c_{_{att}} = K^c_{_D}\, k^c_{_{det}} = S\, k_d\, \frac{D_{mol}^{0.95}\ \overline{v}^{0.05}}{(0.02 + 0.5k_d)\overline{R}^{0.95}} \tag{4.18}$$

This equation may be approximated by

$$k^c_{_{att}} = \frac{S\, D_0}{0.5\, \overline{R}} \tag{4.19}$$

which is the same as the equation derived through the averaging method by Raoof and Hassanizadeh [2010a].

As mentioned above, Equations (4.16) and (4.18) were obtained based on results from a specific pore network. We have verified these equations by applying them to another pore network with the same pore-body size distribution as in Figure (4.2) but with a different mean pore-throat size, as well as a network with different pore-body size distribution and a mean pore-body diameter of $0.36 \times 10^{-3}\, m$. Figures (4.11) and (4.12) show the results of the verification; plotted lines are obtained from Equation (4.16) for these networks while the circles indicate pore-network computations. It is evident that the agreement is excellent.

Equations (4.16) and (4.18) show the upscaling relations for the core scale

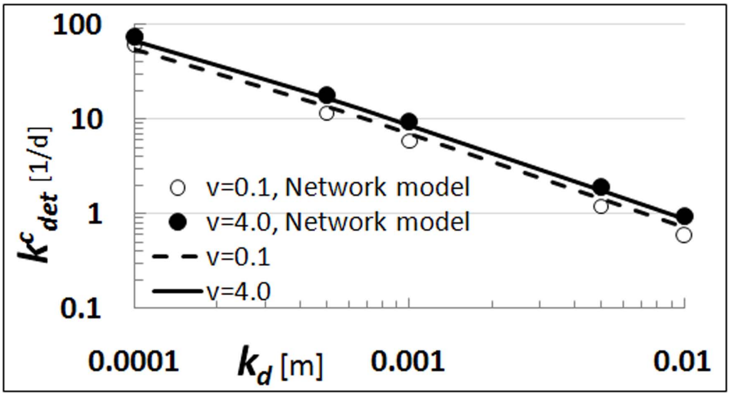

Figure 4.11: Simulated k^c_{det} against local-scale k_d for a network with the same pore-body size distribution as shown in Figure (4.2), but with $\overline{R} = 0.26 \times 10^{-3}m$. The circles are simulated results and the lines are based on Equation (4.16).

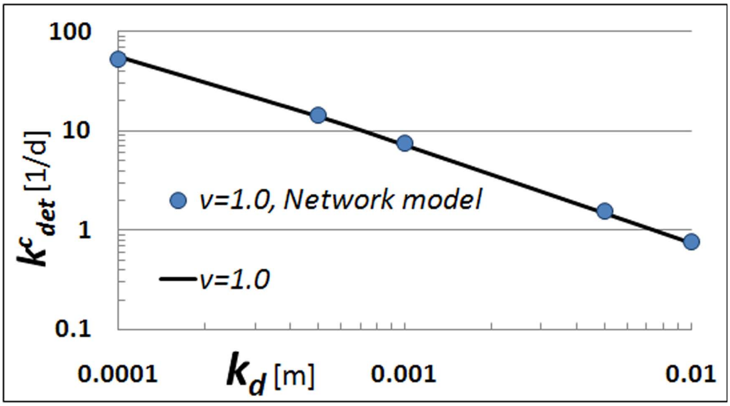

Figure 4.12: Simulated k^c_{det} against local-scale k_d for network with a different pore-body size distribution than shown in Figure 4.2. The mean pore-body size is $0.36 \times 10^{-3}m$. The circles are simulated results and the line is based on Equation (4.16) for corresponding parameter values.

attachment and detachment rate constants. It is of interest to evaluate the degree of non-equilibrium using these relations. An important criterion for the classification of reactive transport problems is the Damkhler number, Da, which is the ratio of the advection time scale ($L/\overline{v}$) to the typical time scale of the adsorption (defined as ($1/k_{det}$)), with L being loosely defined as some characteristic length of the domain

$$Da = \frac{k^{c}_{det} L}{\overline{v}} \tag{4.20}$$

As a rule of thumb, adsorption is considered to be (quasi) equilibrium, if $Da >> 1$, and kinetic for $Da << 1$. While the results of simulations using slower velocities and higher detachment coefficients show equilibrium behavior at the network scale, the behavior was kinetic under higher velocities and lower detachment coefficient values. In this work, using different combinations of pore-water velocity and distribution coefficient, different Da numbers were obtained, which ranged from less than unity (e.g., 0.05) to Da numbers as large as 90.0. Using Equation (4.16), we can calculate k^{c}_{det} to estimate Da number for different values of the local-scale distribution coefficient. An increase in the local-scale k_d will result in a decrease in the core-scale detachment coefficient, which in turn results in a smaller Da number and kinetic effects becoming more significant.

To determine the role of the local-scale heterogeneity, we have made pore-network simulations where different values of local k_d are assigned to different pores, following a log-normal distribution. Figure (4.13) shows the distribution of local-scale k_d used within the network.

In addition to simulations applying the above k_d distribution, we have also repeated the simulations using the average value of the k_d distribution. We have calculated the average of k_d weighted with the specific surface area

$$\overline{k_d} = \frac{\sum\limits_{i=1}^{Ntube} k_{d_i} S_i}{\sum\limits_{i=1}^{Ntube} S_i} \tag{4.21}$$

where S_i and k_{di} are the specific surface area and the local distribution coefficient, respectively, for pore throat i. In both cases, we have fitted the solution of a $1D$ analytical solution of the advection dispersion equation with kinetic adsorption to the breakthrough curve of the average concentration at the outlet of the network to obtain upscaled kinetic parameters. This procedure was

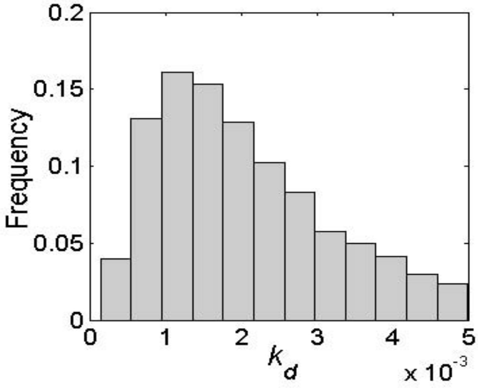

Figure 4.13: Distribution of the local-scale distribution coefficient, k_d, within the network for the calculation of Figure (4.14).

repeated for a range of velocities between 0.5 and 5.5 m/d. Figure (4.14) shows the dependency of the core-scale detachment coefficient on velocity for both cases. It is evident that heterogeneity in local-scale distribution coefficient does not significantly affect the value of the upscaled detachment coefficient.

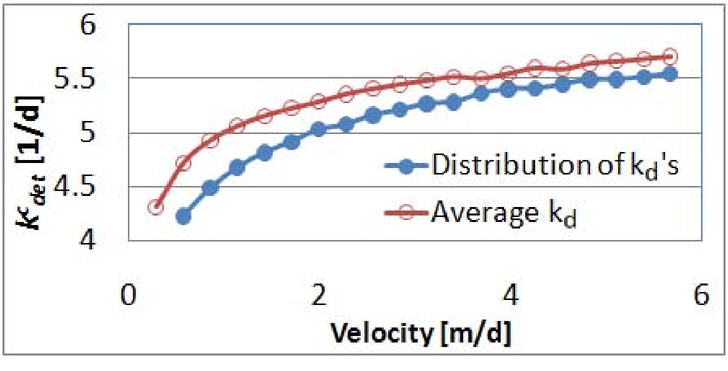

Figure 4.14: Core-scale detachment rate coefficient, k^c_{det}, as a function of average pore-water velocity.

Figure (4.14) shows that the heterogeneity of local-scale k_d does not considerably affect the dependency on velocity.

4.6 Conclusions

The transport of adsorptive solutes in porous media is a scale dependent process. We need to apply effective adsorption parameters at different scales. In our previous study [Raoof and Hassanizadeh, 2010a], we have shown that, starting from equilibrium at the local scale (at the wall of pores), the effective form of adsorption at the pore scale could be kinetic. In this study, using a MDPN model for simulating adsorptive solute transport, we have extended upscaling to the core scale for the case of saturated porous media with homogenous local-scale adsorption. In particular we have challenged the conventional view of reactive transport where a single adsorption parameter is used for the whole network. The model allows us to investigate how various micro-scale parameters affect transport properties of a medium.

Different combinations of local-scale distribution coefficient and pore-scale velocity have been used to obtain upscaled adsorption parameters. Through this procedure, we found relationships between core-scale adsorption parameters and local-scale transport coefficients, including the molecular diffusion coefficient,the grain specific surface area, and average pore-throat size. We have shown that even if there is equilibrium adsorption at the pore wall (or at the grain surface), one may need to employ a kinetic description at larger scales. In contrast to some other studies, which reported dependency of reaction parameters on flow rate, we have shown that these kinetic parameters are only a weak function of velocity; in this aspect, our result is more in agreement with the study done by Zhang et al. [2008] and Zhang and Lv [2009] who have shown that adsorption parameters are not dependent on flow rate.

Natural porous media are most likely to be heterogeneous with correlated spatial distributions. Therefore, treating adsorption as homogenous is an idealization. Quantifying adsorptive heterogeneity and also dependencies of adsorption parameters on velocity for the case of unsaturated porous media are areas that still need to be investigated.

We should state that the statistical distributions (pore sizes, k_d, coordination number, and etc) in this study have been uncorrelated, and under correlated distributions one may need more statistical parameters to define upscaled coefficients.

Part III

Upscaling and Pore Scale Modeling; Partially-Saturated Conditions

Raoof, A. and Hassanizadeh S. M., *"A new formulation for pore-network modeling of two-phase flow"*, accepted for publication at Water Resources Research, 2011.

CHAPTER 5

A NEW FORMULATION FOR PORE-NETWORK MODELING OF TWO-PHASE FLOW

The question is not what you look at, but what you see.

Henry David Thoreau

Abstract

Pore network models of two-phase flow in porous media are widely used to investigate constitutive relationships between saturation and relative permeability as well as capillary pressure. Results of many studies show discrepancy between calculated relative permeability and corresponding measured values. Often calculated values overestimate the measured values. An important feature of almost all pore-network models is that the resistance to flow is assumed to come from pore throats only; i.e., the resistance of pore bodies to the flow is considered to be negligible compare to the resistance of pore throats. We contend that this simplification may considerably affect the magnitude of the relative permeability curves.

In this study, we present a new formulation for pore-network modeling of two-phase flow, which accounts for the resistant to the flow within the pore bodies. In a quantitative investigation, we have shown the significance of this effect under primary drainage conditions. The pore space is represented by cubic pore bodies and parallelepiped pore throats in a MDPN. model, which allows for a distribution of coordination numbers ranging between zero and 26. This topological property, together with geometrical distributions of pore sizes are used to mimic the microstructure of real porous media. Under unsaturated conditions, the wetting fluid is considered to fill only spaces along edges of cubic pore bodies.

We show that the resistance to the flow within these filaments of fluids is comparable to the resistance to the flow within pore throats. The resulting saturation-relative permeability relationships show very good agreement with measured curves.

While our computations have been restricted to relative permeability curves, they demonstrate the significance of this formulation of pore-network modeling to predict other transport properties such as dispersivities and mass transfer coefficients, through including limited mixing within the pore bodies. We will address this issue in Chapter 5.

5.1 Introduction

5.1.1 Pore-network modeling

Understanding of multiphase flow and transport in porous media is of great importance in many fields, including contaminant cleanup and petroleum engineering. Modeling multiphase fluid flow in porous media requires specification of the capillary constitutive properties of the porous medium. Examples are i) the relationship between the capillary pressure, P_c (the difference between the pressures in the nonwetting and wetting fluids) and the fluid saturation, S, ii) the relative permeability, k_r, as a function of either the saturation or capillary pressure, and iii) the relationship between dispersivity and saturation in solute transport processes.

The relative permeability of a fluid is a measure of the conductance of the porous medium for that fluid at a given saturation. Relative permeability measurements on field samples are difficult and time consuming. In general, experimental determination of the $P_c - S$ relationship is easier than measurement of relative permeability. For this reason, empirical relationships, such as those of Brooks and Corey [Brooks and Corey, 1964] and Van Genuchten [van Genuchten, 1980], are often used to model the dependence of relative permeability on capillary pressure or saturation.

Another approach for obtaining multiphase constitutive properties is to use Pore-Network Models (PNMs). One of the early attempts to estimate relative permeability was using a bundle-of-capillary-tubes model. This was based on the assumption that a porous medium may be modeled as bundle of capillary tubes of various diameters. However, such models ignore the interconnected nature of porous media and often do not provide realistic results. PNMs, first

suggested by Fatt [1956b], offer a more realistic approach for calculating multiphase constitutive properties. The vast majority of PNMs consist of pore bodies (or nodes) and pore throats (or channels), along with a selected topological configuration which prescribes how pore bodies are connected via pore throats. The pore bodies are meant to represent larger void spaces found in natural porous media. The narrow openings that connect the adjacent pore bodies are modeled by the pore throats, which are essentially capillary tubes.
The pore-network approach for modeling multiphase flow properties has been employed extensively in the petroleum engineering literature [Chatzis and Dullien, 1977, 1985, Larson et al., 1981, Chandler et al., 1982, Wilkinson and Willemsen, 1983]. In recent years, the pore-network approach has been also explored in the fields of hydrology and soil physics [Ferrand and Celia, 1992, Berkowitz and Balberg, 1993, Ewing and Gupta, 1993a,b] and upscaling of reactive transport [Acharya et al., 2005a, Li et al., 2006b, Raoof and Hassanizadeh, 2010b].

Because of their ability to simulate the highly disordered geometry of pore space and relatively low computational cost, PNMs hold promise as tools for predicting multiphase flow properties of specific porous media. For example, the dependence of capillary pressure on saturation is modeled by determining the location of fluid-fluid interfaces throughout the network using the Young-Laplace equation (e.g., Dullien [1991]). This is sometimes modified by other pore-level mechanisms, such as snapoff during imbibition (e.g., Chandler et al. [1982], Yu and Wardlaw [1986]). Also, the dependence of relative permeability on saturation is determined by computing the resistance to flow in the connected portion of a fluid. In these calculations, resistance to the flow within the pore bodies is commonly ignored, assuming that conductance within the pore bodies is much higher that the conductance within the pore throats (see e.g., Joekar-Niasar et al. [2008a]). This means that fluid fluxes within the pore bodies are not calculated. The significance and effects of this assumption, however, have been never investigated.

5.1.2 Pore-network construction

The pore morphology of natural porous media is quite complex and its description is a formidable problem. However, in many studies related to porous media, geometrical features are crucial even though it is very hard to get detailed information about them [Adler, 1992]. The morphology of a porous medium consists of its geometrical properties (the shape and volume of its pores) and its topological properties, i.e. the way in which the pores are connected to each other. A regular array of spheres and cylinders is one of the simplest representation of porous media, which never occurs in natural systems. Nevertheless, because of the relative simplicity of these patterns, many studies have focused on such network structures, either experimentally, theoretically, or numerically (e.g., Fatt [1956a], Kruyer [1958], Mayer and Stowe [1965]). There are several approaches to identifying and specifying the porous medium morphology. These approaches may be classed into two broad categories: experimental imaging and numerical simulation of porous media.

One approach that can be adopted to get the morphology of porous media is to use synchrotron X-ray microtomography to directly image the three-dimensional pore structure of the rock at very high resolution, so as to capture as much details as possible. These images can then be used to generate a network. This approach has been used, for example, by Ferreol and Rothman [1995], Lindquist et al. [2000] and Arns et al. [2001, 2003a]. This is a direct and accurate method, and generally leads to results that are in reasonable agreement with experiments. However, even with the recent advances of computer technology, this is a time-consuming process, and the size of the modeled domain is typically limited to a few centimeters or less. Another experimental approach is to use information obtained from so-called “serial sectioning”, i.e. cutting the sample and mapping the thin sections [Zinszner and Meynot, 1982].

Since the experimental measurements are time-consuming and expensive, the use of numerically-simulated porous media is conceptually appealing. It is possible to generate porous media based on measured statistical properties of real porous media. Compared to sequential sectioning the numerically-simulated media do not include full details of three-dimensional features. In general, certain features of the real system are selected (such as porosity, pore-size distribution and correlation functions), and then porous media are generated so as to mimic the real porous medium by matching these properties, and to get some major topological properties (such as coordination number distribution). Using these properties, we can generate a simplified, but intricately constructed and well-characterized, pore network that can be used to study various flow processes in a relatively simple yet generally accurate manner [Pan et al., 2001].

In this study, we represent porous media by a numerically simulated domain, which allows a distribution of coordination number ranging between zero and 26. We will show that this topology will result in a more accurate flow field compared to the regular 3D pore network model with a fixed coordination num-

ber of six.
There exist many PNM studies investigating various geometrical and topological properties of porous media and their effect on flow and transport in porous media. They include: the effect of pore size distribution [Lindquist et al., 2000, Jerauld and Salter, 1990], network structure and coordination number [Al-Kharusi and Blunt, 2008, Sok et al., 2002, Mahmud et al., 2007, Arns et al., 2004, Øren and Bakke, 2003a, Mogensen and Stenby, 1998], pore angularity and shape factors [Sholokhova et al., 2009, Zhang et al., 2010, Patzek and Kristensen, 2001, Øren et al., 1998a], and correlation functions [Arns et al., 2003b, Rajaram et al., Ferrand et al., 1994, Lymberopoulos and Payatakes, 1992, Jerauld and Salter, 1990, Tsakiroglou and Payatakes, 1991, Renault, 1991, Ioannidis et al., 1993]. In almost all of these studies, the selected pore size distributions are such that most of the pore space is assigned to the pore bodies. In such cases, the modeling of flow within pore bodies will be of major influence on hydrodynamic properties of the network, certainly in the case of flow on partially drained pore spaces. This issue, however, unlike the above-mentioned properties of porous media has not been addressed in any pore-network study. We will address this particular issue in this study.

5.1.3 Objectives and approach

Under partially-saturated conditions, much of a pore body is occupied by the non-wetting phase, such that the wetting phase can only flow through the edges, similar to the flow conditions within drained pore throats. Under these conditions, the effect of resistance within the pore-bodies become important and comparable to pore throats; taking this effect into account can improve the result of $k_r - S$ calculations. This is, however, not possible within current pore-network modeling approaches. In fact, this is one of the shortcomings of pore-network modeling compared to other pore-scale modeling approaches, such as lattice-Boltzmann method (LBM). LBM has the advantage that it fully discretizes the space within each pore space. In PNM, however, the smallest discretization unit is normally one pore body or pore throat. That is, in PNM, only one (average) pressure (or one average concentration) is assigned to each pore body. Thus, using pore body or pore throat discretization, one needs to apply so-called effective parameters [Meile and Tuncay, 2006, Raoof and Hassanizadeh, 2008, 2010b]. While this assumption may be acceptable for a fully saturated pore body (considering the large size of a pore body compared to pore throats connected to it), it is a crude approximation when the water phase is present only in the corners and edges of a pore body. This could be one of the reasons for the discrepancies often found between PNM prediction of relative permeability and experimental observations.

To include the effect of resistance to flow of the wetting phase within the pore bodies, we propose a new formulation for two-phase flow and transport under partially-saturated conditions. In this new formulation, we further discretize the pore bodies and treat each corner and each edge of a pore body as a separate domain, with its own pressure and concentration, different from those of the wetting phase in other corners of the same pore body. Details of this approach will be given in this chapter and its utility is illustrated by calculation of relative permeability curves.

5.2 Network Generation

5.2.1 Pore size distributions

In the present study, the pore structure is represented using a MDPN model in three-dimensional space. Because natural porous media can be mostly described by a lognormal distribution [Bear, 1988], the pore-body radii are assigned from such a distribution, with no spatial correlation, expressed by:

$$f\left(R_i,\sigma\right)=\frac{\sqrt{2}\exp\left[-\frac{1}{2}\left(\frac{\ln\frac{R_i}{R_m}}{\sigma}\right)^2\right]}{\sqrt{\pi\sigma^2}R_i\left[erf\left(\frac{\ln\frac{R_{\max}}{R_m}}{\sqrt{2\sigma^2}}\right)-erf\left(\frac{\ln\frac{R_{\min}}{R_m}}{\sqrt{2\sigma^2}}\right)\right]} \tag{5.1}$$

where R_{min}, R_{max}, and R_m are the minimum, maximum, and mean of the distribution, respectively; and σ^2 is the variance of the distribution. The pore structure is constrained to be isotropic, in the sense that the same values of R-coefficients and σ^2 are specified for all pores oriented along all network directions.

In this study, five different networks were constructed: three generic networks, and two networks which represented specific porous media. The three generic networks had the same coordination number distribution, the same distribution of pore body radii, but different pore throat size distributions. Figure (5.1) shows the distribution of pore body sizes and the three different distributions for pore throat radii. Pore body radii are taken from the uncorrelated, truncated, lognormal distributions (figure 5.2). Pore throat radii are correlated to the pore body radii. Thus, the three networks have different aspect ratio's (ratio of pore body to pore throat radius). Properties of the two porous-medium-specific networks will be given later.

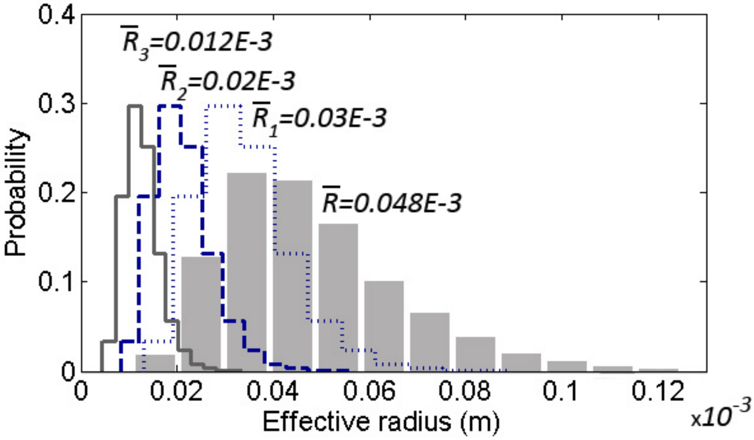

Figure 5.1: The distribution of pore-body radii (columns) together with three distributions of pore-throat radii (R_1, R_2, and R_3) (lines). The mean radii of the pore-body and pore-throat distributions are shown above each distribution.

5.2.2 Determination of the pore cross section and corner half angles

A key characteristic of real porous media is the angular form of pores. It has been demonstrated that having pores with a circular cross section, and thus single-phase occupancy, causes insufficient connectivity of the wetting phase and as a result poor representation of experimental data [Zhou et al., 2000b]. Angular cross sections retain the wetting fluid in their corner and allow two or more fluids to flow simultaneously through the same pore. Pores which are angular in cross section are thus a much more realistic model than the commonly employed cylindrical shape. In the present work, pore bodies are considered to be cubic in shape, whereas, pore throats are assigned a variety of cross sectional shapes including circular, rectangular, and scalene triangular.

The shape of an angular pore cross section is prescribed in terms of a dimensionless shape factor, G, [Mason and Morrow, 1991] which is defined as

$$G = \frac{A}{P^2} \tag{5.2}$$

where A and P are the area and the perimeter of the cross section, respectively. The shape factor replaces the irregular and complicated shape of a pore throat by an equivalent irregular, but simpler, shape. The value of shape factors for pore throats are chosen from a truncated lognormal distribution (Equation 5.1), with a minimum shape factor value of zero corresponding to a slit, and a maximum value of 0.08 corresponding to a circular cross section. Values between zero and 0.048 correspond to triangular cross sections (with maximum value of 0.048 for an equilateral triangle), and values between zero and 0.062 correspond to rectangular cross section (with the maximum value corresponding to a square).

For a triangular cross section, there is a relationship between shape factor and corner angles [Patzek, 2001], given by

$$G = \frac{A}{P^2} = \frac{1}{4\sum\limits_{i=1}^{3}\cot(Angle_i)} = \frac{1}{4}\tan\alpha\tan\beta\cot(\alpha+\beta) \tag{5.3}$$

where α and β are the two corner half-angles subtended by the two longest sides of the triangle. It is clear from the above equation that for a single value of the shape factor, a range of corner half angles are possible. We follow the procedure employed by Patzek [2001] to select a nonunique solution for corner half-angles. We start by selecting the upper and lower limits of the corner half-angle, β, assuming $\beta < \alpha$. These two limits are

$$\beta_{\min} = \arctan\left[\frac{2}{\sqrt{3}}\cos\left(\frac{\arccos\left(-12\sqrt{3}G\right)}{3} + \frac{4\pi}{3}\right)\right] \tag{5.4}$$

$$\beta_{\max} = \arctan\left[\frac{2}{\sqrt{3}}\cos\left(\frac{\arccos\left(-12\sqrt{3}G\right)}{3}\right)\right] \tag{5.5}$$

We randomly pick a value, $\beta = \beta_{\min} + (\beta_{\max} - \beta_{\min})\,.\varphi$, between the two limits. Where φ is a uniformly distributed random number, between 0 and 1. We calculate the corresponding value of α by inverting Equation (5.3)

$$\alpha = -\frac{1}{2}\beta + \frac{1}{2}\arcsin\left(\frac{\tan\beta + 4G}{\tan\beta - 4G}\sin\beta\right) \tag{5.6}$$

The third and smallest corner half-angle, γ, is then obtained from $\gamma = \frac{\pi}{2} - (\alpha + \beta)$. After determining the corner angles, finding the triangle size requires specifying a length scale. We have chosen the radius of the equivalent circle of a pore cross section as the length scale. One way to select this radius is to relate it to the radii sizes of the two terminating pore bodies, as suggested by Raoof and Hassanizadeh [2010b]. By equating the area of the triangle to the area of the equivalent circle we fully specify the triangular cross-section. Similarly, for rectangular pore-throats, the rectangle area is obtained from the area of the equivalent circle. Knowing the area and the shape factor, we can calculate the dimensions of the rectangle by solving a quadratic equation.

5.2.3 Coordination number distribution in MDPN

One of the main features of the MDPN is that pore throats can be oriented not only in the three principal directions, but in 13 different directions, allowing a maximum coordination number of 26, as shown in Figure (2.1). To get a desired coordination number distribution, we follow an elimination procedure to rule out some of the connections. The elimination procedure is such that a pre-specified mean coordination number can be obtained. A coordination number of zero means that the pore body is eliminated from the network, so there is no pore body located at that lattice point. A pore body with a coordination number of one is also eliminated except if it is located at the inlet or outlet boundaries (so it belongs to the flowing fluid backbone). Thus no dead-end pores are included in the network. Details of network generation can be found in Chapter 2.

Since in many pore-network modeling studies, a fixed coordination number of six is employed, we chose to generate a stochastic network with the coordination number ranging from zero to 16, but with a mean coordination number of six. However, we shall also present results for networks with other mean coordination numbers, related to some real porous media. The distribution of coordination number and a representative domain of the network used in this study are given in Figure (5.2).

5.2.4 Pore space discretization

Flow in both pore bodies and pore throats arises from pressure gradients. The conductivity of a flow path is dominated by the narrowest constriction along the path. Under saturated conditions, considering the larger sizes of pore bodies compared to pore throats, one may safely neglect the resistance to the flow within pore bodies (thus assuming zero pressure gradient within a pore body) and assign conductances only to the pore throats. This has been the common practice in almost all pore-network models. However, under unsaturated con-

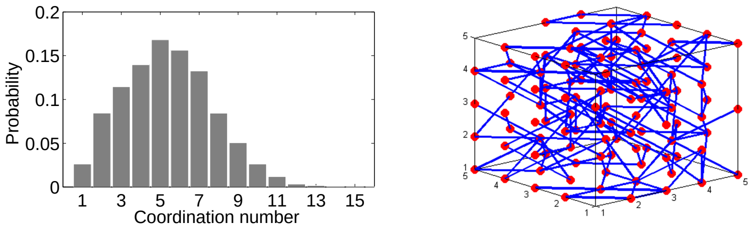

(a) (b)

Figure 5.2: The coordination number distribution and a representative sub-domain of MDPN. The mean coordination number is equal to 6.0.

ditions, a given pore body or pore throat can be invaded and filled mostly by the non-wetting phase, forcing the wetting phase to flow only along the edges. Figure (5.3) shows a schematic example of two pore bodies connected to each other by a pore throat of triangular cross section. Under such conditions, pore throats are no longer necessarily the narrowest constriction along the flow path. In fact, resistance to the flow within the edges of pore bodies may be comparable to, or even larger than, the resistance to flow within the pore throats. Thus, it is more realistic to consider conductance, and calculate fluxes, within the pore bodies as well as pore throats. This lower conductivity of a pore body can also reduce the connectivity among saturated pore throats connected to a drained pore body (such as pore throats number 2, 3, 4 in Figure 5.3b), and thus reduce their effective conductance although they are still saturated.

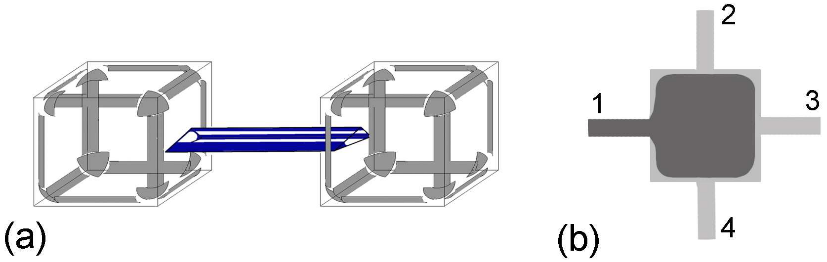

Figure 5.3: (a) Example of two drained pore-bodies connected to each other by a drained pore throat with triangular cross section, and (b) a pore body which is invaded by non-wetting phase, through one of its throats, and as a result reduces the connectivity of the neighboring saturated pore throats.

Our new approach to include the resistance to the flow within pore bodies is implemented as follows. Resistance to flow within a pore body is assumed to be negligible as long as the pore body is saturated; and a single pressure is assigned to the whole pore, assuming the local pressure gradient is negligible. As soon as the non-wetting phase invades the pore body and occupies the bulk space of the pore, we consider each corner of the pore as a separate element with its own pressure. Thus, for a cubic pore body, 8 different corner elements exist with 8 different pressure values assigned to them. We refer to the corner elements as pressure nodes. Flow between the pressure nodes occurs through the 12 edges of the pore body (see Figure 5.3a). The conductance of each edge needs to be determined as a function of the thickness of the water film residing in the edge. This thickness depends on the radius of curvature of the fluid-fluid interface, which in turn depends on the capillary pressure. Pore body corners are connected to the neighboring pore body corners via pore throats. Thus we need to specify connections of pore throats to the corners of pore bodies. The algorithm which has been used to associate different pore throats to different corners of neighboring pore bodies is described in Appendix B.

5.3 Modeling flow in the network

5.3.1 Primary drainage simulations

We wish to simulate primary drainage in a strongly-wet porous medium, and to obtain capillary pressure-saturation and relative permeability-saturation curves. The network is assumed to be initially fully saturated with the wetting phase. The network is placed between two fluid reservoirs each at a specified pressure. The pressure of the wetting phase in the outlet reservoir is fixed to zero. The pressure of the non-wetting phase in the inflow reservoir is also specified but is increased incrementally. Thus, the network will be subjected to incrementally larger capillary pressures. At any given capillary pressure, two kinds of computations are carried out. First, the equilibrium positions of all wetting-nonwetting interfaces within the network are determined. From this information, the average saturation of the network at any given capillary pressure is calculated. The plot of average saturation as a function of imposed capillary pressure results in the capillary pressure-saturation curve.

In another set of calculations, permeabilities of the network to the two fluids are calculated. For these calculations, at any imposed capillary pressure, P_c, and thus for the corresponding distribution of the two fluids in the network, a small flux of each fluid is established. This is done by imposing a small pressure gradient within each fluid; that is a small pressure difference $\Delta p^\alpha \quad (\alpha = w, n)$ is assumed to exist between input and output reservoirs. Δp^n and Δp^w are chosen such that the imposed capillary pressure, P_c is still present throughout the network. The corresponding permeabilities of the network for the two fluids can be determined, as explained shortly in the following sections. This is the common approach in most pore-network models for calculating relative permeabilities. In these computations, the friction between the two fluids at their interface is neglected. Therefore, it may be assumed the the fluids flow does not disturb the equilibrium positions of the fluid-fluid interfaces in the network. Also, the flow of the two fluids is decoupled, i.e., each fluid flows in its own domain. Obviously, the wetting phase occupies the corners and edges of drained pores; whereas the non-wetting phase flows through the middle of the pores. Therefore, it is admissible to assign a single pressure to the non-wetting phase within a given pore body, which is the common assumption in all pore-network models. As explained earlier, the wetting phase occupying corners of a pore body may have different pressure in different corners of the same pore. This is the approach followed here. While this may affect the calculation of permeabilities of the wetting phase, it has no consequence for the determination of permeability of the non-wetting phase. Therefore, in this work, we do not calculate the permeability of the non-wetting phase, as our results will not be different from common pore-network approaches. In the following, we explain the procedure for calculating the wetting phase permeability under drainage conditions.

First, the criterion for the invasion of pores at a given capillary pressure is discussed. As explained above, at any imposed capillary pressure, we determine the location of all fluid-fluid interfaces within the network. The non-wetting phase invades all accessible pore bodies and throats whose capillary pressure is smaller than the imposed capillary pressure. The entry capillary pressure is given by the Laplace equation [Bear, 1988]:

$$P_c = P_n - P_w = \gamma_{wn}\left(\frac{1}{r_1} + \frac{1}{r_2}\right) = \frac{2\gamma_{wn}}{r_c} \tag{5.7}$$

where r_c is the mean radius of curvature. For a capillary tube of radius r, we have $r_c = r/\cos\theta$ (Young-Laplace's equation), in which θ is the contact angle between the fluid-fluid interface and the capillary wall. Comparing this entry pressure with the imposed capillary pressure will determine which pores are invaded by the non-wetting phase, and what the corresponding curvatures of the fluid-fluid interfaces are. Thus the positions of all fluid-fluid interfaces throughout the network is determined.

5.3.2 Fluid flow within drained pores

In order to calculate flow of fluids through the network, we need to calculate fluxes within each individual pore. In our network model, pores, and therefore wetting phase domains, may have different cross sections.

The problem of laminar flow through a circular pipe results in the well-known Hagen-Poiseuille equation. In the case of a non-circular cross-section, the problem has been solved for simple shapes, such as ellipses and rectangles. However, for complex cross-sectional geometries, such as scalene triangles, no analytic solutions exist, so other approaches must be considered.

In the present work, we use numerical solutions to find the conductivity of a pore with a (scalene) triangular cross section. We assume that the pores have a uniform cross section that occupies a two-dimensional region in the (x, y) domain. We assume that there is fully-developed incompressible laminar flow in the axial direction of a pore under a constant pressure gradient. The governing equations are a simplified form of the Navier-Stokes equation and the conservation of mass, which can be combined to provide [Berker, 1963]

$$\nabla^2 v_z = \frac{1}{\mu}\frac{dp}{dz} = \text{constant} \tag{5.8}$$

where z is the co-ordinate along the axis of the tube, v_z is the velocity of the fluid, p is the pressure, and μ is the fluid viscosity. As mentioned above, dp/dz is considered to be constant along the tube. The velocity must satisfy the no-slip boundary condition along the solid-water interface. We assume that no momentum is transferred across the fluid-fluid interface (i.e., a perfect slip condition exists and the surface shear stress is zero)

$$\begin{aligned} v_z &= 0 \quad \text{at the fluid} - \text{solid interface} \\ n \cdot \nabla v_z &= 0 \quad \text{at the fluid} - \text{fluid interface} \end{aligned} \tag{5.9}$$

Figure (5.4) shows an example of a tube with triangular cross section which has been invaded by the non-wetting phase and, as a result, the wetting phase resides in the corners. Next, we make the governing equations dimensionless using the radius of curvature of the air-water interface, r_c (shown in Figure

5.4), as the reference length scale, defining the dimensionless variables

$$l^* = \frac{l}{r_c}; \qquad \nabla^* = r_c \nabla; \qquad v^* = \frac{v}{v_R}; \qquad p^* = \frac{p}{\Delta p} \tag{5.10}$$

where v_R is the characteristic velocity and Δp is the pressure difference across the pore. We have chosen $v_R = \frac{r_c^2 \frac{dp}{dz}}{\mu}$. As a result, Equation (5.8) reduces to

$$\nabla^{*2} v_z^* = 1 \tag{5.11}$$

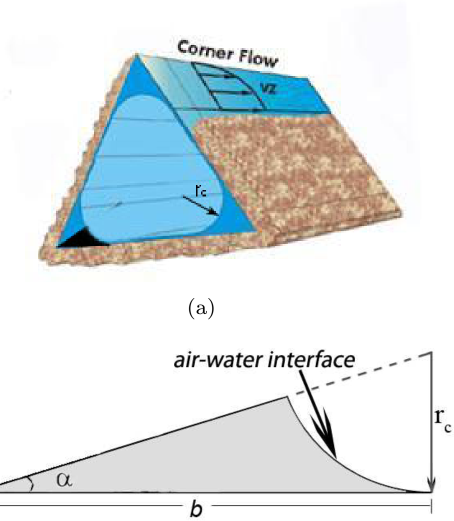

(a)

(b)

Figure 5.4: (a) Corner flow in a tube with triangular cross section. The velocity profile shows change in velocity in middle of the corner flow domain. The half corner colored in dark shows the simulated flow domain, which is shown in part (b) of the figure, where α is the corner half angle.

The dimensionless velocity (i.e., the solution of Equation 5.11) is independent of the pressure gradient and depends only on the cross section geometry, namely the half-angle α. Therefore, we solve Equation (5.11) numerically for a wide range of corner half angles. The flow rate can be determined from

$$Q = \int_A v_z da = g \frac{dp}{dz} \tag{5.12}$$

where g is the conductance of the flow domain. This equation can be made dimensionless to obtain a formula for the dimensionless conductance, g^*

$$g^* = \frac{g\mu}{r_c^4} = \int\limits_{A^*} v_z^* da^* \tag{5.13}$$

We have performed this calculation for corner half-angles ranging from 5 to 75 degrees. The resulting graph is shown in Figure (5.5).

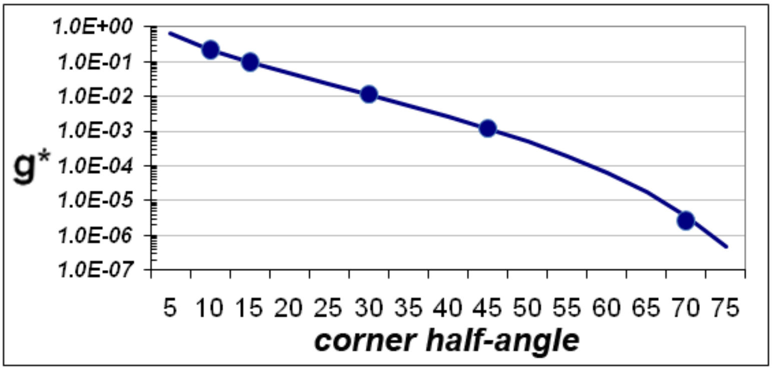

Figure 5.5: The dimensionless hydraulic conductance versus corner half-angle. The line shows the result of this study and circles show the result obtained by Patzek and Kristensen [2001] after rescaling the dimensionless groups used in their study.

Patzek and Kristensen [2001] have also calculated the dimensionless conductance for drained triangular cross-sections. In their work, they used the side length (shown as b in Figure 5.4b) as the reference length. Since r_c and b are related ($r_c = b \times tan(\alpha)$), we can convert the results to each other. Their results are shown as solid circles in Figure (5.5). It is clear that there is an excellent agreement between the two results. However, there is an advantage in choosing r_c as the reference length. Under quasi-static conditions, the capillary pressure and, therefore, the radius of curvature of all interfaces are the same in the network (for all pores). Thus, at any given saturation (or any given capillary pressure) a single curve can be used for all pores. This will not be the case if b is used as the reference length. Also, using b as the reference length, the relation between dimensionless conductance and corner half-angle will be non-monotonic (see Patzek and Kristensen [2001]), while, as shown in Figure (5.5), using r_c as the reference length, we get a monotonic relation.

An important conclusion can be drawn from Figure (5.5) regarding the significance of conductance of edges of pore bodies invaded by the non-wetting phase. Figure (5.5) shows a strong dependency of conductance on corner angle (note the logarithmic scale of the vertical-axis in Figure 5.5). If the angle of the edges within a pore body are larger than the corner angles of the neighboring pore throats, then they will have much less conductance to the flow. In particular, for cubic pore bodies, their edge half angle is 45 and thus their conductance will be less than that of pore throats with triangular cross section.

5.3.3 Regular hyperbolic polygons

It is possible to use similar procedure to calculate conductances for different cross sectional shapes. Considering porous media of type glass beads or well mature sand grains with spherical grain shapes, we may want to consider hyperbolic polygons as the cross-sectional shapes of the pores. Here, we present calculation of dimensionless conductances for saturated pores with hyperbolic polygons as their cross sectional shapes. A given hyperbolic polygons with $'n'$ vertices can be generated using $'n'$ circles with the same length and the same radius of curvature. These circles (with radius R_1 shown in Figure 5.6) could be tangential to each other or merge into each other to give different corner angles (shown as φ in Figure 5.6). For radius of circles, R_1, Area of polygon, A, and shape factor, G, we have the following relations [Joekar-Niasar et al., 2010]

$$R_1 = R\frac{\sin\frac{\pi}{n}}{\cos\varphi - \sin\frac{\pi}{n}} \tag{5.14}$$

$$A = \frac{nR^2\sin^2\frac{\pi}{n}}{\left(\cos\varphi - \sin\frac{\pi}{n}\right)^2}\left[\cos^2\varphi\cot\frac{\pi}{n} - \pi\left(\frac{1}{2} - \frac{1}{n}\right) + \varphi - 0.5\sin 2\varphi\right] \tag{5.15}$$

$$G = \frac{A}{P^2} = \frac{\cos^2\varphi\cot\frac{\pi}{n} - \pi\left(\frac{1}{2} - \frac{1}{n}\right) + \varphi - 0.5\sin 2\varphi}{4n\left(\pi\left(\frac{1}{2} - \frac{1}{n}\right) - \varphi\right)^2} \tag{5.16}$$

We have considered different domain with different number of vertices (n), starting from three up to $n = 5$. For each choice of n, we have considered domains with different corner angles (φ), ranging between zero and the maximum possible value for each polygon, covering a range of shape factors. We have used the same governing equation and boundary conditions. However, here we have chosen the radius of the inscribed circle, R, (which touches (is tangent to) the n sides of polygon) to normalize the governing equation as well as flow domains (R is shown in Figure 5.6). Doing so, all the domains will have inscribed circle of radius one (i.e., $R = 1$).

Figure (5.6) show dimensionless velocity field in different domains with differen dimensionless values of R^*, φ, and A^*.

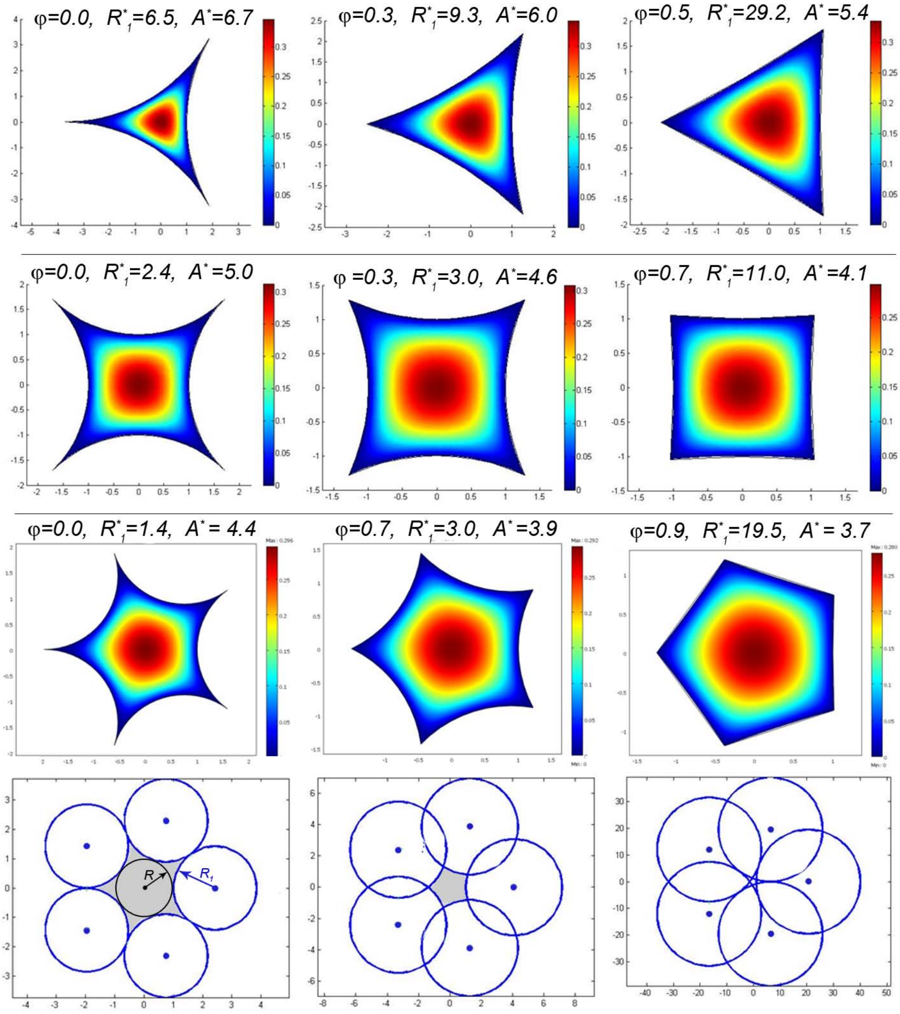

Figure 5.6: Different type of regular polygons with $n = 3, 4,$ and 5 (from top to bottom)

Figure (5.6) show that, for a given cross section type, with increasing the corner angle, the cross section changes from a regular hyperbolic polygonal cross section to a regular polygonal cross section, and the shape factor increases. In practice, the choice of cross section type is based on the measured shape factor distribution of the pore throats acquired by image analysis [Joekar-Niasar et al., 2010].

Integrating dimensionless velocity field over the flow domain, we calculated dimensionless conductance for each domain. Figure 5.7 shows the relation between dimensionless conductance and shape factor and number of vertices.

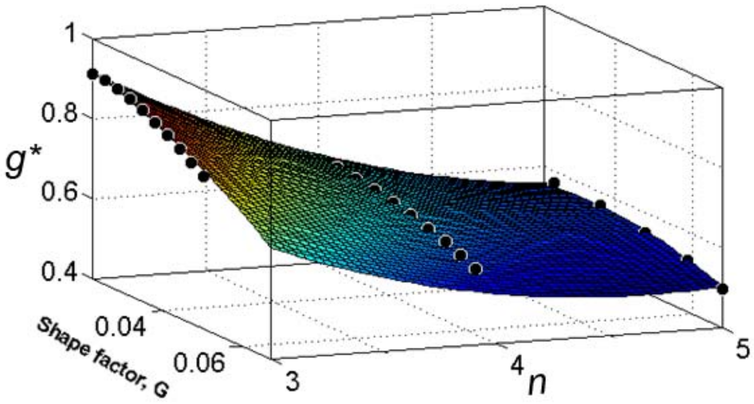

Figure 5.7: relation between dimensionless conductance, g^*, and shape factor, G, and number of vertices, n.

Figure (5.7) shows that dimensionless conductance decreases with increase in number of vertices and decresae in shape factor.

Figure (5.8) shows the relation between dimensionless conductance and φ for polygons with different number of vertices. As shown in Figure (5.8), with increasing of number of vertices, the maximum value of shape factor, possible for a specific type of polygon, increases. The value of g^* decreases with increase in corner angle, φ.

5.3.4 Calculation of relative permeability curves

To calculate relative permeability, we need to solve for fluid flow within all pores simultaneously. The governing system of equations is obtained by writing the volume balance for each and every corner element of all pore bodies. A corner element i is connected to three other corner elements in the same pore body

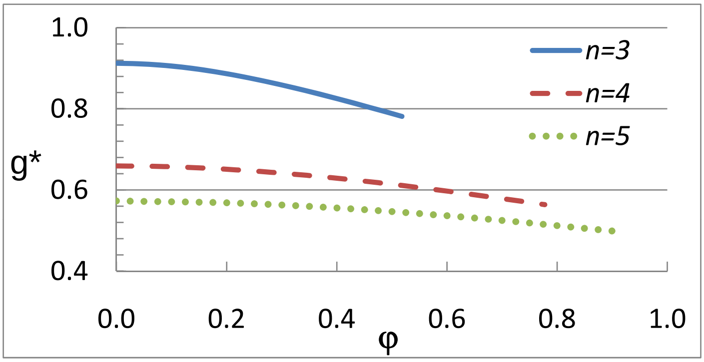

Figure 5.8: Relation between dimensionless conductance g^* and φ for different number of vertices,n.

by edge elements, and also connected to corner elements of neighboring pore bodies, j, through pore throats ij. The pore throat ij itself may have water flowing along its corners (N_{ij}^{corner}). Therefore, the volume balance for a pore body corner i may be written

$$\sum_{n=1}^{N_i^{Edge}} Q_{in} + \sum_{j=1}^{N_i^{Tube}} Q_{ij} = 0 \tag{5.17}$$

where N_i^{Edges} is the number of edges through which corner i is connected to other corner elements, n, within the same pore body, and Q_{in} is the flow through edge in (i.e., between corner i and corner n). For a cubic pore body, $N_i^{Edges} = 3$. Q_{ij} is the total flux through the pore throat ij connecting corner element i and corner element j of a neighboring pore body. For drained pore throats with flow along its edges, Q_{ij} is the summation of fluxes through all edges. N_i^{Tube} is the number of pore throats connected to the corner element i. The combination of Equations (5.12) and (5.17), written for all nodes of pore bodies of the network result in a set of linear equations, whose solution gives the flow field and fluxes in all network elements. Following solution, the overall water flux, Q_t, through the pore network is calculated. Subsequently, the relative permeability of the network to water at a given saturation and capillary pressure is calculated from Darcy's law

$$k_{rw} = \frac{\mu_w Q_t}{k\, A\, \Delta P/L} \tag{5.18}$$

where μ is fluid viscosity, k is the network intrinsic permeability, A is the network cross-sectional area, L is the pore-network length in flow direction, and ΔP is the pressure difference between the inflow and outflow reservoirs.
Repetition of this process at consecutively larger imposed capillary pressures results in a graph of capillary pressure versus saturation and relative permeability versus saturation. Results are presented in Section 5.4.

5.4 Results

5.4.1 Flow field in the MDPN model

The calculation of relative permeability is based on computing local velocity fields within individual pore elements of the network. Thus, the distribution of velocity field within the network has a crucial role in determining the (relative) permeability of the porous medium. Capturing an accurate velocity field can help to calculate more accurate permeabilities. In this section, we show the advantage of MDPN model in capturing a more accurate flow field.
Compared to the MDPN, a regular network with a fixed coordination number of six has connections only in three principal directions. In this case, $1/3$ of the connections are perfectly parallel to the overall flow direction, while the rest are completely perpendicular to the overall flow direction. Since 67% of the connections are perpendicular to the flow direction, the overall flow direction may not be the principal direction of the conductivity tensor. Also, the pore throats which are parallel to the flow direction will have much higher velocities compared to the pore throats perpendicular to the flow direction. This is because parallel pore throats form a continues path from the inlet boundary all the way to the outlet boundary. To illustrate this, we made a network with connections only in direction numbers $1, 2$, and 3 (i.e., a regular pore network with connections only in three principal directions). After simulating the flow, we averaged the velocities in each of the three directions to get three average velocities, one for each direction. These are shown by white columns in Figure (5.9). It is clear that the average velocity in the direction parallel to the flow (nearly 0.04 m/day) is much larger than the average velocities in the other two directions (about 0.015 m/day). Figure (5.10a) shows the scatter diagram of velocities within the pores of the regular network, which also shows that pore throats parallel to the flow direction have higher velocities. We also generated a MDPN model which had connections in all 13 directions, and we averaged velocities in each direction, resulting in 13 average velocities, also shown in

Figure (5.9), as columns with the dark color. Figure (5.10b) shows the scatter diagram of velocities in the MDPN. It is clear that in MDPN, velocities in different directions are comparable and there is no strongly dominant direction. This shows that, using the MDPN model one can get more realistic velocity fields.

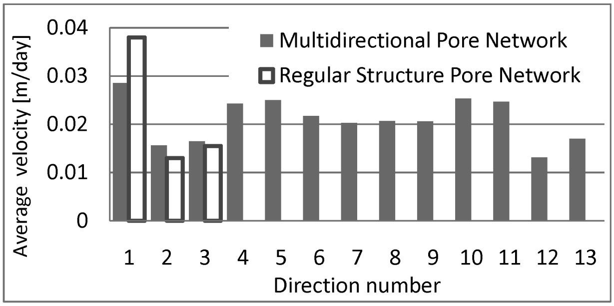

Figure 5.9: Average velocities in the three principal directions of a regular network model (white columns), and in the 13 directions of MDPN Model (dark columns). Direction number 1 is parallel to the overall flow (or pressure gradient) direction, and directions number 2 and 3 are perfectly perpendicular to the flow direction. The other directions are oblique with respect to the overall flow direction (Figure 2.1).

5.4.2 Calculation of relative permeabilities using MDPN model

We have chosen five different networks to study the effect of conductance of drained pore bodies on the network permeability. The first three are the generic network models (R_1, R_2, and R_3) whose properties were presented in Section 5.2. The other two networks were designed on the basis of properties of two real porous media: a carbonate rock [Al-Kharusi and Blunt, 2008] and a Fontainebleau sandstone [Lindquist et al., 2000]. The reason for choosing these two porous media is their different topology; Fontainebleau sandstone has a wide range of coordination numbers with a mean coordination number of around 3.5, while the carbonate rock has a much larger mean coordination number of 8.0.

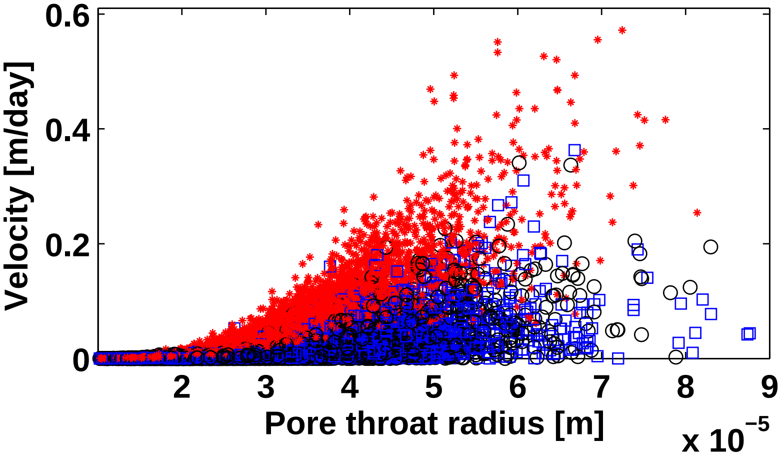

(a)

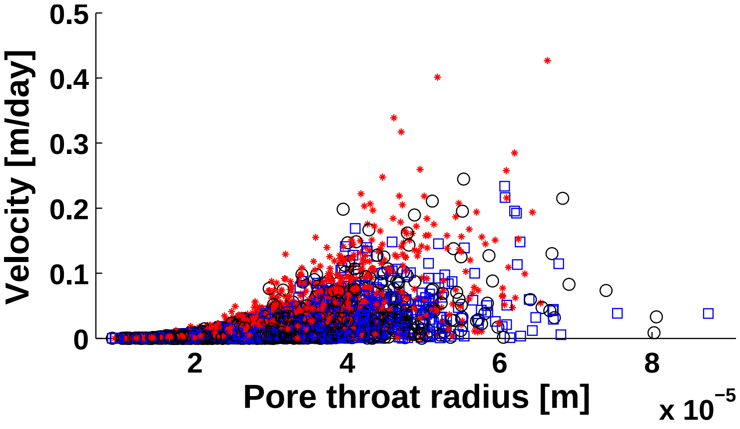

(b)

Figure 5.10: Scatter diagram of velocities vs. pore throat radius in (a) the regular pore network and (b) within the MDPN model. Direction number 1 is shown using (red) dots, where (blue) squares and (black) circles are used to show directions number 2 and 3, respectively. To keep the figure less crowded we have only shown scatter diagram of velocities in directions number 1, 2 and 3 of MPNM.

5.4.2.1 Generic pore networks

We constructed three networks of size $N_i = N_j = N_k = 20$, which results in 8,000 lattice points for each network. The pore size distributions were presented in Figure 5.1. Other properties of these networks are given in Table (5.1).

Table 5.1: Statistical properties of the three generic network models.

Property	**Value**
Number of pore bodies	$7,725$
Number of throats	$20,839$
Number of inlet pore throats	773
Number of outlet pore throats	763
Average coordination number	6.0
Porosity (networks: $R_1\,to\,R_3$)	0.24 *to* 0.11
Conductivity (m/d),(networks:$R_1\,to\,R_3$)	6.5 *to* 0.14

Table (5.1) indicates 7,725 pore bodies in each network, while the potential number of pore bodies is 8,000. The difference is due to the fact that some pore bodies lost all their connections through the elimination process [Raoof and Hassanizadeh, 2009], explained in section 5.2. Figure (5.11) shows the capillary pressure-saturation curves for these three networks.

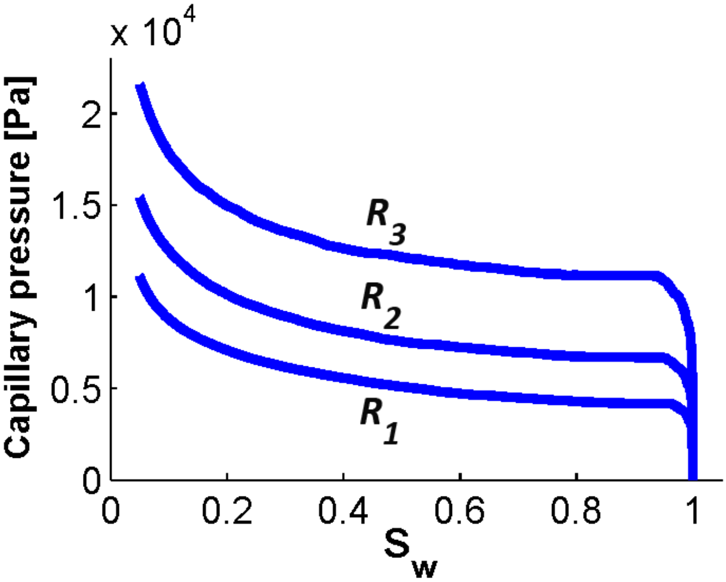

Figure 5.11: Capillary pressure-saturation curves for three generic pore networks. The pore throat size distributions (R_1, R_2, and R_3) are shown in Figure (5.1).

For cubic pore bodies, the edge half-angle is 45° and thus the edge conductance can be calculated from Figure (5.5) at any given capillary pressure. However, to explore the effect of resistance within partially-drained pore bodies, additional simulations were done for two smaller edge angles (thus, larger conductances), and the corresponding $k_r - S_w$ relations were compared. The results are shown in Figure (5.12), where, for the sake of comparison, the $k_r - S$ curves for the cases in which the resistance to the flow within the pore bodies were ignored is also shown (solid lines without markers). This has been done using the same computational algorithm, but assigning a very large conductance to the edges within the drained pore-bodies.

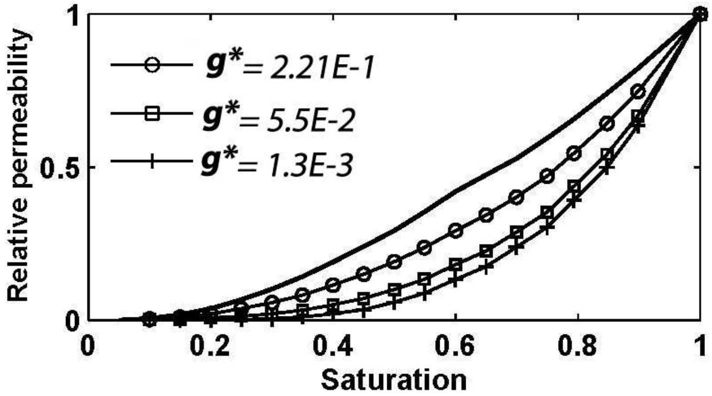

(a)

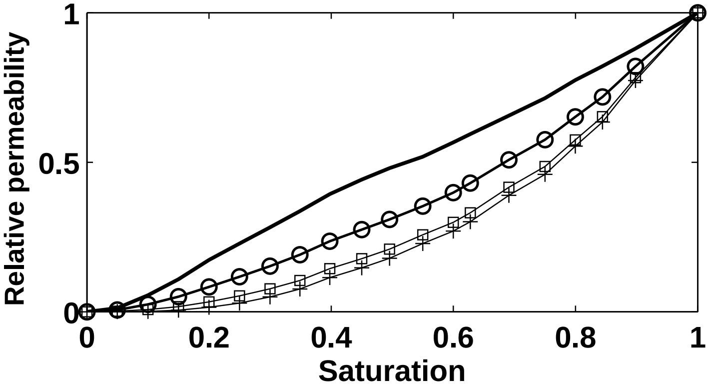

(b)

Figure 5.12: Relative permeability curves for (a) pore network R_1 and (b) pore network R_3 (pore network R_2 showed similar results and is not shown here). The plots with $g^* = 1.3E-3$ show the case of cubic pore bodies (45dge angles). The solid lines (without markers) show the relative permeability when the resistance to the flow within pore bodies is neglected.

From Figure (5.12), it is clear that including the resistance to the flow within the pore bodies results in considerably smaller values for k_r. That is, neglecting the resistance to the flow within pore bodies will cause overestimation of the relative permeability. Clearly, this overestimation is less when pore bodies have high values of conductances.

5.4.2.2 Relative permeability for a carbonate rock

In this section, we are applying the new formulation to a network which is based on the statistical properties of a carbonate rock. Al-Kharusi and Blunt [2008] applied a methodology to extract networks from pore space images of carbonate rock samples, in order to make predictions of multiphase transport properties. They started with a 2D thin-section image; then, converted it statistically to a 3D representation of the pore space. Using concept of maximal ball [Al-Kharusi and Blunt, 2008, 2007], they constructed a 3D pore-network model and simulated primary drainage, waterflooding, and secondary drainage processes [Valvatne and Blunt, 2004]. In that model, the resistance to flow was assigned to pore throats only. The simulated results were compared to the laboratory-measured values obtained though centrifuge experiments. The good agreement for capillary pressure-saturation and intrinsic permeability implied that they had estimated pore and throat sizes correctly (Figure 5.13). However, the predicted wetting-phase relative permeability was overestimated compared to the experimental results, as shown in Figure (5.14). They mentioned the large coordination number (which was derived using imaging technics) as a potential reason for discrepancy between relative permeabilities. As another potential source of discrepancy, they mentioned the fact that the pore-network model did not capture all local heterogeneities of the sample due to the size of the network. All of these arguments could potentially explain the overestimation of the relative permeability. However, we believe that this discrepancy could have been minimized by taking into account the resistance to the flow within (partially-) drained pore bodies. To verify this explanation, we generated a network with similar properties to those used by Al-Kharusi and Blunt [2008]. The capillary pressure-saturation curves obtained from our network and the network model of Al-Kharusi and Blunt [2008] are shown in Figure (5.13), together with the $P_c - S_w$ curve measured in the centrifuge experiments. There is good agreement between the two pore-network modeling results and measured values. There is also a good agreement between calculated values of absolute permeability using our network and that of Al-Kharusi and Blunt [2008] (Table 5.2). The relative permeability results of both pore-network models are shown in Figure (5.14) together with values obtained from the centrifuge experiments.

It is clear that including the resistance to the flow within pore bodies improves the agreement between simulated and measured values of relative permeability. An important observation from Figure (5.14) is that the maximum discrepancy between results from Al-Kharusi and Blunt [2008] and experiments occurs at

Table 5.2: Statistical properties of the Carbonate Network Model.

Property	**value**	
	This study	Al-Kharusi and Blunt [2008]
Number of pores	641	643
Number of throats	2284	2623
Mean coordination number	7.7	7.9
Absolute permeability (mD)	2.80	3.1

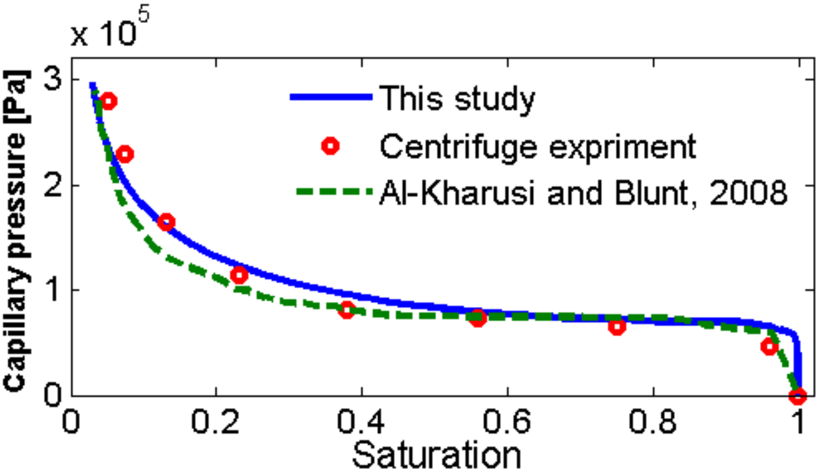

Figure 5.13: Comparison between $P_c - S_w$ curves obtained from two network models together with the measured values of capillary pressure-saturation during primary drainage experiment.

higher saturations ($0.75 < S_w < 1$). This can be explained by the fact that the largest pore bodies, which have the largest contribution to the flow under saturated conditions, are invaded first during drainage. The invasion of such large pores, and the subsequent corner flow along their edges, considerably decreases the permeability of the medium to the wetting phase, which can only be modeled by taking into account the resistance of pore bodies to the flow. As explained earlier, drained pore bodies could also considerably reduce the connectivity of saturated pore throats connected to them. The high coordination number in carbonate rock could increase the accessibility of the non-wetting phase to the larger pores. During recent years, the importance of coordination number distribution on flow and transport has been examined by some

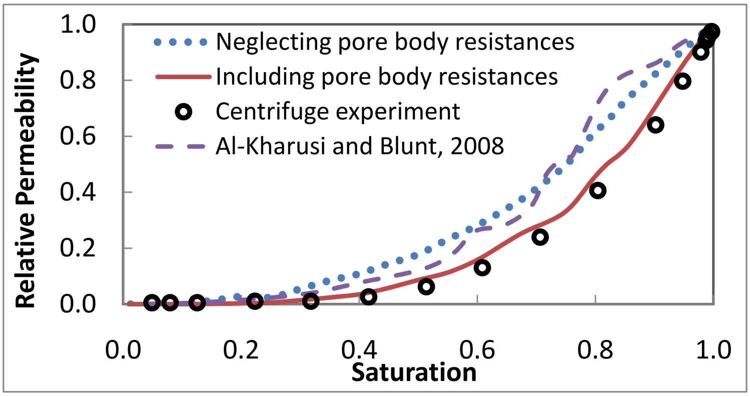

Figure 5.14: Comparison between relative permeability curves obtained from two networks together with the measured values during primary drainage experiment.

researchers [Mahmud et al., 2007, Sok et al., 2002, Arns et al., 2004, 2003b].

5.4.2.3 Pore Network model of Fontainebleau sandstone

In the previous section, we considered a carbonate rock with a mean coordination number close to 8.0. However, this value of coordination number is too high for some other types of porous media, for example, sandstones. In sandstones the average coordination number typically varies between 3 and 4 [Øren and Bakke, 2003a]. To generate pore networks with statistical properties similar to sandstones, we have chosen data reported by Lindquist et al. [2000]. Using direct measurements, they obtained flow-relevant geometrical properties of the void space for a suite of four samples of Fontainebleau sandstone, with porosities ranging from 7.5% to 22%. The measurements were obtained through the analysis of three-dimensional synchrotron X-ray computed microtomographic images. They reported comprehensive data on measured distributions of coordination number, channel length, throat size, and pore volume.

The mean coordination number varied from $\overline{z} = 3.37$ for a sample with $\phi = 7.5$ % to $\overline{z} = 3.75$ with $\phi = 22$ %. Whilst for the majority of pores the coordination number was close to 3, some pores displayed $z > 15$ [Ioannidis and Chatzis, 2000, Lindquist et al., 2000, Øren and Bakke, 2003a]. The detailed information and the distribution of statistical properties of the network can be found in Lindquist et al. [2000] and Lindquist and Venkatarangan [1999]. Table (5.3) shows the mean values of pore sizes together with mean coordination number.

Table 5.3: Statistical properties of sandstone samples analyzed in Lindquist et al. [2000] and Lindquist and Venkatarangan [1999].

Porosity (%)	**Mean coord. number**	**Mean pore radius (μm)**	**Mean throat radius (μm)**
7.5	3.3	50.6	18.4
13	3.49	45.8	21.3
15	3.66	48.5	24.7
22	3.75	43.5	22.6

Since the statistical properties of different samples of the Fontainebleau sandstone are not considerably different, we have chosen the properties of only one of the samples, namely the sample with porosity of 15.0% to generate a network. Figure (5.15) shows the coordination number distribution of the sample (reported by Lindquist et al. [2000]) together with the coordination number distribution of the generated network.

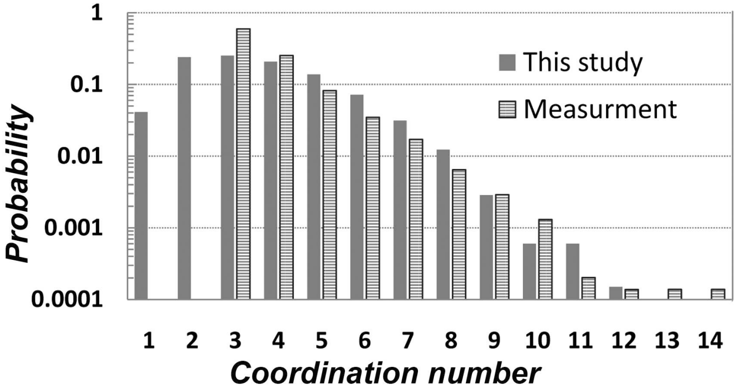

Figure 5.15: Measured coordination number distribution of the Fontainebleau sample, $\phi = 15\%$ (from Lindquist et al. [2000]) together with the coordination number distribution of the equivalent stochastic network used in this study.

Figure (5.15) shows a good agreement between simulated and measured distributions of coordination numbers. From Figure (5.15), it can be seen that the measured coordination number distribution starts from the value of 3.0, while our stochastic network shows coordination numbers as low as one. The reason is that Lindquist et al. [2000] eliminated all pores with coordination number of one and retained only the percolating backbone of the pore space. In our stochastic network, we also eliminated pores with the coordination number of one, except those which were located at the inlet and outlet boundaries of the network, since they are carrying flow and belong to the percolating backbone. The other difference is that Lindquist et al. [2000] defined pores with coordination number two to be part of a channel; in our stochastic network, the pores with coordination number of two are kept as pore bodies.

Figure (5.16) shows the resulting relative permeabilities with and without considering resistance to the flow within the pore bodies. Here again, neglecting pore body resistance to the flow results in a significant overestimation of relative permeability.

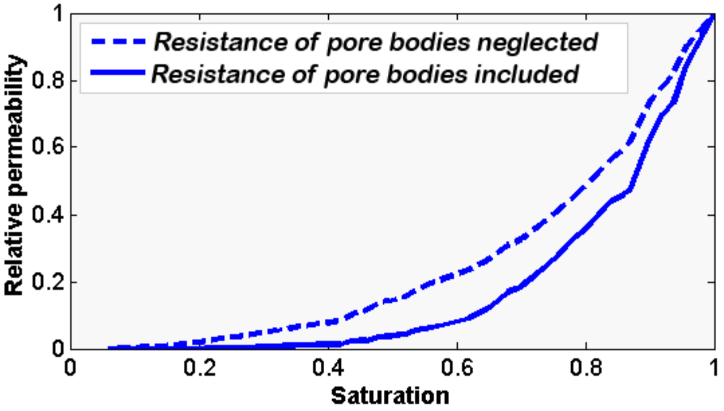

Figure 5.16: Comparison of relative permeability computed with and without consideration of pore body resistance to the wetting flow.

5.4.3 The concept of equivalent pore conductance

An alternative method to the approach presented here is to modify the conductance of pore throats to account for the resistance to the flow within the two adjacent pore bodies [Mogensen and Stenby, 1998, Sholokhova et al., 2009, Fenwick and Blunt, 1998, Dillard and Blunt, 2000]. This can be done through assigning an effective conductance to a given pore throat, for example as the harmonic mean of its own conductances and those of its two neighboring pore bodies [Fenwick and Blunt, 1998, Dillard and Blunt, 2000]:

$$\frac{1}{g_t} = \frac{1}{g_{ij}} + \frac{1}{2}\left(\frac{1}{g_i} + \frac{1}{g_j}\right) \tag{5.19}$$

where g_i and g_j are conductances of pore bodies i and j, respectively, g_{ij} is the conductance of the connecting throat between bodies i and j, and g_t in the total conductance to be assigned to the pore unit.
However, this correction term is constant (i.e., it is independent of saturation). In the presence of the non-wetting phase, one should make the conductances of pore bodies and pore throats a function of saturation. Thus we propose to modify Equation (5.19) as follows:

$$\frac{1}{g_t(S_w)} = \frac{1}{g_{ij}(S_w)} + \frac{1}{2}\left(\frac{1}{g_i(S_w)} + \frac{1}{g_j(S_w)}\right) \tag{5.20}$$

Because a pore body is connected to a few pore throats, one can use half pore-body length to calculate its contribution to the conductance of a pore throat connected to it.
Another approach would be to use g_{ij} but modify it for the effect of pore body resistance using a correction term which is a function of saturation. In this way, we do not need to calculate conductances of pore bodies explicitly. As a first-order correction, we have used the harmonic mean of saturations of two pore bodies adjacent to a pore throat in the following form:

$$g_t(S_w) = 2g_{ij}\frac{S_{w,i}S_{w,j}}{S_{w,i} + S_{w,j}} \tag{5.21}$$

where $S_{w,i}$ and $S_{w,j}$ are saturations of pore bodies i and j, respectively. Figure (5.17) shows the comparison between our formulation and effective conductance approach (i.e., Equations 5.20, and 5.21).

Although, there is some deviation between the curves, the overall good agreement suggests that a simple correction of pore throat conductances with the saturation of its neighboring pore bodies may be sufficient.
However, in the equivalent pore conductance approach, we do not explicitly solve for fluid fluxes within pore bodies. The flow velocity distribution, including flow velocities in edges of pore throats and pore bodies is necessary for an accurate simulation of solute transport. Simulating flow and transport along edges of drained pore bodies allows for modeling limited mixing within the pore bodies in the presents of non-wetting phase.

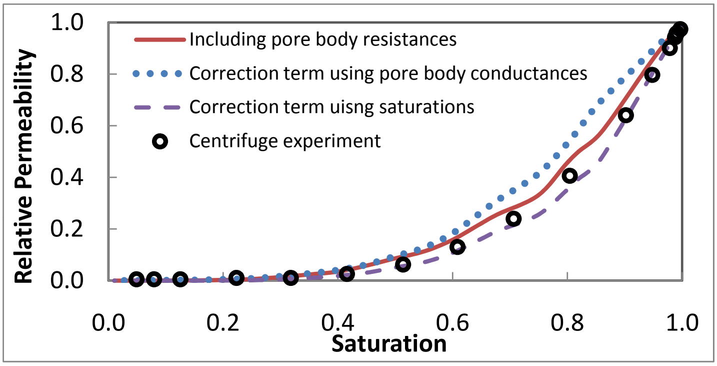

Figure 5.17: Relative permeability curves obtained from our approach, i.e., including conductance of both pore bodies and pore throats (solid line), together with calculation of k_r using effective conductance approaches, Equations (5.20) and (5.21) (dashed lines). Circles show measured values during primary drainage experiment by Al-Kharusi and Blunt [2008].

5.5 Conclusion

In this study, we have presented a new formulation for pore-network modeling of two-phase flow which enables us to calculate more accurate relative permeability-saturation ($k_r - S_w$) relationships. This goal was achieved by including the resistance to the flow within pore bodies of a MDPN model. Through quantitative analysis, we have calculated the influence of pore body resistance under primary drainage conditions. Since pore bodies vary considerably in size in porous media, including their effect will influence the relative permeability curve. Using several pore-network models with different coordination number distributions, we have shown that including the resistance to the flow within the pore bodies significantly affects simulated $k_r - S$ relationship and can improve the accuracy of results of pore-network models.

The approach presented helps to reduce sensitivity of pore-network modeling to pore space discretization, based on direct imaging of porous media samples. As mentioned earlier, based on images, the pore space is commonly partitioned into pore bodies and pore throats. This nontrivial partitioning has a major effect on results of flow calculations in current pore-network models [Sholokhova et al., 2009], because the pore bodies do not contribute to the resistant to the flow. But, because we account for the flow resistance within pore bodies as well as pore throats, the results are less sensitive to the division of pore space into pore bodies and pore throats.

Our approach is also expected to be of significance in determining other transport properties such as dispersivities and mass transfer coefficients. Under unsaturated conditions, because of the presence of the non-wetting phase within the central part of the pore space, there will be limited mixing of solutes or particles within the bore bodies. However, all solute transport models assign one average concentration to each pore body implying that there is full mixing within the pore body. Using our new formulation, since we can calculate pressure and fluxes within pore bodies, limited mixing will result.

Of course, in natural porous media, the pores are mostly irregular. With current measurement and imaging techniques it is possible to extract the sizes and angularity and shape factors for both pore bodies and pore throats (Zhang et al. [2010]). Considering the sizes of pore bodies and their shape factors reported in the literatures, we can conclude that including the effect of them can improve the results of pore-network modeling (Lindquist et al. [2000]; Zhang et al. [2010]).

Raoof, A. and Hassanizadeh S. M., *“Dispersivity under Partially-Saturated Conditions; Pore-Scale Processes”*, prepared for submission to Water Resources Research.

CHAPTER 6

DISPERSIVITY UNDER PARTIALLY-SATURATED CONDITIONS; PORE-SCALE PROCESSES

Make everything as simple as possible, but not simpler.

Albert Einstein

Abstract

It is known that in unsaturated porous media, the dispersion coefficient depends on the Darcy velocity and soil water saturation. In 1D flow, it is commonly assumed that the dispersion coefficient is a linear function of velocity with the coefficient of proportionality being the dispersivity. However, there is not much known about its dependence on saturation. The purpose of this study is to investigate how the longitudinal dispersivity varies non-linearly with saturation using a pore network model. We discretize the porous medium as a network of pore bodies and pore throats of finite volumes. The pore space is modeled using a MDPN which allows for a distribution of coordination numbers ranging between zero and 26. This topological, property together with geometrical distributions, are used to mimic the microstructure of real porous media. The dispersivity was calculated by solving the mass balance equations for solute concentration in all network elements and averaging the concentrations over a large number of pores.

We have introduced a new formulation of solute transport within a pore network which helps to capture the effect of limited mixing within the pores under partially-saturated conditions. This formulation allows a very detailed description of solute transport processes within the pores by accounting for limitations in mixing within drained pore bodies and pore throats as a result of reduced water content. We found that dispersivity increases with the decrease in saturation, reaches a maximum value, and then decreases with further decrease in saturation.

The numerically-computed dispersivities are compared with the results from reported experimental studies. The agreement between the results demonstrates the capability of this formulation to properly produce the effect of saturation on solute dispersion. While these computations have been restricted to the flow and transport of inert solutes and determination of their dispersivities, they demonstrate the significant potential of this formulation of pore-network modeling for predicting other transport properties, such as mass transfer coefficients under reactive/adsorptive solute transport, through including limited mixing within pores.

6.1 Introduction

Mechanical dispersion in porous media occurs because water flow velocity varies in magnitude and direction as a result of meandering through the complex pore structure [Perfect and Sukop, 2001]. The degree of spreading is related to: distribution of the water velocity within the pores; the degree of solute mixing because of convergence and divergence of flow paths; and molecular diffusion [Bolt, 1979, Leij and van Genuchten, 2002].

6.1.1 Dispersion under unsaturated conditions

The most established model for describing solute transport in porous media is the Advection-Dispersion Equation (ADE), which can be used to model the porous medium as a single-porosity domain. However, when there is preferential transport by a secondary pore system, another theoretical description must be used. For the latter case, several models exist, including a two-domain approach for both water and solute transport [Gerke and van Genuchten, 1993], and the mobile-immobile model for solute transport [Smet et al., 1981]. When observed breakthrough curves (BTCs) in unsaturated porous media show a tailing effect, a mobile-immobile model can be applied successfully [Gaudet et al., 1977].

In saturated porous media, the longitudinal dispersion coefficient has often been expressed [Bear, 1972, Scheidegger, 1961, Freeze and Cherry, 1979]

$$D = D_e + \alpha v^n \tag{6.1}$$

where the first term, D_e $[L^2T^{-1}]$, is the effective diffusion coefficient, while the second term describes the coefficient of hydrodynamic dispersion, where α is the (longitudinal) dispersivity, v $[LT^{-1}]$, denotes the pore-water velocity, and n is an empirical constant. Often, D exhibits an almost linear dependence with pore-water velocity, (i.e., $n = 1$), especially in the case of non-aggregated soil or glass beads [Bear, 1972, Bolt, 1979]. The dispersivity, α, is assumed to be an intrinsic soil property for saturated flow.

Equation (6.1) has been also used to describe the dispersion coefficient for solute transport under unsaturated conditions, (e.g., Kirda et al. [1973], Yule and Gardner [1978] and De Smedt et al. [1986]) in a modified form. A commonly employed relationship is

$$D(\theta, v) = D_e(\theta) + \alpha(\theta)v^n \tag{6.2}$$

Hydrodynamic dispersion in unsaturated soils is more complicated than in saturated soils. The resulting BTCs from experiments show greater solute spreading and longer tailing at lower water contents compared to the saturated conditions [Gupta et al., 1973, Krupp and Elrick, 1968].

High values of the dispersion coefficient, which have been observed in unsaturated experiments [Kirda et al., 1973, De Smedt and Wierenga, 1984, Maraqa et al., 1997, Matsubayashi et al., 1997, Padilla et al., 1999], have been attributed to the presence of immobile water [Gaudet et al., 1977, De Smedt and Wierenga, 1979, 1984]. However, dispersion phenomenon of solute movement through unsaturated porous medium has not been fully studied, and there is no single theory which can unify dispersion under both saturated and unsaturated conditions. Although dispersion is known to be strongly dependent on both flow velocity and water content in soil columns [Maciejewski, 1993], there is not much information on the nature and functional form of such dependency [Bear and Alexander, 2008]. This need prompts systematic investigations of the relationships between saturation, and water velocity fluctuations and dispersivity in unsaturated porous media.

The fraction of immobile water (or mobile water with a very low velocity compared to the average pore-water velocity) depends on the pore structure as well as the saturation. When saturation decreases, flow paths will be longer and the arrival time distribution will be more diverse, which causes higher dispersion. Consequently, the variability of microscopic velocity and its direction can be (much) larger than in saturated porous media. These effects, observed in soil column experiments, have been subjected to different interpretations, e.g. by describing molecular diffusion as a function of water content [Nielsen and Biggar, 1960, Bresler, 1973, Kemper, 1966]. As water content decreases, the pore-water velocity decreases and the geometry of the liquid phase in water-conducting pores changes with less opportunity for mixing and increased tortuosity.

6.1.2 Experimental works and modeling studies

Compared to studies done on saturated dispersion, there is much less research conducted on dispersion under unsaturated conditions. De Smedt et al. [1986] observed a substantial increase in dispersivity (by a factor of about 80) when changing from saturated to unsaturated conditions. They have attributed this behavior to the broader distribution of microscopic pore-water velocities encountered under unsaturated conditions. A possible cause for increase in dispersion could also be the existence of mobile and immobile water zones as the soil becomes unsaturated. Results of their modeling showed that, on the average, 64% of the water in the sand column could be considered mobile and 36% immobile, for almost all experiments.

To capture the effect of saturation on solute transport, Krupp and Elrick [1968] performed a series of miscible displacement experiments in an unsaturated column packed with glass beads, all at a constant average velocity. The earliest appearance of tracer in the effluent was observed at an intermediate saturation in the range of 0.54 to 0.56. They attributed this behavior to the large degree of disorder in the water distribution. Presence of filled and partially filled pores and pore sequences cause mixing to be related to saturation in a complex way. At higher water content, flow in filled pores was dominant, whereas at lower water content, flow in partially filled pores and films dominated the displacement.

Although dispersivity increases non-linearly with the decrease in saturation, a major observation is that the relation is not monotonic and dispersivity reaches a maximum value, α_{max}, at an intermediate saturation [Bunsri et al., 2008, Toride et al., 2003]. We refer to this as the *"critical saturation"*, S_{cr}. At saturations lower than the critical saturation (i.e., $S_w < S_{cr}$) the magnitude of dispersivity reduces with further decrease in saturation.

Similar results were found by Bunsri et al. [2008], who performed experiments on sand (with mean particle size of 250 μm) and soil columns (which contained soil particle sizes up to 2.00 mm). They also performed numerical modeling to simulate the experimental data. The simulation results showed that the magnitude of dispersivity under unsaturated conditions was larger than its value under saturated conditions. They found that the dispersivity in the high-saturation range increased non-linearly with decrease in saturation down to a critical saturation, S_{cr}, when dispersivity started to decrease with further decrease in saturation. The maximum dispersivity, $\alpha_{max} = 1.13\ cm$, occurred at a saturation of $S_{cr} = 0.43$.

Toride et al. [2003] have studied hydrodynamic dispersion in non-aggregated dune sand to minimize the effect of immobile water. Experiments at unit-gradient flow (i.e., the water velocity is equal to the unsaturated conductivity) were conducted to measure solute BTCs under steady-state flow conditions. Transport parameters for the ADE and the mobile-immobile model (MIM) were determined by fitting analytical solutions to the observed BTCs. They found the maximum dispersivity, α_{max}, of 0.97 cm occurring at $S_{cr} = 0.40$, whereas for saturated flow, dispersivity was equal to 0.1 cm, irrespective of pore-water velocity, (which ranged from 2.08 to 58.78 m/d). The BTCs for unsaturated flow showed considerable tailing compared with the BTCs for saturated flow. This was also observed by Gupta et al. [1973] and Krupp and Elrick [1968]. The ADE described the observed data better for saturated than for unsaturated conditions. Similar results were obtained by Padilla et al. [1999] for an unsaturated sand with a mean particle size of 0.25 mm.

Since pore channels inside the porous medium are interconnected, solute particles moving in different channels may meet after traveling different distances, resulting in mixing of the solute. Hence, mixing length theory could be applied to dispersion phenomena in a porous medium. Using mixing length theory, Matsubayashi et al. [1997] found that, under unsaturated conditions, the dispersion coefficient increases more rapidly with pore-water velocity compared to saturated conditions, resulting in higher values of dispersivity. The dispersion coefficient was expressed as [Matsubayashi et al., 1997]:

$$D\left(\theta, \overline{v}\right) = \ell \sigma_{vel} = \ell c_v(\theta)\overline{v} \tag{6.3}$$

where ℓ $[L]$ is the mixing length, σ_{vel} is the standard deviation of the pore-water velocity, $\overline{v}$ is the average velocity, and c_v is the coefficient of variation of pore-water velocity, defined as

$$c_v = \frac{\sigma_{vel}}{\overline{v}} = \frac{\overline{\left(v'^2\right)}^{\frac{1}{2}}}{\overline{v}} \tag{6.4}$$

where, $v^{'} \approx overlinev - v$ and v, is the micro-scale pore-water velocity. They found an increase in dispersivity with a decrease in saturation, down to a critical saturation (S_{cr}), beyond which the value of dispersivity was almost constant with saturation (although the variance of the velocity field was still increasing). In their study, the mixing length was equal to 0.23 *cm* for saturations less than S_{cr}, and then mixing length and hence the dispersion coefficient decreased to reach its saturated value. To calculate velocity variations, they assumed a porous medium consisting of bundles of capillary tubes. This assumption ignores the complex and random inter-connectedness of porous media, which is an important factor affecting the relation between degrees of saturation and pore-water velocity variations. Using the same concept, Devkota et al. [1998] developed relationships for dispersivity under unsaturated conditions. They found similar results as Matsubayashi et al. [1997]. They utilized the $P_c - S_w$ and $k_r - S_w$ curves to calculate the mixing length at various saturations; based on this they developed relationships for dispersivity as a function of saturation. They suggested that the coefficient of variation of pore water velocities is a constant, irrespective of saturation. This is not consistent with many other studies. The coefficient of variation of pore water velocities is a constant for saturated media. But, under unsaturated conditions, the change in saturation will change the distribution of phases within the porous medium, which in turn may cause changes in coefficient of variation of velocities.

While there are some studies on solute transport under unsaturated conditions at the column scale, there is a lack of comprehensive research on this subject at the pore scale to elucidate unsaturated dispersion based on pore-scale processes. Investigating these processes is essential for explanation and understanding of dispersion under unsaturated conditions. In addition, experimental work is often difficult and/or expensive to perform. For example, it is difficult to establish uniform saturation and flow velocity throughout a column. This may result in inaccurate estimation of transport parameters. Few data exist for low water content because the concomitant low flow rates lead to time-consuming displacement experiments, and apparatus-induced dispersion may result in biased transport parameters (James and Rubin, 1972). These difficulties make the use of pore-scale modeling conceptually appealing.

The saturation dependency of the dispersion coefficient originates from pore-scale processes governing the flow of water and transport of solute at the scale of individual pores. An accurate prediction of the solute movement needs knowledge of water movement at this scale. Since pore-scale modeling provides a bridge between pore scale and macro scale representation of processes, it is a useful means to study averaging effects. Using pore-scale models, one can relate concentrations at the macro scale to concentrations and transport processes at the scale of individual pores. This could substantially enhance the understanding of processes, such as dispersion, observed at the larger scales (e.g., column scale).

Mohanty [1982] studied dispersivity under two-phase flow conditions using a pore-network model. The pore space was divided into pore bodies (larger openings) and pore throats (channels connecting pore bodies to each other). They neglected solute residence time within the pore throats compared to that through a pore body. The solute travel time through a pore body was calculated as $\tau_i = \frac{V_i}{Q_i}$, where V_i is the volume of pore body i and Q_i is the volumetric flux through the pore. The travel time of a tracer was the sum of the time spent in all pore bodies on its path $T_{tot} = \sum_{t} \tau_i$. Through determination of the longitudinal position of particles, the average and variance, σ, of the location of all tracer particles was calculated. The dispersion coefficient, D, was then calculated as:

$$D = \lim_{t \to 0} \frac{\sigma^2}{2t} \tag{6.5}$$

They found that through smaller pore throats play a more important role in determining dispersivity, they have less importance in determining permeability.

6.1.3 Objectives and computational features

The main objective of this study is to examine dispersion over a wide range of saturations to explain the relation between dispersivity and saturation ($\alpha - S_w$ curve), by taking into account various pore-scale processes affecting this relation. We introduce a new formulation of solute transport within the pore network which helps to capture the effect of limited mixing within drained pores under partially-saturated conditions. In contrast to all former pore-network studies, which assign one (average) pressure and one (average) concentration to each pore element, we discretize pore spaces into separate smaller domains in order to increase the accuracy of simulations. Discretizing the individual pore spaces, fluid fluxes along corners of each pore are calculated and taken into account in the simulation of solute transport. This allows us to model the effect of limited mixing within pores.

In this paper, after construction of a MDPN model, drainage simulations are

performed to determine pore-level distribution of each phase. Then, steady-state flow is established and equations of mass balance are solved to calculate transport properties of such a distribution and to obtain BTCs of solute concentration. The results of the modeling are also compared with experimental observations to show the capability of this formulation.
The following morphological and computational features are introduced in the present study

(1) The topology of the pore space is modeled using a MDPN which allows a distribution of coordination numbers ranging between one and 26.

(2) To take into account the angularity of pores in natural porous media, pore throats with various cross sections, with a wide range of shape factor values and pore sizes, are used in the network. This includes rectangular, circular, and various irregular triangular cross sections.

(3) The pore body size distributions are assumed to follow a truncated log-normal distribution, without any correlation. The pore-throat size distributions are related to the pore body size distributions.

(4) Both pore bodies and pore throats are considered to have volume. This means we solve mass balance equations and calculate solute concentrations and mass fluxes within both pore bodies and pore throats.

(5) As soon as a pore body is (partially) saturated, it will be discretized further into smaller regions occupied by water, each with its own flow rate and concentration, in order to capture the effect of limited mixing due to the partial filling of the pore.

(6) Upon invasion of a pore throat by the non-wetting phase, each edge of the pore throat will be considered as a separate domain with its own flow rate and concentration.

(7) Employing a fully implicit numerical scheme to calculate the unknown connections, a substitution method is introduced which considerably reduces the computational time.

(8) Various parameters and relations, including coefficient of variation of the velocities field, relative permeability-saturation ($k_r - S_w$) curves, capillary pressure-saturation ($Pc - S_w$) curves, and fraction of percolating saturated pores are also computed.

Since we are employing angular pores, the wetting phase is always connected through the edges. This, together with the fact that we are ignoring the effect of diffusion, means we do not have any tailing effect, as there is no diffusive mass flux from zones of immobile water to the domain of mobile water. However, there are many pores with velocities much smaller than average velocity, in which the fluid is practically immobile. It has been shown that the effect of diffusion under unsaturated condition is mostly negligible. For example, Maraqa et al. [1997] found the relative contribution of molecular diffusion to the value of dispersion coefficient to be less than 1.0%. This is of course not the case for the saturated experiments with low pore-water velocities (e.g., velocities around 1 cm/h or less), where there is a potential contribution of molecular diffusion to the value of the hydrodynamic dispersion coefficient [Maraqa et al., 1997].

6.2 Network Generation

6.2.1 Pore size distributions

In the present study, the pore structure is represented using a 3D MDPN model. Because natural porous media can be mostly described by a lognormal distribution [Bear, 1988], the pore-body radii are assigned from such a distribution, with no spatial correlation, expressed by:

$$f\left(R_i,\sigma\right)=\frac{\sqrt{2}\exp\left[-\frac{1}{2}\left(\frac{\ln\frac{R_i}{R_m}}{\sigma}\right)^2\right]}{\sqrt{\pi\sigma^2}R_i\left[erf\left(\frac{\ln\frac{R_{\max}}{R_m}}{\sqrt{2\sigma^2}}\right)-erf\left(\frac{\ln\frac{R_{\min}}{R_m}}{\sqrt{2\sigma^2}}\right)\right]} \tag{6.6}$$

where R_{min}, R_{max}, and R_m, are the minimum, maximum, and mean of the distribution, respectively; and σ^2 is the variance. The pore structure is constrained to be isotropic, in the sense that the same values for the R parameters σ^2 are specified for all pores oriented along all network directions.

In this study, four different networks were constructed: three generic networks, and one network which represented a specific porous medium. The three generic networks had different distributions of pore body and pore throat sizes, shown in Figure (6.1), but the same coordination number distribution (figure 6.2). Pore body radii are taken from uncorrelated truncated lognormal distributions, and pore throat radii are correlated to the pore body sizes. The difference between the generic networks is in the variances of pore sizes. The properties of the porous-medium-specific network will be given later.

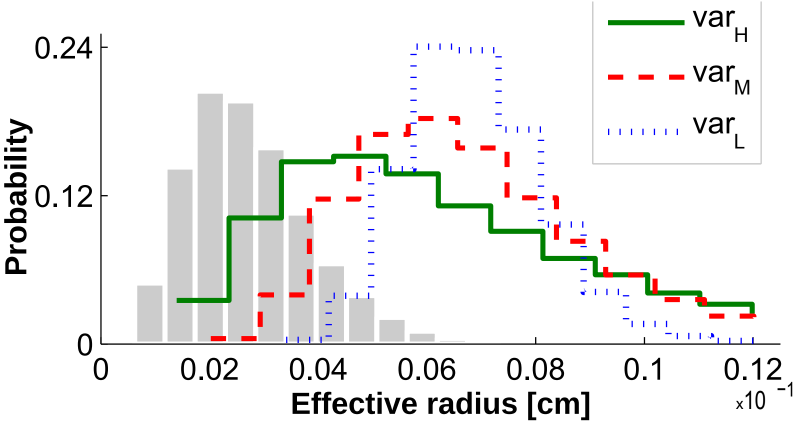

Figure 6.1: Distributions of pore-body sizes (columns) together with distributions of pore-throat sizes (R_1, R_2, and R_3) shown with lines. The mean sizes of pore-body and pore-throat distributions are shown above each distribution.

6.2.2 Determination of the pore cross section and corner half angles

A key characteristic of real porous media is the angular form of pores. It has been demonstrated that having pores with a circular cross section, and thus single-phase occupancy, causes insufficient connectivity of the wetting phase and as a result poor representation of experimental data [Zhou et al., 2000a]. Angular cross sections retain the wetting fluid in their corners and allow two or more fluids to flow simultaneously through the same pore. Pores which are angular in cross section are thus a much more realistic model of a porous medium than the commonly employed cylindrical shape. In the present work, pore bodies are considered to be cubic in shape, whereas, pore throats are assigned a variety of cross sectional shapes including circular, rectangular, and scalene triangular.

The shape of an angular pore cross section is prescribed in terms of a dimensionless shape factor, G, [Mason and Morrow, 1991] defined as

$$G = \frac{A}{P^2} \tag{6.7}$$

where A and P are the area and the perimeter of the cross section, respectively. The shape factor allows for replacing the irregular and complicated shape of a pore by an equivalent irregular, but simpler, shape. The values of shape factors for pore throats are chosen from a truncated lognormal distribution (Equation 6.6) with a minimum of zero corresponding to a slit, and a maximum of 0.08 corresponding to a circular cross section. Values for triangular cross sections vary between zero and 0.048 (with the maximum corresponding to an equilateral triangle), and for rectangular cross sections are between zero and 0.062 (with the maximum corresponding to a quare). The formulation for specifying angle values to triangular pores is presented in Section 5.2.2. After determining the three angles, we still need to specify a length scale in order to find the actual triangle size. As the length scale, we have chosen the radius of a circle with an area equal to the pore cross-section area. One way to select this radius is to relate it to the sizes of the two neighboring pore bodies, as suggested by Raoof et al. [2010]. By equating the area of the triangle (which is still unknown) to the area of the circle we can fully specify the triangular cross section. Similarly, for rectangular pore throats, the rectangle size is obtained from the area of the equivalent circle. Knowing the area and the shape factor, we can calculate the actual dimensions of the rectangle by solving a quadratic equation.

6.2.3 Coordination number distribution in MDPN

One of the main features of the MDPN approach is that pore throats can be oriented not just in the three principal directions, but in 13 different directions, allowing a maximum coordination number of 26, as shown in Figure (2.1). To get a desired coordination number distribution, we follow an elimination procedure to rule out some of the connections. The elimination procedure is such that a pre-specified mean coordination number can be obtained. A coordination number of zero means that the pore body is eliminated from the network, so no pore body located at that lattice point. A pore body with a coordination number of one is also eliminated except if it is located at the inlet or outlet boundaries (so it belongs to the flowing fluid backbone). Thus, no dead-end pores are included in the network. Details of the network generation can be found in Chapter 2.

Since in many pore-network modeling studies, a fixed coordination number of six is employed, we chose to generate a stochastic network with the coordination number ranging from zero to 16, but with a mean coordination number of six. However, we shall also present results for networks with other mean coordination numbers, related to real porous media. The distribution of coordination number and a representative domain of the network used in this study are given in Figure (6.2).

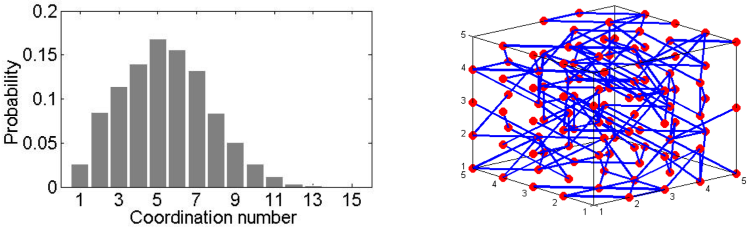

(a) (b)

Figure 6.2: The coordination number distribution and representative MDPN domain. The mean coordination number is equal to 6.0.

6.2.4 Pore space discretization

The conductivity of a flow path is dominated by the narrowest constriction along the path. Under saturated conditions, and considering the larger sizes of pore bodies compared to pore throats, one may safely neglect the resistance to the flow within the pore bodies (thus zero pressure gradient within a pore body) and assign conductances only to the pore throats. Similarly, it makes sense to assign one (average) concentration to the pore body, assuming that the solution is fully mixed within the pore body. This has been the common practice in almost all pore-network models for simulation of flow and solute transport [Li et al., 2007b,a, Acharya et al., 2005a]. However, in the the case of unsaturated or two phase flow, a given pore body or pore throat can be invaded and filled mostly by the non-wetting phase, forcing the wetting phase to flow only along the edges. Figure (6.3) shows a schematic example of two pore bodies connected to each other by a pore throat of triangular cross section. Under such conditions, pore throats are no langer necessarily the narrowest constriction along the flow path. In fact, resistance to the flow within the edges of pore bodies may be comparable to or even larger than the resistance to flow within the pore throats. To calculate more accurate relative permeability values, Raoof and Hassanizadeh [2011a] considered pore body conductances, and calculated fluxes of the wetting phases along edges of pore bodies as well as pore throats. Through comparison with experimental measurement, they found that including resistance to the flow within drained pore bodies can improve the results of simulations and can provide information on fluxes within pore bodies, which could be used to simulate solute transport.

In addition to its effect on flow within drained pores, the presence of non-wetting phase within the bulk space of the pore also reduces the efficiency of diffusion in smearing concentration gradients. Thus, under unsaturated conditions, it is more appropriate to assign different concentrations to each edge of a drained pore body, instead of assigning one average concentration to the whole pore. It is worth mentioning that the lower conductivity of a drained pore body can also reduce the connectivity and solute mass flux among any saturated pore throats connected to a drained pore body (such as pore throats number 2, 3, 4 in Figure 6.3b).

For the case of pore throats with angular cross section, after invasion of the non-wetting phase, there will be flow of the water only along the edges of the pore throats. Since the edges are separated from each other by the non-wetting phase, there will be no mixing between them.

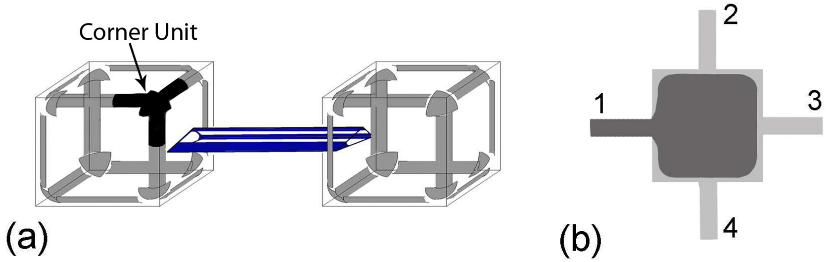

Figure 6.3: (a) Example of two drained pore-bodies connected to each other by a drained pore throat with triangular cross section. Explicitly labeled is a Corner Unit, which is comprised of a corner domain together with half of the three neighboring edges connected to it. (b) A pore body which is invaded by the non-wetting phase through throat number 1. this results in reduced connectivity of the neighboring saturated pore throats (connected through throats number 2,3, and 4).

Our new approach to include concentration differences within pore bodies is implemented as fellows. The concentration gradient within a pore body is assumed to be negligible as long as the pore body is saturated; i.e., a single concentration is assigned to the pore body. As soon as the non-wetting phase invades the pore body and occupies the bulk space of the pore, we consider each corner of the pore as a separate element with its own pressure and concentration. Thus, for a cubic pore body, 8 different corner elements exist with 8 different pressure and concentration values assigned to them. Fluid flow and solute mass fluxes between these elements occurs through the 12 edges of the pore body (see Figure 6.3(a)).

In the same manner, we assign only one concentration to a saturated pore throat. However, after invasion of the pore throat by the non-wetting, each edge of the pore throat will have its own conductance (and flow rate), and we assign separate concentrations to each edge.

The conductance of each edge needs to be determined as a function of the thickness of water film residing in the edge. This thickness depends on the radius of curvature of the fluid-fluid interface, which in turn depends on the capillary pressure. Corner elements of a given drained pore body are connected to the neighboring pore body corners via pore throats. Therefore, we need to specify connections of pore throats to the corners of pore bodies. The algorithm used to associate different pore throats to different corners of neighboring pore bodies is described in Appendix B.

6.3 Unsaturated flow modeling

We wish to simulate drainage in a strongly water wet porous media saturated with water. The non-wetting phase is assumed to be air, which can flow under negligibly small pressure gradient. To simulate drainage in our network, the displacing air is considered to be injected through an external reservoir which is connected to every pore-body on the inlet side of the network. Displaced water escapes through the outlet face on the opposite side. Impermeable (no flow) boundary conditions are imposed along the sides parallel to the main direction of flow.

6.3.1 Drainage simulation

Initially, the network is fully saturated with water. At low flow rates, the progress of the displacement is controlled by capillary forces. This forms the basis for the invasion percolation algorithm used to model drainage [Wilkinson and Willemsen, 1983, Chandler et al., 1982]. At every stage of the process, air invades all accessible pore bodies and throats with the lowest entry capillary pressure. The capillary pressure of a meniscus is given by the Laplace equation [Bear, 1988]

$$P_c = P_n - P_w = \gamma_{wn}\left(\frac{1}{r_1} + \frac{1}{r_2}\right) = \frac{2\gamma_{wn}}{r^*} \tag{6.8}$$

where r^* is the mean radius of curvature. For a capillary tube of radius r, we have $r^* = r/\cos(\theta)$ (Young-Laplace's equation), in which θ is the contact angle between fluid interface and the capillary wall. The invading fluid enters and fills a pore throat only when the injection pressure equals or exceeds to or larger than the entry capillary pressure of the pore.

We assume that the wetting phase is everywhere hydraulically connected. This means that there will be no trapping of the wetting phase, as it can always escape along the edges. The capillary pressure is increased incrementally so that fluid-fluid interfaces will move only a short distance before coming to rest in equilibrium at the opening of smaller pore throats.

6.3.2 Fluid flow within drained pores

To calculate the flow across the network, we need to calculate the flow of water in saturated pores as well as along edges of drained pores. The conductance of an angular drained pore depends on its degree of local saturation, which is directly related to the radius of curvature of the meniscus formed along the pore edges. However, Raoof and Hassanizadeh [2011a] have shown that if the conductance is made dimensionless using the radius of curvature, then it becomes independent of saturation. They used a numerical solution to calculate the dimensionless conductances of drained pores with scalene triangular cross section. This was done by numerically solving the dimensionless form of the Navier-Stokes equations and the equation of conservation of mass. They performed calculations for a range of corner half-angles, from 5 degree to a wide corner half-angle of 75 degrees. Figure (6.4) shows the computed dimensionless conductance as a function of corner half-angle.

The dimensional form of conductance, g, which is a function of capillary pressure, is

$$g = g^* \frac{r_c^4}{\mu} \tag{6.9}$$

where r_c is the radius of curvature of the interface and μ is the wetting fluid viscosity. The radius of curvature r_c depends on the capillary pressure prevaling

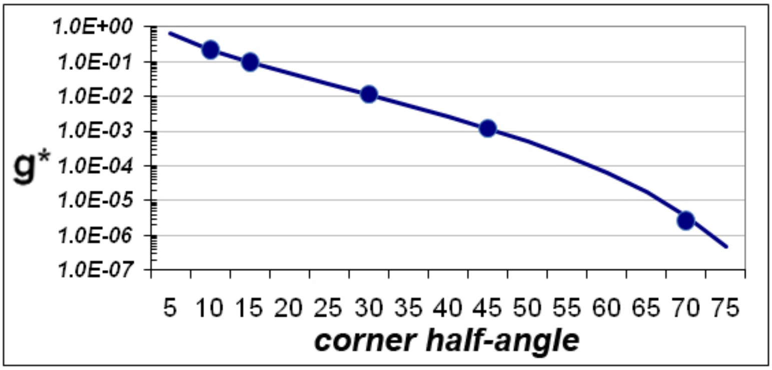

Figure 6.4: The dimensionless hydraulic conductance versus corner half-angle [Raoof and Hassanizadeh, 2011a].

in the pore. Thus, at any given capillary pressure, the dimensional conductance of pore edges can be calculated.

From Figure (6.4) it is seen that the conductance is a very strong function of corner angle(note the logarithmic scale of the y-axis in Figure 6.4). Therefore, for a pore throat with irregular triangle cross section, each of its edges after drainage can have quite different conductances. As a consequence, the flow rates and residence times of different edges within the same pore throat could be significantly different, even up to few orders of magnitude. For the case of pore bodies, due to the random connection of pore throats to different corners of pore bodies, different pore edges will have different fluxes. Under such conditions, the solution coming from upstream pores may not be fully mixed within the whole pore body; the solution may exit the pore body via some fast flow edges reducing mixing with other corners within the same pore body.

6.4 Simulating flow and transport within the network

6.4.1 Flow simulation

In this work, we consider unsaturated flow through a porous medium. A flow field is established in the network by imposing two different pressures on two opposing boundaries of the network. All other boundaries of the network parallel to the overall flow direction are no- flow boundaries. We assume that the discharge, q_{ij}, through a given pore throat can be prescribed by the Hagen-Poiseuille equation [Raoof et al., 2010]

$$q_{ij} = g\frac{(p_j - p_i)}{l} \tag{6.10}$$

where q_{ij} is the volumetric flow rate through pore throat ij, g is the conductance of the pore, and p_i and p_j are pressures at pore bodies i and j, respectively. Equation (6.10) is valid for laminar flow over a wide range of Reynolds numbers and is assumed to be appropriate for describing flow in pores [Bear, 1972]. For pore throats with irregular triangular cross section, the volumetric flow though the pore throat is the summation of flow within its three three edges

$$q_{ij} = \sum_{k=1}^{N_{edge}} g_k \frac{(p_j - p_i)}{l_{ij}} \tag{6.11}$$

where g_k is the conductance of the k^{th} edge of the pore throat, which can be determined using graph of Figure (6.4) and Equation (6.10).

For incompressible, steady-state flow, the sum of discharges into and out a pore body, or a pore-body corner in the case of a drained pore body, must be zero. Considering fluxes within the pore bodies, the continuity equation is

$$\sum_{n=1}^{N_{Edge}} q_{i,n} + \sum_{j=1}^{z_i} q_{ij} = 0; \qquad j = 1, 2, \ldots, z_i \tag{6.12}$$

where N_{Edges} is the number of edges through which corner i is connected to other corners through edge(n) within the same pore body. z_i is the coordination number of pore body i, which can be up to 26. Equation (6.12) is applied to all pore bodies except those on the two flow boundaries where pressures are specified. Combination of Equations (6.10) and (6.12) for all pores results in a linear system of equations, with a sparse, symmetric and positive-definite coefficient matrix, to be solved for pore body pressures [Suchomel et al., 1998a]. The flow velocity in all pore throats can be calculated using Equation (6.10). Considering the network as a REV, the average pore-water velocity, $\overline{v}$, for the network can be determined as

$$\overline{v} = \frac{QL}{V_f} \tag{6.13}$$

where Q is the total discharge through the network (i.e., the sum of fluxes through all pore throats at the inlet or outlet boundary of the network), L is the network length in the flow direction, V_f is total fluid volume, θ is porosity, and A is cross-sectional area of the network perpendicular to the overall flow direction.

Knowing the total discharge through the network, we can also calculate the relative permeability. The relative permeability of the network to water at a given saturation and capillary pressure is calculated from Darcy's law

$$k_{rw} = \frac{\mu_w Q_t}{k\, A\, \Delta P / L} \tag{6.14}$$

where μ is the wetting phase viscosity, k is the intrinsic permeability, and ΔP is the pressure difference between inflow and outflow reservoirs.

Repetition of this process at consecutively larger imposed capillary pressures results in a graph of capillary pressure versus wetting saturation and relative permeability versus wetting saturation.

6.4.2 Simulating solute transport through the network

Commonly, under saturated conditions, one average concentration is assigned to each pore body or throat [Raoof et al., 2010, Li et al., 2006a, Acharya et al., 2005a, Sugita et al., 1995a]. This is done assuming that each pore space is a connected well-mixed domain and that diffusion is fast enough compared to the fluid flow within individual pores (i.e., gradients in concentration are negligible within a single pore). This assumption may be reasonable under saturated conditions, but, under partially saturated conditions the situation is different.

Under partially saturated conditions, in the case of cubic pore body, we have eight corner units, each comprised of a corner domain together with half of the three neighboring edges, as shown in Figure (6.3). Thus, we assign eight different concentrations to a drained pore body, one for each corner unit. In the case of drained pore throats, we assign different concentrations to each pore throat edge.

Thus, in our formulation, the unknowns will be either concentrations of saturated pore bodies, c_i, and saturated pore throats, c_{ij}, or concentrations of edges of drained pore throats, $c_{ij,k}$, and corner units of drained pore bodies, $c_{CU,i}$. We assume that each corner unit is a fully mixed domain. To show the formulation, we introduce mass balance equations for a system of two drained pores connected using a drained pore throat, as the most general case. We assume that flow is from corner unit j towards corner unit i through corners of drained pore throat ij. For a given corner unit (with concentration $c_{CU,i}$ and volume $V_{CU,i}$), we can write the mass balance equation

$$V_{CU,i}\frac{d}{dt}(c_{CU,i}) = \sum_{j=1}^{N_{in}^{tube}}\sum_{k=1}^{N_{edge}^{ij}} c_{ij,k}q_{ij,k} + \sum_{n=1}^{N_{in,edge}^{CU,i}} c_{CU,n}q_{i,n} - Q_{CU,i}c_{CU,i} \quad (6.15)$$

where the first term on the r.h.s. is due to the mass arriving via N_{edge}^{ij} edges of N_{in}^{tube} throats with flow towards the corner unit. The second term on the r.h.s. accounts for the mass arriving from $N_{in,edge}^{CU,i}$ neighboring corner units (within the same pore body) with flow towards the corner unit. The last term shows the mass leaving the corner unit. $Q_{CU,i}$ is the total water flux leaving (or entering) the corner unit i.

We note that, for the case of saturated pores, the second term on the right-hand-side of Equation (6.15) vanishes and the value of N_{ij}^{edge} in the first term will be equal to one, since there is no edge flow present.

The mass balance equation for an edge element of a drained pore throat may be written (assuming that corner unit j is the upstream node)

$$V_{ij,k}\frac{d}{dt}(c_{ij,k}) = |q_{ij,k}|\, c_{CU,j} - |q_{ij,k}|\, c_{ij,k} \quad (6.16)$$

where $V_{ij,k}$, $q_{ij,k}$, and $c_{ij,k}$ are the volume, volumetric flow rate, and concentration of k^{th} edge of the pore throat ij, respectively.

Combination of appropriate forms of Equations (6.15) and (6.16) results in a linear set of equations to be solved for c_{ij}, $c_{ij,k}$, c_i, and $c_{CU,i}$. Since we discretize pore bodies and pore throats on the basis of their saturation state, the number of unknowns are different for simulations at different saturation values. For the case of a fully saturated domain, the number of unknowns is equal to $N_{tube} + N_{node}$ (N_{tube} is the number of pore throats and N_{node} is the number of pore bodies). In general, the number of pore throats is larger than the number of pore bodies in a pore network model. To get a more efficient numerical scheme, first, applying a fully implicit scheme, we discretized Equation (6.16) and determined $c_{ij,k}$ in terms of $c_{CU,i}$. This was then substituted into the discretized form of Equation (6.15). This resulted in a set of equations for $c_{CU,i}$. In this way, we considerably reduced the number of unknowns, and thus the computational time. The details of the method are given in Chapter 8, Section 8.3.1. For the accuracy of the scheme, the minimum time step was chosen on the basis of residence times [Suchomel et al., 1998c, Sun, 1996]

$$\Delta t \leq min\left\{T_{ij}, T_{ij,k}, T_{CU,i}, T_i\right\} \tag{6.17}$$

where T_α denotes the residence time pertaining to the elements α within the pore network.

After obtaining the solution for concnetrations, at any given time, BTCs at a given longitudinal position were found by averaging the concentrations of pores that possess the same longitudinal coordinate. In calculating BTCs, the concentrations of pore bodies were weighted by their volumetric flow rate; resulting in a flux-averaged concentration. That is, the normalized average concentration, $\overline{c}(x,t)$, is given by

$$\overline{c}(x,t) = \left[\frac{\sum_i^{N_t^x} c_i(x,t)Q_i}{\sum_i^{N_t^x} Q_i}\right]\frac{1}{c_0} \qquad i = 1, 2, 3, \ldots, N_t \tag{6.18}$$

where c_0 is inlet solute concentration, and N_t^x denotes the total number of pore body elements that are centered at the longitudinal coordinate x. The longitudinal coordinate could be written as multiples an interval of an ℓ, i.e. $x = 1\ell, 2\ell, \ldots, L$. where ℓ is the horizontal distance between centers of two adjacent pore bodies. The breakthrough curve at the outlet is obtained by plotting $c(x = L, t)$. Figure (6.5) shows an example BTC at the outlet of the network. We use these results to calculate (macroscopic) dispersivity as described in the next section.

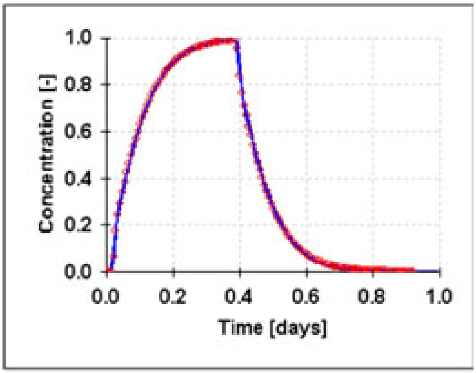

Figure 6.5: Example of resulting breakthrough curve of average concentration computed from the network (shown by symbols). The solid line is the solution of 1D advection-dispersion equation.

6.5 Results

BTCs obtained by means of our pore-network model were will be compared to results from macro-scale dispersion equations to determine the relationship between dispersivity and saturation. We also calculated the relationship between relative permeability and saturation. We considered two macro scale models; the Advection-Dispersion Equation (ADE) and Mobile-Immobile transport equations (MIM).

At each equilibrium saturation step, the imposed capillary pressure and the average saturation are recorded. Then, a small pressure gradient is imposed on the water phase to compute the steady-state flow of water. For the flow field computation, we assume that the saturation and positions of all interfaces remain unchanged. Water velocities within all pore bodies and pore throat edges are calculated. The overall water flux is calculated, which is used to determine the effective permeability of the network to water at that saturation from Darcy's law (Equation 6.14).

To start the simulation for solute transport, a constant pulse concentration, c_0, is assigned to the inflow side of the network. As water velocities within all the pores are known, Equations (6.15) and (6.16) can be solved to obtain the spread of the solute within the network as a function of time. Thus, the BTC of the average concentration corresponding to the specific saturation is obtained. To get the BTCs of average concentration for different saturations, capillary pressure is then increased to reach the next equilibrium saturation, and the above procedure is repeated.

6.5.1 Advection-Dispersion Equation (ADE)

The transport of a solute through a porous medium is usually described by the hydrodynamic dispersion theory [Bear, 1972]. The one-dimensional transport equation for a conservative solute is:

$$\frac{\partial \theta C}{\partial t} = \frac{\partial}{\partial z}\left(\theta D \frac{\partial C}{\partial z}\right) - \frac{\partial q C}{\partial z} \tag{6.19}$$

where C is the solute concentration, θ is the water content of the porous medium, q is the water flux, D is the hydrodynamic longitudinal dispersion coefficient, and z is distance. The dispersion coefficient is commonly expressed by Equation (6.1), assuming $n = 1$. In our simulations, when BTCs are obtained, the only parameter, in Equation (6.19), to be determined is the dispersion coefficient, D, since water content and average pore-water velocity are known from the pore-network mode. The dispersion coefficient (and thus dispersivity) at a given saturation is determined by optimizing the analytical solution of the ADE to the computed BTCs of average concentration at the outlet of the network at that saturation.

Figure (6.6) shows the resulting relationship between dispersivity and saturation ($\alpha - S_w$ curve) for the three networks described in Section 6.2.3.

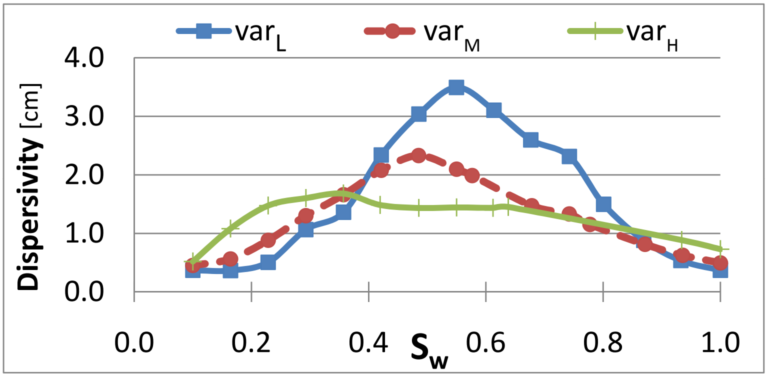

Figure 6.6: The relationship between dispersivity (based on the ADE model) and wetting phase saturation computed from the MDPN model for the three networks whose pore size distributions are shown in Figure (6.1).

From Figure (6.6), it is clear that there is a strong relation between dispersivity and saturation. The relation is non-monotonic, with the maximum dispersivity (α_{max}) occuring at an intermediate saturation, S_{cr}. This non-monotonic behavior has been observed in laboratory experiments [Bunsri et al., 2008, Toride et al., 2003]. To explore this non-monotonic behavior, we have analyzed various pore-scale properties of the pore-network model under different saturations.

It is well known that dispersion in porous media is a result of velocity variation within different pores. Under unsaturated conditions, velocity variations depend on saturation, which may not be a simple relationship. While, under saturated conditions the whole cross-section of a pore is available for the flow of wetting phase (resulting in a high conductance), under unsaturated conditions, the wetting phase flows only along the pore edges (which have less conductance to flow) with much lower velocities. This means that the variation of conductance is much larger under unsaturated conditions, leading to a larger variations of velocities. We have calculated the coefficient of variation, c_v, of pore-scale velocities at different saturations. This is a normalized measure of variability of the velocity distribution. Figure (6.7) shows the coefficient of variation, c_v, as a function of saturation.

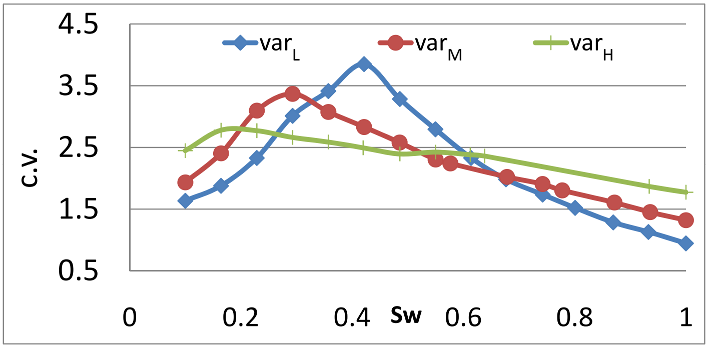

Figure 6.7: Coefficient of variation (c_v) as a function of saturation, S_w.

It is evident that the coefficient of variation increases with decrease in wetting phase saturation up to a maximum value, and then decreases with further decrease in saturation. This relationship is more or less the same as the relationship between dispersivity and saturation shown in Figure (6.6).

Since the saturation state of pores (i.e., being saturated or drained by the non wetting phase) is an important factor determining the flow field and velocity distribution within the phases, one important parameter under partially-saturated conditions could be the fraction of the percolating saturated pores. We define this as the fraction of pores which are filled with water and connected to both inlet and outlet boundaries of the pore network. This fraction is obviously equal to unity under saturated conditions, since all the pores are saturated with the wetting phase and connected to inlet and outlet boundaries. With a decrease in saturation, the fraction of percolating saturated pores will start to decrease. At some saturation, which we refer to as S_{per}, there will be no percolating saturated pores any more, i.e., the fraction of percolated saturated pores will be zero. We should note that, at S_{per} some pores are still saturated, however, they are surrounded by drained pores. We have calculated the fraction of percolating saturated pores as a function of saturation for the three networks considered here. Results are shown in Figure (6.8). Comparison with Figure (6.7) reveals that the coefficient of variation of pore-scale velocities for each network peaks near the corresponding S_{per}.

At saturations higher than S_{per} the saturated percolating pore system will cre-

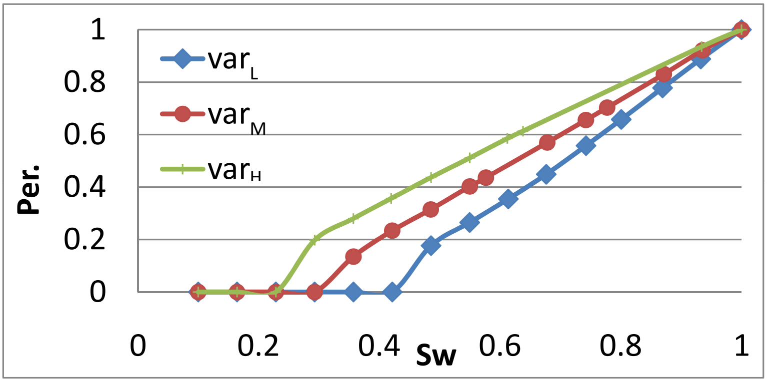

Figure 6.8: The relation between fraction of percolating saturated pores and saturation shown for three networks.

ate a "fast" flowing domain, since they are saturated and also connected to inlet boundary which imposes boundary pressure on these series of pores. The unsaturated pore system will create a "slow" flowing domain. The residence time of solute will be much higher in the unsaturated pore system compared to the saturated pore system, which could cause extra dispersion. It worth mentioning that, for a given pore network, the value of coefficient of variation for a fixed saturation is a constant irrespective of applied pressure gradients (different pore-water velocities). This is because, although the higher pressure gradient increases the velocities within pore throats and also increases the variance of velocities within different pore throats, the increase in variance is canceled out with the increase in the average velocity, and the coefficient of variation remains constant. This is obviously not the case when the saturation changes, since saturation changes will change the distribution of the phase available to flow.

6.5.2 Mobile-Immobile Model (MIM)

Under unsaturated conditions, non-equilibrium effects may exist due to preferential flow paths. There are experimental studies which can not be properly described via the ADE model [Beven and Young, 1988]. Under such conditions, modified forms of ADE should be used to take into account the effects of preferential flow or bypassing in the pore system. Drainage of pores will cause changes in velocity distributions and magnitudes of pore scale velocities. In particular, zones of low velocity or practically stagnant zones may be created.

Although the entire fluid-occupied domain forms a single fluid continuum at the microscopic level, it is assumed to be occupied by two apparent fluid phases: mobile and immobile water. Drained pores, as well as saturated pores which are surrounded by drained pores, may have very small velocities compared to the average pore-water velocity. Saturated pores with very small sizes may also have negligible velocities compared to velocities within larger saturated pores. The fluid occupying these very low conductive pores could practically be considered as an immobile phase. The water content of these two domains, θ_{im} and θ_m, sum up to the total water content $\theta_{im} + \theta_m = \theta_w$.

It should be noted that mobile and immobile pores may be interconnected in a complex way, with the solute being present in both of them. Bear and Alexander [2008] note that the fraction of the void space that contains an immobile wetting liquid is not constant, but is rather a function of the saturation, reaching its maximum when $S_w = S_r$, with S_r being the residual saturation. However, Toride et al. [2003] found that the maximum fraction of immobile phase could appear at an intermediate saturation which is higher than the residual saturation (i.e., when $S_w > S_r$). For example, they observed the maximum fraction of immobile phase at a saturation of $S_w = 0.47$, which was rather an intermediate saturation compared to the residual saturation. We will discuss this issue later, based on our pore-network results.

Using the concept of mobile and immobile water, advective-dispersive transfer of solute occurs only through the mobile water phase with accompanying exchange of solute between the mobile and immobile phases. This is captured by the following equations

$$\frac{\partial \theta_m C_m}{\partial t} = \frac{\partial}{\partial z}\left(\theta_m D_m \frac{\partial C_m}{\partial z}\right) - \frac{\partial q C_m}{\partial z} - \omega \theta_m \left(C_m - C_{im}\right) \tag{6.20}$$

$$\frac{\partial \theta_{im} C_{im}}{\partial t} = \omega \theta_m \left(C_m - C_{im}\right) \tag{6.21}$$

where the subscripts, m, and, im, refer to mobile and immobile water zones, respectively, and ω $[T^{-1}]$ is the rate coefficient of mass transfer between these two zones.

Figure (6.9) shows the relationship between the dispersivity of the mobile phase and the saturation ($\alpha - S_w$ curve) for the three networks.

Similarly to the case of the ADE model, we have fitted BTCs obtained from our pore network modeling with Equation (6.20) to determine dispersivity as a function of saturation.

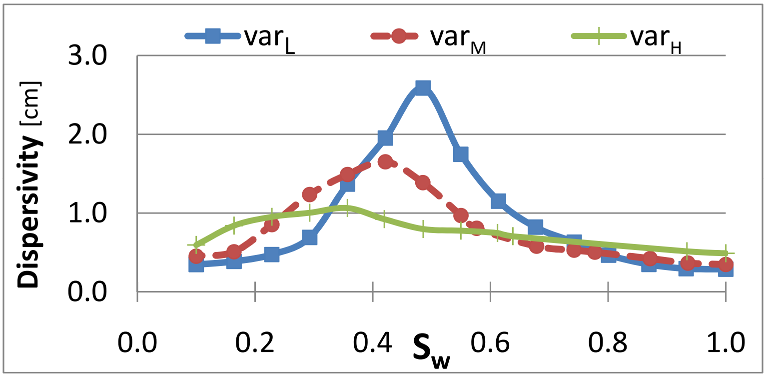

Figure 6.9: The relation between dispersivity of the MIM model and the wetting phase saturation ($\alpha - S_w$) for three networks shown in Figure (6.1)

The dispersivity values obtained using MIM (Figure 6.9) are lower than those obtained using the ADE model (Figure 6.6). This result has been observed by others [Toride et al., 2003]. The reason for lower dispersivities using MIM is that the contribution of mass transfer between mobile and immobile domains causes extra mixing.

Compared to the ADE model, the MIM model fits the BTCs better under unsaturated conditions (results not shown). Functionally, the ADE model provides mean transport characteristics, e.g. average velocity, necessary to predict solute transport. ADE results will be appropriate provided it is possible to estimate effective (or average) values for the transport characteristics. However, under intermediate saturations, due to the high velocity variations, one single average velocity (such as the one used in the ADE model) may not sufficiently describe the mean advective flux within the system. Under such a condition, the MIM model gives better results, since it divides the pore-scale velocities into two groups, one with a non-zero average velocity and the other one with a velocity of zero.

At saturated conditions the velocity field variation is narrower (i.e., with an smaller value for *c.v.*), and transport may be described well using the ADE.

6.5.3 Case study

In this section, we use our pore-network model to simulate solute transport within a real porous medium. We have chosen data reported by Toride et al. [2003], who studied the hydrodynamic dispersion coefficient under unsaturated conditions. In their experiment, they used non-aggregated dune sand to minimize the effect of immobile water. Unit-gradient flow experiments (i.e., the water flux being equal to the unsaturated conductivity) were conducted to measure solute BTCs under uniform saturations and steady-state flow conditions. Transport parameters for the ADE and MIM models were determined by fitting analytical solutions to the observed BTCs. They found a maximum dispersivity, α_{max}, of 0.97 cm corresponding to $S_{cr} = 0.40$, whereas for saturated flow dispersivity was equal to 0.1 cm, irrespective of pore-water velocity. The maximum value of dispersivity was almost ten times greater than it's value under saturated conditions. The BTCs for unsaturated flow tended to be less symmetrical with considerable tailing compared with the BTCs for saturated flow. The ADE model described the observed data better for saturated than for unsaturated conditions.

To model the experimental results, first, we have constructed a MDPN model, based on the information reported by Toride et al. [2003]. They have used a well-sorted dune sand, which was uniformly packed. The dune sand had an average particle size of 0.28 mm. The average coordination number for a sand packing is about 4.5 [Talabi and Blunt, 2010, Talabi et al., 2008].

We have used the same procedure mentioned in earlier sections to generate a MDPN model to match an average coordination number of 4.5 and calculate the BTCs under different saturations, and to plot the dispersivity-saturation relationship ($\alpha - S_w$ curve) shown in Figure (6.10).

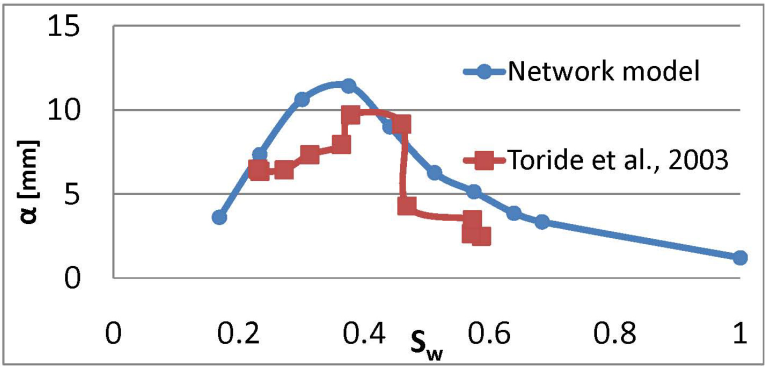

Figure 6.10: Comparison between dispersivities calculated using the MDPN model and results based on experiments [Toride et al., 2003] for various degrees of saturation.

Considering the complications of flow and solute transport under unsaturated conditions, there is a reasonable agreement between the results obtained from the pore-network model and experiments. The deviation between the two results could be due to the simple geometries used within the network model, together with the fact that we did not have detailed information on the pore size distributions of the sand sample used by Toride et al. [2003]. Considering the small size of the pore network compared to the experimental sample, we believe that our network does not capture all heterogeneities present within the real sample. However, the comparison shows the capability of pore-network modeling to capture dispersion under unsaturated conditions.

Figure (6.11) compares the fraction of the mobile phase, $\beta = {}^{\theta_m}\!/_{\theta}$, as of a function of saturation, calculated by the MDPN model with that obtained through experiment [Toride et al., 2003].

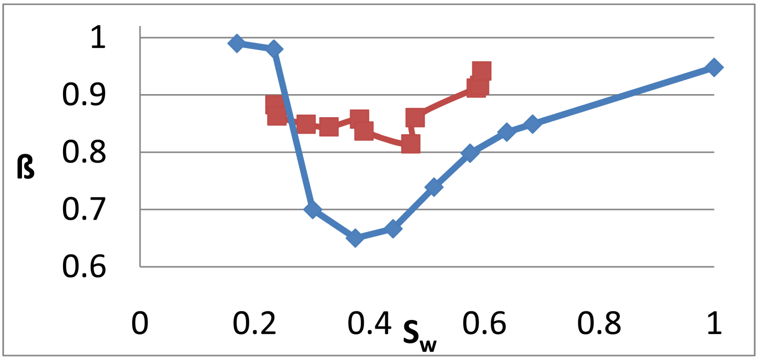

Figure 6.11: Comparison between fraction of the mobile phase calculated using the MDPN model and the results based on experiments by Toride et al. [2003].

Under saturated conditions, the number of immobile pores is very small and the mobile fraction is close to unity. As a result the ADE model adequately describes the BTC under saturated conditions. Padilla et al. [1999] and Toride et al. [2003] observed the same for a saturated sand packing (e.g., $\beta > 0.95$). The fraction of (practically) immobile water will increase as saturation decreases up to some extent, and then it starts to decrease with further decrease in saturation. This is also seen in Figure (6.11) in both the pore-scale modeling and experimental results.

When the porous medium is at higher saturation, some pores (mostly percolating saturated pores) have higher velocities creating the mobile phase. The rest of pores (mostly drained pores) with much lower velocities create a relatively immobile phase. Under such conditions, the coefficient of variation of the velocity distribution increases, and the resulting BTCs can only be described well by assuming that a large percentage of the water phase is immobile. Thus, the value of β will decrease with decrease in saturation.

Under low saturation, there is no strongly dominant flow path. Our results showed that, this regime starts mostly at saturations close to the percolation threshold, S_{per}. Under this regime, there is less variations in velocity (as shown in Figure 6.7) and as a result the BTCs can be described well by assuming a smaller immobile fraction.

6.5.4 Relative permeability

Our results show a relation between dispersivity and variation of the pore-scale velocity field. The relation was explained using c_v of the pore-scale velocity field (Figure 6.7), as well as the fraction of percolating saturated pores (Figure 6.8). These observations are pore-scale properties; in practice, it is quite a formidable job to precisely measure variations of pore-scale velocities throughout a pore space domain. It would be more practical and useful to relate dispersivity variations to a macro-scale quantity which is easier to measure. Such a quantity, under unsaturated conditions, could be relative permeability. Figure (6.12) shows the relative permeability curves for different networks.

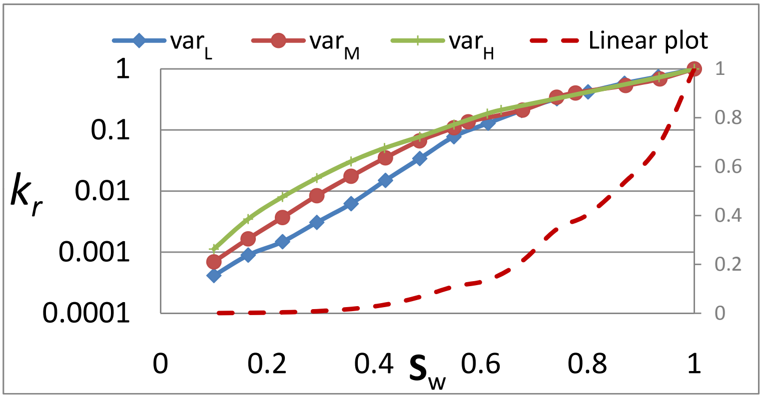

Figure 6.12: Relative permeability-saturation ($k_r - S_w$) curves shown on the semi-log scale for the three networks. The $k_r - S_w$ curve for the network var_M is also shown on the linear scale (corresponding to the secondary axis on the right side of the figure).

In Figure (6.12) we can distinguish a trend in each $k_r - S_w$ curve. Each $k_r - S_w$ curve is composed of two nearly linear parts (on semi-log scale). We have also shown one of the $k_r - S_w$ curves on linear scale, as a dotted line. The linear scale plot shows that the slope of $k_r - S_w$ is larger at higher saturation. This is due to the fact that the non-wetting phase first occupies larger pores (which have the most contribution to the conductivity of the phase), after which there is a considerable drop in conductivity of the wetting phase. The substantial drop in conductivity of the wetting phase will continue until the fraction of percolating saturated pores is very low. After this point, further decrease in saturation will cause only slight decrease in permeability of the wetting phase, since almost all larger pores are already drained. Thus, the location of the change in slope in the $k_r - S_w$ curve, in the semi-log scale, can be related to the fraction of percolating saturated pores. We may use the corresponding saturation as an approximation for the critical saturation, S_{cr}, at which maximum dispersivity occurs. Figure (6.12) shows that the saturation at which change in slope of the $k_r - S_w$ curves occur is lower for networks with higher variance, in which the α_{max} also occurs at lower saturations. This observation is in agreement with pore-scale observations such as change in fraction of percolating saturated pores (Figure 6.8) and coefficient of variations of pore-scale velocities (Figure 6.7).

6.6 Conclusion

Multi-phase and unsaturated transport in porous media is characterized by means of several macroscopic transport properties including relative permeability, capillary pressure, and dispersivity. These properties have been found to depend on macro-scale parameters, such as fluid saturation, but also on pore-space morphology. Indeed, distribution of fluid phase within the pores is important in determining transport properties.

In contrast to the relation between capillary pressure and saturation ($P_c - S_w$ curve), which has been investigated in many studies, there are only a few studies on the relationship between dispersivity and saturation (i.e., $\alpha - S_w$ curve). Although, the dependency of dispersivity on saturation has been clearly shown through experimental studies, almost all simulators of solute transport at the macro scale, under unsaturated conditions, use a constant dispersivity (i.e., do not include a dependance on saturation). This is mainly due to the unresulved and complex functionality of dependence of dispersion on saturation.

In this study, we have used a MDPN model to simulate flow and transport within the pore space of a porous medium. The capability of MDPN to produce a distribution of coordination numbers together with various angular pore cross sections and a more complex formulation of solute transport within the network has provided a valuable pore-scale flow and transport simulator for investigating dispersivity under unsaturated conditions.

Our results show that, under unsaturated conditions, the dispersivity coefficient is strongly depended on saturation. The relation appears to be non-monotonic, with the maximin dispersivity, α_{max}, corresponding to a specific saturation, which we refer to as the critical saturation, S_{cr}. We have investigated an explanation of the $\alpha - S_w$ relation by investigating pore-scale properties such as the fraction of percolating saturated pores and the coefficient of variation of pore velocities under different saturations.

In generale, the unsaturated dispersion may be explained by limited mixing within pores due to the presence of the non-wetting and also change of connectivity between assemblage of pores. The collection of saturated pores percolating through the whole domain will create a relatively fast domain which is shown on the left side of figure (6.13) using a flow line percolating thought the domain. On the other hand, corner flows within drained pores together with trapped saturated pores (shown in the right side of figure 6.13) create a relatively slow flow domain compared to the velocities within percolating saturated pores.

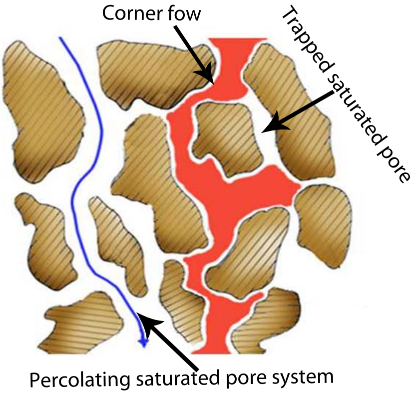

Figure 6.13: Schematic representation of unsaturated porous medium occupied partially by non-wetting phase. Corner flows together with trapped saturated pores create a relatively slow flow domain compared to the velocities within percolating saturated pores.

Moving from fully saturated conditions to unsaturated conditions, velocity variations will increase due to the presence of drained pores which have smaller velocities compared to velocities within saturated pores. However, at lower saturations, when the fraction of percolating saturated pores is very low, the velocity distributions will start to converge, resulting in a smaller value of dispersivity, and a decrease in the fraction of the immobile water.

We have shown that saturation-relative permeability ($k_r - S_w$) curve may be utilized to get insight into the behavior of $\alpha - S_w$ curve and to approximate the critical saturation at which the maximum dispersivity, α_{max}, occurs.

While these computations have been restricted to the transport of tracer solutes, they demonstrate the significant potential of this formulation of pore-network model for investigating other transport properties such as mass transfer coefficients for reactive/adsorptive solute and colloid transport, through including limited mixing within the pore bodies.

Raoof, A. and Hassanizadeh S. M., *"Adsorption under Partially-Saturated Conditions; Pore-Scale Modeling and Processes"*, prepared for submission to Water Resources Research.

CHAPTER 7

ADSORPTION UNDER PARTIALLY-SATURATED CONDITIONS; PORE-SCALE MODELING AND PROCESSES

> *Anyone who attempts to generate random numbers by deterministic means is, of course, living in a state of sin.*
>
> *John von Neumann*

Abstract

Adsorptive transport, such as transport of viruses and colloids, is of great importance in studies of porous media. Compared to the number of column-scale experimental studies, there are very few pore scale modeling studies, especially for unsaturated porous media. Under unsaturated conditions, principal interactions usually occur not only at the solid-water (SW) interfaces, but also at air-water (AW) interfaces. These interactions are greatly influenced by the water content.

In this paper, we study adsorptive transport under unsaturated conditions using a MDPN model, which allows for a distribution of coordination numbers ranging between zero and 26. This topological property together with geometrical distributions are used to mimic the microstructure of real porous media. Transport of adsorptive solute was calculated by solving local mass balance equations for solute concentration in all network elements and averaging the concentrations over a large number of pores. We have employed a fully implicit numerical scheme for transport of adsorptive solute under unsaturated conditions. The numerical scheme is developed based on the assumption that the porous medium is composed of a network of pore bodies and pore throats, both having finite volume.

We have introduced a new formulation of adsorptive solute transport within a pore network which helps to capture the effect of limited mixing within the pores under partially-saturated conditions. This formulation allows a very detailed description of solute transport processes within the pores by accounting for limitations in mixing within drained pore bodies and pore throats as a result of reduced water content. We have considered various types of adsorption such as i) two-site kinetic (at SW or AW interfaces), ii) two-site equilibrium, and iii) one-site kinetic and one-site equilibrium. Our results show that, even if there is equilibrium adsorption at the SW and AW interfaces at the pore scale, one may need to apply a nonequilibrium formulation for the adsorption process at the macro scale. We have found that the kinetic description of the adsorption process at the macro scale can accurately describe the results of pore network simulations. Using the kinetic description, we can employ dispersivity values obtained from tracer simulations. However, using the equilibrium macro-scale model, we needed to use higher values of the dispersion coefficient, modeled as a function of adsorption in addition to saturation.

7.1 Introduction

7.1.1 Major colloid transport processes

Understanding colloid transport mechanisms in unsaturated porous media has always attracted significant attention in management of groundwater contamination, especially in the case of groundwater polluted by contaminants that could adsorb to colloids. Colloids presence can enhance pollutant mobility [McCarthy and Zachara, 1989]; field results suggest the importance of colloids in the transport of low-solubility contaminants [Vilks et al., 1997, Kersting et al., 1999]. The enhanced mobility, together with the very limited acceptable concentration of hazardous solutes (in the range of few parts per billion), mean that we must pay more attention to modeling and accurate prediction of colloid (facilitated) transport processes. Since contaminants migrate and reach the groundwater through the vadose zone, the transport of adsorbing solute in the vadose zone becomes an important issue.

Commonly the breakthrough curves (BTCs) for reactive/adsorptive solutes display earlier appearance, greater spreading, and more tailing compared to the solution of classical models with equilibrium adsorption. Even under saturated conditions, adsorption processes may cause non-ideal behavior in the BTCs. However, under unsaturated conditions, in addition to the adsorption processes, the non-ideal behavior of the BTCs could be a result of partial occupation of the pore space by the non-wetting phase.

Under unsaturated conditions, various mechanisms may account for (non-ideal) behavior of colloids under different flow and transport conditions. Under low flow rates, diffusion may act as the rate-limiting process. Most of experimental studies which support this idea (e.g., Jacobsen et al. [1997], Laegdsmand et al. [1999], Schelde et al. [2002]) suggest a linear relationship between the cumulative mass of mobilized colloids and the square root of time. During transient conditions, such as drainage or imbibitions, colloid scavenging by air-water interfaces may be a dominant process [Jacobsen et al., 1997, Laegdsmand et al., 1999, Bradford and Torkzaban, 2008]. At high flow rates, however, hydrodynamic shear [O'neill, 1968] may be the dominant process [Kaplan et al., 1993, Laegdsmand et al., 1999, Weisbrod et al., 2002]. The induced shear force is opposed by an attractive force due to Derjaguin-Landau-Verwey-Overbeek (DLVO) interactions [Bradford and Torkzaban, 2008]. Under very low saturations, due to the discontinuity of water films between grains, film-straining may be the dominant process [Lenhart and Saiers, 2002, DeNovio et al., 2004, Bradford et al., 2006, Torkzaban et al., 2008], and transport of suspended colloids can be retarded due to physical restrictions imposed by thin water films [Wan and Tokunaga, 1997].

7.1.2 Experimental studies

Experimental studies are a major source of information for adsorptive transport in porous media. They are also instrumental in guiding the development of mathematical models for colloid transport and deposition. Studies of reactive/adsorptive transport in porous media can be categorized into three groups: pore-scale studies, column-scale studies of ideal systems (mostly under uniform saturation and constant pore water velocity), and studies conducted on non-ideal systems (such as natural vadose zone environments). Laboratory studies of colloid and colloid-facilitated transport have focused primarily on the interpretation of breakthrough of colloids (e.g, using latex microspheres, clays, oxides, or microorganisms, with or without other tracers) in sand or glass bead systems. While many studies have been carried out under saturated flow conditions [Weisbrod et al., 2003, Toran and Palumbo, 1992, Noell et al., 1998, Elimelech et al., 2000, Bradford and Bettahar, 2005, Bradford et al., 2007], some have examined unsaturated conditions [Wan and Wilson, 1994b,a, Wan and Tokunaga, 1997, 1998, Schafer et al., 1998, Thompson et al., 1998, Thompson and Yates, 1999, Jewett et al., 1999, Sim and Chrysikopoulos, 2000, Jin et al., 2000, Gamerdinger and Kaplan, 2001, Saiers and Lenhart, 2003b,a, Wan and Tokunaga, 2002, Simunek et al., 2006, Gargiulo et al., 2007, Torkzaban et al., 2008].

The most important aspect in unsaturated porous media is the presence of the air-water interface. Relatively few studies have investigated the role of the air-water interface in the transport of colloids [Goldenberg et al., 1989, Wan and Wilson, 1994b,a].

Wan and Wilson [1994a] conducted experiments to study colloid migration through sand columns at different saturations to examine interactions between various types of colloids (latex spheres, bacteria, and clay particles) and solid-water and air-water interfaces. They concluded that the AW interface played a very significant role in the migration of colloidal particles. The colloidal particles attached preferentially on the air-water interface by capillary forces, which are more dominant than other forces (e.g., the gravitational force). Particle transport was tremendously retarded by the presence of the air-water interface, acting as a strong adsorption site [Wan and Wilson, 1994a]. Wan and Wilson [1994b] also observed that the particle sorption increased with increasing ionic strength of the solution.

Lenhart and Saiers [2002] found that colloid transport in unsaturated porous media depended principally on the degree of pendular ring discontinuity, pore water velocity, and the retention capacity of the air-water-solid (*aws*) common line. The mechanisms for colloid retention at the *aws* line were not clear, but could be related to factors such as pore water motion with the pendular rings, low laminar flow velocity near the grain surface, and/or retention of colloids or colloidal aggregates in the thin water films near the *aws* contact line.

One method to study pore scale adsorptive processes is by direct observation of colloid transport under unsaturated conditions. In contract to the results of column experiments which provide BTCs of concentrations, small scale observations can provide useful information on colloid retention mechanisms at the pore scale. Sirivithayapakorn and Keller [2003] found that carboxylated polystyrene latex spheres and the bacteriophage MS2 were attracted to the AW interface of trapped air bubbles in micromodel pore space. Zevi et al. [2005] carried out pore-scale visualization studies of colloid transport in unsaturated quartz sand. They observed colloid retention at *aws* common line where the film thickness approximately equaled colloids diameter. Crist et al. [2004] used a real-time pore-scale visualization technique to study colloid retention in a three-dimensional sandy porous medium. They also observed trapping in the thin film of water at the (*aws*) line. Observation of colloid retention at the *aws* common line is also consistent with the batch experiments of Thompson and Yates [1999] and Thompson et al. [1998].

7.1.3 Mathematical models

Mathematical and conceptual models of adsorptive transport were initially developed for saturated porous media [Van der Lee et al., 1992, Corapcioglu and Jiang, 1993, Song and Elimelech, 1994, Swanton, 1995, Grindrod and Lee, 1997, Sun and Walz, 2001, Elimelech et al., 2003] and were later adapted to unsaturated media [Darnault et al., 2004, Saiers, 2002, Lenhart and Saiers, 2002, Corapcioglu and Choi, 1996, Wan and Tokunaga, 1997]. These models usually assume that the convective dispersive equation is valid; some models also accounted for preferential (or bypass) flow. Colloid deposition was included as a sink-source term. The sink term for colloid retention, in some models, was described as the product of two factors: (1) the collision efficiency, which is the probability of a mobile particle contacting a collector surface, comprising the effects of interception, sedimentation, and Brownian motion; and (2) the sticking efficiency, which is the probability that such a collision will result in attachment [Elimelech and O'Melia, 1990, Yao et al., 1971]. Descriptions of colloid retention in partially saturated media are complicated by the existence of the two AW and SW interfaces that can each serve as collector surfaces, albeit with distinct electrostatic and surface tension properties. The water film thickness can vary under partial saturation, depending not only on the water content, but also by the position of the film relative to the pendular rings of water between grains. In addition, some studies suggested attachment of colloids to the *aws* line.

Kinetic effects in the transport of adsorptive solutes could be due to physical and/or chemical kinetic processes. The physical kinetic (two-region) models explain nonideality based on the presence of both mobile regions, where solute is transported by advection and dispersion, and immobile regions, where only solute diffusion takes place [van Genuchtan and Wieranga, 1976, van Genuchten and Cleary, 1979, Rao et al., 1980a,b, Nkedi-Kizza et al., 1982]. Because these models attribute nonideality to the physical makeup of the soil, nonideal BTCs would be expected not only for reactive solutes but also for nonreactive solutes. Among chemical kinetic models, the two-site model, in which the porous medium is considered to contain two types of sites having different adsorption kinetic characteristics, is the most common; one site is considered to be in equilibrium, while the other site is assumed to undergo time-dependent kinetic adsorption

[Selim et al., 1976, Cameron and Klute, 1977]. Physical and chemical kinetic models have kinetic terms which contribute to both early breakthrough and longer tailing in BTCs, comparing to the solution of the Advection-Dispersion Equation (ADE) with equilibrium adsorption. Both two-region and two-site kinetic models have four independent parameters which are functions of one or two of the following parameters: the dispersion coefficient, D, the distribution coefficient, K_d, the equilibrium mobile fraction, f) and the first-order rate coefficient, ω. Curve fitting has been the most commonly used method to determine the parameters of these models.

Among other types of models, Choi and Corapcioglu [1997] modeled colloid-facilitated transport under unsaturated conditions considering four phases: an aqueous phase; a carrier phase (the colloids); a stationary solid matrix phase; and the air phase. Colloidal mass transfer between the aqueous and solid matrix phases and between the aqueous phase and the air-water interface, and the contaminant mass transfer between aqueous and colloidal phases and between the aqueous phase and the air-water interface were represented by kinetic expressions.

Wan and Tokunaga [1997] developed a model based on film-straining in which transport of suspended colloids can be retarded due to physical restrictions imposed by thin water films in partially saturated porous media. In their model, they introduced critical matric potential and a critical saturation, at which thick film interconnections between pendular rings are broken and film straining begins to become effective. They observed that the conventional filtration theory was not sufficient, but, film-straining theory could explain their results. They found that the magnitude of colloid transport through water films depended on the ratio of colloid size to film thickness as well as flow velocity. Additional factors which might influence film straining in more general cases include distributions in grain size, grain shape and surface roughness, grain packing and aggregation, and colloid shape.

7.1.4 Objectives

Although there are some studies on pore-network modeling of reactive/adsorptive solute under saturated conditions [Acharya et al., 2005a, Algive et al., 2007a, Li et al., 2006a], there are many fewer studies conducted under unsaturated conditions. In this paper, we present a new pore-scale model to study flow and transport of adsorptive/reactive solutes under unsaturated conditions. We calculate the concentration of solutes in each individual pore element using the equations of mass balance. Under different saturation states, the flow equations are first solved and the resulting pore scale velocities are then used to simulate reactive solute transport.

The main objective of this study is a better understanding of transport of adsorptive/reactive solutes under unsaturated conditions. Although various mechanisms, such adsorption to the *aws* common line or moving AW interfaces have been suggested to affect the adsorptive transport, the exact role of these processes are still unclear. In this study, adsorption over a wide range of saturations was considered by taking into account adsorption to both AW and SW interfaces. Regions of the pore space for which a wetting film of water coats the surface remain water-wet, as do the corners of the pore space where water still resides; however, we neglect adsorptive to interfaces associated with the water films. We have introduced a new formulation of adsorptive solute transport within a pore network which helps to capture the effect of limited mixing and adsorption under partially-saturated conditions. In contrast to former pore-network studies, which assign one (average) pressure and one (average) concentration to each pore element, we discretize an individual pore space into separate smaller domains, each with its own flow rate and solute concentration, in order to increase the accuracy of simulations. Thus, fluid fluxes along edges of each pore are calculated and taken into account in the simulation of adsorptive solute transport.

In this paper, after construction of a Multi-Directional Pore-Network (MDPN) model, quasi-static drainage simulations are performed to determine pore-level distribution of each fluid phase. Then, steady-state flow is established and equations of mass balance for adsorptive solutes are solved to calculate transport properties of such a distribution and to obtain BTCs of solute concentration. Adsorption to both air-water (AW) and solid-water (SW) interfaces is modeled. These adsorption processes are independent of each other and each of them can have its own distribution coefficient and adsorbing area.

7.2 Network Generation

7.2.1 Pore size distributions

In the present study, the pore structure is represented using a 3D MDPN model. Pore-body radii are assigned from a lognormal distribution, with no spatial correlation, explained in Section 6.2.

Figure (7.1) shows the bore body size distribution used within the MDPN. Pore body sizes are taken from uncorrelated truncated lognormal distributions, and pore throat sizes are correlated to the pore body sizes.

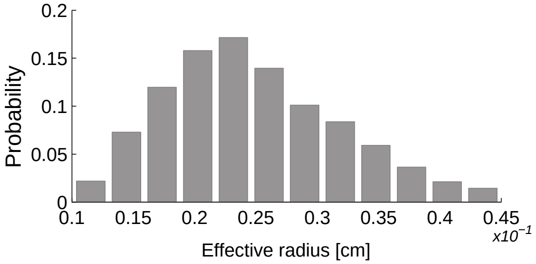

Figure 7.1: Distributions of pore-body sizes within the pore network model.

7.2.2 Determination of the pore cross section and corner half angles

A key characteristic of real porous media is the angular form of pores. It has been demonstrated that having pores with a circular cross section, and thus single-phase occupancy, causes insufficient connectivity of the wetting phase and as a result poor representation of experimental data [Zhou et al., 2000a]. In the present work, pore bodies are considered to be cubic in shape. Pore throats are assigned a variety of cross sectional shapes including circular, rectangular, and scalene triangular, as it was explained in Section 6.2.2.

7.2.3 Coordination number distribution in MDPN

One of the main features of the MDPN is that pore throats can be oriented not only in the three principal directions, but in 13 different directions, allowing a maximum coordination number of 26, as shown in Figure (2.1). Then, to get a desired coordination number distribution, we fallow an elimination procedure to rule out some of the connections. The elimination procedure is such that a pre-specified mean coordination number can be obtained. A coordination number of zero means that the pore body is eliminated from the network, so there is no pore body located at that lattice point. A pore body with a coordination number of one is also eliminated except if it is located at the inlet or outlet boundaries (so it belongs to the owing fluid backbone). This means that no dead-end pores are included in the network. Details of network

generation can be found in Chapter (2).
In this study, we have chosen to make a MDPN with an average coordination number of 4.5. This value corresponds to the sand packing [Talabi and Blunt, 2010, Talabi et al., 2008]. The distribution of coordination number is given in Figure (7.2).

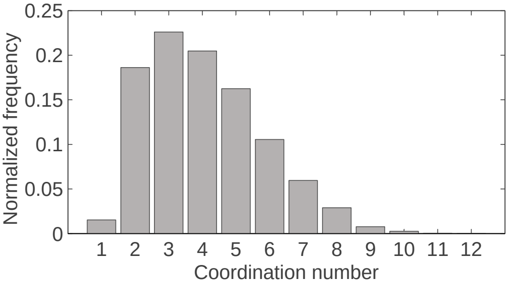

Figure 7.2: The coordination number distribution of the MDPN model. The mean coordination number is equal to 4.5.

7.2.4 Pore space discretization

To take into account the effect of limited mixing within the drained pores we follow our approach which was explained in Section 6.2.4, i.e., under unsaturated conditions, we consider each corner of the pore, occupied by the wetting space, as a separate element with its own pressure and concentration. In addition, since we take into account adsorption process, We also calculate separate adsorbed mass concentration for each of these elements. Thus, for a cubic pore body, 8 different corner elements exist with 8 different pressure and concentration of solution and adsorbed mass assigned to them (see Figure 6.3a).

7.3 Unsaturated flow modeling

We wish to simulate drainage in a strongly water wet porous medium, initially saturated with water. The non-wetting phase is assumed to be air, which can flow under negligibly small pressure gradients. To simulate drainage in our network, the displacing air is considered to be injected through an external reservoir which is connected to every pore-body on the inlet side of the network. The displaced water escapes through the outlet face on the opposite side.

Impermeable boundary conditions are imposed along the sides parallel to the main direction of flow.

We follow the procedure explained in Section 6.3 to perform drainage and applying a steady state flow fluid, under a different saturations, to calculate the total volumetric flow though the network and the relative permeability.

7.4 Simulating adsorptive transport within the network

In order to take limited mixing, due to existence of the non-wetting phase, into account, we subdivided a drained pore body into corner units. In the case of a cubic pore body, we have eight corner units, each comprised of a corner domain together with half of the three neighboring edges (Figure 6.3a).

In our formulation, the unknowns will be either concentrations of saturated pore bodies, c_i, and saturated pore throats, c_{ij}, or concentrations of edges of drained pore throats, $c_{ij,k}$, and corner units of drained pore bodies, $c_{CU,i}$. The adsorbed mass concentration will be either adsorbed mass concentrations of saturated pore bodies, s_i^{sw}, and saturated pore throats, s_{ij}^{sw}, or adsorbed mass concentrations at SW and AW interfaces of drained pore throats, s_{ij}^{sw}, and, $s_{CU,i}^{aw}$, respectively, or corner units of drained pore bodies, $s_{CU,i}^{sw}$, and, $s_{CU,i}^{aw}$, respectively.

To describe the formulation, we introduce mass balance equations for a system of two drained pores connected by a drained angular pore throat, as the most general case, shown in Figure (6.3a). We assume that the flow is from corner unit j towards corner unit i through corners of drained pore throat ij. For a given corner unit (with concentration $c_{CU,i}$ and volume $V_{CU,i}$), we can write the mass balance equation

$$V_{CU,i}\frac{d}{dt}\left(c_{CU,i}\right) = \sum_{j=1}^{N_{in}^{tube}}\sum_{k=1}^{N_{edge}^{ij}} q_{ij,k}c_{ij,k} + \sum_{n=1}^{N_{in,edge}^{CU,i}} q_{i,n}c_n - Q_{CU,i}c_{CU,i} \tag{7.1}$$

$$-V_{CU,i}\frac{d}{dt}\left(s_{CU,i}^{sw}\right) - V_{CU,i}\frac{d}{dt}\left(s_{CU,i}^{aw}\right)$$

where the first term on the r.h.s. is due to the mass arriving via N_{edge}^{ij} edges of N_{in}^{tube} throats with flow towards the corner unit. The second term on the r.h.s. accounts for the mass arriving from $N_{in,edge}^{CU,i}$ neighboring corner units (within the same pore body) with flow towards the corner unit. The third term shows the mass leaving the corner unit. $Q_{CU,i}$ is the total water flux leaving (or entering) the corner unit i. The last two terms account for the mass adsorbed onto the solid walls of the corner unit and on the AW interface within the corner unit, respectively. $s^{sw}_{CU,i}$ $[ML^{-3}]$ and $s^{aw}_{CU,i}$ are the mass adsorbed to SW and AW interfaces per unit volume of the corner unit.

We should note that, in the case of saturated pores, the second term on the right-hand-side of Equation (7.1) vanishes, and the value of N^{ij}_{edge} in the first term will be equal to one, since there is no edge flow present.

To close the system, we need extra equations for $s^{sw}_{CU,i}$ and $s^{aw}_{CU,i}$. Here, we assume local equilibrium adsorption at both SW and AW interfaces:

$$s^{sw}_{_{CU,i}} = k^{sw}_{d,i} a^{sw}_{CU,i} c_{CU,i} \tag{7.2}$$

$$s^{aw}_{_{CU,i}} = k^{aw}_{d,i} a^{aw}_{CU,i} c_{CU,i}$$

where $k^{sw}_{d,i}$ and $k^{aw}_{d,i}$ [L] are pore scale adsorption distribution coefficients at SW and AW interfaces, respectively. The specific surface area, $a^{\alpha w}_{CU,i}$, is defines as:

$$a^{\alpha w}_{CU,i} = \frac{A^{\alpha w}_{CU,i}}{V_{CU,i}} \quad \text{where } \alpha = s, a \tag{7.3}$$

s$A^{\alpha w}_{CU,i}$ is the total area of the appropriate αw interface within corner unit i.

The mass balance equation for an edge element of a drained pore throat may be written as (assuming that corner unit j is the upstream node)

$$V_{ij,k}\frac{dc_{ij,k}}{dt} = |q_{ij,k}|\, c_{CU,j} - |q_{ij,k}|\, c_{ij,k} - V_{ij,k}\frac{d}{dt}\left(s^{sw}_{_{ij,k}}\right) - V_{ij,k}\frac{d}{dt}\left(s^{aw}_{_{ij,k}}\right) \tag{7.4}$$

where $V_{ij,k}$, $q_{ij,k}$, and $c_{ij,k}$ are the volume, volumetric flow rate, and concentration of k^{th} edge of pore throat ij, respectively. $s^{sw}_{ij,k}$ ML^{-3} and $s^{aw}_{ij,k}$ are the adsorption at SW and AW interfaces, respectively.

Within the pore throats we also assume equilibrium adsorption, and we will have:

$$s^{sw}_{_{ij,k}} = k^{sw}_{d,ij,k} a^{sw}_{ij,k} c_{ij,k} \tag{7.5}$$

$$s^{aw}_{_{ij,k}} = k^{aw}_{d,ij,k} a^{aw}_{ij,k} c_{ij,k}$$

where, $k^{sw}_{d,ij,k}$ and $k^{aw}_{d,ij,k}$ [L] are pore scale adsorption distribution coefficients at SW and AW interfaces, respectively. The specific surface area, $a^{\alpha w}_{ij,k}$, is defines as

$$a^{\alpha w}_{ij,k} = \frac{A^{\alpha w}_{ij,k}}{V_{ij,k}} \quad \text{where } \alpha = s, a \tag{7.6}$$

and $A^{\alpha w}_{ij,k}$ is the total area of the appropriate αw interface within the k^{th} edge of pore throats ij.

Combining Equations (7.1) through (7.5) results in a linear set of equations to be solved for $c_{ij,k}$ and $c_{CU,i}$. Since we discretize pore bodies and pore throats on the basis of their saturation state (i.e., depending on that a pore is saturated or drained by the non-wetting phase), the number of unknowns are different for different simulations. In the case of a fully saturated domain, the number of unknowns is equal to $N_{tube} + N_{node}$ (N_{tube} is the total number of pore throats and N_{node} is the total number of pore bodies). In general, the number of pore throats is larger than the number of pore bodies in pore network models. In order to increase numerical efficiency, first, applying a fully implicit scheme, we discretized Equation (7.5) and determined $c_{ij,k}$ in terms of $c_{CU,i}$. This was then substituted into the discretized form of Equation (7.1), resulting in a set of equations for $c_{CU,i}$. This method considerably reduced the number of unknowns, and thus the computational times. The details of the method are given in Chapter 8, Section 8.3.2. For the accuracy of the scheme, the minimum time step was chosen on the basis of residence times [Suchomel et al., 1998a, Sun, 1996]

$$\Delta t \leq min \left\{ T_{ij}, T_{ij,k}, T_{CU,i}, T_i \right\} \tag{7.7}$$

where T denotes the residence time pertaining to different elements within the pore network.

After obtaining the solution at any given time, BTCs at a given longitudinal position were found by averaging the concentrations of pore bodies that possess the same longitudinal coordinate. In calculating BTCs, the concentrations of pore bodies were weighted by their volumetric flow rate, resulting in a flux-averaged concentration. That is, the normalized average concentration, $\overline{c}(x,t)$, given by

$$\overline{c}(x,t) = \left[\frac{\sum_i^{N_t^x} c_i(x,t) Q_i}{\sum_i^{N_t^x} Q_i} \right] \frac{1}{c_0} \qquad i = 1, 2, 3, \ldots, N_t \tag{7.8}$$

where c_0 is inlet solute concentration, and N_t^x denotes the total number of pore body elements that are located at the longitudinal coordinate x. The longitudinal coordinate can be written as multiples of lattice size ℓ, i.e. $x = 1\ell, 2\ell, \ldots, L$. where ℓ is the horizontal distance between centers of two adjacent pore bodies. The breakthrough curve at the outlet is obtained by plotting $c(x = L, t)$.

7.5 Macro-scale formulations of solute transport

At the macro scale we consider two models: Advection-Dispersion Equation (ADE) with adsorption, and a two-site kinetic model. Indeed, the nonequilibrium transport model could be in terms of alternative physical or chemical nonequilibrium models.

For the ADE model, the dispersion coefficient, D, and retardation factor, R, are the only parameters to be estimated since average flow velocity is obtained directly from the corresponding pore network model simulations. For the nonequilibrium model, in addition to the dispersion coefficient, D, and the retardation factor, R, the coefficient of partitioning between the equilibrium and nonequilibrium sites, f, and the mass transfer coefficient, ω, for transfer between the mobile and immobile zones need to be determined.

7.5.1 Advection-Dispersion Equation (ADE)

The transport of a adsorptive solute through a porous medium may be described by the hydrodynamic dispersion theory [Bear, 1972]. The one-dimensional transport equation for a adsorptive solute is:

$$R\frac{\partial \theta C}{\partial t} = \frac{\partial}{\partial z}\left(\theta D\frac{\partial C}{\partial z}\right) - \frac{\partial qC}{\partial z} \tag{7.9}$$

where C is the solute concentration, θ is the water content of the porous medium, q is the water flux, D is the hydrodynamic longitudinal dispersion coefficient, R is the retardation factor, and z is the distance. Dispersion coefficient (and thus dispersivity) at a given saturation could be determined by fitting the analytical solution of ADE to the BTCs of average concentration at the outlet of the network at that saturation.

7.5.2 Nonequilibrium model

The non-equilibrium formulation has been used to model both chemical [Selim et al., 1976] and physical non-equilibrium [van Genuchtan and Wieranga, 1976]. Either formulation reduces to the same dimensionless form in the case of linear adsorption under steady state flow [Nkedi-Kizza et al., 1984, van Genuchten and Wagenet, 1989].
The nonequilibrium formulation can be used for both chemical and physical nonequilibrium models. Even though they are based on different concepts, they have the same dimensionless form for the case of linear adsorption and steady-state water flow.

Physical nonequilibrium is often modeled by using a two-region (dual-porosity) type formulation. The medium contains two distinct mobile (flowing) and immobile (stagnant) regions [Coats and Smith, 1964, van Genuchtan and Wieranga, 1976]. Chemical nonequilibrium models consider adsorption on some of the adsorption sites to be instantaneous, while adsorption on the remaining sites is governed by first-order kinetics [Selim et al., 1976, Cameron and Klute, 1977]. The two-site nonequilibrium model makes a distinction between type-l (equilibrium) and type-2 (first-order kinetic) adsorption sites [van Genuchten and Wagenet, 1989]. For steady-state flow in a homogeneous soil, transport of a linearly adsorbed solute is given by [Toride et al., 1995]

$$\left(1+\frac{f\rho_b K_D}{\theta}\right)\frac{\partial c}{\partial t}=D\frac{\partial^2 c}{\partial x^2}-v\frac{\partial c}{\partial x}-\frac{\omega\rho_b}{\theta}\left(\left(1-f\right)K_D c-s_k\right) \tag{7.10}$$

$$\frac{\partial s_k}{\partial t}=\omega\left(\left(1-f\right)K_D c-s_k\right) \tag{7.11}$$

where ω $[T^{-1}]$ is a first-order kinetic rate coefficient, f is the fraction of adsorption sites that are always at equilibrium, and the subscript k refers to kinetic adsorption sites. Equations (7.10) and (7.11) use the customary first-order rate expression for describing kinetic adsorption on type-2 sites. The two-site adsorption model reduces to the one-site fully kinetic adsorption model if $f = 0$ (only type-2 sites are present).

7.6 Results

In this section, we optimize the solution of continuum-scale equations to the computed BTCs obtained from pore-network model to determine macro-scale adsorption parameters. In addition, we determine the relationships between relative permeability and saturation ($k_r - S_w$ curve) and between dispersivity and saturation (the $\alpha - S_w$ curve).

Figure (7.3) shows the relative permeability-saturation relation for our pore network model.

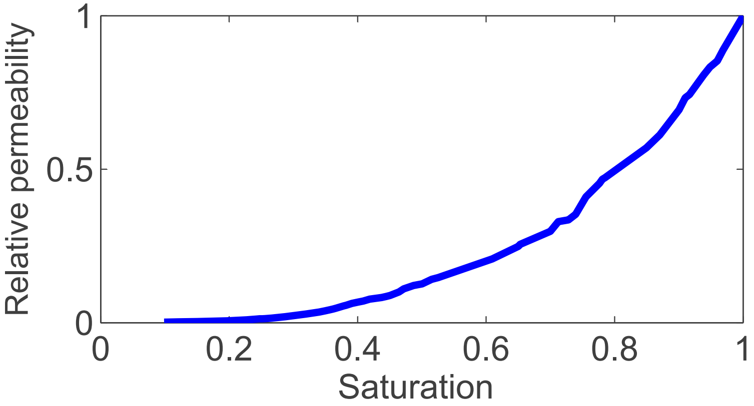

Figure 7.3: Relative permeability-saturation relation ($k_r - S_w$ curve) from the pore network. The pore radii distribution is shown in Figure (7.1)

.

After obtaining the BTC from the network, we used the (one-dimensional) CXTFIT code, version 2.1 [Toride et al., 1995], to estimate the transport parameters under steady state flow conditions. The inverse problem is solved by minimizing an objective function, which consists of the sum of the squared differences between observed (obtained from pore network model) and fitted concentrations. The objective function is minimized using a nonlinear least-squares inversion method according to Marquardt [1963].

Equations (7.2) and (7.5) show that the concentration of adsorbed mass depends on interface specific surface areas, which are, in turn, functions of saturation. Figure (7.4) shows the total interfacial areas as a function of the average saturation of the pore network.

As shown in Figure (7.4), the SW interfacial area decrease during drainage (interfaces associated with the water films are neglected). This is due to the invasion of pores by the non wetting phase. Initially, under saturated conditions ($S_w = 1$), there is no AW interface present. Thus, the area of AW interface starts at zero, and increases with the decrease in saturation.

In our pore-network simulations, in addition to simulating adsorptive transport

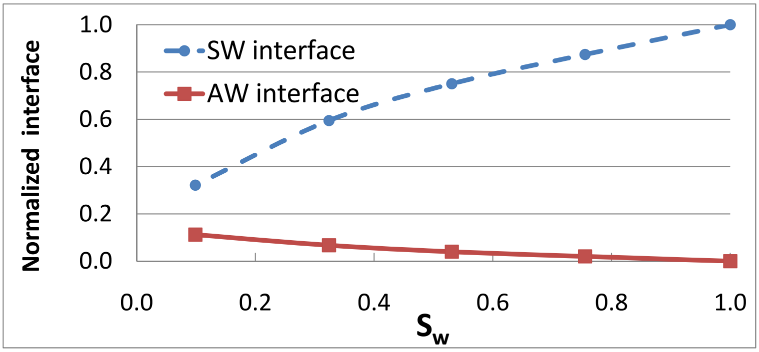

Figure 7.4: The solid-water, SW, and air-water, AW, total interfacial area as a function of average saturation, S_w. The areas are normalized to the total area under saturated conditions (which only belongs to the solid-water surfaces). Interfaces associated with the water films are neglected.

at fixed saturation values, we have also simulated the dispersion of a conservative (non adsorptive) solute under the same conditions. Doing so, for each saturation, we will have two dispersion coefficients, one for the tracer solute and the other one for the adsorptive solute. The ratio of dispersivity of adsorbing solute to the dispersivity of a conservative solute, as a function of the pore scale distribution coefficient is shown in Figure (7.5), obtained using the ADE model. The dispersivity of the adsorptive solute increases with the increase in pore-scale distribution coefficient (figure 7.5).

In fact, under partially-saturated conditions, dispersivity is not constant and its value is a function of saturation [Raoof and Hassanizadeh, 2011b]. Figure (7.6) shows the resulting relationship between dispersivity and saturation ($\alpha - S_w$ curve). A detailed discussion of this issue was given in Chapter 6

From Figure (7.6), it is clear that there is a relation between dispersivity and saturation. The relation is non-monotonic, with the maximum dispersivity (α_{max}) occurring at an intermediate saturation, which we refer to it as the critical saturation (S_{cr}).

Figure (7.7) shows the BTC from pore network-model together with the BTC obtained from analytical solution of the ADE model. It shows that although increase in dispersivity for adsorptive transport would result in a better fit, however there is still discrepancy between BTCs. This means that the choice of the ADE model with equilibrium adsorption term is probably not appropriate.

In addition to the adsorptive dispersivity, the solution of the ADE would pro-

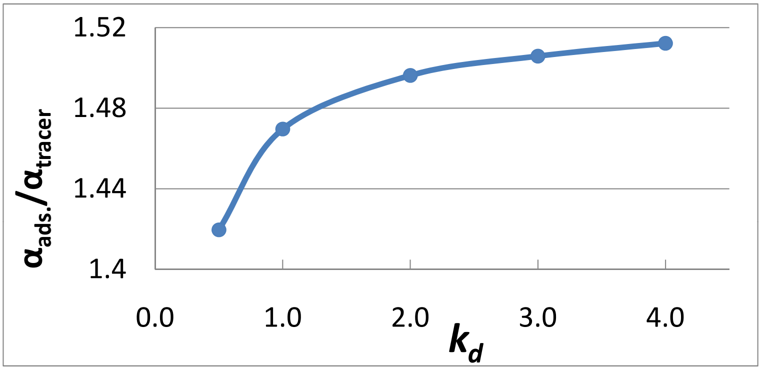

Figure 7.5: The relationship between ratio of adsorptive solute dispersivity (α_{ads}) to tracer solute dispersivity (α_{tracer}) obtained from ADE model, and pore scale distribution coefficient, k_d. The results are shown for a pore network model with water saturation of 0.53.

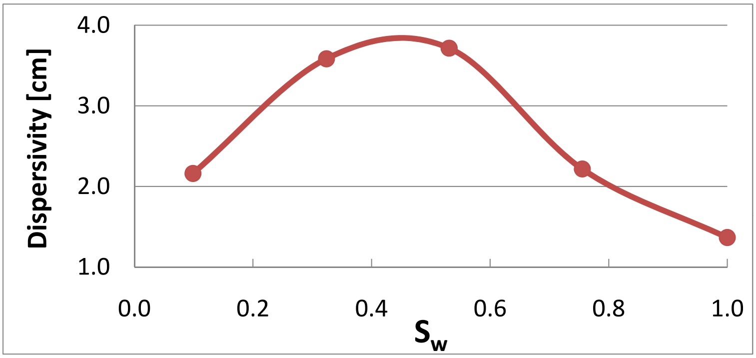

Figure 7.6: The relationship between solute dispersivity, α, and saturation, S_w.

vides a macro-scale distribution coefficient. For saturated conditions, we found (in Chapter 4) a linear relationship between pore scale and macro scale distribution coefficients, with the average specific surface area as the proportionality constant [Raoof and Hassanizadeh, 2010a]. Under unsaturated conditions, the value of the average specific surface areas for SW and AW interfaces will change with saturation (Figure 7.4). Knowing average specific surface area for each saturation, we can calculate a value for the macro-scale distribution coefficient. Figure (7.8) shows the calculated and fitted values of macro-scale distribution

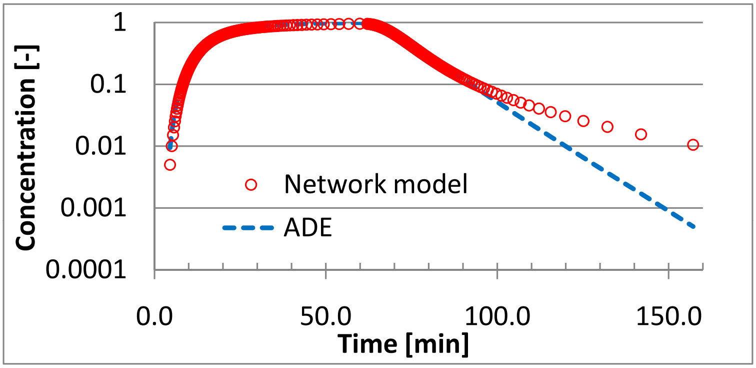

Figure 7.7: The resulting BTC from the network together with the BTC obtained using the ADE model. Dispersion coefficient values obtained from the fit to the computed BTCs.

coefficient as a function of saturation for a network with micro-scale distribution coefficient equal to 1.0.

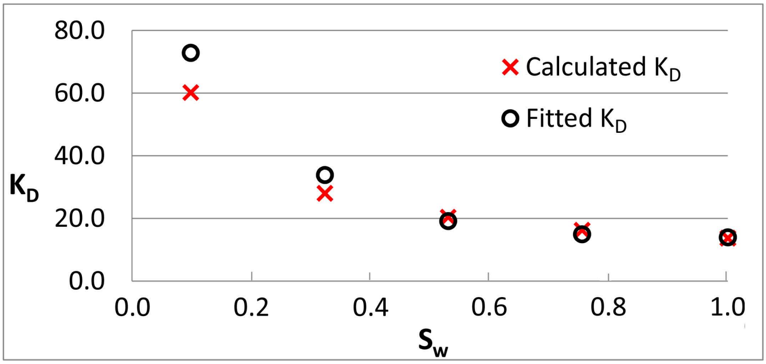

Figure 7.8: Calculated and fitted values of macro-scale distribution coefficient, K_D, as a function of saturation.

Figure (7.8) shows an increase in the macro-scale distribution coefficient, K_D, with decrease in saturation, (for a constant micro-scale distribution coefficient equal to 1.0) resulting from the increase in average specific surface area with decrease in saturation. There is better agreement between the calculated and fitted K_D values at higher saturations.

We also use a non-equilibrium formulation for describing the macro-scale behavior of the adsorptive solute. We use the same BTCs computed from the network model and optimize the solution of non-equilibrium model to these BTCs. Our results (Figure 7.9) show that the chemical non-equilibrium model accurately fits the BTCs obtained from the pore network model, resulting in a better fit compared to that obtained via the ADE model. Figure (7.9) shows an example of fitting the analytical solution of the nonequilibrium model to the BTC obtained from the pore network. In this case, we estimated the dispersion coefficient independently using the BTC of a conservative (non adsorptive) solute. This value for the dispersion coefficient was then used for adsorptive solute (under the same saturation) and only the adsorptive parameters were estimated.

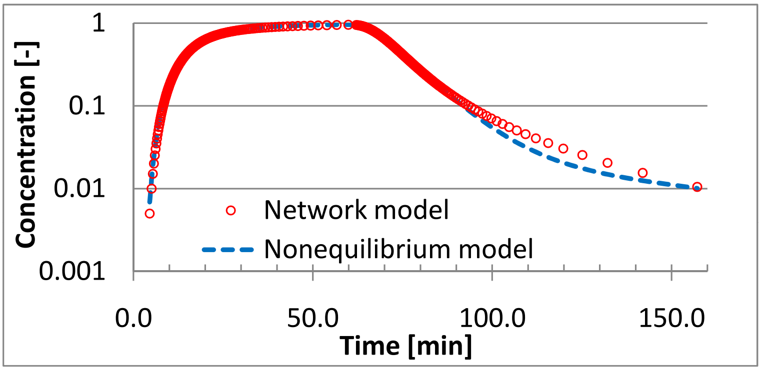

Figure 7.9: The resulting BTC from the network together with the fitted BTC using the Nonequilibrium model. The BTC belong to a pore network with a pore scale adsorption distribution coefficient of 1.0 and saturation of 0.53.

Compared with the ADE model, the non-equilibrium model provides a more appropriate model for the tailing behavior of the BTCs under different saturations.

7.7 Conclusion

Multi-phase and (partially-) saturated reactive/adsorptive transport in porous media is characterized by means of several macroscopic transport properties including: relative permeability; capillary pressure; unsaturated dispersivity; and upscaled reactive/adsorptive transport parameters. These properties have been found to depend on macro-scale parameters such as average saturation but also on pore-scale properties. Indeed, the state of fluid distribution within the pores is important in determining the transport properties.

In this study, we have used a MDPN model to simulate fluid flow and transport of adsorptive solute within the pore space of a porous medium. We have considered adsorption at the solid-water (SW) interfaces as well as air-water (AW) interfaces to obtain BTCs of average concentration obtained from the pore network. Our results showed that, even if there is equilibrium adsorption at the solid-water and air-water interfaces at the pore scale, one may need to use a non-equilibrium description of adsorptive process at the macro scale. The equilibrium description of adsorption at the macro scale produced by an ADE model could not appropriately fit the computed BTCs. Applying the equilibrium macro scale model required higher values of dispersivity which, in addition to saturation, will depend on the value of pore scale adsorption coefficient.

On the other hand, we found that the kinetic description of adsorptive process at the macro scale could accurately model the resulting BTCs obtained from the pore network simulations. Using the kinetic description, we could use the same dispersivity values which were obtained from tracer simulations. We have applied pore-scale distribution coefficient to each pore element of the network and, utilizing the BTCs of average concentrations, calculated macro scale distribution coefficient, under different saturations. Decrease in saturation causes increase in average specific surface area which in turn results in an increase of macro-scale distribution coefficient.

CHAPTER 8

EFFICIENT FULLY IMPLICIT SCHEME FOR MODELING OF ADSORPTIVE TRANSPORT; (PARTIALLY-) SATURATED CONDITIONS

Bad times have a scientific value. These are occasions a good learner would not miss.

Ralph Waldo Emerson

Abstract

PORE network modeling has been widely used to study variety of flow and transport processes in porous media. To do so, equations of mass balance should be discretize to be used within network elements. Different formulations of solute transport within the pore-network model have been introduces in the literature for the case of saturated conditions. However, there are much less studies under partially saturated conditions. Under partially saturated conditions the system contains three phases: air, water, and solid. The principal interactions usually occur at the solid-water(SW) interfaces and air-water(AW) interfaces, thus greatly influenced by water content. In this chapter, we introduce a fully implicit numerical scheme for transport of adsorptive solute under (partially-) saturated conditions, undergoing both/either equilibrium and/or kinetic types of adsorption. We have considered absorption to the SW as well as AW interfaces. The numerical scheme is developed based on the assumption that porous media is composed of a network of pore bodies and pore throats, both with finite volumes. While under saturated conditions we have assigned one concentrations to a pore body or pore throat, under unsaturated conditions we assign separate concentrations to each edge of a drained pore body or pore throat. Through applying an efficient numerical algorithm, we have reduced the size of system of linear equations by a factor of at least three, which significantly decreases the

computational times. For the case of partially saturated, the formulations are written for the most general case, in which solute mass transport occurs through edges of drained pore throats and edges of drained pore bodies. Under drainage, each corner, k, of a drained pore throat is a separate domain. In the same manner, each corner, n, of a drained pore body is also a separate domain for which solute concentration and adsorbed mass concentrations are calculated. We covered different types of adsorption to air-water (AW) interfaces as well as solid-water (SW) interfaces. Adsorption could be: equilibrium type at both AW and SW interfaces; kinetic adsorption at both AW and SW interfaces; and kinetic adsorption at one of either SW or AW interfaces and equilibrium at the other one.

8.1 Introduction

Two well known approaches to describe solute transport are: deterministic [Bear, 1972], and probabilistic or statistical approaches [Sahimi et al., 1986, Dagan, 1988, Sorbie and Clifford, 1991, Damion et al., 2000]. Applying equations of mass balance for each network element is an example of the first, whereas the particle tracking approach serves as an example of the second approach.

Both methods are capable of simulating advective and diffusive processes. In particle tracing, one can upscale 3D Brownian motion of particles subjected to a velocity field within the network elements, representing both local diffusion and advection. Such a statistical approach originated from the Einstein's dispersion theory and the theory of Brownian motion [Chandrasekhar, 1943]. In this approach, random walkers that represent the tracer particles are allowed to describe Brownian and advective displacement within the chosen porous medium [Saffman, 1959, Sahimi et al., 1986, Sorbie and Clifford, 1991]. By tracking the paths of these particles the Spatial Positions Distribution (SPD) for particles is found from which the dispersion tensor is derived [Chandrasekhar, 1943]. Alternatively, First-arrival Times Distribution (FTD) at the outlet face of the soil-column (or network) is used to derive DL [Sahimi et al., 1986, Sorbie and Clifford, 1991].

To track the particles within the pore spaces we need to use velocity profiles within the pore throats and apply jump conditions at the intersections of the pore throats (i.e., pore bodies) [Acharya et al., 2007b].

Acharya et al. [2007b] applied particle tracking to obtain the macroscopic longitudinal dispersion coefficient. Through comparison with experimental observations, they found appropriate jump conditions at the intersections and concluded that a parabolic velocity profile in pore throats must be implemented to get a good agreement for a wide range of Peclet number.

In applying equations of mass balance to simulate solute transport, usually pore scale mixing is assumed within each network element. Different definitions of network element have been used in literature. The choice commonly depends on the process under consideration as well as computational load. Acharya et al. [2005a] modeled porous medium with a network of pore-units, as the network element. Each pore unit comprised of pore bodies and bonds of finite volume. Such a pore-unit was assumed to be a mixing cell with steady state flow condition [Sun, 1996, Suchomel et al., 1998b, Acharya et al., 2005a]. By solving the mixing cell model for each pore unit and averaging the concentrations for a large number of pore units as a function of time and space, the dispersivity was calculated.

Li et al. [2006b] considered pore bodies as network elements to simulate reactive transport within porous media. They have simulated reactive transport by applying the mass balance equation which accounted for advection, diffusion between adjacent pores, and reaction in each pore. Considering the network domain as a REV, the reaction rates from network models were compared to rates from continuum scale models, that use uniform concentrations, to examine the scaling behavior of reaction kinetics.

Commonly the similarity between numerical and physical dispersion is used to represent dispersion in porous media. The numerically generated dispersion is a function of time step. Such a dispersion could be analyzed by fitting the numerical solution to the Taylor's expansion [Sun, 1996, Suchomel et al., 1998b].

To solve the transport equation within pore network, Suchomel et al. [1998b] used a finite-difference approximation to the one-dimensional transport problem in each pore. They discretized the space within each individual pore throat to calculate mass transfer within a given pore. They have used upwind explicit finite-difference method to discretize the advection term. This scheme is numerically diffusive. They have used such a numerical diffusion to represent physical diffusion. Through comparison with Taylor expansion, they have calculated numerical dispersion due to scheme approximations.

In this chapter we use a deterministic approach by applying equations of mass balance to each network element to simulate reactive/adsorptive transport under (partially-) saturated conditions. Under saturated conditions we use pore bodies and pore throats, both with finite volumes, as network elements. However, under partially-saturated conditions, the choice of network elements is different. Upon drained of a pore body, the non-wetting phase occupies the bulk space of the pore. We consider each corner of the pore body as a separate network element (i.e., with its own pressure and concentration). Thus, for a cubic pore body, 8 different corner elements exist. Fluid flow and solute mass fluxes between these elements occurs through the 12 edges of the pore body (see Figure 6.3(a)). In the same manner, after invasion of the pore throat by the non-wetting, each edge of the pore throat will be a separate network element (i.e., with separate flow rate and concentration assigned to it). For example a pore throat with triangular cross section, upon drainage will break into three network elements, one for each edge flow.

We applied a fully implicit numerical scheme for transport of adsorptive solute under (partially-) saturated conditions, undergoing both/either equilibrium and/or kinetic types of adsorption. Although defining edges of drained pores as separate network elements will increase accuracy of modeling, it will make the computational process heavier, since each network element will be an unknown variable during the simulation. Under such a conditions, applying an efficient numerical algorithm becomes very important. We have developed, and did modeling using efficient numerical algorithms which, though substitution of unknown variables, reduced the size of system of linear equations by a factor of at least three. This significantly decreased the computational times.

In this chapter we first present numerical scheme for kinetic adsorption under saturated conditions and then we proceed with transport of non-adsorptive solutes well as adsorptive solutes under partially saturated conditions.

Table 8.1: Nomenclature

Abbr.	**Description**	**Dimension**
N_{in}^{tube}	number of pore throats flowing into the corner unit i	—
N_{edge}^{ij}	number of edges within angular pore throat ij (e.g., for triangular cross section, $N_{edge}^{ij} = 3$)	—
$N_{in,edge}^{CU,i}$	number of pore body edges (within the same pore body) flowing into corner unit i	—
Δt	discretized time step	[T]
c_{ij}	concentration of saturated pore throat ij	$[ML^{-3}]$
$c_{ij,k}$	concentration of k^{th} edge of drained angular pore throat ij	$[ML^{-3}]$
V_{ij}	volume of saturated pore throat ij	$[L^3]$
$V_{ij,k}$	volume of k^{th} edge of drained angular pore throat ij	$[L^3]$
q_{ij}	volumetric flow of saturated pore throat ij	$[L^{-3}T^{-1}]$
$q_{ij,k}$	volumetric flow of k^{th} edge of drained angular pore throat ij	$[L^{-3}T^{-1}]$
s_{ij}	adsorbed mass concentration of saturated pore throat ij	$[ML^{-3}]$
$s_{ij,k}^{sw}$	adsorbed mass concentration at SW interface in k^{th} edge of pore throat ij	$[ML^{-3}]$
$s_{ij,k}^{aw}$	adsorbed mass concentration at AW interface in k^{th} edge of pore throat ij	$[ML^{-3}]$
$K_{D,ij}^{sw}$	upscaled distribution coefficient of SW interface in pore throat ij	[-]
$K_{D,ij}^{aw}$	upscaled distribution coefficient of AW interface in pore throat ij	[-]
$k_{d,ij,k}^{sw}$	pore-scale distribution coefficient of SW interface in pore throat ij	$[L]$
$k_{d,ij,k}^{aw}$	pore-scale distribution coefficient of AW interface in pore throat ij	$[L]$
$a_{ij,k}^{sw}$	specific surface area of SW interface in k^{th} edge of pore throat ij	$[L^{-1}]$
$a_{ij,k}^{aw}$	specific surface area of AW interface in k^{th} edge of pore throat ij	$[L^{-1}]$

Abbr.	**Description**	**Dimension**
$c_{CU,i}$	concentration of saturated pore body i	$[ML^{-3}]$
$c_{CU,i}$	concentration of corner unit i within a drained pore body	$[ML^{-3}]$
V_i	volume of (saturated) pore body i	$[L^3]$
$V_{CU,i}$	volume of corner unit i within a drained pore body	$[L^3]$
$q_{i,n}$	volumetric flow from corner unit n to corner unit i within the same (drained) pore body	$[L^3T^{-1}]$
Q_i	total (outflow or inflow) volumetric flow for (saturated) pore body i	$[L^3T^{-1}]$
$Q_{CU,i}$	total (outflow or inflow) volumetric flow for corner unit i within a drained pore body	$[L^3T^{-1}]$
$s^{sw}_{CU,i}$	adsorbed mass concentration at SW interface in corner unit i	$[ML^{-3}]$
$s^{aw}_{CU,i}$	adsorbed mass concentration at AW interface in corner unit i	$[ML^{-3}]$
$K^{aw}_{D,i}$	upscaled distribution coefficient of AW interface in corner unit i	[-]
$k^{sw}_{d,i}$	pore-scale distribution coefficient of SW interface in corner unit i	$[L]$
$k^{aw}_{d,i}$	pore-scale distribution coefficient of AW interface in corner unit i	$[L]$
a^{sw}_i	specific surface area of SW interface in corner unit i	$[L^{-1}]$
a^{aw}_i	specific surface area of AW interface in corner unit i	$[L^{-1}]$

8.2 Numerical scheme; saturated conditions

8.2.1 Adsorption; saturated conditions

To write mass balance equations for each element of the network we assume flow directions from pore body j into pore body i, through pore throat ij. An example of interconnected pore bodies and pore throats is shown in Figure (4.3) where pore body j is the upstream node.

Mass balance for an adsorbing solute within a saturated pore throat may be written as

$$V_{ij}\frac{dc_{ij}}{dt} = |q_{ij}|\,c_j - |q_{ij}|\,c_{ij} - V_{ij}k_{att,ij}c_{ij} + V_{ij}k_{det,ij}s_{ij} \tag{8.1}$$

discretization of Equation (8.1) in fully implicit scheme gives

$$V_{ij}\frac{\left(\overline{c_{ij}}^{t+\Delta t}-\overline{c_{ij}}^{t}\right)}{\Delta t}=q_{ij}\left(\overline{c_{j}}^{t+\Delta t}-\overline{c_{ij}}^{t+\Delta t}\right)\quad -V_{ij}\alpha_{ij}\left(K_{d,ij}\overline{c_{ij}}^{t+\Delta t}-\overline{s_{ij}}^{t+\Delta t}\right) \tag{8.2}$$

the kinetic adsorption within a pore throat we be written as

$$\frac{ds_{ij}}{dt}=k_{att,ij}c_{ij}-k_{det,ij}s_{ij} \tag{8.3}$$

discretization of Equation (8.3) gives

$$\frac{\left(\overline{s_{ij}}^{t+\Delta t}-\overline{s_{ij}}^{t}\right)}{\Delta t}=\alpha_{ij}\left(K_{d,ij}\overline{c_{ij}}^{t+\Delta t}-\overline{s_{ij}}^{t+\Delta t}\right) \tag{8.4}$$

solving for $\overline{s_{ij}}^{t+\Delta t}$ we will have

$$\overline{s_{ij}}^{t+\Delta t}=\frac{\alpha_{ij}\Delta t K_{d,ij}}{(1+\alpha_{ij}\Delta t)}\overline{c_{ij}}^{t+\Delta t}+\frac{1}{(1+\alpha_{ij}\Delta t)}\overline{s_{ij}}^{t} \tag{8.5}$$

substituting Equation (8.5) into Equation (8.2) gives:

$$\overline{c_{ij}}^{t+\Delta t}=\frac{1}{B}\overline{c_{ij}}^{t}+\frac{\Delta t\alpha_{ij}}{B\,(1+\alpha_{ij}\Delta t)}\overline{S_{ij}}^{t}+\frac{1}{B}\frac{q_{ij}\Delta t}{V_{ij}}\overline{c_{j}}^{t+\Delta t} \tag{8.6}$$

where

$$B=1+\frac{q_{ij}\Delta t}{V_{ij}}+\Delta t\alpha_{ij}K_{d,ij}-\frac{\Delta t^{2}\alpha_{ij}^{2}K_{d,ij}}{(1+\alpha_{ij}\Delta t)}$$

mass balance for a saturated pore throat may be written as

$$V_{i}\frac{dc_{i}}{dt}=\sum_{j=1}^{N_{in}}q_{ij}c_{ij}-Q_{i}c_{i} \tag{8.7}$$

discretization of Equation (8.7) using a fully implicit scheme results in

$$V_{i}\frac{\overline{c}_{i}^{t+\Delta t}-\overline{c}_{i}^{t}}{\Delta t}=\sum_{j=1}^{N_{in}}q_{ij}\overline{c}_{ij}^{t+\Delta t}-Q_{i}\overline{c}_{i}^{t+\Delta t} \tag{8.8}$$

this equation can be rearranged to get

$$\left(1+\frac{\Delta t Q_i}{V_i}_{\;i}\right)\overline{c}_i^{t+\Delta t} - \frac{\Delta t}{V_i}\sum_{j=1}^{N_{in}} q_{ij}\overline{c}_{ij}^{t+\Delta t} = \overline{c}_i^{t} \qquad (8.9)$$

we use Equation (8.6) to substitute for $\overline{c}_{ij}^{t+\Delta t}$ in Equation (8.9), and collect unknown term on the l.h.s. and known terms on r.h.s. to get

$$E\overline{c}_i^{t+\Delta t} - I\sum_{j=1}^{N_{in}} F\overline{c}_j^{t+\Delta t} = \overline{c}_i^{t} + I\sum_{j=1}^{N_{in}}\left(G\overline{c}_{ij}^{t} + H\overline{s_{ij}}^{t}\right) \qquad (8.10)$$

where:

$$E_{(N_{node})} = 1+\frac{\Delta t Q_i}{V_i}; \qquad \mathtt{I}_{(N_{node})} = \frac{\Delta t}{V_i}; \qquad \mathtt{F}_{(N_{tube})} = \frac{1}{B}\frac{q_{ij}^2\Delta t}{V_{ij}}$$

$$G_{(N_{tube})} = \frac{q_{ij}}{B}; \qquad \mathtt{H}_{(N_{tube})} = \frac{q_{ij}\Delta t\alpha_{ij}}{B\left(1+\Delta t\alpha_{ij}\right)}$$

Note that, through substitution, we end up with Equation (8.10) in which the number of unknowns is N_{node}, concentration in pore bodies (i.e., $\overline{c}_i^{t+\Delta t}$ and $\overline{c}_j^{t+\Delta t}$). In this way we could decrease the size of coefficient matrix by about 3 times since we don't need to solve simultaneously for concentration of solute and adsorbed concentration in pore throats in Equation (8.10) (the number of pore throats is much more than the number of pore bodies in the network). After each time step the concentration of pore throats and adsorbed concentrations can be calculated using Equations (8.6) and (8.5), respectively.

8.3 Numerical scheme; partially saturated conditions

For the case of partially saturated conditions, we write formulations for the most general case, in which solute mass transport occurs through edges of drained pore throats and edges of drained pore bodies. We divide the volume of a drained pore body into element which we call as "corner unit". Each corner unit comprised of a corner domain together with half of the three neighboring edges connected to it within the same pore body, as shown in Figure (6.3). Therefore, in the case of cubic pore body, we will have eight corner units. Thus, we assign eight different concentrations to a drained pore body, one for each corner unit. In the case of drained pore throats, we assign different concentrations to each pore throat edge. For example, we assign three different concentrations to each edge of a drained pore throat with triangular cross section.

Throughout this section we assume flow from corner unit j to corner unit i (i.e., corner unit j is the upstream node) through an edge of drained pore throat ij. We start the formulation for the case of a non-adsorptive solute and then proceed with adsorptive solutes.

8.3.1 Non-adsorptive solute

Mass balance equation for edge of a drained pore throat may be written as

$$V_{ij,k}\frac{d}{dt}\left(c_{ij,k}\right) = \left|q_{ij,k}\right| c_{CU,j} - \left|q_{ij,k}\right| c_{ij,k} \tag{8.11}$$

we apply a fully implicit scheme to Equations (8.11), to get

$$V_{ij,k}\frac{c_{ij,k}^{t+\Delta t} - c_{ij,k}^{t}}{\Delta t} = \left|q_{ij,k}\right| c_{CU,j}^{t+\Delta t} - \left|q_{ij,k}\right| c_{ij,k}^{t+\Delta t} \tag{8.12}$$

From this point forward, for the sake of simplicity in our notation, we drop the $t+\Delta t$ superscript, and we only keep superscript of terms with time t, such as $c_{ij,k}^{t}$.

the equation for $c_{ij,k}$ will be:

$$c_{ij,k} = \frac{1}{B_{ij,k}}\left(\frac{\Delta t q_{ij,n}}{V_{ij,k}} c_{CU,j} + c_{ij,k}^{t}\right) \tag{8.13}$$

where the constant coefficient, $B_{ij,k}$, is defined as

$$B_{ij,k} = 1 + \frac{\Delta t q_{ij,k}}{V_{ij,k}} \tag{8.14}$$

The mass balance equation for corner units i, within a drained pore body, may be written as

$$V_{CU,i}\frac{d}{dt}\left(c_{CU,i}\right) = \sum_{j=1}^{N_{in}^{tube}} \sum_{k=1}^{N_{edge}^{ij}} q_{ij,k} c_{ij,k} + \sum_{n=1}^{N_{in,edge}^{CU,i}} q_{i,n} c_{CU,n} - Q_{CU,i} c_{CU,i} \tag{8.15}$$

for a drained triangular pore throat $N_{edge}^{ij} = 3$, and for a drained cubic pore body $N_{in,edge}^{CU,i} = 3$. discretization of Equation (8.15) in a fully implicit scheme results in

$$V_{CU,i}\frac{c_{CU,i}-c^{t}_{CU,i}}{\Delta t}=\sum_{j=1}^{N^{tube}_{in}}\sum_{k=1}^{N^{ij}_{edge}}q_{ij,k}c_{ij,k}+\sum_{n=1}^{N^{CU,i}_{in,edge}}q_{i,n}c_{CU,n}-Q_{CU,i}c_{CU,i} \tag{8.16}$$

solving for $c_{CU,i}$, we will have

$$c_{CU,i}=\frac{1}{B_{CU,i}}\frac{\Delta t}{V_{CU,i}}\sum_{j=1}^{N^{tube}_{in}}\sum_{k=1}^{N^{ij}_{edge}}q_{ij,k}c_{ij,k}+\frac{1}{B_{CU,i}}\frac{\Delta t}{V_{CU,i}}\sum_{n=1}^{N^{CU,i}_{in,edge}}q_{i,n}c_{CU,n}+\frac{1}{B_{CU,i}}c^{t}_{CU,i} \tag{8.17}$$

where, the constant coefficient, $B_{CU,i}$, is defined as

$$B_{CU,i}=1+\frac{\Delta t Q_{CU,i}}{V_{CU,i}}$$

The subscript i in the $B_{CU,i}$ implies that $B_{CU,i}$ is defined for each corner unit, i.
substituting Equation (8.13) into Equation (8.17) results in

$$\begin{aligned}c_{CU,i}=&\frac{1}{B_{CU,i}}\frac{\Delta t}{V_{CU,i}}\sum_{j=1}^{N^{tube}_{in}}\sum_{k=1}^{N^{ij}_{edge}}\frac{q_{ij,k}}{B_{ij,k}}\left[\frac{\Delta t q_{ij,k}}{V_{ij,k}}c_{j}+c^{t}_{ij,k}\right]\\&+\frac{1}{B_{CU,i}}\frac{\Delta t}{V_{CU,i}}\sum_{n=1}^{N^{CU,i}_{in,edge}}q_{i,n}c_{CU,n}+\frac{1}{B_{CU,i}}c^{t}_{CU,i}\end{aligned} \tag{8.18}$$

rearranging Equation (8.18) and collecting all the unknown concnerations (at time $t+\Delta t$) on the l.h.s. and all the terms at time t on the r.h.s., we will have the final form of system of equations to be solved for the concentrations of corner units (i.e., $c_{CU,i}$ and $c_{CU,j}$):

$$\begin{aligned}&\frac{B_{CU,i}V_{CU,i}}{\Delta t}c_{CU,i}-\sum_{j=1}^{N^{tube}_{in}}\sum_{k=1}^{N^{ij}_{edge}}q_{ij,k}\left[\frac{1}{B_{ij,k}}\frac{\Delta t q_{ij,k}}{V_{ij,k}}c_{j}\right]-\sum_{n=1}^{N^{CU,i}_{in,edge}}q_{i,n}c_{CU,n}=\\&\sum_{j=1}^{N^{tube}_{in}}\sum_{k=1}^{N^{edge}_{ij}}q_{ij,k}\left[\frac{1}{B_{ij,k}}c^{t}_{ij,k}\right]+\frac{V_{CU,i}}{\Delta t}c^{t}_{CU,i}\end{aligned} \tag{8.19}$$

having concentration of the pore units calculated, using Equation (8.13), we can calculate concentrations within pore throat edges ($c_{ij,k}$). Note that, doing this substitution, we will end up with Equation (8.19) in which the unknowns are only of corner units. In this way we could decrease the size of coefficient matrix considerably since we don't need to solve for concentrations in the pore throat edges at the same time.

8.3.2 Two sites equilibrium adsorption

In this section we consider equilibrium adsorption at both SW and AW interfaces. We assume flow from corner unit j to corner unit i. Mass balance equation with equilibrium adsorption, within a pore throat, may be written as

$$\begin{aligned} V_{ij,k}\frac{d}{dt}\left(c_{ij,k}\right) = \left|q_{ij,k}\right| c_j - \left|q_{ij,k}\right| c_{ij,k} - V_{ij,k}K^{sw}_{D,ij}\frac{d}{dt}\left(c_{ij,k}\right) \\ - V_{ij,k}K^{aw}_{D,ij}\frac{d}{dt}\left(c_{ij,k}\right) \end{aligned} \tag{8.20}$$

$K^{sw}_{D,ij}$ and $K^{aw}_{D,ij}$ [-] are upscaled adsorption distribution coefficients at the solid-water (SW) and air-water (AW) interfaces within tube ij, where

$$K^{\alpha w}_{D,ij,k} = k^{\alpha w}_{d,ij,k}a^{\alpha w}_{ij,k}; \quad \text{where } \alpha = s, a \tag{8.21}$$

where $a^{\alpha w}_{ij,k}$ is the specific surface area. Rearranging and applying a fully implicit scheme to Equation (8.20), we get

$$V_{ij,k}\left(1 + K^{sw}_{D,ij} + K^{aw}_{D,ij}\right)\frac{c^{t+\Delta t}_{ij,k} - c^{t}_{ij,k}}{\Delta t} = \left|q_{ij,k}\right| c^{t+\Delta t}_j - \left|q_{ij,k}\right| c^{t+\Delta t}_{ij,k} \tag{8.22}$$

From this point forward, for the sake of simplicity in our notation, we drop the $t + \Delta t$ superscript, and we only keep superscript of terms with time t (such as in $c^t_{ij,k}$).
the equation for $c_{ij,k}$ (i.e., $c^{t+\Delta t}_{ij,k}$) will be

$$c_{ij,k} = \frac{1}{B_{ij,k}}\left(\frac{\Delta t q_{ij,n}}{V_{ij,k}\left(1 + K^{sw}_{D,ij} + K^{aw}_{D,ij}\right)}c_{CU,j} + c^t_{ij,k}\right) \tag{8.23}$$

where the constant coefficient, $B_{ij,k}$, is defined as

$$B_{ij,k} = 1 + \frac{\Delta t q_{ij,k}}{V_{ij,k}\left(1 + K^{sw}_{D,ij} + K^{aw}_{D,ij}\right)}$$

mass balance equation for a corner unit i with equilibrium adsorption may be written as

$$V_{CU,i}\tfrac{d}{dt}\left(c_{CU,i}\right) = \sum_{j=1}^{N_{in}^{tube}} \sum_{k=1}^{N_{edge}^{ij}} q_{ij,k}c_{ij,k} + \sum_{n=1}^{N_{in,edge}^{CU,i}} q_{i,n}c_{CU,n} - Q_{CU,i}c_{CU,i} -$$

$$V_{CU,i}K_{D,i}^{sw}\frac{dc_{CU,i}}{dt} - V_{CU,i}K_{D,i}^{aw}\frac{dc_{CU,i}}{dt} \tag{8.24}$$

where N_{in}^{tube} is the number of pore throats flowing into the corner unit i; N_{edge}^{ij} is the number of edges within the angular pore throat (for example, for a tube with triangular cross section, $N_{edge}^{ij} = 3$), each with the volumetric flow rate of $q_{ij,k}$. $N_{in,edge}^{CU,i}$ is the number of pore body edges, within the same pore body, flowing into corner unit i, each with the volumetric flow rate of $q_{i,n}$ (for example, the maximum value of $N_{in,edge}^{CU,i}$ for the case of a cubic pore body is equal to three). $K_{D,i}^{sw}$ and $K_{D,i}^{aw}$ [-] are upscaled adsorption distribution coefficients at the solid-water (SW) and air-water (AW) interfaces within corner unit i, respectively, where

$$K_{D,i}^{\alpha w} = k_{d,i}^{\alpha w}a_i^{\alpha w}; \quad \text{where } \alpha = s, a \tag{8.25}$$

where $a_i^{\alpha w}$ is the specific surface area within corner unit i. discretization of Equation (8.24) in fully implicit scheme, and rearranging, gives

$$V_{CU,i}\left(1 + K_{D,i}^{sw} + K_{D,i}^{aw}\right)\tfrac{c_{CU,i} - c_{CU,i}^{t}}{\Delta t} = \sum_{j=1}^{N_{in}^{tube}} \sum_{k=1}^{N_{ij}^{edge}} q_{ij,k}c_{ij,k} +$$

$$\sum_{n=1}^{N_{in}^{CU,i}} q_{i,n}c_{CU,n} - Q_{CU,i}c_{CU,i} \tag{8.26}$$

solving for $c_{CU,i}$, we will have

$$c_{CU,i} = \frac{1}{B_{CU,i}}\frac{\Delta t}{V_{CU,i}\left(1 + K_{D,i}^{sw} + K_{D,i}^{aw}\right)}\sum_{j=1}^{N_{in}^{tube}} \sum_{k=1}^{N_{edge}^{ij}} q_{ij,k}c_{ij,k} +$$

$$\frac{1}{B_{CU,i}}\frac{\Delta t}{V_{CU,i}\left(1 + K_{D,i}^{sw} + K_{D,i}^{aw}\right)}\sum_{n=1}^{N_{in,edge}^{CU,i}} q_{i,n}c_{CU,n} + \frac{1}{B_{CU,i}}c_{CU,i}^{t} \tag{8.27}$$

where, the constant coefficient, $B_{CU,i}$, is defined as

$$B_{CU,i} = 1 + \frac{\Delta t Q_{CU,i}}{V_{CU,i}\left(1 + K^{sw}_{D,i} + K^{aw}_{D,i}\right)}$$

the subscript i in the $B_{CU,i}$ implies that $B_{CU,i}$ is defined for each corner unit, i.

through Equation (8.23) we can relate $c_{ij,k}$ to $c^t_{ij,k}$ and $c_{CU,j}$; substituting Equation (8.23) into Equation (8.27) we will have

$$c_{CU,i} =$$

$$\frac{1}{B_{CU,i}} \frac{\Delta t}{V_{CU,i}\left(1+K^{sw}_{D,i}+K^{aw}_{D,i}\right)} \sum_{j=1}^{N^{tube}_{in}} \sum_{k=1}^{N^{ij}_{edge}} \frac{q_{ij,k}}{B_{ij,k}} \left[\frac{\Delta t q_{ij,k}}{V_{ij,k}\left(1+K^{sw}_{D,ij}+K^{aw}_{D,ij}\right)} c_{CU,j} + c^t_{ij,k}\right] +$$
$$\frac{1}{B_{CU,i}} \frac{\Delta t}{V_{CU,i}\left(1 + K^{sw}_{D,i} + K^{aw}_{D,i}\right)} \sum_{n=1}^{N^{CU,i}_{in,edge}} q_{i,n} c_{CU,n} + \frac{1}{B_{CU,i}} c^t_{CU,i} \qquad (8.28)$$

rearranging Equation (8.28) and collecting all the unknown concentrations (i.e., at time $t+\Delta t$) on the l.h.s. and all (known) terms at time t on the r.h.s., we will have the final form of system of equations to be solved for the concentrations within corner units ($c_{CU,i}$ and $c_{CU,j}$)

$$\begin{aligned}
&\frac{B_{CU,i} V_{CU,i}\left(1 + K^{sw}_{D,i} + K^{aw}_{D,i}\right)}{\Delta t} c_{CU,i} \\
&- \sum_{j=1}^{N^{tube}_{in}} \sum_{k=1}^{N^{ij}_{edge}} \left[\frac{q_{ij,k}}{B_{ij,k}} \frac{\Delta t q_{ij,k}}{V_{ij,k}\left(1 + K^{sw}_{D,ij} + K^{aw}_{D,ij}\right)} c_j\right] - \sum_{n=1}^{N^{CU,i}_{in,edge}} q_{i,n} c_{CU,n} \\
&= \sum_{j=1}^{N^{tube}_{in}} \sum_{k=1}^{N^{ij}_{edge}} q_{ij,k} \left[\frac{1}{B_{ij,k}} c^t_{ij,k}\right] + \frac{V_{CU,i}\left(1 + K^{sw}_{D,i} + K^{aw}_{D,i}\right)}{\Delta t} c^t_{CU,i} \qquad (8.29)
\end{aligned}$$

having concentration of the pore units calculated, we can calculate concentrations within pore throats edges ($c_{ij,k}$), using Equation (8.23).

8.3.3 Two sites kinetic adsorption

For a pore throat with two sites kinetic, the mass balance equation may be written as

$$\begin{aligned}V_{ij,k}\frac{d}{dt}\left(c_{ij,k}\right) = \left|q_{ij,k}\right| c_{CU,j} - \left|q_{ij,k}\right| c_{ij,k} - V_{ij,k}\alpha_{ij}^{sw}\left(K_{D,ij}^{sw}c_{_{ij,k}} - s_{ij,k}^{sw}\right) \\ - V_{ij,k}\alpha_{ij}^{aw}\left(K_{D,ij}^{aw}c_{ij,k} - s_{ij,k}^{aw}\right) \qquad (8.30)\end{aligned}$$

From this point, we drop the superscript of $t+\Delta t$, and only we show superscript for time t, such as $c_{ij,k}^{t}$. kinetic adsorption for corner k^{th} of a drained pore body may be written as

$$\frac{ds_{ij,k}^{\beta}}{dt} = \alpha_{ij}^{\beta}\left(K_{D,ij}^{\beta}c_{ij,k} - s_{ij,k}^{\beta}\right); \quad \beta = sw,\ aw \qquad (8.31)$$

solving for concentration of adsorbed mass

$$s_{ij,k}^{\beta} = \frac{\alpha_{ij}^{\beta}K_{D,ij}^{\beta}\Delta t}{1+\alpha_{ij}^{\beta}\Delta t}c_{ij,k} + \frac{1}{1+\alpha_{ij}^{\beta}\Delta t}s_{ij,k}^{\beta,t}; \quad \beta = sw,\ aw \qquad (8.32)$$

we substitute the Equation (8.32) into pore throat mass balance Equation (8.30) to get

$$\begin{aligned}V_{ij,k}\frac{\left(c_{ij,k} - c_{ij,k}^{t}\right)}{\Delta t} = q_{ij,k}\left(c_{_j} - c_{ij,k}\right) - \\ V_{ij,k}\alpha_{ij}^{sw}\left(K_{D,ij}^{sw}c_{ij,k} - \frac{\alpha_{ij}^{sw}K_{D,ij}^{sw}\Delta t}{1+\alpha_{ij}^{sw}\Delta t}c_{ij,k} - \frac{1}{1+\alpha_{ij}^{sw}\Delta t}s_{ij,k}^{sw,t}\right) \\ - V_{ij,k}\alpha_{ij}^{aw}\left(K_{D,ij}^{aw}c_{ij,k} - \frac{\alpha_{ij}^{aw}K_{D,ij}^{aw}\Delta t}{1+\alpha_{ij}^{aw}\Delta t}c_{ij,k} - \frac{1}{1+\alpha_{ij}^{aw}\Delta t}s_{ij,k}^{aw,t}\right) \qquad (8.33)\end{aligned}$$

solving for $c_{ij,k}$ and rearranging gives

$$c_{ij,k} = \frac{1}{B_{ij,k}}\left[\frac{q_{ij,k}\Delta t}{V_{ij,k}}c_{_j} + \frac{\Delta t\alpha_{ij}^{sw}}{1+\alpha_{ij}^{sw}\Delta t}s_{ij,k}^{sw,t} + \frac{\Delta t\alpha_{ij}^{aw}}{1+\alpha_{ij}^{aw}\Delta t}s_{ij,k}^{aw,t} + c_{_{ij,k}}^{t}\right] \qquad (8.34)$$

where

$$B_{ij,k} = 1 + \frac{q_{ij,k}\Delta t}{V_{ij,n}} + \Delta t\alpha_{ij}^{sw}K_{D,ij}^{sw} - \frac{\alpha_{ij}^{sw^2}K_{D,ij}^{sw}\Delta t^2}{1+\alpha_{ij}^{sw}\Delta t} + \Delta t\alpha_{ij}^{aw}K_{D,ij}^{aw} - \frac{\alpha_{ij}^{aw^2}K_{D,ij}^{aw}\Delta t^2}{1+\alpha_{ij}^{aw}\Delta t}$$

The mass balance equation for adsorptive transport within a corner unit of a drained pore body, with two sites kinetic, may be written as

$$V_{CU,i}\frac{d}{dt}\left(c_i\right) = \sum_{j=1}^{N_{in}^{tube}}\sum_{k=1}^{N_{edge}^{ij}} q_{ij,k}c_{ij,k} + \sum_{n=1}^{N_{in,edge}^{CU,i}} q_{CU,i,n}c_{CU,n} - Q_{CU,i}c_{CU,i} -$$

$$V_{CU,i}\alpha^{sw}_{CU,i}\left(K^{sw}_{D,i}c_{_{CU,i}} - s^{sw}_{CU,i}\right) - V_{CU,i}\alpha^{aw}_{CU,i}\left(K^{aw}_{D,i}c_{CU,i} - s^{aw}_{CU,i}\right) \qquad (8.35)$$

The kinetic adsorption for a corner unit may be written as

$$\frac{ds^{\beta}_{CU,i}}{dt} = \alpha^{\beta}_{CU,i}\left(K^{\beta}_{D,i}c_{CU,i} - s^{\beta}_{CU,i}\right); \quad \beta = sw,\ aw \qquad (8.36)$$

solving for concentration of adsorbed mass

$$s^{\beta}_{CU,i} = \frac{\alpha^{\beta}_{CU,i}K^{\beta}_{D,i}\Delta t}{1+\alpha^{\beta}_{CU,i}\Delta t}c_{CU,i} + \frac{1}{1+\alpha^{\beta}_{CU,i}\Delta t}s^{\beta,t}_{CU,i}; \quad \beta = sw,\ aw \qquad (8.37)$$

substituting for $s^{aw}_{CU,i}$ and $s^{sw}_{CU,i}$ in Equation (8.35), and solving for $c_{CU,i}$

$$\frac{B_iV_{CU,i}}{\Delta t}c_{CU,i} - \sum_{j=1}^{N_{in}^{tube}}\sum_{k=1}^{N_{edge}^{ij}} q_{ij,k}c_{ij,k} - \sum_{n=1}^{N_{in,edge}^{CU,i}} q_{CU,i,n}c_{CU,n} =$$

$$V_{CU,i}\left(\frac{\alpha^{sw}_{CU,i}}{1+\alpha^{sw}_{CU,i}\Delta t}s^{sw,t}_{CU,i} + \frac{\alpha^{aw}_{CU,i}}{1+\alpha^{aw}_{CU,i}\Delta t}s^{aw,t}_{CU,i}\right) + \frac{V_{CU,i}}{\Delta t}c^{t}_{CU,i} \qquad (8.38)$$

where

$$B_i = 1 + \frac{\Delta t Q_{CU,i}}{V_{CU,i}} + \Delta t\alpha^{sw}_{CU,i}K^{sw}_{D,i} - \frac{\alpha^{sw^2}_{CU,i}K^{sw}_{D,i}\Delta t^2}{1+\alpha^{sw}_{CU,i}\Delta t} + \Delta t\alpha^{aw}_{CU,i}K^{aw}_{D,i} - \frac{\alpha^{aw^2}_{CU,i}K^{aw}_{D,i}\Delta t^2}{1+\alpha^{aw}_{CU,i}\Delta t}$$

substituting for cij,k in Equation (8.38) and rearranging to have all the unknowns on the l.h.s and knows on the r.h.s, the final form of system of equations to be solved for the concentrations within corner units is

$$\begin{aligned}&\frac{B_{CU,i}V_{CU,i}}{\Delta t}c_{CU,i} - \sum_{j=1}^{N_{in}^{tube}}\sum_{k=1}^{N_{edge}^{ij}} \frac{q_{ij,k}^2\Delta t}{B_{ij,k}V_{ij,k}} c_{CU,j} - \sum_{n=1}^{N_{in,edge}^{CU,i}} q_{CU,i,n}c_{CU,n} = \\ &\sum_{j=1}^{N_{in}^{tube}}\sum_{k=1}^{N_{edge}^{ij}} q_{ij,k}\frac{1}{B_{ij,k}}\left(\frac{\Delta t\alpha_{ij}^{sw}}{1+\alpha_{ij}^{sw}\Delta t}s_{ij,k}^{sw,t} + \frac{\Delta t\alpha_{ij}^{aw}}{1+\alpha_{ij}^{aw}\Delta t}s_{ij,k}^{aw,t} + c_{ij,k}^t\right)+ \\ &V_{CU,i}\left(\frac{\alpha_{CU,i}^{sw}}{1+\alpha_{CU,i}^{sw}\Delta t}s_{CU,i}^{sw,t}+\frac{\alpha^{aw}_{CU,i}}{1+\alpha^{aw}_{CU,i}\Delta t}s^{aw,t}_{CU,i}\right)+\frac{V_{CU,i}}{\Delta t}c^t_{CU,i}\end{aligned} \tag{8.39}$$

having concentration of the pore units calculated, we can calculate concentrations within pore throat edges ($c_{ij,k}$), using Equation (8.34). Equation (8.32) can be used to calculate the adsorbed mass concentrations, $s_{ij,k}^{sw}$ and $s_{ij,k}^{aw}$, in pore throat edges, and Equation (8.37) can be used to calculate the adsorbed mass concentrations, $s_{CU,i}^{sw}$ and $s_{CU,i}^{aw}$, in corner units.

8.3.4 One site equilibrium and one site kinetic adsorption

The following formulation is for a drained pore, in which the adsorption is kinetic at either SW or AW interface, and is equilibrium at the other interface. The mass balance equation for k^{th} edge of a drained pore throat may be written as

$$\begin{aligned}V_{ij,k}\frac{d}{dt}\left(c_{ij,k}\right) = &\left|q_{ij,k}\right| c_{CU,j} - \left|q_{ij,k}\right| c_{ij,k} - V_{ij,k}\alpha_{ij,k}^{\beta}\left(K_{D,ij,k}^{\beta}c_{ij,k} - s_{ij,k}^{\beta}\right) - \\ &V_{ij,k}K_{D,ij,k}^{\alpha}\frac{d}{dt}\left(c_{ij,k}\right)\end{aligned} \tag{8.40}$$

where $K_{D,ij}^{\beta}$, $\beta = sw$ or aw shows the interface at which kinetic adsorption occurs, and $K_{D,ij}^{\alpha}$, $\alpha = sw$ or aw is the distribution coefficient for the interface with equilibrium adsorption. The mass balance equation for adsorbed mass due to kinetic adsorption is similar to Equation (8.31). Substitution for $s_{ij,k}^{\beta}$ in mass balance equation for the pore throat, and solving for $c_{ij,k}$, we get

$$c_{ij,k} = \frac{1}{B_{ij,k}}\left(\frac{q_{ij,k}\Delta t}{V_{ij,k}\left(1+K_{D,ij}\right)}c_j + \frac{\Delta t\alpha_{ij}^{\beta}}{\left(1+K_{D,ij}\right)\left(1+\alpha_{ij}^{\beta}\Delta t\right)}s_{ij,k}^{\beta,t} + c_{ij,k}^t\right) \tag{8.41}$$

where B_{ij} is defined as

$$B_{ij} = 1 + \frac{q_{ij,k}\Delta t}{V_{ij,k}\left(1+K_{D,ij}\right)} + \frac{\Delta t \alpha_{ij}^{\beta} K_{D,ij}^{\beta}}{\left(1+K_{D,ij}\right)} + \frac{\Delta t^2 \alpha_{ij}^{\beta^2} K_{D,ij}^{\beta^2}}{\left(1+K_{D,ij}\right)\left(1+\alpha_{ij}^{\beta}\Delta t\right)}$$

The mass balance equation for a corner unit within a drained pore body, with one site kinetic and one site equilibrium, may be written as

$$\begin{aligned} V_i \frac{d}{dt}\left(c_{CU,i}\right) = {} & \sum_{j=1}^{N_{in}^{tube}} \sum_{k=1}^{N_{ij}^{edge}} q_{ij,k} c_{ij,k} + \sum_{n=1}^{N_{in,edge}^{CU,i}} q_{i,n} c_{CU,n} - Q_{CU,i} c_{CU,i} \\ & - V_{CU,i} \alpha_{CU,i}^{\beta} \left(K_{D,i}^{\beta} c_{CU,i} - s_{CU,i}^{\beta}\right) \\ & - V_{CU,i} K_{D,i}^{\alpha} \frac{d}{dt}\left(c_{CU,i}\right) \end{aligned} \tag{8.42}$$

The mass balance equation for adsorbed mass due to kinetic adsorption, $s_{CU,i}^{\beta}$, is similar to Equation (8.36). Substitution for $s_{CU,i}^{\beta}$ in mass balance equation for the pore throat, and solving for $c_{CU,i}$ results in

$$\begin{aligned} & c_{CU,i} = \\ & - \frac{\Delta t Q_{CU,i}}{V_{CU,i}\left(1+K_{D,i}\right)} c_{CU,i} + \frac{\Delta t}{V_{CU,i}\left(1+K_{D,i}\right)} \sum_{j=1}^{N_{in}^{tube}} \sum_{k=1}^{N_{ij}^{edge}} q_{ij,k} c_{ij,k} \\ & + \frac{\Delta t}{V_{CU,i}\left(1+K_{D,i}\right)} \sum_{n=1}^{N_{in,edge}^{CU,i}} q_{i,n} c_{CU,n} \\ & - \frac{\Delta t \alpha_{CU,i}^{\beta}}{\left(1+K_{D,i}\right)} \left(K_{D,i}^{\beta} c_{CU,i} - \frac{\alpha_{CU,i}^{\beta} K_{D,i}^{\beta} \Delta t}{1+\alpha_{CU,i}^{sw}\Delta t} c_{CU,i} - \frac{1}{1+\alpha_{CU,i}^{sw}\Delta t} s_{CU,i}^{sw,t}\right) + c_{CU,i}^{t} \end{aligned} \tag{8.43}$$

where B_i is defined as

$$B_i = 1 + \frac{\Delta t Q_i}{V_i\left(1+K_{D,i}\right)} + \frac{\Delta t \alpha_i^{\beta} K_{D,i}^{\beta}}{\left(1+K_{D,i}\right)} - \frac{\alpha_i^{\beta^2} \Delta t^2 K_{D,i}^{\beta}}{\left(1+\alpha_i^{\beta}\Delta t\right)\left(1+K_{D,i}\right)}$$

substituting for $c_{ij,k}$ (Equation 8.41) in Equation (8.43), we get

$$\frac{V_{CU,i}\left(1+K_{D,i}\right)B_i}{\Delta t}c_{CU,i} =$$
$$\sum_{j=1}^{N_{in}^{tube}}\sum_{k=1}^{N_{in}^{edge}} q_{ij,k}\frac{1}{B_{ij,k}}\left(\frac{q_{ij,k}\Delta t}{V_{ij,k}\left(1+K_{D,ij}\right)}c_{CU,j} + \frac{\Delta t\alpha_{ij}^{\beta}}{\left(1+K_{D,ij}\right)\left(1+\alpha_{ij}^{\beta}\Delta t\right)}s_{ij,k}^{\beta,t} + c_{ij,k}^{t}\right)$$
$$+\sum_{n=1}^{N_{in,edge}^{CU,i}} q_{i,n}c_{CU,n} - \frac{V_{CU,i}\alpha_{CU,i}^{\beta}}{\left(1+\alpha_{CU,i}^{sw}\Delta t\right)}s_{CU,i}^{sw,t} + \frac{V_{CU,i}\left(1+K_{D,i}\right)}{\Delta t}c_{CU,i}^{t} \qquad (8.44)$$

Rearranging Equation (8.44) and collecting unknowns on the l.h.s. and know terms on the r.h.s, we obtain the final form of system of equations to be solved for the concentrations within corner units

$$\frac{V_{CUi}\left(1+K_{D,i}\right)B_i}{\Delta t}c_{CU,i} - \sum_{j=1}^{N_{in}^{tube}}\sum_{k=1}^{N_{edge}^{ij}}\frac{q_{ij,k}^{2}\Delta t}{B_{ij,k}V_{ij,k}\left(1+K_{D,ij}\right)}c_{CU,j}$$
$$-\sum_{n=1}^{N_{in,edge}^{CU,i}} q_{i,n}c_{CU,n} = -\frac{V_{CU,i}\alpha_{CU,i}^{\beta}}{\left(1+\alpha_{CU,i}^{sw}\Delta t\right)}s_{CU,i}^{sw,t} + \frac{V_{CU,i}\left(1+K_{D,i}\right)}{\Delta t}c_{CU,i}^{t}$$
$$\sum_{j=1}^{N_{in}^{tube}}\sum_{k=1}^{N_{edge}^{ij}}\frac{q_{ij,k}}{B_{ij,k}}\left(\frac{\Delta t\alpha_{ij}^{\beta}}{\left(1+K_{D,ij}\right)\left(1+\alpha_{ij}^{\beta}\Delta t\right)}s_{ij,k}^{\beta,t} + c_{ij,k}^{t}\right) \qquad (8.45)$$

having concentration of the pore units calculated, we can calculate concentrations within pore throat edges ($c_{ij,k}$), using Equation (8.41).

CHAPTER 9

SUMMARY AND CONCLUSIONS

> *If I have seen further than others, it is by standing upon the shoulders of giants.*
>
> *Isaac Newton*

THE focus of this research was to identify and describe the physical/chemical processes that govern the transport of both passive and reactive/adsorptive solutes in porous media by using pore network modeling. We consider transport of reactive/adsorptive solutes under both saturated and partiality saturated conditions. While under saturated conditions the interfaces are only those of solid-water interfaces, under saturated conditions in addition to solid-water interfaces there will be mass transfer though air-water interfaces as well.

We developed an extensive FORTRAN 90 modular package whose capabilities include the generation of random structure networks, simulation of drainage process, the discretization of pore spaces on the basis of saturation state of each pore, and solving flow and reactive transport under both saturated and unsaturated conditions, using several complex algorithms. The governing equations are solved applying a fully implicit numerical scheme; however, efficient substitution methods have been applied to make the algorithm more computationally effective and appropriate for parallel computations.

Through this study we have tried to address some fundamental issues regarding flow and transport of (reactive/adsorptive) solute in porous media. Specific issues addressed in the work could be categorized into three parts: I) generation of a Multi-Directional Pore Network (MDPN); II) upscaling under saturated conditions; and III) upscaling under partially-saturated conditions.

Part I: Generation of a Multi-Directional Pore Network (MDPN)

Chapter 2 presented a method to construct a Multi-Directional Pore Network (MDPN) model. In to this technique, the continuum pore space domain is discretized into a network of pore bodied and pore throats. The multi-directional capability of the MDPN allows a distribution of coordination number ranging between zero and 26, with pore throats orientated in 13 different directions, rather than the only 3 directions commonly applied in pore network studies. The results of Chapter 2 indicate that the MDPN model can provide a better way to reconstruct a porous medium. Construction of the MDPN is optimized using a Genetic Algorithm (GA) method and the morphological characteristics of such a networks are compared with those of physically based real sandstone and granular samples through utilizing information on their coordination number distributions. Good agreement was found between simulation results and observation data on coordination number distribution, number of pore bodies and pore throats, and average coordination number. Throughout this thesis, MDPN has been used as the network model to simulate fluid flow and transport of solutes. We have shown the capability of MDPN in producing a more accurate velocity field, which is essential in determining upscaled parameters such as (relative) permeability or (unsaturated) dispersions coefficients.

Part II: Upscaling under saturated conditions

Part II (Chapters 3 and 4) of the dissertation deals with pore-scale modeling and upscaling of adsorptive transport under saturated conditions.

Chapter 3 deals with the upscaling of adsorptive solute transport from the micro scale to the effective pore scale. Here, we assumed micro scale equilibrium adsorption, which means that concentration of adsorbed solute at a point on the grain surface is algebraically related to the concentration in solution next to the grain surface. We utilized two approaches; theoretical averaging and numerical upscaling. In the averaging approach, equilibrium adsorption was assumed at the pore-scale and solute transport equations are averaged over REV. This leads to explicit expressions for macro-scale adsorption rate constants as a function of micro-scale parameters such as pore scale Peclet number and the pore scale distribution coefficient. Our results indicate that, due to concentration gradients developed within the pore space, equilibrium adsorption may not hold at larger scales where average concentrations are applied. A major result of Chapter 3 is that we developed relationships between pore-scale adsorption coefficient and corresponding upscaled attachment and detachment adsorption parameters. The upscaled adsorption parameters are found to be only weak functions of velocity; they strongly depend on geometry of the pore and diffusion coefficient in the solution as well as the pore-scale distribution coefficient. Results of two approaches (i.e., theoretical averaging and numerical upscaling) agree very well. The upscaling relations from this chapter are appropriate to be used within models in which subpore scale concentration gradients are neglected.

Chapter 4 continues the upscaling process, going from effective pore scale to the core scale where Darcy-scale flow and transport parameters are applied. This is done by utilizing the upscaling relations developed in Chapter 3 and applying them to the MDPN model developed in Chapter 2. This enabled us to scale up from a simplified but reasonable representation of microscopic physics to the scale of interest in practical applications. This procedure has resulted in relationships for core scale adsorption parameters in terms of micro-scale parameters. We found relations between core-scale adsorption parameters and local-scale transport coefficients, including molecular diffusion coefficient, specific surface area, and average pore-throat size. Results of Chapter 4 show that, even if there is equilibrium adsorption at the pore wall (i.e., grain surface), one may need to employ a kinetic description at the larger scales. In contrast to some other studies that reported dependency of reaction parameters on flow rate, we found that that these upscaled kinetic parameters are only a weak function of velocity.

Part III: Upscaling under partially-saturated conditions

Part III (Chapters 5 through 7) deal with pore-scale modeling of adsorptive transport under partially saturated conditions.

Chapter 5 presents a new formulation for pore-network modeling of two-phase flow. Pore-network models of two-phase flow in porous media are widely used to investigate constitutive relationships between saturation and relative permeability as well as capillary pressure. Results of many studies show discrepancy between calculated relative permeability and corresponding measured values. An important feature of almost all pore-network models is that the resistance to flow is assumed to come from pore throats only; i.e., the resistance of pore bodies to the flow is considered to be negligible compare to the resistance of pore throats. We have shown that the resistance to the flow within filaments of fluids in drained pore bodies is comparable to the resistance to the flow within (drained) pore throats. In this chapter, we present a new formulation for pore-network modeling of two-phase flow, which explicitly accounts for the resistant to the flow within the drained pore bodies and calculates different fluxes within drained pore bodies. The results of Chapter 5 shows the significance of this effect under primary drainage conditions, by applying our formulation into a MDPN model. Resulting saturation-relative permeability relationships, with taking account the resistance due to the drained pore bodies, show a better agreement with experimentally measured values. The difference obtained using our method could be considerable especially at higher saturations when larger pore bodies are getting invaded by the non-wetting phase. We have also examined the concept of equivalent pore conductance and compared the results with our method. The comparison shows that making the correction terms for conductances of pore throats as a function of saturation can improve the results, however, using the concept of equivalent pore conductance, we do not solve for fluid flow within pore bodies. In this way, we do not get information on fluxes within pore bodies. This information is needed for an accurate simulation of solute transport, where because of the presence of non-wetting phase, there is limited mixing within the pore bodies.

Chapter 6 intended to study dispersion coefficient under partially saturated conditions using a new formulation. It is known that in unsaturated porous media, the dispersion coefficient depends on the Darcy velocity as well as saturation. The dependency of dispersion on velocity is fairly studied, however, there is not much known about its dependence on saturation and the underlying process. The purpose of this chapter is to investigate how the longitudinal dispersivity varies with saturation. In our formulation, both pore bodies and pore throats have volumes and we assign separate concentrations to each of them. Further, since pore geometry and corner flows greatly influence transport properties, efforts are made to include different angular cross sectional shapes for the pore throats. This includes circular, rectangular, and all kind of irregular triangular cross sections, which are important especially under unsaturated/two-phase flow and reactive transport. We have introduced a new formulation of solute transport within pore network which helps to capture the effect of limited mixing under partially-saturated conditions. In this formulation we refine the discretization on the basis of saturation state of pores. We assign separate concentration for different corners of a given drained pore body and also we assign different concentrations for different edges of a drained angular pore throat. This formulation allows a very detailed description of pore-scale solute transport processes by accounting for limitations in mixing as a result of reduced water content. The numerically computed dispersivities could successfully explain the results obtained through experimental studies, and shows the underplaying pore scale processes contributing to dispersion under unsaturated conditions. Results of Chapter 6 show that, under partially saturated conditions, dispersivity coefficient is strongly depended on saturation. The relation could be non-monotonic, with the maximum dispersivity (α_{max}) corresponding to a specific saturation, which we refer to it as the critical saturation (S_{cr}). We could explain the $\alpha - S_w$ relation by investigating pore-scale properties such as fraction of percolating saturated pores and coefficient of variation of pore velocities under different saturations. These pore scale observations could clearly explain the relation between solute dispersivity and saturation under partially saturated conditions. We have shown that saturation-relative permeability ($k_r - S_w$) curve may be utilized to get insight into the behavior of $\alpha - S_w$ curve and to approximate the critical saturation at which the maximum dispersivity (α_{max}) occurs.

Chapter 7 is specified to transport of adsorptive solute under partially saturated conditions. Under partially saturated conditions, the system contains three phases: air, water, and solid. The principal interactions usually occur at the solid-water interfaces (SW) and air-water interfaces (AW), thus greatly influenced by water content. All of the modeling capabilities which were implemented through last chapters are also included in this chapter. In addition, we have formulated various types of adsorption such as i) two site (SW and AW interfaces) kinetic, ii) two site equilibrium, and iii) one site (SW or AW interfaces) kinetic and one site equilibrium. For the macro scale representation of equilibrium adsorptive transport, we have chosen two models: Advection-Dispersion Equation (ADE) with equilibrium adsorption term and Mobile-Immobile Model (MIM) which models the non-equilibrium transport. Comparing the results from analytical solutions of these two macro-scale models with the results obtained from pore network model show that the Mobile-Immobile Model (MIM) provides a better fit to the results of the pore network modeling. Applying equilibrium macro-scale model (ADE), we need to apply higher values of dispersivity which in addition to saturation will depend on the value of pore scale adsorption coefficient. However, using MIM we could use the dispersion coefficients which were independently determined through tracer simulations to simulate adsorptive transport. The results of this chapter show that, even if there is equilibrium adsorption at the solid-water (SW) and air-water (AW) interfaces at the pore scale, one may need to use a so called non-equilibrium description of adsorptive process at the macro scale.

Appendices

A. Search algorithm in Multi-Directional Pore Network (MDPN) model

In order to find the isolated clusters, we need to employ tracking.We have employed an algorithm based on the frequency of bonds. In order to illustrate the procedure, considering the network of Figure (2.2), we randomly eliminated some bonds by changing the states of them from open to block in the connection matrix of Figure (2.2). Figure (A.1) shows the network configuration after this random elimination.

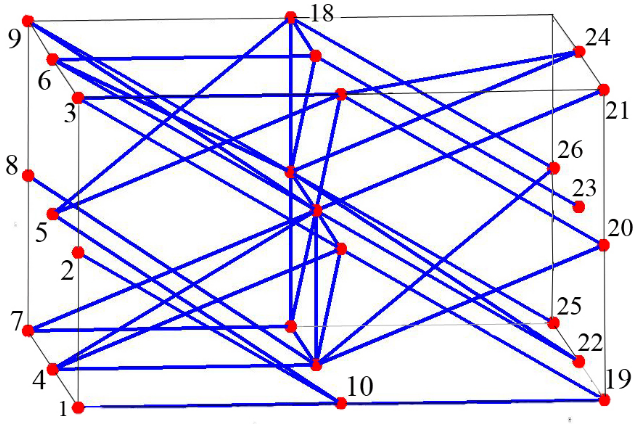

Figure A.1: A network of size: $N_i = 3, N_j = 3, N_k = 3$ after random elimination. Site numbers are shown for some nodes; system of numbering is the same as in Fig. 1. $N_{bond} = 42, N_{site} = 26$.

The connection matrix is a sparse matrix. Hence, we convert it in to compact form. This results in a matrix of the size $3N_{bond}$ (N_{bond} =number of bonds). Table A.1 shows the corresponding compact matrix for upper triangle part of connection matrix belonging to Figure (A.1). In the compact form shown in Table A.1, the first row (ROW in Table A.1) contains the row index of original sparse matrix, the second row (COL) contains the column index, and the third row (Entry) contains the corresponding nonzero direction numbers. Since this is compact form of connection matrix, it means that site numbers in ROW are connected in the forward direction to site numbers in COL. For example, first column of Table A.1 indicates that site number 1 is connected in the forward direction to site number 10 along lattice direction number 1.

Table A.1: Compact form of connection matrix for example of Figure (A.1).

ROW	1	2	3	3	4	4	4	5	5	5	6	6	6	7	7	8	9	9	10	11	11
COL	10	10	12	11	13	11	14	10	12	18	15	17	14	16	14	13	14	17	19	14	19
Entry	1	11	1	11	1	8	10	6	8	9	1	7	11	1	8	6	6	11	1	3	11
ROW	11	12	12	12	13	13	13	13	14	14	14	14	15	15	15	16	17	17	17	17	18
COL	13	24	20	14	14	16	20	26	17	21	22	16	18	23	17	17	18	22	24	25	26
Entry	13	4	11	13	2	3	8	9	3	8	11	13	3	11	13	2	2	6	8	11	11

Table A.2: Frequency and cumulative matrix of the forward connections.

Site no.	1	2	3	4	5	6	7	8	9	10	11	12	13	14
Frequency	1	1	2	3	3	3	2	1	2	1	3	3	4	4
Cumulative	1	2	4	7	10	13	15	16	18	19	22	25	29	33
Site no.	15	16	17	18	19	20	21	22	23	24	25	26	27	
Frequency	3	1	4	1	0	0	0	0	0	0	0	0	0	
Cumulative	36	37	41	42	42	42	42	42	42	42	42	42	42	

As we can see, the site numbers in the first row(ROW) of Table are sorted in increasing order. The number of times a site number appears in ROW of Table A.1 corresponds to the number of forward connections of that site. This information in taken up in a frequency table (see second row of Table A.2) together with its cumulative number of bonds (see third row of Table A.2).
Table A.2 along with second row of Table A.1 can be used to determine to which sites a given site, N, is connected based on the following formula:
Forward sites
for site N $= COL(cumulative(N) - frequency(N) + 1 : cumulative(N))$
For example, for site number 12 $(N = 12)$ we will have:
Forward sites
for site 12 $= COL(cumulative(12) - frequency(12) + 1 : cumulative(12))$
$= COL(25 - 3 + 1 : 25) = COL(23 : 25) = [24, 20, 14]$
Hence, the sites to which site number 12 is connected forward are located in position 23 – 25 in the COL of Table A.1 which are sites number 24, 20, and 14.
To find the backward connections, we need to replace ROW and COL of Table A.1 with each other (since in the connection matrix backward connections are

transpose of forward connections) and then sort the matrix in this new ROW and next calculate the frequency vector in the same manner as before. For example, for site 12, we will find that backward sites for site 12 are sites 3 and 5. Hence, site number 12 is connected overall to sites number 24, 20, 14, 3, and 5. In the next step, we can apply this formula again for each of these sites to find their connections and repeat this tracking. These sites together are one group. At the end, if there is at least one site from right boundary in this group, it means the sites belonging to this group are not isolated clusters; on the other hand, they are isolated clusters and we should delete the whole group from connection matrix.

It is worth mentioning that after construction of frequency vectors (for forward and backward directions) no longer we need ROW in Table A.1. Also we do not need to record entry because if we know the connection of two sites then we can calculate the direction number according to formulas in Table (2.1) to see which of the formulas in Table (2.1) can produce this connection.

B. Connections in a Multi-Directional Pore Network (MDPN) model

As it was mentioned in section 2.2, in a MDPN model a maximum of 26 pore throats may be connected to a pore body. As shown in Figure B.1, for a cubic pore body, three kinds of connections can be distinguished: (a) 8 connections to the corners (we refer to them as corner pore throats), (b) 12 connections to the edges (edge pore throats), and (c) 6 connections to the faces of the pore body (face pore throats). All these three types of connections are shown in Figure B.1d.

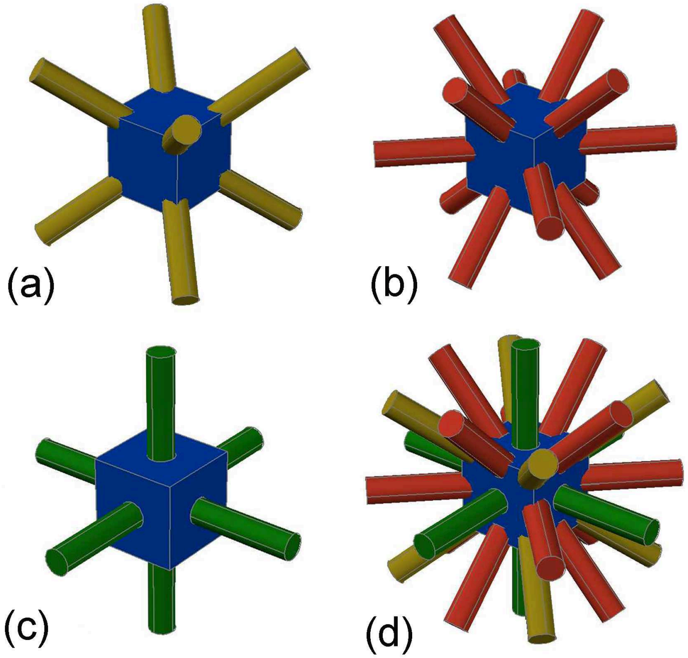

Figure B.1: Different types of connections that pore throats can be connected to a pore body; which are: (a) 8 connections to the corners, (b) 12 connections to the edges, and (c) 8 connections to the faces of pore body. The combination of all types of connections is also shown (d).

Of course, many of these connection will be eliminated in order to obtain a desired coordination number distribution [Raoof and Hassanizadeh, 2009]. When a pore body is invaded by the non-wetting phase, we assign 8 different pressures to its 8 corner elements. So, in order to be able to calculate the flow of wetting phase in the pore network, we should decide which corners of neighboring pore bodies are connected by the pore throats. In the case of corner pore throat, as shown in Figure B.1a, this is straightforward as it connects the corners of pore bodies. In the case of edge or face pore throats, shown in figures B.1b and B.1c, respectively, we assume that they connect corners of neighboring pore bodies to each other. The question is which corners do they connect. We have done this though a random processes. For example, in Figure B.2, face pore throat number 1 connects the faces of pore bodies A and B. Through a random process, we assign the A-end of pore throat 1 to be connected to one of the corners a, b, c, or d. the same will be done for the B-end of the pore throat 1. As a result, pore throat number 1 will be assumed to be connecting one corner of pore body A to one corner of pore body B. A similar process is applied to pore throat number 2 in Figure B.2, which is an edge pore throat; one end will be assigned to corner b or d, and the other end will be assigned to corner f or e. At the end of this process, all pore throats are assigned to the corners of pore bodies.

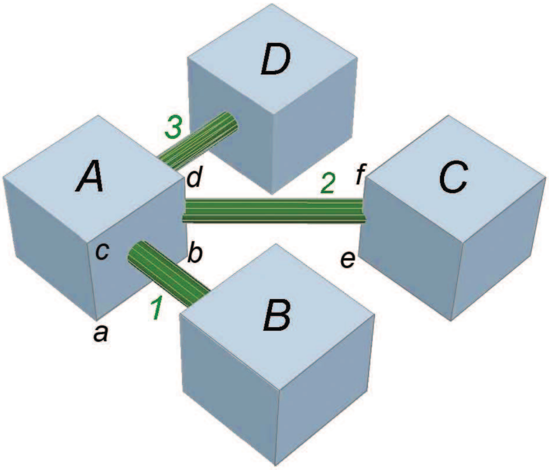

Figure B.2: An example of connections of pore throats (designated by numbers) to pore bodies (designated by capital letters). Pore body corners are shown using small letters. To keep the Figure less crowded, only three pore throats are shown.

C. Averaging of pore-scale transport equation

To upscale Equation (3.1), we need to integrate it over V^f. To do so, we need averaging theorems which relate the average of a derivative to the derivative of the average. These are called averaging theorems:
Special Averaging Theorem:

$$\begin{aligned}\frac{1}{V}\int\limits_{V^f} \nabla\cdot\left(c^i v\right)dV &= \nabla\cdot\left[\frac{1}{V}\int\limits_{V^f} c^i v dV\right] + \frac{1}{V}\int\limits_{A^{fs}} c^i v.n dA \\ &= \nabla\cdot\left(\overline{c^i v}\right) + \frac{1}{V}\int\limits_{A^{fs}} c^i v\cdot n dV \qquad \text{(C.1)}\end{aligned}$$

Time Averaging Theorem:

$$\begin{aligned}\frac{1}{V}\int\limits_{V^f} \frac{\partial c^i}{\partial t}dV &= \frac{\partial}{\partial t}\left[\frac{1}{V}\int\limits_{V^f} c^i dV\right] - \frac{1}{V}\int\limits_{A^{fs}} c^i w\cdot n dA \\ &= \frac{\partial \bar{c}^i}{\partial t} - \frac{1}{V}\int\limits_{A^{fs}} c^i w\cdot n dA \qquad \text{(C.2)}\end{aligned}$$

where w is the velocity of the solid-fluid interface. If the porous medium is rigid, then w will be identically zero.

integrating Equation (3.1) over V^f and dividing by V to obtain

$$\frac{1}{V}\int\limits_{V^f}\left[\frac{\partial c^i}{\partial t} + \nabla\cdot\left(c^i v\right)\right]dV + \frac{1}{V}\int\limits_{V^f}\nabla\cdot j^i dV = \frac{1}{V}\int\limits_{A^f}\widehat{r}^i dV \qquad \text{(C.3)}$$

application of the averaging theorems to the integrals on the l.h.s. and employment of the averaging definitions yields

$$\frac{\partial n\bar{c}^i}{\partial t} + \nabla\cdot\left(\overline{c^i v}\right) + \nabla.\left(n\bar{j}^i\right) = n\bar{r}^i - \frac{1}{V}\int\limits_{A^{fs}}\left[\mathrm{c}^{\mathrm{i}}\left(v-w\right) + j^i\right]\cdot n dA \qquad \text{(C.4)}$$

the total pore-scale advective flux $\overline{c^i v}$ may be broken into two parts: a macro-scale advective flux $n\bar{c}^i\bar{v}$ and a macro-scale dispersive flux $\overline{nc^i\widetilde{v}}$ where $\widetilde{v}$ denotes the deviation of flow velocity at a pore-scale point within a pore from the average velocity:

$$\widetilde{v} = v - \overline{v} \tag{C.5}$$

The term $n\overline{c^i\widetilde{v}}$ represents the mixing of the solute within an REV as a result of pore-scale velocity fluctuations within the pores. Together with the diffusive flux $n\overline{j}^i$, it is known as macro-scale hydrodynamic dispersion and is denoted by J^i

$$J^i = n\overline{c^i\widetilde{v}} + n\overline{j}^i \tag{C.6}$$

substituting Equation (C.6) into Equation (C.4), the final form of averaged mass transport equation is obtained

$$\frac{\partial n\overline{c}^i}{\partial t} + \nabla \cdot \left(n\overline{c}^i\overline{v}\right) + \nabla \cdot \left(n\overline{J}^i\right) = n\overline{r}^i - \frac{1}{V}\int\limits_{A^{fs}} \left[c^i\left(v-w\right) + j^i\right] \cdot ndA \tag{C.7}$$

REFERENCES

L.M. Abriola and G.F. Pinder. A multiphase approach to the modeling of porous media contamination by organic compounds: 1. Equation development. *Water Resources Research*, 21(1):11–18, 1985. 4

R.C. Acharya, S.E. van der Zee, and A. Leijnse. Porosity-permeability properties generated with a new 2-parameter 3D hydraulic pore-network model for consolidated and unconsolidated porous media. *Advances in Water Resources*, 27(7):707–723, 2004. 35, 73

R.C. Acharya, S. van der Zee, and A. Leijnse. Transport modeling of nonlinearly adsorbing solutes in physically heterogeneous pore networks. *Water Resources Research*, 41(2):W02020, 2005a. 93, 136, 142, 162, 179

R.C. Acharya, S. van der Zee, and A. Leijnse. Transport modeling of nonlinearly adsorbing solutes in physically heterogeneous pore networks. *Water Resources Research*, 41(2):W02020, 2005b. 6, 43, 68, 69

R.C. Acharya, A.J. Valocchi, C.J. Werth, and T.W. Willingham. Pore-scale simulation of dispersion and reaction along a transverse mixing zone in two-dimensional porous media. *Water Resources Research*, 43(10):W10435, 2007a. 68

R.C. Acharya, M.I.J. van Dijke, K.S. Sorbie, S. van der Zee, and A. Leijnse. Quantification of longitudinal dispersion by upscaling brownian motion of tracer displacement in a 3d pore-scale network model. *Advances in Water Resources*, 30(2): 199–213, 2007b. 178

P.M. Adler. *Porous Media: Geometry and Transports.* Butterworth-Heinemann, 1992. 93

S. Akratanakul, L. Boersma, and G.O. Klock. Sorption processes in soils as influenced by pore water velocity: 2. experimental results. *Soil Science*, 135(6):331, 1983. 67

A.S. Al-Kharusi and M.J. Blunt. Network extraction from sandstone and carbonate pore space images. *Journal of Petroleum Science and Engineering*, 56(4):219–231, 2007. 116

A.S. Al-Kharusi and M.J. Blunt. Multiphase flow predictions from carbonate pore space images using extracted network models. *Water Resources Research*, 44(6), 2008. 95, 111, 116, 117, 122

Blunt M.J. Al-Kharusi, A.S. Permability prediction and network extraction from pore space images. *CMWR XVI Compitational Methods in Water Resources*, 2006. URL `http://proceedings.cmwr-xvi.org/contributionDisplay.py?contribId=293&sessionId=9&confId=a051`. 34, 36

R.I. Al-Raoush and C.S. Willson. A pore-scale investigation of a multiphase porous media system. *Journal of Contaminant Hydrology*, 77(1-2):67–89, 2005. 23

L. Algive, S. Bekri, M. Robin, and O. Vizika. Reactive transport: Experiments and pore-network modelling. In *Paper SCA2007-10 presented at the International Symposium of the Society of Core Analysts, Calgary, Canada*, pages 10–12, 2007a. 162

L. Algive, S. Bekri, M. Robin, and O. Vizika. Reactive transport: Experiments and pore-network modelling. In *Paper SCA2007-10 presented at the International Symposium of the Society of Core Analysts, Calgary, Canada*, pages 10–12, 2007b. 70

V. Ambegaokar, B.I. Halperin, and J.S. Langer. Hopping conductivity in disordered systems. *Physical Review B*, 4(8):2612–2620, 1971. 30

R. Aris. A. On the dispersion of a solute in a fluid flowing through a tube. *Process Systems Engineering*, 1:109–120, 1999. 43, 57

C.H. Arns, M.A. Knackstedt, W.V. Pinczewski, and WB Lindquist. Accurate computation of transport properties from microtomographic images. *Geophysical Research Letters*, 28(17):3361–3364, 2001. 94

C.H. Arns, M.A. Knackstedt, and K.R. Mecke. Reconstructing complex materials via effective grain shapes. *Physical Review Letters*, 91(21):215506, 2003a. 94

J.Y. Arns, C.H. Arns, A.P. Sheppard, R.M. Sok, M.A. Knackstedt, and W. Val Pinczewski. Relative permeability from tomographic images; effect of correlated heterogeneity. *Journal of Petroleum Science and Engineering*, 39(3-4): 247–259, 2003b. 95, 118

J.Y. Arns, V. Robins, A.P. Sheppard, R.M. Sok, WV Pinczewski, and M.A. Knackstedt. Effect of network topology on relative permeability. *Transport in Porous Media*, 55(1):21–46, 2004. 7, 21, 22, 28, 32, 95, 118

J.L. Auriault and J. Lewandowska. Diffusion/adsorption/advection macrotransport in soils. *European Journal of Mechanics. A. Solids*, 15(4):681–704, 1996. 45

K. Aziz and A. Settari. *Petroleum Reservoir Simulation.* Chapman & Hall, 1979. 4

Y. Bachmat and J. Bear. Macroscopic Modelling of Transport Phenomena in Porous Media. 1: The Continuum Approach. *Transport in Porous Media*, 1(3):213–240, 1986. 47

Y. Bachmat and J. Bear. On the concept and size of a representative elementary volume (REV). *Advances in Transport Phenomena in Porous Media. NATO Advanced Study Institute on Fundamentals of Transport Phenomena in Porous Media Series E*, 128:3–19, 1987. 47

S. Bakke and P.E. Øren. 3-D pore-scale modelling of sandstones and flow simulations in the pore networks. *Society of Petroleum Engineers*, 2(2):136–149, 1997. 21

J. Bear. Dynamics of Fluids in Porous Media, 764 pp, 1972. 3, 126, 127, 141, 145, 169, 178

J. Bear. Dynamics of Fluids in Porous Media. *Courier Dover, New York*, 1988. 47, 74, 96, 102, 133, 139

J. Bear and H.D.C. Alexander. *Modeling Groundwater Flow and Contaminant Transport.* Springer Verlag, 2008. ISBN 1402066813. 127, 149

R. Berker. Handbuch der Physik, Bd VIII. *Springer Verlag*, 1963. 103

B. Berkowitz and I. Balberg. Percolation theory and its application to groundwater hydrology. *Water resources research*, 29(4):775–794, 1993. 93

B. Berkowitz and R.P. Ewing. Percolation theory and network modeling applications in soil physics. *Surveys in Geophysics*, 19(1):23–72, 1998. 30

K.J. Beven and P.C. Young. An aggregated mixing zone model of solute transport through porous media. *Journal of Contaminant Hydrology*, 3(2-4):129–143, 1988. 148

P.J. Binning and M.A. Celia. Pseudokinetics arising from the upscaling of geochemical equilibrium. *Water Resources Research*, 44(7):W07410, 2008. 43, 70

M. Blunt, M.J. King, and H. Scher. Simulation and theory of two-phase flow in porous media. *Physical Review A*, 46(12):7680–7699, 1992. 20

M.J. Blunt. Flow in porous media–pore-network models and multiphase flow. *Current Opinion in Colloid & Interface Science*, 6(3):197–207, 2001. 5, 6, 68

M.J. Blunt, D.H. Fenwick, and D. Zhou. What determines residual oil saturation in three-phase flow? In *Society of Petroleum Engineers/Dept. of Energy; Improved Oil Recovery Symposium*, 1994. 20

G.H. Bolt. Movement of solutes in soil: principles of adsorption/exchange chromatography. *Developments in Soil Science*, 5:285–348, 1979. 43, 126, 127

E.W. Bolton, A.C. Lasaga, and D.M. Rye. Long-term flow/chemistry feedback in a porous medium with heterogenous permeability: Kinetic control of dissolution and precipitation. *American Journal of Science*, 299(1):1, 1999. 66

D.C. Bouchard, A.L. Wood, M.L. Campbell, P. Nkedi-Kizza, and P.S.C. Rao. Sorption nonequilibrium during solute transport. *Journal of Contaminant Hydrology*, 2(3):209–223, 1988. copy. 67

S.A. Bradford and M. Bettahar. Straining, attachment, and detachment of cryptosporidium oocysts in saturated porous media. 2005. 159

S.A. Bradford and S. Torkzaban. Colloid transport and retention in unsaturated porous media: A review of interface-, collector-, and pore-scale processes and models. *Vadose Zone Journal*, 7(2):667, 2008. 159

S.A. Bradford, J. Simunek, M. Bettahar, M.T. van Genuchten, and S.R. Yates. Significance of straining in colloid deposition: Evidence and implications. *Water Resour. Res*, 42(10.1029), 2006. 159

S.A. Bradford, S. Torkzaban, and S.L. Walker. Coupling of physical and chemical mechanisms of colloid straining in saturated porous media. *Water research*, 41(13): 3012–3024, 2007. 159

E. Bresler. Simultaneous transport of solutes and water under transient unsaturated flow conditions. *Water Resources Research*, 9(4):975–986, 1973. 127

R.H. Brooks and A.T. Corey. Hydraulic properties of porous media. 1964. 92

M.L. Brusseau. Nonequilibrium transport of organic chemicals: The impact of pore-water velocity. *Journal of Contaminant Hydrology*, 9(4):353–368, 1992a. copy. 67

M.L. Brusseau, T. Larsen, and T.H. Christensen. Rate-limited sorption and nonequilibrium transport of organic chemicals in low organic carbon aquifer materials. *Water Resources Research*, 27(6), 1991a. 67

M.L. Brusseau, R.E. Jessup, and P.S.C. Rao. Nonequilibrium sorption of organic chemicals: Elucidation of rate-limiting processes. *Name: Environmental Science and Technology*, 1991b. 67

S.L. Bryant and K.E. Thompson. Theory, modeling and experiment in reactive transport in porous media. *Current Opinion in Colloid & Interface Science*, 6(3):217–222, 2001. 42, 44

J.J. Buckles, R.D. Hazlett, S. Chen, K.G. Eggert, D.W. Grunau, and W.E. Soll. Toward improved prediction of reservoir flow performance. *Los Alamos Science*, 22:112–121, 1994. 5

T. Bunsri, M. Sivakumar, and D. Hagare. Influence of dispersion on transport of tracer through unsaturated porous media. *Journal of Applied Fluid Mechanics (JAFM)*, 1(2):37–44, 2008. 128, 146

D.T. Burr, E.A. Sudicky, and R.L. Naff. Nonreactive and reactive solute transport in three-dimensional heterogeneous porous media: Mean displacement, plume spreading, and uncertainty. *Water Resources Research*, 30(3), 1994. 70

D.R. Cameron and A. Klute. Convective-dispersive solute transport with a combined equilibrium and kinetic adsorption model. *Water Resources Research*, 13(1):183–188, 1977. 162, 170

J. Cao and P.K. Kitanidis. Pore-scale dilution of conservative solutes: An example. *Water Resources Research*, 34(8):1941–1949, 1998. 43, 44

M.A. Celia, H. Rajaram, and A. Ferrand. A multi-scale computational model for multiphase flow in porous media. *Advances in Water Resources*, 16(1):81–92, 1993. 3

M.A. Celia, P.C. Reeves, and L.A. Ferrand. Recent advances in pore scale models for multiphase flow in porous media. *Reviews of Geophysics*, 33(2):1049, 1995. 6, 68

R. Chandler, K. Lerman, J. Koplik, and J.F. Willemsen. Capillary displacement and percolation in porous media. *Journal of Fluid Mechanics*, 119:249–67, 1982. 93, 138

S. Chandrasekhar. Stochastic Problems in Physics and Astronomy. *Rev. Mod. Phys.*, 15:189, 1943. 178

I. Chatzis and F. Dullien. Modelling pore structure by 2-D And 3-D networks with application to sandstones. *Journal of Canadian Petroleum Technology*, 16(1), 1977. 21, 93

I. Chatzis and F.A.L. Dullien. The modeling of mercury porosimetry and the relative permeability of mercury in sandstones using percolation theory. *Int. Chem. Eng.;(United States)*, 25(1), 1985. 93

S. Chen and G.D. Doolen. Lattice boltzmann method for fluid flows. *Annual Review of Fluid Mechanics*, 30(1):329–364, 1998. 68

H. Choi and M. Corapcioglu. Transport of a non-volatile contaminant in unsaturated porous media in the presence of colloids. *Journal of contaminant hydrology*, 25 (3-4):299–324, 1997. 162

L. Chou, R.M. Garrels, and R. Wollast. Comparative study of the kinetics and mechanisms of dissolution of carbonate minerals. *Chemical Geology*, 78(3-4):269–282, 1989. 56

K.H. Coats and B.D. Smith. Dead-end pore volume and dispersion in porous media. *Old Society of Petroleum Engineers*, 4(1):73–84, 1964. 170

M.Y. Corapcioglu and H. Choi. Modeling colloid transport in unsaturated porous media and validation with laboratory column data. *Water resources research*, 32 (12):3437–3449, 1996. 161

M.Y. Corapcioglu and S. Jiang. Colloid-facilitated groundwater contaminant transport. *Water Resources Research*, 29(7):2215–2226, 1993. 161

J.T. Crist, J.F. McCarthy, Y. Zevi, P. Baveye, J.A. Throop, and T.S. Steenhuis. Pore-scale visualization of colloid transport and retention in partly saturated porous media. *Vadose Zone Journal*, 3(2):444, 2004. 160

G. Dagan. Time-dependent macrodispersion for solute transport in anisotropic heterogeneous aquifers. *Water Resources Research*, 24(9):1491–1500, 1988. 178

RA Damion, KJ Packer, KS Sorbie, and SR McDougall. Pore-scale network modelling of flow propagators derived from pulsed magnetic field gradient spin echo nmr measurements in porous media. *Chemical engineering science*, 55(24):5981–5998, 2000. 178

C.J.G. Darnault, T.S. Steenhuis, P. Garnier, Y.J. Kim, M.B. Jenkins, W.C. Ghiorse, P.C. Baveye, and J.Y. Parlange. Preferential flow and transport of Cryptosporidium parvum oocysts through the vadose zone: Experiments and modeling. *Vadose Zone Journal*, 3(1):262, 2004. 161

HJ Daugherty and J.B. Franzini. Steady flow of incompressible fluids in pipes. *Fluid mechanies with Enegineering Applications. 6th edn, McGraw-Hill, New York*, 191, 1965. 52

J.A. Davis, S.B. Yabusaki, C.I. Steefel, J.M. Zachara, G.P. Curtis, G.D. Redden, L.J. Criscenti, and B.D. Honeyman. Assessing conceptual models for subsurface reactive transport of inorganic contaminants. *Eos, Transactions, American Geophysical Union*, 85(44):449, 2004a. 66

L. Davis. *Handbook of genetic algorithms*. Arden Shakespeare, 1991. 34

G.D.J. De Jong. Longitudinal and transverse diffusion in granular deposits. *Transactions - American Geophysical Union*, 39(1), 1958. 7, 75

F. De Smedt and P. Wierenga. Solute transfer through columns of glass beads. *Water Resourses Research*, 20(2):225–232, 1984. 127

F. De Smedt and P.J. Wierenga. Mass transfer in porous media with immobile water. *Journal of Hydrology*, 41(1-2):59–67, 1979. 127

F. De Smedt, F. Wauters, and J. Sevilla. Study of tracer movement through unsaturated sand. *Geoderma*, 38(1-4):223–236, 1986. 127, 128

N.M. DeNovio, J.E. Saiers, and J.N. Ryan. Colloid movement in unsaturated porous media: Recent advances and future directions. *Vadose Zone Journal*, 3(2):338, 2004. 159

L.P. Devkota, U. Matsubayashi, and F. Takagi. A new form of dispersion coefficient model for porous media. *Japan Society of Civil Engineers*, 42(1-4):355–360, 1998. 130

L.A. Dillard and M.J. Blunt. Development of a pore network simulation model to study nonaqueous phase liquid dissolution. *Water Resources Research*, 36(2):439–454, 2000. 20, 120

F.A.L. Dullien. Characterization of porous media-pore level. *Transport in Porous Media*, 6(5):581–606, 1991. 93

J.H. Dunsmuir, S.R. Ferguson, K.L. D'Amico, and J.P. Stokes. X-ray microtomography: a new tool for the characterization of porous media. In *SPESociety of Petroleum Engineers; Annual Technical Conference and Exhibition*, 1991. 21

H.J. Dupin, P.K. Kitanidis, and P.L. McCarty. Pore-scale modeling of biological clogging due to aggregate expansion: a material mechanics approach. *Water Resources Research*, 37(12):2965–2979, 2001. 6, 68

A.M.J. Edward and A. David. Diffusion and convective dispersion through arrays of spheres with surface adsorption, diffusion, and unequal solute partitioning. *Chemical Engineering Science*, 50(9):1441–1454, 1995. 42

D.A. Edwards, M. Shapiro, and H. Brenner. Dispersion and reaction in two-dimensional model porous media. *Physics of Fluids A: Fluid Dynamics*, 5:837, 1993. 42

M. Elimelech and C.R. O'Melia. Kinetics of deposition of colloidal particles in porous media. *Environmental Science & Technology*, 24(10):1528–1536, 1990. 161

M. Elimelech, M. Nagai, C.H. Ko, and J.N. Ryan. Relative insignificance of mineral grain zeta potential to colloid transport in geochemically heterogeneous porous media. *Environmental Science and Technology*, 34(11):2143–2148, 2000. 159

M. Elimelech, J.Y. Chen, and Z.A. Kuznar. Particle deposition onto solid surfaces with micropatterned charge heterogeneity: The hydrodynamic bump effect. *Langmuir*, 19(17):6594–6597, 2003. 161

C. Espinoza and A.J. Valocchi. Stochastic analysis of one-dimensional transport of kinetically adsorbing solutes in chemically heterogeneous aquifers. *Water Resources Research*, 33(11), 1997. 70

R.P. Ewing and S.C. Gupta. Modeling percolation properties of random media using a domain network. *Water resources research*, 29(9):3169–3178, 1993a. 93

R.P. Ewing and S.C. Gupta. Percolation and permeability in partially structured networks. *Water Resources Research*, 29(9):3179–3188, 1993b. 93

I. Fatt. The network model of porous media. *Transactions of the American Institute of Mining, Metallurgical and Petroleum Engineers*, 207:144–181, 1956a. 94

I. Fatt. The network model of porous media. *Transactions of the American Institute of Mining, Metallurgical and Petroleum Engineers*, 207:144–181, 1956b. 5, 68, 93

D.H. Fenwick and M.J. Blunt. Three-dimensional modeling of three phase imbibition and drainage. *Advances in Water Resources*, 21(2):121–143, 1998. 21, 120

L.A. Ferrand and M.A. Celia. The effect of heterogeneity on the drainage capillary pressure–saturation relation. *Water Resources Research*, 28(3):859–870, 1992. 93

L.A. Ferrand, J.A. Sulayman, H. Rajaram, and P.C. Reeves. Calibration of a pore-scale network model for unsaturated soils. *American Geophysical Union*, pages 99–109, 1994. 95

B. Ferreol and D.H. Rothman. Lattice-Boltzmann simulations of flow through Fontainebleau sandstone. *Transport in Porous Media*, 20(1):3–20, 1995. 5, 94

B.P. Flannery, H.W. Deckman, W.G. Roberge, and K.L. D'amico. Three-dimensional X-ray microtomography. *Science*, 237(4821):1439, 1987. 21

R.A. Freeze and J.A. Cherry. Groundwater. 176:161–177, 1979. 126

S.P. Friedman and N.A. Seaton. On the transport properties of anisotropic networks of capillaries. *Water Resources Research*, 32(2):339–347, 1996. 30

L. Gallo, O. Bildstein, and E. Brosse. Coupled reaction-flow modeling of diagenetic changes in reservoir permeability, porosity and mineral compositions. *Journal of Hydrology*, 209(1-4):366–388, 1998. 66

A.P. Gamerdinger and D.I. Kaplan. Physical and chemical determinants of colloid transport and deposition in water-unsaturated sand and Yucca Mountain tuff material. *Environmental Science and Technology*, 35(12):2497–2504, 2001. 159

G. Gargiulo, S. Bradford, J. Simunek, P. Ustohal, H. Vereecken, and E. Klumpp. Bacteria transport and deposition under unsaturated conditions: The role of the matrix grain size and the bacteria surface protein. *Journal of contaminant hydrology*, 92(3-4):255–273, 2007. 160

J.P. Gaudet, H. Vachaud, G. Wierenga, et al. Solute Transfer, with Exchange between Mobile and Stagnant Water, through Unsaturated Sand1. *Soil Science Society of America Journal*, 41(4):665, 1977. 126, 127

O. Genabeek and D.H. Rothman. Macroscopic manifestations of microscopic flows through porous media: Phenomenology from simulation. *Annual Review of Earth and Planetary Sciences*, 24(1):63–87, 1996. 4

H.H. Gerke and M.T. van Genuchten. A dual-porosity model for simulating the preferential movement of water and solutes in structured porous media. *Water Resources Research*, 29:305–305, 1993. 126

D.E. Goldberg. *Genetic algorithms in search, optimization, and machine learning.* Addison-wesley, 1989. 34

L.C. Goldenberg, I. Hutcheon, and N. Wardlaw. Experiments on transport of hydrophobic particles and gas bubbles in porous media. *Transport in porous media*, 4(2):129–145, 1989. 160

C.M. Gramling, C.F. Harvey, and L.C. Meigs. Reactive transport in porous media: A comparison of model prediction with laboratory visualization. *Environmenal Science Technology*, 36(11):2508–2514, 2002. 42

W.G. Gray and S.M. Hassanizadeh. Paradoxes and realities in unsaturated flow theory. *Water Resour. Res*, 27(8):1847–1854, 1991a. 4

W.G. Gray and S.M. Hassanizadeh. Unsaturated flow theory including interfacial phenomena. *Water Resources Research*, 27(8):1855–1863, 1991b. 4

W.G. Gray and S.M. Hassanizadeh. Macroscale continuum mechanics for multiphase porous-media flow including phases, interfaces, common lines and common points. *Advances in Water Resources*, 21(4):261–281, 1998. 48

P. Grindrod and A.J. Lee. Colloid migration in symmetrical non-uniform fractures: Particle tracking in three dimensions. *Journal of contaminant hydrology*, 27(3-4): 157–175, 1997. 161

A.K. Gunstensen and D.H. Rothman. Lattice-boltzmann studies of immiscible two-phase flow through porous media. *Journal of Geophysical Research-Solid Earth*, 98 (B4), 1993. 68

G. Guo and K.E. Thompson. Experimental analysis of local mass transfer in packed beds. *Chemical Engineering Science*, 56(1):121–132, 2001. 42, 44

R.A. Gupta, R.J. Millington, and A. Klute. Hydrodynamic dispersion in unsaturated porous media I. Concentration distribution during dispersion. *J. Indian Soc. Soil Sci*, 21:1–7, 1973. 127, 129

M. Hassanizadeh and W.G. Gray. General conservation equations for multi-phase systems: 3. Constitutive theory for porous media flow. *Advances in Water Resources*, 3(1):25–40, 1980. 4

M. Hassanizadeh et al. Derivation of basic equations of mass transport in porous media, Part 1. Macroscopic balance laws. *Advances in Water Resources*, 9(4): 196–206, 1986. 48

S.M. Hassanizadeh and W.G. Gray. General conservation equations for multiphase systems: 2. Mass, momenta, energy, and entropy equations. *Adv. Water Resour*, 2 (3):191–203, 1979. 4, 42, 47

S.M. Hassanizadeh and W.G. Gray. Toward an improved description of the physics of two-phase flow. *Advances in Water Resources*, 16(1):53–67, 1993. 4

A.A. Helba, M. Sahimi, L.E. Scriven, and H.T. Davis. Percolation theory of two-phase relative permeability. *Society of Petroleum Engineers; Reservoir Engineering*, 7(1): 123–132, 1992. 7, 20

R.J. Held and M.A. Celia. Pore-scale modeling and upscaling of nonaqueous phase liquid mass transfer. *Water Resources Research*, 37(3):539–549, 2001. 6, 68

M.R. Hestenes and M.R. Hestenes. *Conjugate direction methods in optimization.* Springer-Verlag, 1980. ISBN 0387904557. 11

R. Hilfer, T. Rage, and B. Virgin. Local percolation probabilities for a natural sandstone. *Physica A: Statistical and Theoretical Physics*, 241(1-2):105–110, 1997. 7

J.H. Holland. Adaptation in natural and artificial systems. 1975. *Ann Arbor MI: University of Michigan Press.* 34

C.R. Houck, J.A. Joines, and M.G. Kay. A genetic algorithm for function optimization: a Matlab implementation, North Carolina State University, Raleigh. Technical report, NC, Technical Report, 1995. 34

P. Huttenloch, K.E. Roehl, and K. Czurda. Sorption of nonpolar aromatic contaminants by chlorosilane surface modified natural minerals. *Environmental Science and Technology*, 35(21):4260–4264, 2001. copy. 67

M.A. Ioannidis and I. Chatzis. A mixed-percolation model of capillary hysteresis and entrapment in mercury porosimetry. *Journal of Colloid and Interface Science*, 161 (2):278–291, 1993a. 7

M.A. Ioannidis and I. Chatzis. Network modelling of pore structure and transport properties of porous media. *Chemical Engineering Science*, 48(5):951–972, 1993b. 20

M.A. Ioannidis and I. Chatzis. On the geometry and topology of 3D stochastic porous media. *Journal of Colloid and Interface Science*, 229(2):323–334, 2000. 21, 23, 118

M.A. Ioannidis, I. Chatzis, and E.A. Sudicky. The effect of spatial correlations on the accessibility characteristics of three-dimensional cubic networks as related to drainage displacements in porous media. *Water Resources Research*, 29:1777–1786, 1993. 95

M.A. Ioannidis, M.J. Kwiecien, I. Chatzis, I.F. MacDonald, and F.A.L. Dullien. Comprehensive pore structure characterization using 3D computer reconstruction and stochastic modeling. In *Society of Petroleum Engineers; Annual Technical Conference and Exhibition*, 1997a. 21, 22

O.H. Jacobsen, P. Moldrup, C. Larsen, L. Konnerup, and L.W. Petersen. Particle transport in macropores of undisturbed soil columns. *Journal of Hydrology*, 196 (1-4):185–203, 1997. 159

D.B. Jaynes. Field study of bromacil transport under continuous-flood irrigation. *Soil Science Society of America Journal*, 55(3):658, 1991. 67

G.R. Jerauld and S.J. Salter. The effect of pore-structure on hysteresis in relative permeability and capillary pressure: pore-level modeling. *Transport in Porous Media*, 5(2):103–151, 1990. 30, 31, 95

G.R. Jerauld, L.E. Scriven, and H.T. Davis. Percolation and conduction on the 3D Voronoi and regular networks: a second case study in topological disorder. *Journal of Physics C: Solid State Physics*, 17:3429, 1984. 22, 33

D.G. Jewett, B.E. Logan, R.G. Arnold, and R.C. Bales. Transport of Pseudomonas fluorescens strain P17 through quartz sand columns as a function of water content. *Journal of Contaminant Hydrology*, 36(1-2):73–89, 1999. 159

Y. Jin, Y. Chu, and Y. Li. Virus removal and transport in saturated and unsaturated sand columns. *Journal of Contaminant Hydrology*, 43(2):111–128, 2000. 159

V. Joekar-Niasar, S.M. Hassanizadeh, and A. Leijnse. Insights into the relationships among capillary pressure, saturation, interfacial area and relative permeability using pore-network modeling. *Transport in Porous Media*, 74(2):201–219, 2008a. 93

V. Joekar-Niasar, S.M. Hassanizadeh, and A. Leijnse. Insights into the relationships among capillary pressure, saturation, interfacial area and relative permeability using pore-network modeling. *Transport in Porous Media*, 74(2):201–219, 2008b. 6, 35, 68

V. Joekar-Niasar, M. Prodanović, D. Wildenschild, and S. M. Hassanizadeh. Network model investigation of interfacial area, capillary pressure and saturation relationships in granular porous media. *Water Resources Research*, 46, 2010. doi: 10.1029/2009WR008585. 6, 68, 106, 108

D.I. Kaplan, P.M. Bertsch, D.C. Adriano, and W.P. Miller. Soil-borne mobile colloids as influenced by water flow and organic carbon. *Environmental science & technology*, 27(6):1193–1200, 1993. 159

V. Kapoor, C.T. Jafvert, and D.A. Lyn. Experimental study of a bimolecular reaction in Poiseuille flow. *Water Resources Research*, 34(8):1997–2004, 1998. 43

P.E. Kechagia, I.N. Tsimpanogiannis, Y.C. Yortsos, and P.C. Lichtner. On the upscaling of reaction-transport processes in porous media with fast or finite kinetics. *Chemical Engineering Science*, 57(13):2565–2577, 2002. 42, 43

W.D. Kemper. Diffusion of Salts in Clay-Water Systems. *Soil Science Society of America Journal*, 30(5):534, 1966. 127

D.B. Kent, J.A. Davis, J.L. Joye, and G.P. Curtis. Influence of variable chemical conditions on edta-enhanced transport of metal ions in mildly acidic groundwater. *Environmental Pollution*, 153(1):44–52, 2008. 66

A.B. Kersting, D.W. Efurd, D.L. Finnegan, D.J. Rokop, D.K. Smith, and J.L. Thompson. Migration of plutonium in ground water at the Nevada Test Site. *Nature*, 397 (6714):56–59, 1999. 1, 158

D.S. Kim and H.S. Fogler. Biomass evolution in porous media and its effects on permeability under starvation conditions. *Biotechnology and bioengineering*, 69(1): 47–56, 2000. 6, 68

S.B. Kim, H.C. Ha, N.C. Choi, and D.J. Kim. Influence of flow rate and organic carbon content on benzene transport in a sandy soil. *Hydrological Processes*, 20 (20):4307–4316, 2006. copy. 67

C.N. Kirda, D.R. Biggar, and J.W. Biggar. Simultaneous Transport of Chloride and Water During Infiltration. *Soil Science Society of America Journal*, 37(3):339, 1973. 127

M.A. Knackstedt, A.P. Sheppard, and W.V. Pinczewski. Simulation of mercury porosimetry on correlated grids: Evidence for extended correlated heterogeneity at the pore scale in rocks. *Physical Review E*, 58(6):6923–6926, 1998. 20

C.E. Knutson, C.J. Werth, and A.J. Valocchi. Pore-scale modeling of dissolution from variably distributed nonaqueous phase liquid blobs. *Water Resources Research*, 37 (12):2951–2963, 2001a. 44, 45

C.E. Knutson, C.J. Werth, and A.J. Valocchi. Pore-scale modeling of dissolution from variably distributed nonaqueous phase liquid blobs. *Water Resources Research*, 37 (12), 2001b. 6, 68

M. Kohler, G.P. Curtis, D.E. Meece, and J.A. Davis. Methods for estimating adsorbed uranium (vi) and distribution coefficients of contaminated sediments. *Environmental Science and Technology*, 38(1):240–247, 2004. 66

H.K. Krupp and D.E. Elrick. Miscible displacement in an unsaturated glass bead medium. *Water Resources Research*, 4(4):809–815, 1968. 127, 128, 129

S. Kruyer. The penetration of mercury and capillary condensation in packed spheres. *Transactions of the Faraday Society*, 54:1758–1767, 1958. 94

M. Laegdsmand, K.G. Villholth, M. Ullum, and K.H. Jensen. Processes of colloid mobilization and transport in macroporous soil monoliths. *Geoderma*, 93(1-2): 33–59, 1999. 159

R.G. Larson, L.E. Scriven, and H.T. Davis. Percolation theory of two phase flow in porous media. *Chemical Engineering Science*, 36(1):57–73, 1981. 20, 93

A.C. Lasaga. *Kinetic Theory in the Earth Sciences.* Princeton Univ Pr, 1998. 66

L.S. Lee, P.S.C. Rao, M.L. Brusseau, and R.A. Ogwada. Nonequilibrium sorption of organic contaminants during flow through columns of aquifer materials. *Environmental Toxicology and Chemistry*, 7(10):779–793, 1988. 67

F.J. Leij and M.T. van Genuchten. Solute Transport. *Soil Physics Companion*, pages 189–248, 2002. 126

J.J. Lenhart and J.E. Saiers. Transport of silica colloids through unsaturated porous media: Experimental results and model comparisons. *Environmental science & technology*, 36(4):769–777, 2002. 159, 160, 161

L. Li, C.A. Peters, and M.A. Celia. Upscaling geochemical reaction rates using pore-scale network modeling. *Advances in Water Resources*, 29(9):1351–1370, 2006a. 142, 162

L. Li, C.A. Peters, and M.A. Celia. Upscaling geochemical reaction rates using pore-scale network modeling. *Advances in Water Resources*, 29(9):1351–1370, 2006b. 6, 43, 44, 68, 70, 93, 179

L. Li, C.A. Peters, and M.A. Celia. Applicability of averaged concentrations in determining geochemical reaction rates in heterogeneous porous media. *American Journal of Science*, 307(10):1146–1166, 2007a. 136

L. Li, C.A. Peters, and M.A. Celia. Effects of mineral spatial distribution on reaction rates in porous media. *Water Resour. Res*, 43(1), 2007b. 136

L. Li, C.A. Peters, and M.A. Celia. Effects of mineral spatial distribution on reaction rates in porous media. *Water Resour. Res*, 43(1), 2007a. 7, 69

L. Li, C.A. Peters, and M.A. Celia. Applicability of averaged concentrations in determining geochemical reaction rates in heterogeneous porous media. *American Journal of Science*, 307(10):1146–1166, 2007b. 7, 66, 69, 75

L. Li, C.I. Steefel, and L. Yang. Scale dependence of mineral dissolution rates within single pores and fractures. *Geochimica et Cosmochimica Acta*, 72(2):360–377, 2008. 43, 56

P.C. Lichtner. Continuum model for simultaneous chemical reactions and mass transport in hydrothermal systems. *Geochimica et Cosmochimica Acta*, 1985. 68

W.B. Lindquist and A. Venkatarangan. Investigating 3d geometry of porous media from high resolution images. *Physics and Chemistry of the Earth, Part A*, 24(7): 593–599, 1999. 118, 119

W.B. Lindquist, S.M. Lee, D.A. Coker, K.W. Jones, and P. Spanne. Medial axis analysis of void structure in three-dimensional tomographic images of porous media. *Journal of Geophysical Research*, 101:8297–8310, 1996. 21

W.B. Lindquist, A. Venkatarangan, J. Dunsmuir, and T. Wong. Pore and throat size distributions measured from synchrotron x-ray tomographic images of fontainebleau sandstones. *Journal of Geophysical Research*, 105(B9):21–21, 2000. 6, 68, 94, 95, 111, 118, 119, 120, 123

D.P. Lymberopoulos and A.C. Payatakes. Derivation of topological, geometrical, and correlational properties of porous media from pore-chart analysis of serial section data. *Journal of Colloid and Interface Science*, 150(1):61–80, 1992. 95

S. Maciejewski. Numerical and experimental study of solute transport in unsaturated soils. *Journal of contaminant hydrology*, 14(3-4):193–206, 1993. 127

K. Maher, D.J. DePaolo, and J.C.F. Lin. Rates of silicate dissolution in deep-sea sediment: In situ measurement using 234U/238U of pore fluids. *Geochimica et Cosmochimica Acta*, 68(22):4629–4648, 2004. 44, 66

W.M. Mahmud, J.Y. Arns, A. Sheppard, M.A. Knackstedt, and W.V. Pinczewski. Effect of network topology on two-phase imbibition relative permeability. *Transport in Porous Media*, 66(3):481–493, 2007. 95, 118

M.A. Maraqa, B. Wallace, et al. Effects of degree of water saturation on dispersivity and immobile water in sandy soil columns. *Journal of Contaminant Hydrology*, 25 (3-4):199–218, 1997. 127, 133

M.A. Maraqa, R.B. Wallace, and T.C. Voice. Effects of residence time and degree of water saturation on sorption nonequilibrium parameters. *Journal of Contaminant Hydrology*, 36(1-2):53–72, 1999. copy. 67

D.W. Marquardt. An algorithm for least-squares estimation of nonlinear parameters. *Journal of the society for Industrial and Applied Mathematics*, 11(2):431–441, 1963. 171

N.S. Martys and H. Chen. Simulation of multicomponent fluids in complex three-dimensional geometries by the lattice boltzmann method. *Physical Review E*, 53 (1):743–750, 1996. 68

G. Mason and N.R. Morrow. Capillary behavior of a perfectly wetting liquid in irregular triangular tubes. *J. Colloid Interface Sci*, 141(1):262–274, 1991. 97, 134

U. Matsubayashi, L.P. Devkota, and F. Takagi. Characteristics of the dispersion coefficient in miscible displacement through a glass beads medium. *Journal of Hydrology*, 192(1-4):51–64, 1997. 127, 129, 130

R. Mauri. Dispersion, convection, and reaction in porous media. *Physics of Fluids A: Fluid Dynamics*, 3:743, 1991. 42

A.S. Mayer and C.T. Miller. The influence of porous medium characteristics and measurement scale on pore-scale distributions of residual nonaqueous-phase liquids. *Journal of Contaminant Hydrology*, 11(3-4):189–213, 1992. 20

A.S. Mayer, C.T. Kelley, and C.T. Miller. Optimal design for problems involving flow and transport phenomena in saturated subsurface systems. *Advances in Water Resources*, 25(8-12):1233–1256, 2002. 66

R.P. Mayer and R.A. Stowe. Mercury porosimetry–breakthrough pressure for penetration between packed spheres. *Journal of Colloid Science*, 20(8):893–911, 1965. 94

J.F. McCarthy and J.M. Zachara. Subsurface transport of contaminants. *Environmental Science & Technology*, 23(5):496–502, 1989. 1, 158

C. Meile and K. Tuncay. Scale dependence of reaction rates in porous media. *Advances in Water Resources*, 29(1):62–71, 2006. 43, 44, 95

Z. Michalewicz. *Genetic Algorithms Plus Data Structures Equals Evolution Programs.* Springer-Verlag New York, Inc. Secaucus, NJ, USA, 1994. 34

C.T. Miller and W.G. Gray. Hydrogeological research: Just getting started. *Ground Water*, 40(3):224–231, 2002. 3

C.T. Miller, G. Christakos, P.T. Imhoff, J.F. McBride, J.A. Pedit, and J.A. Trangenstein. Multiphase flow and transport modeling in heterogeneous porous media: challenges and approaches. *Advances in Water Resources*, 21(2):77–120, 1998. ISSN 0309-1708. 4, 68

Z. Mo and J.C. Friedly. Local reaction and diffusion in porous media transport models. *Water Resources Research*, 36(2):431–438, 2000. 44

K. Mogensen and E.H. Stenby. A dynamic two-phase pore-scale model of imbibition. *Transport in Porous Media*, 32(3):299–327, 1998. 95, 120

K. Mohanty. Multiphase flow in porous media: Ii. pore-level modeling. In *Society of Petroleum Engineers; Annual Technical Conference and Exhibition*, 1982. 131

R. Mojaradi and M. Sahimi. Diffusion-controlled reactions in disordered porous media–II. Nonuniform distribution of reactants. *Chemical Engineering Science*, 43(11):2995–3004, 1988. 42

A.I. Murdoch and S.M. Hassanizadeh. Macroscale balance relations for bulk, interfacial and common line systems in multiphase flows through porous media on the basis of molecular considerations. *International Journal of Multiphase Flow*, 28(7): 1091–1123, 2002. 42

D.R. Nielsen and J.W. Biggar. Miscible Displacement in Soils: I. Experimental Information1. *Soil Science Society of America Journal*, 25(1):1, 1960. 127

P. Nkedi-Kizza, P.S.C. Rao, R.E. Jessup, and J.M. Davidson. Ion exchange and diffusive mass transfer during mis-cible displacement through an aggregated oxisol. *Soil Science Society of America Journal*, 46:471–476, 1982. 161

P. Nkedi-Kizza, P.S.C. Rao, and J.W. Johnson. Adsorption of diuron and 2, 4, 5-t on soil particle-size separates. *Journal of Environmental Quality*, 12(2):195, 1983. 67

P. Nkedi-Kizza, J.W. Biggar, H.M. Selim, and M. van Genuchten. On the equivalence of two conceptual models for describing ion exchange during transport through an aggregated oxisol. *Water Resources. Res*, 20(8):1123–1130, 1984. 170

A.L. Noell, J.L. Thompson, M.Y. Corapcioglu, and I.R. Triay. The role of silica colloids on facilitated cesium transport through glass bead columns and modeling. *Journal of Contaminant Hydrology*, 31(1-2):23–56, 1998. 159

A.G. O'Donnell, I.M. Young, S.P. Rushton, M.D. Shirley, and J.W. Crawford. Visualization, modelling and prediction in soil microbiology. *Nature Reviews Microbiology*, 5(9):689–699, 2007. 69

ME O'neill. A sphere in contact with a plane wall in a slow linear shear flow. *Chemical Engineering Science*, 23(11):1293–1298, 1968. 159

P.E. Øren and S. Bakke. Process based reconstruction of sandstones and prediction of transport properties. *Transport in Porous Media*, 46(2):311–343, 2002a. 21

P.E. Øren and S. Bakke. Reconstruction of berea sandstone and pore-scale modelling of wettability effects. *Journal of Petroleum Science and Engineering*, 39(3-4):177–199, 2003a. 95, 118

P.E. Øren and S. Bakke. Reconstruction of Berea sandstone and pore-scale modelling of wettability effects. *Journal of Petroleum Science and Engineering*, 39(3-4):177–199, 2003b. 21, 22, 23

P.E. Øren and W.V. Pinczewski. The Effect of Wettability and Spreading Coefficients on the Recovery of Waterflood Residual Oil by Miscible Gasflooding. *Society of Petroleum Engineers; Formation Evaluation*, 9(2):149–156, 1994. 20

P.E. Øren, J. Billiotte, and W.V. Pinczewski. Mobilization of waterflood residual oil by gas injection for water-wet conditions. *Society of Petroleum Engineers; Formation Evaluation*, 7(1):70–78, 1992. 20

P.E. Øren, S. Bakke, and O.J. Arntzen. Extending predictive capabilities to network models. soc. pet. *Eng. J*, 3(4):324–336, 1998a. 95

P.E. Øren, S. Bakke, and O.J. Arntzen. Extending predictive capabilities to network models. *Society of Petroleum Engineers*, 3(4):324–336, 1998b. 6, 7, 21, 68

I.Y. Padilla, T.C.J. Yeh, and M.H. Conklin. The effect of water content on solute transport in unsaturated porous media. *Water Resources Research*, 35(11):3303–3313, 1999. 127, 129, 152

M. Pagitsas, A. Nadim, and H. Brenner. Multiple time scale analysis of macrotransport processes. *Physica A: Statistical and Theoretical Physics*, 135(2-3):533–550, 1986. 42

C. Pan, M. Hilpert, and C.T. Miller. Pore-scale modeling of saturated permeabilities in random sphere packings. *Physical Review E*, 64(6):66702, 2001. 68, 94

C. Pan, J.F. Prins, and C.T. Miller. A high-performance lattice boltzmann implementation to model flow in porous media. *Computer Physics Communications*, 158 (2):89–105, 2004. 68

C. Pan, L.S. Luo, and C.T. Miller. An evaluation of lattice boltzmann schemes for porous medium flow simulation. *Computers and Fluids*, 35(8-9):898–909, 2006. 68

L. Pang and M. Close. Field-scale physical non-equilibrium transport in an alluvial gravel aquifer. *Journal of Contaminant Hydrology*, 38(4):447–464, 1999a. 67

L. Pang, M. Close, D. Schneider, and G. Stanton. Effect of pore-water velocity on chemical nonequilibrium transport of cd, zn, and pb in alluvial gravel columns. *Journal of contaminant hydrology*, 57(3-4):241–258, 2002. 67

L. Paterson, S. Painter, X. Zhang, and V. Pinczewski. Simulating residual saturation and relative permeability in heterogeneous formations. In *Society of Petroleum Engineers; Annual Technical Conference and Exhibition*, 1996b. 20

T. Patzek. Verification of a complete pore network simulator of drainage and imbibition. *Society of Petroleum Engineers*, 2001. 98

T.W. Patzek and J.G. Kristensen. Shape factor correlations of hydraulic conductance in noncircular capillaries ii. two-phase creeping flow. *Journal of Colloid and Interface Science*, 236(2):305–317, 2001. 95, 105

G.G. Pereira. Numerical pore-scale modeling of three-phase fluid flow: Comparison between simulation and experiment. *Physical Review E*, 59(4):4229, 1999. 5

G.G. Pereira, W.V. Pinczewski, D.Y.C. Chan, L. Paterson, and P.E. Øren. Pore-scale network model for drainage-dominated three-phase flow in porous media. *Transport in Porous media*, 24(2):167–201, 1996. 20

E. Perfect and M.C. Sukop. 3 models relating solute dispersion to pore space geometry in saturated media: A review. 2001. 126

CJ Ptacek and RW Gillham. Laboratory and field measurements of non-equilibrium transport in the borden aquifer, ontario, canada. *Journal of contaminant hydrology*, 10(2):119–158, 1992. 67

M. Quintard and S. Whitaker. Aerosol filtration: an analysis using the method of volume averaging. *Journal of Aerosol Science*, 26(8):1227–1255, 1995. 42

H. Rajaram. Time and scale dependent effective retardation factors in heterogeneous aquifers. *Advances in Water Resources*, 20(4):217–230, 1997. 70

H. Rajaram, L.A. Ferrand, and M.A. Celia. Prediction of relative permeabilities for unconsolidated soils using pore-scale network models. *Water Resources Research*, 33(1). 95

D.S. Raje and V. Kapoor. Experimental study of bimolecular reaction kinetics in porous media. *Environmental Science and Technology*, 34(7):1234–1239, 2000. 42

P.S.C. Rao, R.E. Jessup, D.E. Rolston, J.M. Davidson, and D.P. Kilcrease. Experimental and mathematical description of nonadsorbed solute transfer by diffusion in spherical aggregates. *Soil Science Society of America Journal*, 44(4):684–687, 1980a. 161

P.S.C. Rao, D.E. Rolston, R.E. Jessup, and J.M. Davidson. Solute transport in aggregated porous media: Theoretical and experimental evaluation. *Soil Science Society of America Journal*, 44(6):1139–1146, 1980b. 161

A. Raoof and S.M. Hassanizadeh. Upscaling Transport of Adsorbing Solutes in Porous Media. *Journal of Porous Media*, 11(4), 2008. 95

A. Raoof and S.M. Hassanizadeh. A new method for generating pore-network models of porous media. *Transport in Porous Media*, pages 1–17, 2009. doi: 10.1007/s11242-009-9412-3. 6, 7, 8, 68, 69, 71, 113, 205

A. Raoof and S.M. Hassanizadeh. Upscaling transport of adsorbing solutes in porous media. *Journal of Porous Media*, 13(5):395–408, 2010a. 67, 69, 76, 82, 83, 87, 173

A. Raoof and S.M. Hassanizadeh. Upscaling transport of adsorbing solutes in porous media: Pore-network modeling. *Vadose Zone Journal*, Accepted for publication, 2010b. 93, 95, 99

A. Raoof and S.M. Hassanizadeh. A new formulation for pore-network modeling of two-phase flow. *WRR*, 2011a. 136, 139, 140

A. Raoof and S.M. Hassanizadeh. Dispersivity under partially-saturated conditions; pore-scale processes. 2011b. 172

A. Raoof, S.M. Hassanizadeh, and A. Leijnse. Upscaling transport of adsorbing solutes in porous media: Pore-network modeling. *Vadose Zone Journal*, 9(3):624, 2010. 135, 141, 142

A. Raoof, C.J. Spiers, and S.M. Hassanizadeh. Reactive pore-scale modeling of porosity and permeability evolution in porous media. *American Geophysical Union, Fall Meeting*, 2011. 13, 14

M. Rashidi, L. Peurrung, A.F.B. Tompson, and T.J. Kulp. Experimental analysis of pore-scale flow and transport in porous media. *Advances in Water Resources*, 19 (3):163–180, 1996. 43

P.C. Reeves and M.A. Celia. A functional relationship between capillary pressure, saturation, and interfacial area as revealed by a pore-scale network model. *Water Resources Research*, 32(8):2345–2358, 1996. 20

P. Regnier, J.P. O'Kane, C.I. Steefel, and J.P. Vanderborght. Modeling complex multi-component reactive-transport systems: towards a simulation environment based on the concept of a knowledge base. *Applied Mathematical Modelling*, 26(9): 913–927, 2002. 13

P. Regnier, P. Jourabchi, and C.P. Slomp. Reactive-transport modeling as a technique for understanding coupled biogeochemical processes in surface and subsurface environments. *Netherlands Journal of Geosciences/Geologie en Mijnbouw*, 82(1):5–18, 2003. 13

P. Renault. The effect of spatially correlated blocking-up of some bonds or nodes of a network on the percolation threshold. *Transport in porous media*, 6(4):451–468, 1991. 31, 95

B.A. Robinson and H.S. Viswanathan. Application of the theory of micromixing to groundwater reactive transport models. *Water Resources Research*, 39(11):1313, 2003. 44

D. Ryan, RG Carbonell, and S. Whitaker. Effective diffusivities for catalyst pellets under reactive conditions. *Chemical Engineering Science*, 35(1-2):10–16, 1980. 42

P.G. Saffman. A theory of dispersion in a porous medium. *Journal of Fluid Mechanics*, 6(03):321–349, 1959. 178

M. Sahimi. Diffusion-controlled reactions in disordered porous media–I. Uniform distribution of reactants. *Chemical Engineering Science*, 43(11):2981–2993, 1988. 42

M. Sahimi, B.D. Hughes, LE Scriven, and H. Ted Davis. Dispersion in flow through porous media–i. one-phase flow. *Chemical engineering science*, 41(8):2103–2122, 1986. 178

J.E. Saiers. Laboratory observations and mathematical modeling of colloid-facilitated contaminant transport in chemically heterogeneous systems. *Water resources research*, 38(4):1032, 2002. 161

J.E. Saiers and J.J. Lenhart. Colloid mobilization and transport within unsaturated porous media under transient-flow conditions. *Water Resour. Res*, 39(1):1019, 2003a. 159

J.E. Saiers and J.J. Lenhart. Ionic-strength effects on colloid transport and interfacial reactions in partially saturated porous media. *Water Resour. Res*, 39(9):1256, 2003b. 159

J.A. Saunders and L.E. Toran. Modeling of radionuclide and heavy metal sorption around low-and high-ph waste disposal sites at oak ridge, tennessee. *Applied Geochemistry*, 10(6):673–684, 1995. 66

A. Schafer, P. Ustohal, H. Harms, F. Stauffer, T. Dracos, and A.J.B. Zehnder. Transport of bacteria in unsaturated porous media. *Journal of contaminant Hydrology*, 33(1-2):149–169, 1998. 159

A.E. Scheidegger. On the theory of flow of miscible phases in porous media. *International Union of Geodesy and Geophysics in Toronto (Sept., 1957)*, 1957. 7

A.E. Scheidegger. General theory of dispersion in porous media. *Journal of Geophysical Research*, 66(10):3273–3278, 1961. 126

K. Schelde, P. Moldrup, O.H. Jacobsen, H. De Jonge, L.W. De Jonge, and T. Komatsu. Diffusion-limited mobilization and transport of natural colloids in macroporous soil. *Vadose Zone Journal*, 1(1):125, 2002. 159

R. Schulin, P.J. Wierenga, H. Fluhler, and J. Leuenberger. Solute transport through a stony soil. *Soil Science Society of America Journal*, 51(1):36, 1987. 67

H.M. Selim, J.M. Davidson, and R.S. Mansell. Evaluation of a two-site adsorption-desorption model for describing solute transport in soils. In *Proc. Summer Computer Simulation Conf., Washington, DC*, pages 12–14, 1976. 162, 170

S.E. Serrano. Propagation of nonlinear reactive contaminants in porous media. *Water Resources Research*, 39(8):1228, 2003. 43

X. Shan and H. Chen. Simulation of nonideal gases and liquid-gas phase transitions by the lattice boltzmann equation. *Physical Review E*, 49(4):2941–2948, 1994. 68

M. Shapiro and P.M. Adler. Coupled transport of multi-component solutes in porous media. *Journal of Engineering Mathematics*, 31(2):357–378, 1997. 43

M. Shapiro and H. Brenner. Taylor dispersion of chemically reactive species: irreversible first-order reactions in bulk and on boundaries. *Chemical Engineering Science*, 41(6):1417–1433, 1986. 42

M. Shapiro and H. Brenner. Chemically reactive generalized Taylor dispersion phenomena. *AIChE Journal*, 33(7):1155–1167, 1987. 42

M. Shapiro and H. Brenner. Dispersion of a chemically reactive solute in a spatially periodic model of a porous medium. *Chemical Engineering Science*, 43(3):551–571, 1988. 42

E. Shimojima and M.L. Sharma. The influence of pore water velocity on transport of sorptive and non-sorptive chemicals through an unsaturated sand. *Journal of Hydrology*, 164(1-4):239–261, 1995. copy. 67

Y. Sholokhova, D. Kim, and W. Brent Lindquist. Network flow modeling via lattice-boltzmann based channel conductance. *Advances in Water Resources*, 32(2):205–212, 2009. 95, 120, 122

D.B. Silin, G. Jin, and T.W. Patzek. Robust determination of pore space morphology in sedimentary rocks. In *Proceedings of Society of Petroleum Engineers; Annual Technical Conference and Exhibition*, 2003. 34

Y. Sim and C.V. Chrysikopoulos. Virus transport in unsaturated porous media. *Water Resources Research*, 36(1):173–179, 2000. 159

J. Simunek, C., L. Pang, and S.A. Bradford. Colloid-facilitated solute transport in variably saturated porous media: Numerical model and experimental verification. *Vadose Zone Journal*, 5(3):1035, 2006. 160

S. Sirivithayapakorn and A. Keller. Transport of colloids in saturated porous media: A pore-scale observation of the size exclusion effect and colloid acceleration. *Water Resour. Res*, 39(4):1109, 2003. 160

F. Smet, P.J. Wierenga, and A. Beken. Theoretical and experimental study of solute movement through porous media with mobile and immobile water. *VUB Hydrologie (Belgium)*, 1981. 126

R.M. Sok, M.A. Knackstedt, A.P. Sheppard, W.V. Pinczewski, W.B. Lindquist, A. Venkatarangan, and L. Paterson. Direct and stochastic generation of network models from tomographic images; effect of topology on residual saturations. *Transport in Porous Media*, 46(2):345–371, 2002. 6, 7, 20, 95, 118

W.E. Soll, S.Y. Chen, K.G. Eggert, D.W. Grunau, and D.R. Janecky. Application of the Lattice Boltzmann/Lattice Gas technique to multi-fluid flow in porous media. Technical report, Los Alamos National Lab., NM (United States), 1994. 5

L. Song and M. Elimelech. Transient deposition of colloidal particles in heterogeneous porous media. *Journal of Colloid and Interface Science*, 167(2):301–313, 1994. 161

K.S. Sorbie and P.J. Clifford. The inclusion of molecular diffusion effects in the network modelling of hydrodynamic dispersion in porous media. *Chemical engineering science*, 46(10):2525–2542, 1991. 178

P. Spanne, JF Thovert, CJ Jacquin, WB Lindquist, KW Jones, and PM Adler. Synchrotron computed microtomography of porous media: topology and transports. *Physical Review Letters*, 73(14):2001–2004, 1994. 5, 21

C.I. Steefel and A.C. Lasaga. A coupled model for transport of multiple chemical species and kinetic precipitation/dissolution reactions with applications to reactive flow in single phase hydrothermal systems. *American Journal of Science*, 294(5): 529–592, 1994. 66

B.J. Suchomel, B.M. Chen, and M.B. Allen. Network model of flow, transport and biofilm effects in porous media. *Transport in porous media*, 30(1):1–23, 1998a. 141, 168

B.J. Suchomel, B.M. Chen, and M.B. Allen. Macroscale properties of porous media from a network model of biofilm processes. *Transport in porous media*, 31(1):39–66, 1998b. 179

B.J. Suchomel, B.M. Chen, and M.B. Allen. Network model of flow, transport and biofilm effects in porous media. *Transport in porous media*, 30(1):1–23, 1998c. 6, 68, 74, 77, 143

F. Sugita, R.W. Gillham, and C. Mase. Pore scale variation in retardation factor as a cause of nonideal reactive breakthrough curves 2. pore network analysis. *Water Resources Research*, 31(1):103–112, 1995a. 142

F. Sugita, R.W. Gillham, and C. Mase. Pore scale variation in retardation factor as a cause of nonideal reactive breakthrough curves 2. pore network analysis. *Water Resources Research*, 31(1), 1995b. 6, 68

M.C. Sukop and D.T. Thorne. *Lattice Boltzmann modeling: An introduction for geoscientists and engineers.* Springer Verlag, 2006. 68

N. Sun and J.Y. Walz. A model for calculating electrostatic interactions between colloidal particles of arbitrary surface topology. *Journal of Colloid and Interface Science*, 234(1):90–105, 2001. 161

N.Z. Sun. *Mathematical modeling of groundwater pollution.* Springer New York, 1996. 77, 143, 168, 179

S.W. Swanton. Modelling colloid transport in groundwater; the prediction of colloid stability and retention behaviour. *Advances in Colloid and Interface Science*, 54: 129–208, 1995. 161

J.E. Szecsody, J.M. Zachara, A. Chilakapati, P.M. Jardine, and A.S. Ferrency. Importance of flow and particle-scale heterogeneity on CoII/IIIEDTA reactive transport. *Journal of Hydrology*, 209(1-4):112–136, 1998. 44

O. Talabi and M.J. Blunt. Pore-scale network simulation of nmr response in two-phase flow. *Journal of Petroleum Science and Engineering*, 72(1-2):1–9, 2010. 151, 165

O. Talabi, S. Alsayari, M.J. Blunt, H. Dong, and X. Zhao. Predictive pore-scale modeling: from three-dimensional images to multiphase flow simulations. *Proceedings of the Society of Petroleum Engineers*, 115535, 2008. 151, 165

A.M. Tartakovsky, P. Meakin, T.D. Scheibe, and B.D. Wood. A smoothed particle hydrodynamics model for reactive transport and mineral precipitation in porous and fractured porous media. *Water Resources Research*, 43(5):W05437, 2007. 68

G. Taylor. Dispersion of soluble matter in solvent flowing slowly through a tube. *Proceedings of the Royal Society of London. Series A, Mathematical and Physical Sciences*, 219(1137):186–203, 1953. 43, 57

K.E. Thompson, C.S. Willson, and W. Zhang. Quantitative computer reconstruction of particulate materials from microtomography images. *Powder Technology*, 163 (3):169–182, 2006. 36, 37

S.S. Thompson and M.V. Yates. Bacteriophage inactivation at the air-water-solid interface in dynamic batch systems. *Applied and environmental microbiology*, 65 (3):1186, 1999. 159, 161

S.S. Thompson, M. Flury, M.V. Yates, and W.A. Jury. Role of the air-water-solid interface in bacteriophage sorption experiments. *Applied and environmental microbiology*, 64(1):304, 1998. 159, 161

J.F. Thovert, J. Salles, and P.M. Adler. Computerized characterization of the geometry of real porous media: their discretization, analysis and interpretation. *Journal of microscopy*, 170:65–79, 1993. 21

L. Toran and A.V. Palumbo. Colloid transport through fractured and unfractured laboratory sand columns. *Journal of Contaminant Hydrology*, 9(3):289–303, 1992. 159

N. Toride, F.J. Leij, and M.T. van Genuchten. The CXTFIT code for estimating transport parameters from laboratory or field tracer experiments. *Res. Rep*, 119, 1995. 58, 79, 170, 171

N. Toride, M. Inoue, and F.J. Leij. Hydrodynamic dispersion in an unsaturated dune sand. *Soil Science Society of America Journal*, 67(3):703–712, 2003. 128, 129, 146, 149, 150, 151, 152

S. Torkzaban, S.A. Bradford, M.T. van Genuchten, and S.L. Walker. Colloid transport in unsaturated porous media: The role of water content and ionic strength on particle straining. *Journal of contaminant hydrology*, 96(1-4):113–127, 2008. 159, 160

C.D. Tsakiroglou and A.C. Payatakes. Effects of pore-size correlations on mercury porosimetry curves. *Journal of Colloid and Interface Science*, 146(2):479–494, 1991. 95

P.H. Valvatne and M.J. Blunt. Predictive pore-scale modeling of two-phase flow in mixed wet media. *Water Resources Research*, 40(7):W07406, 2004. 116

J. Van der Lee, E. Ledoux, and G. De Marsily. Modeling of colloidal uranium transport in a fractured medium. *Journal of Hydrology*, 139(1-4):135–158, 1992. 161

S.E. van der Zee. Analytical traveling wave solutions for transport with nonlinear and nonequilibrium adsorption. *Water Resources Research*, 26(10):2563–2578, 1990. 43

C.J. Van Duijn, A. Mikelic, I.S. Pop, and C. Rosier. Effective dispersion equations for reactive flows with dominant Peclet and Damkohler numbers. *Advances in Chemical Engineering*, 34:1–45, 2008. 45

M.T. van Genuchtan and P.J. Wieranga. Mass transfer studies in sorbing porous media. part 1. analytical solutions. *Soil Science Society of America Journal*, 40(4), 1976. 161, 170

M. van Genuchten. Th. 1980. a closed-form equation for predicting the hydraulic conductivity of unsaturated soils. *Soil Science Society of America Journal*, 44: 892–898, 1980. 92

M.T. Van Genuchten and W.J. Alves. Analytical solutions of the one-dimensional convective-dispersive solute transport equation. *Technical Bulletin*, (1661), 1982. 79

M.T. van Genuchten and R.W. Cleary. Movement of solutes in soil: computer-simulated and laboratory results. *Developments in Soil Science*, 5:349–386, 1979. 161

M.T. van Genuchten and R.J. Wagenet. Two-site/two-region models for pesticide transport and degradation: Theoretical development and analytical solutions. *Soil Science Society of America Journal*, 53(5):1303–1310, 1989. 170

A. Venkatarangan, W.B. Lindquist, J. Dunsmuir, and T.F. Wong. Pore and throat size distributions measured from synchrotron X-ray tomographic images of Fontainebleau sandstones. *Jopurnal of Geophysical Reserach–Solid Earth*, 105 (9):21509–21527, 2000. 22, 23

P. Vilks, L.H. Frost, and D.B. Bachinski. Field-scale colloid migration experiments in a granite fracture. *Journal of Contaminant Hydrology*, 26(1-4):203–214, 1997. 1, 158

H.J. Vogel and K. Roth. Quantitative morphology and network representation of soil pore structure. *Advances in Water Resources*, 24(3-4):233–242, 2001. 6, 68

H.J. Vogel, J. Tolke, V.P. Schulz, M. Krafczyk, and K. Roth. Comparison of a lattice-boltzmann model, a full-morphology model, and a pore network model for determining capillary pressure-saturation relationships. *Vadose Zone Journal*, 4 (2):380, 2005. 68

J. Wan and T.K. Tokunaga. Film straining of colloids in unsaturated porous media: Conceptual model and experimental testing. *Environmental science & technology*, 31(8):2413–2420, 1997. 159, 161, 162

J. Wan and T.K. Tokunaga. Measuring Partition Coefficients of Colloids at Air-Water Interfaces. *Environmental Science and Technology*, 32(21):3293–3298, 1998. 159

J. Wan and T.K. Tokunaga. Partitioning of clay colloids at air-water interfaces. *Journal of Colloid and Interface Science*, 247(1):54–61, 2002. 159

J. Wan and J.L. Wilson. Colloid transport in unsaturated porous media. *Water Resources Research*, 30(4):857–864, 1994a. 159, 160

J. Wan and J.L. Wilson. Visualization of the role of the gas-water interface on the fate and transport of colloids in porous media. *Water Resources Research*, 30(1): 11–23, 1994b. 159, 160

W.J. Weber, P.M. McGinley, and L.E. Katz. Sorption phenomena in subsurface systems: concepts, models and effects on contaminant fate and transport. *Water Research*, 25(5):499–528, 1991. 43

N. Weisbrod, O. Dahan, and E.M. Adar. Particle transport in unsaturated fractured chalk under arid conditions. *Journal of contaminant hydrology*, 56(1-2):117–136, 2002. 159

N. Weisbrod, M.R. Niemet, and J.S. Selker. Light transmission technique for the evaluation of colloidal transport and dynamics in porous media. *Environmental Science and Technology*, 37(16):3694–3700, 2003. 159

S. Whitaker. Advances in theory of fluid motion in porous media. *Industrial & Engineering Chemistry*, 61(12):14–28, 1969. 42, 48

S. Whitaker. Flow in porous media I: A theoretical derivation of Darcy's law. *Transport in Porous Media*, 1(1):3–25, 1986. 42, 48

A.F. White and S.L. Brantley. The effect of time on the weathering of silicate minerals: why do weathering rates differ in the laboratory and field? *Chemical Geology*, 202 (3-4):479–506, 2003. 43, 66

D. Wildenschild, C.M.P. Vaz, M.L. Rivers, D. Rikard, and B.S.B. Christensen. Using x-ray computed tomography in hydrology: systems, resolutions, and limitations. *Journal of Hydrology*, 267(3-4):285–297, 2002. 69

D. Wilkinson and J.F. Willemsen. Invasion percolation: a new form of percolation theory. *Journal of Physics A: Mathematical and General*, 16:3365, 1983. 21, 93, 138

B.D. Wood, M. Quintard, and S. Whitaker. Jump conditions at non-uniform boundaries: the catalytic surface. *Chemical Engineering Science*, 55(22):5231–5245, 2000. 42

B.D. Wood, M. Quintard, and S. Whitaker. Estimation of adsorption rate coefficients based on the Smoluchowski equation. *Chemical engineering science*, 59(10):1905–1921, 2004. 42

B.D. Wood, K. Radakovich, and F. Golfier. Effective reaction at a fluid-solid interface: applications to biotransformation in porous media. *Advances in Water Resources*, 30(6-7):1630–1647, 2007. 42

T. Xu, S.P. White, K. Pruess, and G.H. Brimhall. Modeling of pyrite oxidation in saturated and unsaturated subsurface flow systems. *Transport in porous media*, 39 (1):25–56, 2000. 66

K.M. Yao, M.T. Habibian, and C.R. O'Melia. Water and waste water filtration. Concepts and applications. *Environmental Science & Technology*, 5(11):1105–1112, 1971. 161

Li Yu and C. Wardlaw. Mechanisms of nonwetting phase trapping during imbibition at slow rates. *Journal of Colloid and Interface Science*, 109(2):473–486, 1986. 93

D.F. Yule and W.R. Gardner. Longitudinal and transverse dispersion coefficients in unsaturated Plainfield sand. *Water Resources Research*, 14(4):582–588, 1978. 127

Y. Zevi, A. Dathe, J.F. McCarthy, B.K. Richards, and T.S. Steenhuis. Distribution of colloid particles onto interfaces in partially saturated sand. *Environmental Science and Technology*, 39(18):7055–7064, 2005. 160

D. Zhang, R. Zhang, S. Chen, and W.E. Soll. Pore scale study of flow in porous media: Scale dependency, rev, and statistical rev. *Geophysical Research Letters*, 27(8):1195–1198, 2000. 68

T. Zhang, D.L. Li, D.T. Lu, and J.Q. Yang. Research on the reconstruction method of porous media using multiple-point geostatistics. *SCIENCE CHINA Physics, Mechanics & Astronomy*, 53(1):122–134, 2010. 95, 123

X. Zhang and M. Lv. The nonlinear adsorptive kinetics of solute transport in soil does not change with pore-water velocity: Demonstration with pore-scale simulations. *Journal of Hydrology*, 2009. 67, 87

X. Zhang, J.W. Crawford, and I.M. Young. Does pore water velocity affect the reaction rates of adsorptive solute transport in soils? demonstration with pore-scale modelling. *Advances in Water Resources*, 31(3):425–437, 2008. 6, 67, 69, 87

X. Zhao and JF Sykes. Macroscopic scale solute transport in groundwater using the lattice boltzmann equation. *COMPUTATIONAL MECHANICS PUBLICATIONS, SOUTHAMPTON, SO 40 7 AA(UK).*, pages 235–243, 1996. 68

D. Zhou, L.A. Dillard, and M.J. Blunt. A physically based model of dissolution of nonaqueous phase liquids in the saturated zone. *Transport in Porous Media*, 39(2): 227–255, 2000a. 134, 164

D. Zhou, L.A. Dillard, and M.J. Blunt. A physically based model of dissolution of nonaqueous phase liquids in the saturated zone. *Transport in Porous Media*, 39(2): 227–255, 2000b. 6, 68, 97

B. Zinszner and C. Meynot. Visualisation des propriétés capillaires des roches réservoir. *Oil & Gas Science and Technology*, 37(3):337–361, 1982. 94

Samenvatting

Transportverschijnselen zijn met behulp van porienetwerk modellen op fundamentele wijze te bestuderen, omdat de fysische processen die plaatsvinden op de porieschaal eenduidig kunnen worden verwerkt. Hierdoor kunnen we dergelijke modellen gebruiken om consistente opschalingsrelaties te ontwikkelen en een potentiele brug te slaan tussen de anders vaak moeilijk verenigbare procesbeschrijvingen op de porie- en macroscopische schaal.

In dit proefschrift hebben we een MultiDirectioneel PorieNetwerk (MDPN) model ontwikkeld. In principe bestaat een porienetwerk uit bolvormige lichamen, porielichamen genoemd, die met elkaar verbonden zijn door een of meerdere connecties, porienekken. MDPN onderscheidt zich van andere porienetwerken door een grotere variatie in mogelijke porienek connecties en -orintaties, waardoor poreuze media realistischer benaderd worden.

Stroming en transport door (on)verzadigde poreuze media worden in MDPN gesimuleerd door de massabalansvergelijking op te lossen op het niveau van individuele porielichamen en -nekken; elementen waarvoor deze processen goed gedefinieerd zijn. Locale concentraties opgeloste stoffen worden verkregen door stofoverdracht en adsorptie/reactie aan het poriewandoppervlak, en op de fasegrensvlakken, te modelleren. Macroscopische eigenschappen, zoals permeabiliteit, dispersie en gemiddelde concentraties, worden bepaald door deze locale waardes te middelen over het gehele porienetwerk of over specifieke secties door het domein.

We hebben opgeschaalde parameters, zoals permeabiliteit, de spreidingscoefficient en adsorptie, bepaald voor verzadigde poreuze media. Er is gekeken naar de relatie tussen capillaire druk en saturatie, de relatieve permeabiliteit, dispersie en adsorptie in onverzadigde systemen. De verkregen resultaten zijn, waar mogelijk, vergeleken met experimentele waarnemingen en macroschaal modellen, om zo de toereikendheid en limitaties van opschalingsvergelijkingen te onderzoeken.

رسید مژده که آمد بهار و سبزه دمید وظیفه گر برسد مصرفش گل است و نبید

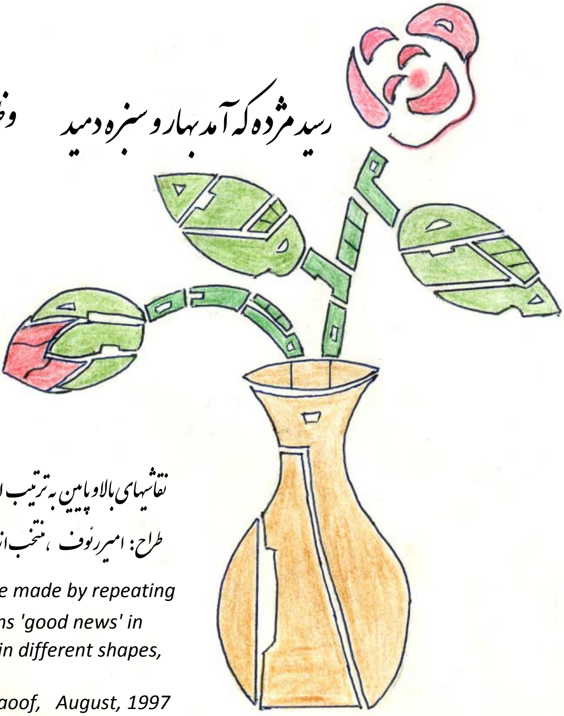

نقاشیهای بالا و پایین به ترتیب از ۷ و ۸ بار تکرار کلمه مژده تشکیل شده‌اند.

طراح: امیر رئوف ، منتخب از دفتر ۳۳ مژده، ۲۶ مرداد ۱۳۷۶

The top and bottom paintings are made by repeating the word 'Mozhdeh' (مژده means 'good news' in Persian poetry) by 7 and 8 times in different shapes, respectively.

by: Amir Raoof, August, 1997